Journal of the Serbian Chemical Society

*e*Version
*e*lectronic

Society
115th
Anniversary
1897 - 2012

VOLUME 77

No 3

BELGRADE 2012

Available on line at

СХД
1897

www.shd.org.rs/JSCS/

CONTENTS

Modeling key interactions between the second extracellular loop of the dopamine D2 receptor and arylpiperazine ligands

VLADIMIR ŠUKALOVIĆ[1*#], VUKIĆ ŠOŠKIĆ[2], DEANA ANDRIĆ[3], GORAN ROGLIĆ[3]
and SLADJANA KOSTIĆ-RAJAČIĆ[1#]

[1]*ICTM – Department of Chemistry, University of Belgrade, Njegoševa 12, 11000 Belgrade, Serbia,* [2]*ProteoSys AG, Carl Zeiss 51, 55129 Mainz, Germany and* [3]*Faculty of Chemistry, University of Belgrade, Studentski trg 12–16, 11000 Belgrade, Serbia*

Abstract: Second extracellular loop (ecl2) of the dopamine (DA) D2 receptor is an essential part of the binding pocket of dopaminergic ligands. To form a part of the ligand-binding surface, it has to fold down into the transmembrane domain of the DA receptor. The current study describes the modeling of the D2 DA receptor ecl2 and its interactions with arylpiperazine ligands. In order to model the D2 DA receptor ecl2, several arylpiperazine ligands were used to propose a pharmacophore model. D2 DA receptor ecl2 model was built using Accelrys Discovery Studio. To test the proposed model, docking analysis was performed and key amino acid residues were determined. The proposed receptor–ligand interactions were rationalized and compared with measured binding affinities. It is shown that D2 DA receptor ecl2 significantly participates in the formation of the receptor–ligand complex through aromatic, hydrophobic and polar interaction. Considering them would benefit molecular modeling of G-protein-coupled receptors (GPCRs) and facilitate the design of novel active compounds.

Keywords: extracellular loop; dopamine; arylpiperazine; molecular modeling; GPRC.

INTRODUCTION

The catecholamine dopamine (DA) has been associated with many physiological functions such as fine movement coordination, cognition, emotion and memory by the mesocortical and mesolimbic reward systems.[1]

Alterations in dopaminergic function are involved in the pathogenesis of Parkinson's disease,[2] psychomotor diseases and schizophrenia.[3]

259

The DA receptor system has been aggressively targeted for drug development for the treatment of psychiatric illnesses, neurodegeneration, drug abuse, and other therapeutic areas.[4,5] The DA receptors, belonging to the class of G-protein-coupled receptors (GPCRs), are found in both the peripheral and central nervous system (CNS).[3] The D2 DA receptor is a GPCR located on postsynaptic dopaminergic neurons that is heavily involved in reward-mediating mesocortico-limbic pathways. Signaling through D2 DA receptors governs physiological functions related to locomotion, hormone production, and drug abuse. D2 DA receptors are also known targets for antipsychotic drugs used to treat psychomotor diseases such as schizophrenia.[6] Although the biophysical and pharmacological properties of D2 DA receptors have been the subject of a number of studies,[7] many questions remain unresolved due to the lack of three-dimensional structures and other experimental limitations.

An enormous amount of work has been performed toward the development of various D2 DA receptor ligands. These efforts yielded a class of compounds known as dopaminergic arylpiperazine ligands.[8]

The pharmacophore of dopaminergic arylpiperazines has been well studied in experiments and molecular simulations.[9] Published results and 3D models explain to some extent the binding mechanism of arylpiperazine to the D2 DA receptor,[10–12] but still a complete understanding of the process is lacking, notably in the case of ligands that protrude from the canonical receptor binding site into the extracellular loop area. To obtain a better understanding of receptor–ligand interactions, a more precise model of the D2 DA receptor is required.

In this paper, focus will be centered on the extracellular loop area of the D2 DA receptor, particularly on the E2 loop segment. Considering that the crystal structures of D2 DA receptors are not available, *in silico* methods were used to gain further insight into the binding interactions between the extracellular loop area of D2 DA receptors and a new series of dopaminergic arylpiperazines.

EXPERIMENTAL
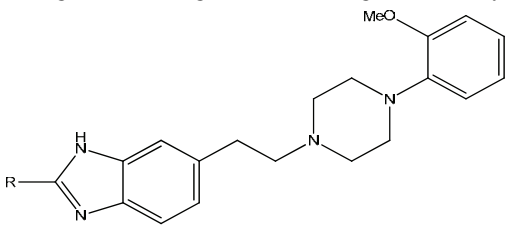
Ligand construction
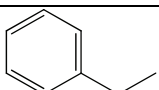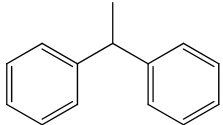
The 3D structures of the ligands were generated using the Discovery Studio program.[12] Assuming physiological conditions, the basic aliphatic nitrogen atom of the piperazine was protonated. The geometry was optimized using the CHARMM force field applying the conjugate gradient method until the energy difference between successive cycles was below 0.0042 kJ mol^{-1}.

Pharmacophore model generation

The set of ligands used for pharmacophore generation consisted of the structures shown in Tables I and II with their dopamine D2 receptor binding affinities listed. The molecules were stored in a molecular database. This database was used as an input in the Discovery Studio pharmacophore protocol[12].

TABLE I. Arylpiperazine ligands showing moderate to high D2 affinity

No.	R	K_i / nM
1[13]		2.9
2[13]		56.0
3[14]	CH_3SCH_2-	15.4
4[14]	CH_3SOCH_2-	24.8

The objective of the pharmacophore protocol is to generate all popular pharmacophore queries (with coverage *n*, typically 90 % or more of all active molecules) considering all possible discrete geometries with all possible combinations of input query expressions. The pharmacophore protocol operates on the 3D conformations of the molecules present in the input database. In the present study, the Conformations option in Pharmacophore protocol panel was set to BEST quality, wherein the rotatable bonds of each molecule were explored systematically to specific torsion angles from a collection of rules. The ring conformations were not searched; the chair conformation was assumed preferred as most of the docking runs finished with the ligands having the ring in the chair conformation.

Using these features for the determination of the minimal pharmacophore together with the enabled alignment of the aromatic ring atoms led to meaningful pharmacophore hypotheses. The pharmacophore protocol generated pharmacophores compatible with the minimal number of set features. Other parameter values in the pharmacophore protocol panel were kept at their default values. The results of the pharmacophore generation were written to an output database, which was analyzed further to visualize the appropriate pharmacophore hypothesis. The selection of the final hypothesis was based on an overall alignment score and the associated pharmacophore features.

Molecular modeling of D2 DA receptor extracellular loops

The starting point for molecular modeling was the currently valid loop-less dopamine D2 receptor model.[9] The Discovery Studio program package[12] was used to model the sequences of D2 DA receptor loops. Missing loops sequences were aligned with the D2 receptor sequence and this alignment was supplied along with the 3D coordinates of the existing model as an input to the program. A key determinant of the correct orientation of the extracellular loops is the constrain imposed by the position of the corresponding receptor helixes and a disulfide bond between the ecl2 and the top of the TM domain 3. The Discovery Studio loop refining implements protein loop modeling by satisfying these restraints while keeping the

existing part of the model fixed. This was followed by spatial constraints that were imposed to selected amino acid residues in order to satisfy the pharmacophore hypothesis. In order to obtain a relaxed conformation, the generated models were initially subjected to an energy minimization process using the conjugate gradient method for about 4000 iterations and to 2-ns isothermal, constant-volume MD simulation, with CHARMM all-hydrogen amino acid parameters in the Discovery Studio program running on a PC.[15] To assess the quality of the minimized models, Proteincheck[12] analysis was also undertaken. Initially, several possible models were constructed but the best possible model was considered the receptor "energy minima".

Docking analysis

Docking of the selected ligands as presented in Tables I–III was realized by simulated annealing using the LIBDOCK module from Discovery Studio. All ligands were docked as protonated, using the CHARMM force field. Amino acid residue charges were adjusted when needed. The protein-binding site was determined by combining results from experimental data and the Discovery Studio bind site analysis module.[12] Initial position of the ligand in the binding site was defined by keeping the protonated nitrogen on the ligand in close proximity to the Asp80 of the D2 receptor. After initial ligand placement, no further constraints were applied and the docking procedure based on Monte Carlo methodology was performed. Up to 100 structures were produced in every run and each finally optimized in order to remove steric interaction with a gradient limit of 0.0042 kJ mol^{-1} or 4000 optimization steps.

TABLE II. The arylpiperazine ligands used in the generation of the pharmacophore model and the docking analysis (marked +)

No.	R$_1$	R$_2$	K_i / nM
5[16]		–CONH(CH$_2$)$_4$–	83±5
6[16]		–CONH(CH$_2$)$_4$–	84±2
7+[16]		–CONH(CH$_2$)$_4$–	75±12

TABLE II. Continued

No.	R_1	R_2	K_i / nM
8+[16]		–CONH(CH$_2$)$_4$–	59±9
9[16]		–CONH(CH$_2$)$_4$–	87±19
10[16]			86±1
11[16]		–(CH$_2$)$_4$–	45±7
12[17]		–CH=CH–CONH–(CH$_2$)$_4$–	13±1
13[17]		–CH=CH–CONH–(CH$_2$)$_4$–	20±1
14[17]		–CH=CH–CONH–(CH$_2$)$_4$–	23±1
15[17]		–CH=CH–CONH–(CH$_2$)$_4$–	37±6
16+[17]		–CH=CH–CONH–(CH$_2$)$_4$–	10±0.7
17[17]		–CH=CH–CONH–(CH$_2$)$_4$–	14±3

TABLE II. Continued
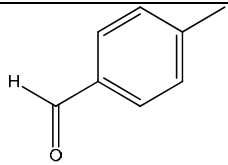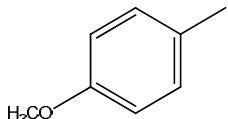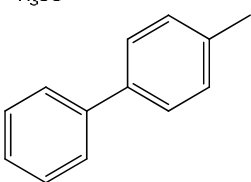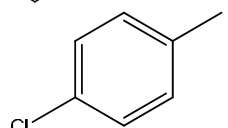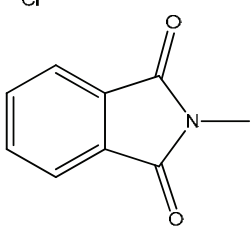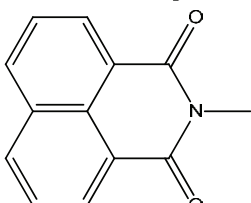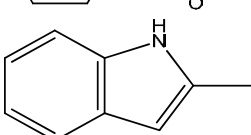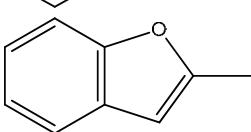
No.	R$_1$	R$_2$	K_i / nM
18+[17]		–CH=CH–CONH–(CH$_2$)$_4$–	11±2
19[17]		–CH=CH–CONH–(CH$_2$)$_4$–	12±1
20[17]		–CH=CH–CONH–(CH$_2$)$_4$–	37±15
21[17]		–CONH(CH$_2$)$_4$–	19±1
22[17]		–(CH$_2$)$_4$–	50±6
23+[17]		–(CH$_2$)$_4$–	40±3
24[18]		–CONH–(CH$_2$)$_4$–	37±6
17+[18]		–CONH–(CH$_2$)$_4$–	36±4

TABLE II. Continued
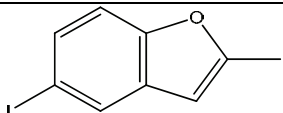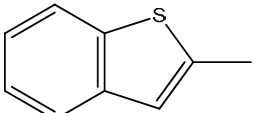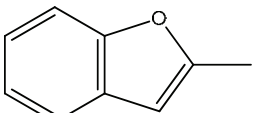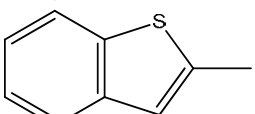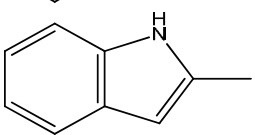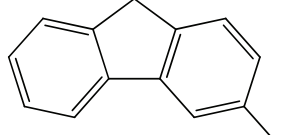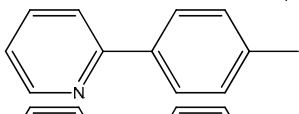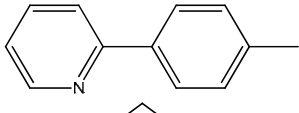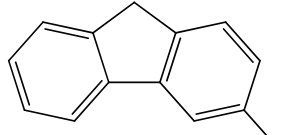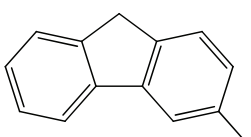
No.	R$_1$	R$_2$	K_i / nM
18[18]		–CONH–(CH$_2$)$_4$–	77±17
19+[18]		–CONH–(CH$_2$)$_4$–	21±2
28[18]		–CONH–CH$_2$CH=CHCH$_2$–	79±2
29[18]		–CONH–CH$_2$CH=CHCH$_2$–	60±7
30[18]		–CONH–CH$_2$CHOH–(CH$_2$)$_2$–	52±3
31[19]		–CONH–(CH$_2$)$_4$–	55±5
32+[19]		–CONH–(CH$_2$)$_4$–	28±6
33[19]		–CONH–CH$_2$CH=CHCH$_2$–	69±13
34+[19]		–CONH–CH$_2$CH=CHCH$_2$–	48±7
35[19]		–CONH–CH$_2$CHOH–(CH$_2$)$_2$–	68±6

TABLE II. Continued
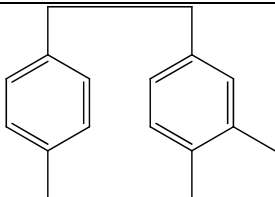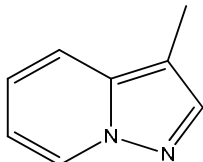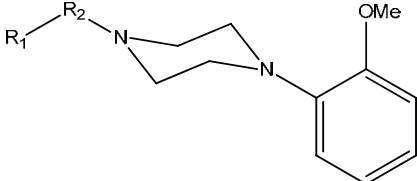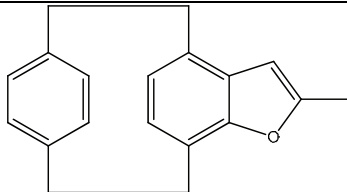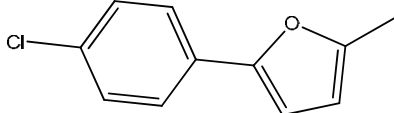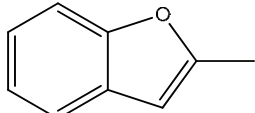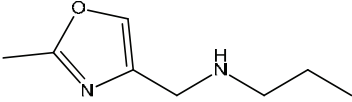
No.	R₁	R₂	K_i / nM
36+[20]		–CONH–(CH$_2$)$_4$–	15±1
37+[21]		–CONH–(CH$_2$)$_3$–	11±1

TABLE III. Arylpiperazine ligands used in the testing of the receptor model

No.	R₁	R₂	K_i / nM
38[19]		–CONH(CH$_2$)$_4$–	83±5
39[16]		–CONH(CH$_2$)$_4$–	200±30
40[22]			518±193

The obtained docked structures were examined, and those with the lowest total energy were further filtered to obtain docking structures with the best ligand fit. We selected structures based on the following criteria: lowest total energy of the complex, shortest salt bridge formed between Asp80 of the D2 receptor and the proton on nitrogen, chair conformation of arylpiperazine ring and the aryl part of the molecule positioned in the rear hydrophobic pocket of the receptor were selected. After the initial criterion was satisfied, the second step was examination of different interactions that could be formed between the receptor and ligand (hyd-

rogen bonds, aromatic–aromatic interactions, *etc*.). In this way, the best possible docking structures were selected. Structures were visualized using DS Visualise v2.5.1[23] and the obtained images were rendered using PovRay Raytracer v3.6.[24]

RESULTS AND DISCUSSION

The currently used loop-less D2 DA receptor model could not explain the binding affinities for a number of synthesized arylpiperazine ligands (Table I). Docking analysis suggested that these ligands are not able to fit into the existing binding site[9] due to their size, and that they protruded into the extracellular loop (ecl) area of the D2 DA receptor. The importance of the ecls for accommodating high molecular weight GPCR ligands (peptides and proteins) is widely accepted.[25] Recent studies indicate the same could be true for low molecular weight ligands.[22,26,27]

These findings emphasized that a new D2 model that includes the loops, should be constructed. In this study the focus was on the modeling of the extracellular loops as they border the receptor binding site and could interact with ligand molecules.[28]

Receptor loop modeling is a challenging task because, in contrast to the alpha helix or beta sheet, they do not fit into the defined 3D template and a careful decision has to be made on how to differentiate between a myriad of possible conformations.

Initial attempts to model the D2 receptor with loops *in silico*, using different existing templates, failed to produce a viable model. Construction of the ecls should be realized with care and guided by receptor-specific experimental data, rather than being performed in a high-throughput fashion and derived directly from the known crystal structure.[29]

In order to solve this problem, computational methods, pharmacophore model generation and docking analysis, together with experimental results, were applied in this study. Apart from general ecl2 modeling, the aim of this study was to discover the ecl2 amino acid residues responsible for D2 DA receptor–ligand interactions. The pharmacophore model hypothesis predicts the type of receptor––ligand interactions, thus ecl2 was modeled in a way to facilitate such interactions, and docking analysis was employed to confirm that these interactions are *de facto* possible.

Pharmacophore model generation requires a considerable ligand database, which was obtained from available literature sources.

To facilitate the search, the molecular structure of the arylpiperazine ligands was divided into three distinct substructure motives: tail (arylpiperazine substructure), flexible linker and head part (usually the bulky aromatic group, see Fig. 1). The tail part of the ligand was kept fixed, while the linker and head part were subjected to variations in length and size. The tail part was fixed to 1-(2-methoxyphenyl)piperazine since the interaction of this structural motive with the D2

DA receptor is well investigated.[10] The length of the linker is crucial for the receptor–ligand interaction, since it positions the head of the ligand against the amino acid residues located in the extracellular loops of the receptor, and was therefore allowed to vary. In addition, differences in size, shape and functionality of the head were tolerated, allowing investigation of the influence of these molecular diversities on the ligand binding affinity. More than 80 ligands were considered of which, 33 were selected for further investigation. Only ligands with a moderate to high affinity (K_i under 100 nM) were taken into consideration.
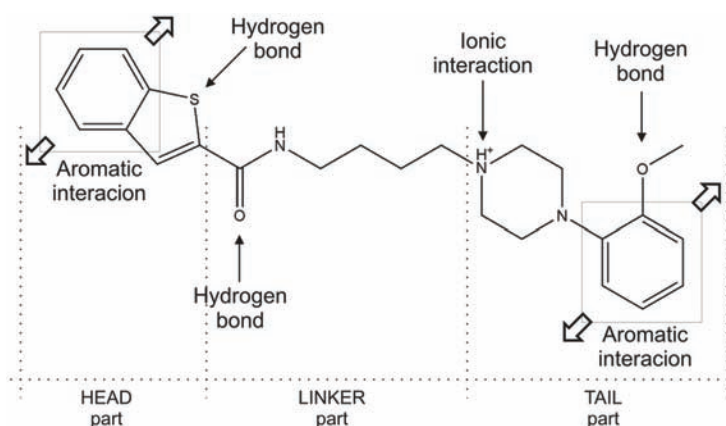
Fig. 1. Schematic presentation of the proposed key interactions, generated by the pharmacophore hypothesis.

Pharmacophore model generation was performed using Discovery Studio, as described. In total, 33 ligands were used to generate the pharmacophore model hypothesis. The obtained results are shown in Figs. 1 and 2. The pharmacophore model hypothesis suggests salt bridge formation between the protonated piperazine nitrogen atom and the receptor, one or more aromatic interactions at the tail part of the ligand, together with a hydrogen bond between the oxygen atom of the methoxy group and the receptor. In the linker part, there is the possibility of hydrogen bond formation, while in the head part of the ligand, one or more interactions were expected. These interactions could be of an aromatic nature or a hydrogen bond, depending of the chemical structure of the head of the ligand.

Docking studies of these bulky ligands performed with the loop-less D2 DA receptor model could not explain the high affinities obtained in the binding studies. Therefore, it was hypothesized that some additional interaction with the out--of-membrane receptor domain is involved. Molecular modeling that took into consideration interactions with ecl2 gave the best results. The ligands that can form additional aromatic type interaction or hydrogen bond in the head part can do so exclusively with amino acid residues located in the ecl2 region of the D2

DA receptor. Other proposed ligand–receptor interactions, such as the salt bridge formed between ASP80 and the protonated piperazine nitrogen, hydrophobic interactions between PHE178, TRP182 and TYR212 and arylpiperazine, and hydrogen bond formation between the 2-methoxy group oxygen and TYR212, are located in the transmembrane domain of the receptor molecule and are described in an earlier publication.[9]
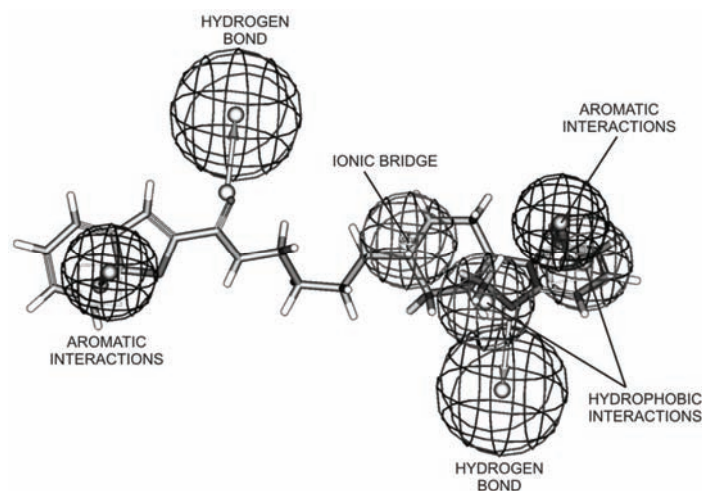
Fig. 2. Proposed pharmacophore hypothesis mapped on ligand **9**. Proposed key interactions are shown as vectors and spheres, depicting the direction and space where a particular interaction is expected.

Modeling of the ecl2 is described in the experimental part; particular attention was given to the orientation of the hydrophobic amino acid residues as good candidates to form aromatic interactions with ligands.

The generated DA D2 receptor models with extracellular loops were tested using docking analysis until a satisfactory model that could explain the binding and activities of the selected ligands was obtained.

In total, 11 literature ligands with activities ranging from 10 to 75 nM were selected for the docking analysis (Table II). It was decided to use ligands that had a significant affinity towards the D2 DA receptor while taking into account the structural diversity that could account for the proposed aromatic interactions and hydrogen bond formation with the ecl2 of the D2 DA receptor.

Preliminary ligand docking was performed to allow the ligand to position itself inside the binding site. After a satisfactory ligand orientation had been obtained (salt bridge formation between ASP80 and the protonated ligand nitrogen atom, aryl moiety positioned inside the hydrophobic pocket formed by PHE178, TRP182 and TYR212, one or more hydrogen bonds formed with SER149 and/or SER122), fixed atom constraints were applied on the ligand and receptor amino

acids backbone, excluding those in the ecls that were allowed to move freely. An additional docking run was executed whereby optimal positioning of the ecls amino acid residues was allowed. Finally, molecular dynamics calculations followed by energy minimization were performed to remove any steric interactions. The obtained results are shown in Figs. 3–6. Thus, it is shown that the selected ligands can bind into proposed D2 DA receptor model and form interactions with the amino acid residues of the ecl2 loop, as required by the pharmacophore hypothesis, while simultaneously concurring with recent findings (Fig. 3).[12,28]
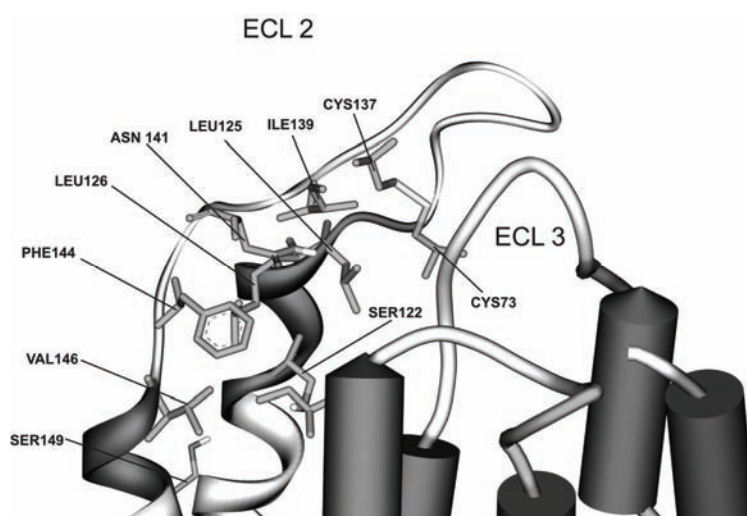
Fig. 3. Generated model of ecl2. Key amino acid residues responsible for interactions with the investigated ligands obtained by docking analysis are shown together with the conserved disulfide bond between ecl2 and ecl3.

All the investigated ligands bind in a similar manner. The main features of the docked complexes are short salt bridges between the protonated nitrogen of the piperazine ligand and ASP80 and the number of interactions formed by the aryl tail section and the corresponding amino acids (PHE178, TRP182 and TYR212).

Ligand **36** is the bulkiest ligand, with a high receptor affinity (Fig. 4). Its large hydrophobic head must be docked into the appropriate hydrophobic receptor pocket that is formed by the amino acid residues LEU125, LEU126, ILE139, VAL146, PHE144, HIS189 and ILE190. The head of the ligand can form a number of hydrophobic interactions with the listed amino acid residues. Special attention should be given to PHE144 and HIS189, as they are in a range that could lead to the formation of edge-to-face (etf) interactions. These interactions together with the hydrogen bond formed with SER122 are responsible for the high ligand affinity.
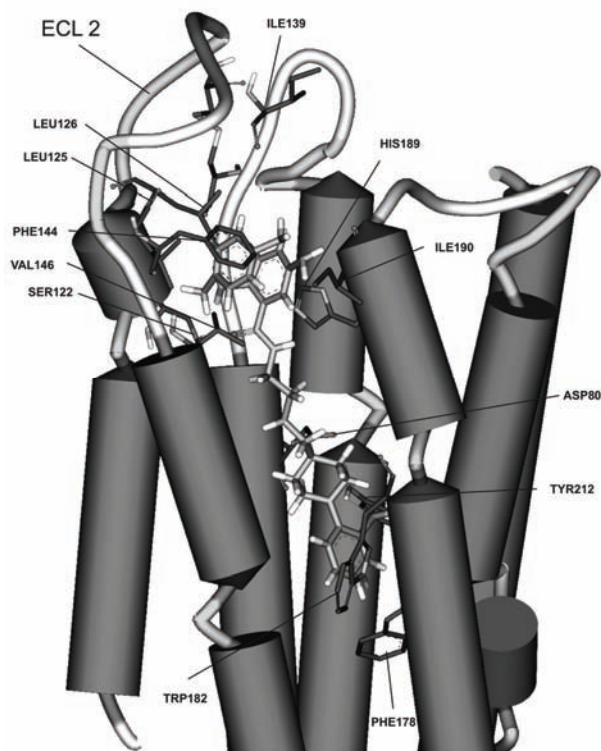
Fig. 4. Docking results for ligand **36**. Only key amino acid residues are shown for clarity.

Ligands that have large hydrophobic groups in the head part (ligands **7**, **8**, **23**, **25**, **32**, **34** and **37**) bind to the hydrophobic pocket that is formed in part by ecl2 (Fig. 5). This is the same pocket formed by PHE144, LEU125, ILE139, LEU126, VAL146 and ILE190, as in case of ligand **36**. Docking analysis shows possible interactions formed by PHE144 (edge-to-face) and HIS189 on TM6 (NH⋯Pi or CH⋯Pi) interactions with the ligand.

Ligand **16** (Fig. 5) and ligands **13**–**15** and **17**–**19** are somewhat different as their head part contains groups capable of forming polar interactions or hydrogen bonds. In the case of these ligands, in addition to the already listed interactions, polar interactions with ASN141 in ecl2 could account for their activity.

All ligands from Table II form one or more interactions with ecl2, based on their structure, and these interactions are responsible for their activity. For example, ligands **12**, **13**, **24**, **36**, **38**–**41** form aromatic interactions with hydrophobic amino acid residues. These interactions may include edge-to-face interactions with PHE144 and HIS189. Ligands **16**–**23** can form either hydrogen bonds or polar interactions with ASN141. Ligands **4**–**14**, **26**–**35** and **42** can benefit from listed aromatic interactions and hydrogen bond with SER122.
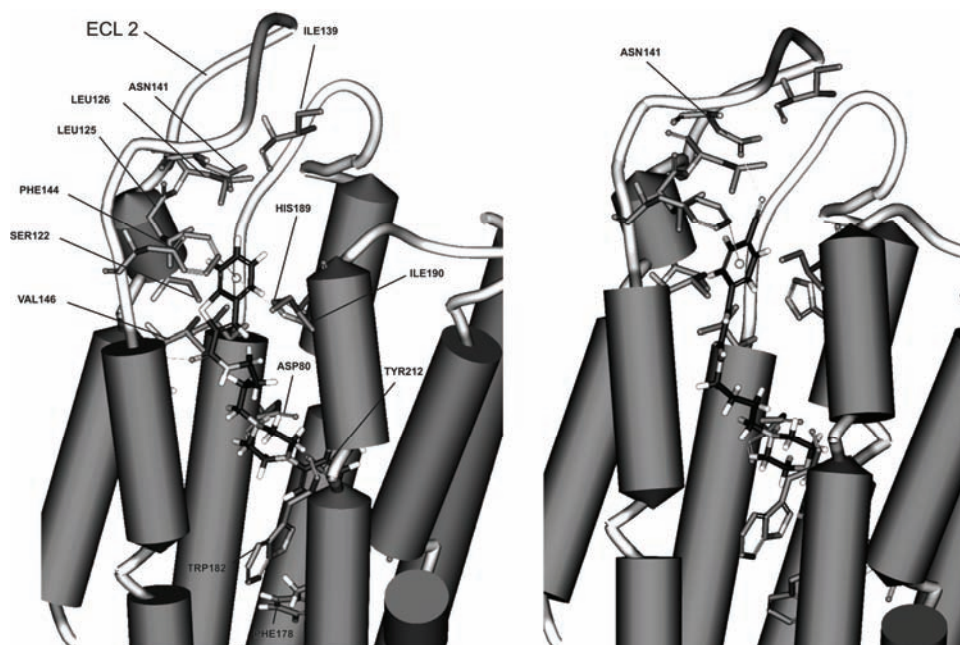
Fig. 5. Ligands **27** (left) and **16** (right) docked into the D2 receptor.
Only key amino acid residues are shown for clarity.
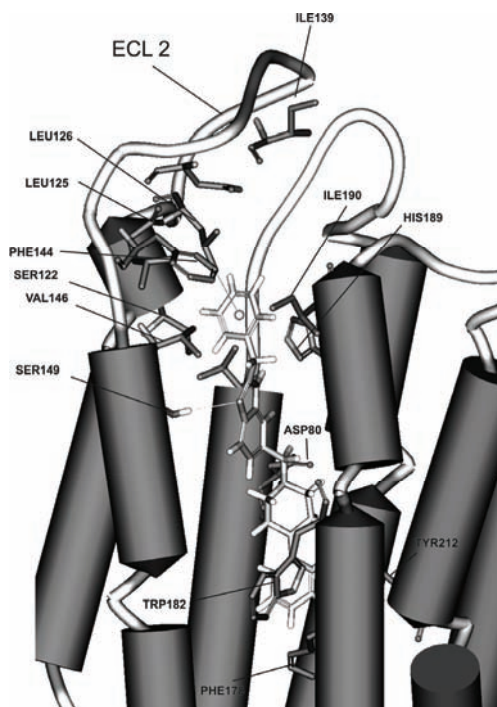
Fig. 6. Ligand **1** docked into the proposed D2 model. Possible interactions with PHE144 and SER 149 are marked as lines.

The final test of the model was its ability to discriminate high affinity *versus* low affinity ligands. The test was performed on compounds homologous to the active ligands (Table II) but with significantly lower D2 DA receptor affinity. Chemical structures alongside the affinity data of these compounds are presented in Table III.

The results of docking analysis are shown in Fig. 7. Ligand **38** is similar to **36**, yet its binding affinity is 10-fold lower. The ligand cannot optimally fit into the proposed pocket, formed by elc2 amino acid residues, as multiple bump interactions with SER122 and HIS189 are observed (Fig. 7, left), furthermore due to different ligand orientation hydrogen bound with SER122 is lacking.
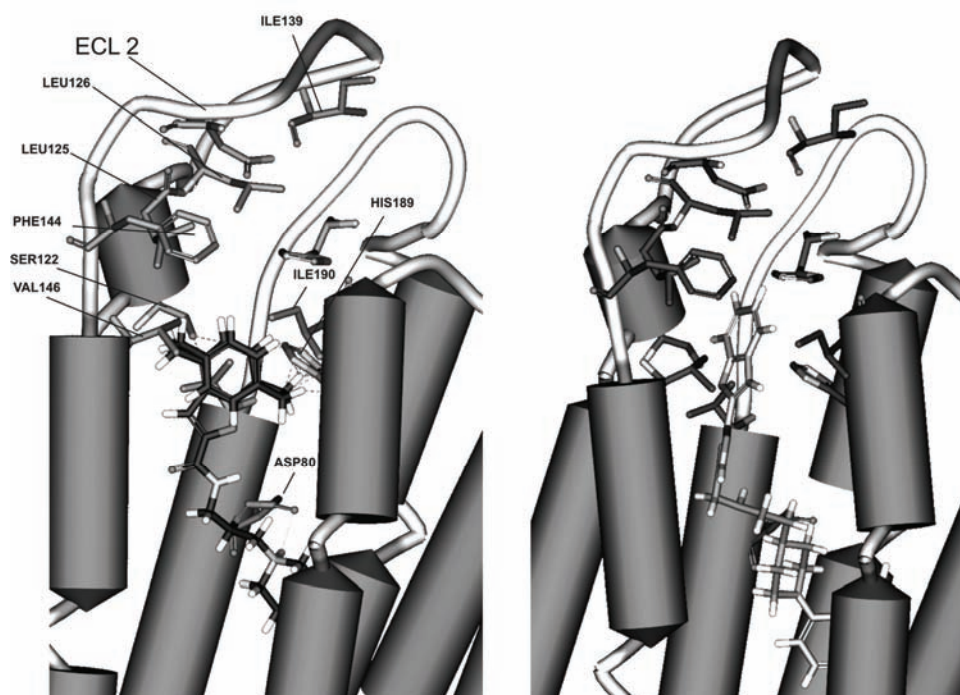
Fig. 7. Docking results for the low affinity arylpiperazine ligands **38** (left) and **40** (right). Only key amino acid residues are shown. Bump interactions are marked as dashed lines.

Ligand **40** is similar to ligand **10**. The increase in overall length of ligand **40** is a key factor for its ten-fold decrease in affinity. Being both long and rigid, ligand **40** suffers from unfavorable steric interactions with amino acid residues in the receptor ecl2. Due to its inability to fit into the binding site, all the observed key interactions have longer distances. Most notably, the salt bridge with ASP80 is elongated by 1 Å, and the hydrogen bonds with SER122 and SER149 are con-

ŠUKALOVIĆ *et al.*

siderably longer (3.57 and 3.92 Å compared to 2.47 and 2.98 Å in ligand **10**, Fig. 7, right).

Similar factors can explain the seven-fold decrease in affinity of **39** *vs*. **21**. In the case of ligand **39**, the introduction of the furan ring into the head segment leads to a loss in binding affinity, due to steric interaction between the chlorine atom and ASN141. This steric interaction pushes the ligand down into the binding site, making the key interactions with ASP80 and SER122 longer by 1 Å (Fig. 8).
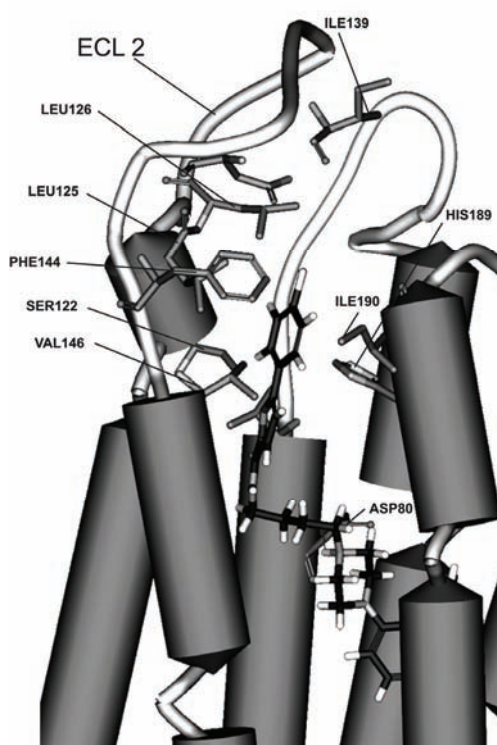
Fig. 8. Docking result for the low affinity arylpiperazine ligand **39**. Only key amino acid residues are shown.

Finally, the proposed D2 DA receptor model was used to explain the binding affinities of the ligands shown in Table I. Docking results showed that ligands **1** and **2** forms multiple aromatic interactions with PHE144, LEU125, LEU126 and VAL146 (Fig. 6). Ligands **3** and **4**, which cannot form aromatic interactions, still benefit from hydrogen bonds formation or polar interactions with ASN141 in ecl2.

CONCLUSION

The primary aim of the current study was to provide a new D2 DA receptor model that includes ecls that is capable of explaining existing experimentally obtained affinity data for bulky arylpiperazine type ligands.

Modeling ecls residues *in silico* is highly speculative as they are located in the part of the molecule that cannot be directly derived from the existing structural templates. Although the recent publishing of the crystal structure of the D3 DA receptor[17] is a significant step forward, it was decided to employ the existing, experimentally proved D2 DA receptor model, which was made by combining *in silico* methods and experimental data and proved by experimental results.[9–11] Still, the exact structure of the D2 DA receptor remains unknown and, therefore, every model that can explain experimental data should be considered. The model described in this study can explain the DA receptor binding properties of arylpiperazine classes of ligands; hence, it could be of great value for virtual screening studies.

The employed approach in modeling ecls was twofold. First, a pharmacophore model was constructed using a number of different ligands, having a common arylpiperazine moiety. This model indicated to a number of possible interactions between a ligand and the receptor, including interactions in the ecl2 part. Based on these assumptions, the ecls were modeled. Then, docking analysis was performed to position the ligand inside the receptor-binding site, until all known interactions were established. The ecl2 residues were then adjusted to form other interactions predicted by the pharmacophore model. Further energy minimization and molecular dynamics were used to refine the obtained results.

During the modeling process, a number of key amino acid residues located in the ecl2 that could form interactions with ligands were observed. These interactions, which lead to high ligand affinity, included aromatic interactions with PHE144, LEU125, LEU126, VAL146 and ILE190 and polar interactions with ASN141. Aromatic interactions are most likely edge-to-face type with PHE144 or CH···Pi (or NH···Pi) interactions with HIS189. Polar interaction with ASN135 could also be responsible for the high binding affinity of ligands with the corresponding functional groups. The size of the ligand is important. Short ligands do not benefit from interactions with ecl2, while long ones suffer from steric interactions with amino acid residues in the loop. The head part of the ligand should have at least one aromatic ring, but systems with two or more aromatic rings are well tolerated unless the maximum allowed length of the ligand is attained. High affinity could be achieved by aromatic interactions alone, or together with polar interactions. Ligands with halogen atoms or polar groups have affinities comparable with those of their aromatic analogues. The linker part of the ligand should be as flexible as possible, since its primary function is to allow the optimum positioning of the head part into the space formed by the ecl2.

For the sake of verification of the proposed D2 DA receptor model, further work on the target-driven synthesis of new ligands that can distinguish between the proposed molecular interactions are necessary. The final goal is to obtain a

workable D2 DA receptor model that will facilitate the design of new specific dopaminergic drugs.

И З В О Д

МОДЕЛОВАЊЕ КЉУЧНИХ ИНТЕРАКЦИЈА ИЗМЕЂУ ДРУГЕ ЕКСТРАЦЕЛУЛАРНЕ ПЕТЉЕ ДОПАМИНСКОГ D2 РЕЦЕПТОРА И АРИЛПИПЕРАЗИНА КАО ЛИГАНАДА

ВЛАДИМИР ШУКАЛОВИЋ[1], ВУКИЋ ШОШКИЋ[2], ДЕАНА АНДРИЋ[3], ГОРАН РОГЛИЋ[3] и СЛАЂАНА КОСТИЋ-РАЈАЧИЋ[1]

[1]*ИХТМ – Центар за хемију, Универзитет у Београду, Његошева 12, 11000 Београд,* [2]*ProteoSys AG, Carl Zeiss 51, 55129 Mainz, Germany и* [3]*Хемијски факултет, Универзитет у Београду, Студентски трг 12–16, 11000 Београд*

Друга екстрацелуларна петља допаминског D2 рецептора је есенцијални део везивног места рецептора. Да би се дефинисала горња страна везивног места, она мора да се савије надоле, и оријентише ка трансмембранском домену рецептора. У овом раду описан је процес моделовања друге екстрацелуларне петље допаминског D2 рецептора и њене интеракције са арилпиперазинским лигандима. За моделовање је коришћен *Accelrys Discovery Studio* пакет програма. Предложени модел је тестиран докинг анализом литературно доступних лиганада и поређењем добијених резултата са њиховим афинитетом везивања за D2 рецептор. Одређени су амино-киселински остаци који ступају у интеракције са лигандима. Кључне интеракције су дефинисане и упоређене са афинитетима лиганада према рецептору како би се предложеним моделом објасниле разлике у експерименталним резултатима. Наша истраживања су показала да друга екстрацелуларна петља допаминског D2 рецептора може ступати у различите интеракције са арилпиперазинским лигандима које између осталих укључују хидрофобне, ароматичне интеракције али и водоничне везе. Ова сазнања, у комбинацији са предложеним моделом D2 рецептора, који укључује екстрацелуларне петље, могу бити од велике користи приликом будућег дизајна нових допаминергичких лиганада.

(Примљено 28. октобра 2011)

REFERENCES

1. C. Missale, S. R. Nash, S. W. Robinson, M. Jaber, M. G. Caron, *Physiol. Rev*. **78** (1998) 189
2. J. Lotharius, P. Brundin, *Nat. Rev. Neurosci*. **3** (2002) 932
3. S. Kapur, D. Mamo, *Prog. Neuropsychopharmacol. Biol. Psychiatry* **27** (2003) 1081
4. G. Emilien, J. M. Maloteaux, M. Geurts, K. Hoogenberg, S. Cragg, *Pharmacol. Ther.* **84** (1999) 133
5. E. P. Noble, *Am. J. Med. Genet., B* **116** (2003) 103
6. S. L. Payne, A. M. Johansson, P. G. Strange, *J. Neurochem*. **82** (2002) 1106
7. J. A. Javitch, D. Fu, J. Chen, A. Karlin, *Neuron* **14** (1995) 825
8. A. Zhang, J. L. Neumeyer, R. J. Baldessarini, *Chem. Rev*. **107** (2007) 274
9. V. Sukalovic, D. Andric, G. Roglic, S. Kostic-Rajacic, A. Schrattenholz, V. Soskic, *Eur. J. Med. Chem.* **40** (2005) 481
10. V. Sukalovic, M. Zlatovic, D. Andric, G. Roglic, S. Kostic-Rajacic, V. Soskic, *Arzneimittelforschung* **55** (2005) 145

11. V. Sukalovic, M. Zlatovic, D. Andric, G. Roglic, S. Kostic-Rajaccic, V. Soskic, *Arch. Pharm. (Weinheim)* **337** (2004) 502
12. Accelrys Software Inc., *Discovery Studio Modeling Environment, Release 2.5*, San Diego, CA, 2009
13. S. Kostic-Rajacic, V. Soskic, J. Joksimovic, *Arch. Pharm. (Weinheim)* **331** (1998) 22
14. S. Kostic-Rajacic, V. Soskic, J. Joksimovic, *Pharmazie* **53** (1998) 438
15. Intel Quad-Core CPU 2.4 GHz, 4 GB Ram, ATI Radeon 4570 HD Graphics
16. G. Campiani, S. Butini, F. Trotta, C. Fattorusso, B. Catalanotti, F. Aiello, S. Gemma, V. Nacci, E. Novellino, J. A. Stark, A. Cagnotto, E. Fumagalli, F. Carnovali, L. Cervo, T. Mennini, *J. Med. Chem*. **46** (2003) 3822
17. A. Hackling, R. Ghosh, S. Perachon, A. Mann, H. D. Holtje, C. G. Wermuth, J. C. Schwartz, W. Sippl, P. Sokoloff, H. Stark, *J. Med. Chem*. **46** (2003) 3883
18. A. H. Newman, P. Grundt, G. Cyriac, J. R. Deschamps, M. Taylor, R. Kumar, D. Ho, R. R. Luedtke, *J. Med. Chem*. **52** (2009) 2559
19. P. Grundt, E. E. Carlson, J. Cao, C. J. Bennett, E. McElveen, M. Taylor, R. R. Luedtke, A. H. Newman, *J. Med. Chem*. **48** (2005) 839
20. K. Schlotter, F. Boeckler, H. Hubner, P. Gmeiner, *J. Med. Chem*. **49** (2006) 3628
21. K. Ehrlich, A. Gotz, S. Bollinger, N. Tschammer, L. Bettinetti, S. Harterich, H. Hubner, H. Lanig, P. Gmeiner, *J. Med. Chem*. **52** (2009) 4923
22. E. Y. Chien, W. Liu, Q. Zhao, V. Katritch, G. W. Han, M. A. Hanson, L. Shi, A. H. Newman, J. A. Javitch, V. Cherezov, R. C. Stevens, *Science* **330** (2010) 1091
23. Discovery Studio Visualiser 2.5.1, Accelrys Software Inc., *Discovery Studio Modeling Environment, Release 2.5*, San Diego: Accelrys Software Inc., 2009
24. Pov-Ray *The Persistence of Vision Ray-Tracer, version 3.6*, 2003–2011, http://www.povray.org/ (Accessed Jun 12, 2011)
25. T. H. Ji, M. Grossmann, I. Ji, *J. Biol. Chem*. **273** (1998) 17299
26. J. S. Surgand, J. Rodrigo, E. Kellenberger, D. Rognan, *Proteins* **62** (2006) 509
27. J. L. Baneres, D. Mesnier, A. Martin, L. Joubert, A. Dumuis, J. Bockaert, *J. Biol. Chem*. **280** (2005) 20253
28. L. Shi, J. A. Javitch, *Proc. Natl. Acad. Sci. USA* **101** (2004) 440
29. C. de Graaf, N. Foata, O. Engkvist, D. Rognan, *Proteins* **71** (2008) 599.

The design, synthesis and antimicrobial activity of new biquinoline derivatives

NIRAV K. SHAH, NIMESH M. SHAH, MANISH P. PATEL and RANJAN G. PATEL*

Department of Chemistry, Sardar Patel University, Vallabh Vidyanagar-388120, Gujarat, India

Abstract: A simple and efficient method has been developed for the synthesis of some novel biquinoline derivatives bearing a thiazole moiety through a one-pot three-component condensation of 2-chloro-3-formylquinolines, ethyl cyanoacetate and a *β*-enaminone using a catalytic amount of piperidine in refluxing ethanol. These molecules were evaluated *in vitro* for their antibacterial and antifungal activity. Most of the compounds exhibited moderate antibacterial and antifungal activity against all the tested strains.

Keywords: quinoline; thiazole; antibacterial; antifungal.

INTRODUCTION

The quinoline nucleus is one of the most important and widely exploited heterocyclic rings for the development of bioactive molecules. Recent literature is enriched with progressive findings about the synthesis and pharmacological actions of quinoline and its derivatives. A number of quinoline derivatives are known to possess antimicrobial, antimycobacterial, antidepressant, antimalarial, anticonvulsant, antiviral, anticancer, hypotensive and anti-inflammatory activities.[1]

Compounds containing thiazole rings have remarkable medicinal value due to their potential chemotherapeutic,[2] fungicidal,[3] antiviral[4] and pesticidal[5] properties. In addition, 2-aminothiazole derivatives were reported to exhibit significant biological activities, such as anti-tuberculosis,[6] anti-inflammatory,[7] enzyme inhibition[8] and antitumor activities.[9]

After an extensive literature search, it was observed that quinoline and thiazole are important pharmacophores, but to date, insufficient effort has been made to combine these two moieties as a single molecular scaffold. Hence, the aim of this study was to synthesize and biologically screen a series of new compounds incorporating these moieties.

---

* Corresponding author. E-mail: patelranjanben@yahoo.com

RESULTS AND DISCUSSION

Chemistry

In continuation of the synthesis of biologically potent antimicrobials,[10] a new series of biquinolines synthesized by the one-pot three-component cyclocondensation reaction of 2-chloro-3-formylquinolines **2(a–d)**, ethyl cyanoacetate and 3-[(4-arylthiazol-2-yl)amino]cyclohex-2-en-1-ones (enaminone) **3(a–c)** is reported herein. The synthetic route depicted in Scheme 1 outlines the chemistry part of the present work. The key intermediates 2-chloro-3-formylquinolines **2(a–d)** were prepared according to a literature method[11] (Scheme 2). The solid phase reaction of 4-substituted acetophenone, thiourea and iodine for 4 h at 120 °C afforded the respective 2-amino-4-arylthiazole[12] (Scheme 2). The required β-enaminones **3(a–c)** were prepared by the reaction of β-diketone with 2-amino-4-arylthiazole in methanol under reflux in the presence of a catalytic amount of acetic acid.
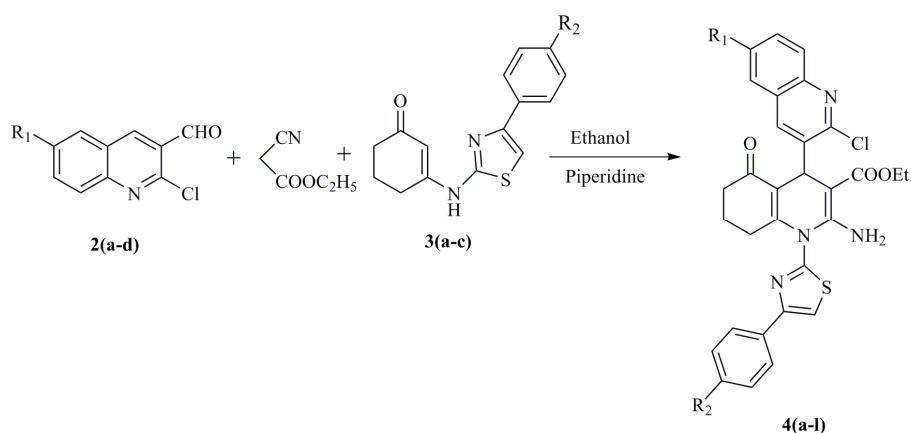
Compd.	4a	4b	4c	4d	4e	4f	4g	4h	4i	4j	4k	4l
R_1	H	CH₃	OCH₃	Cl	H	CH₃	OCH₃	Cl	H	CH₃	OCH₃	Cl
R_2	H	H	H	H	Cl	Cl	Cl	Cl	OH	OH	OH	OH

Scheme 1. Synthetic pathway for the compounds **4(a–l)**.

To choose the most appropriate medium to synthesize compounds **4(a–l),** several reaction conditions were investigated. Looking for the optimal reaction solvent, the reaction was examined in ethylene glycol, dimethylformamide, acetic acid, tetrahydrofuran and ethanol as solvent under reflux. The reaction in ethanol resulted in higher yields and shorter reaction time than the others, hence, ethanol

was chosen as the appropriate solvent. Moreover, to improve further the reaction yields, different bases, such as NaOH, K_2CO_3, 4-dimethylaminopyridine (DMAP), Et_3N and piperidine were examined in ethanol. Piperidine afforded the target product 4a in 87 % yield. Therefore, it was chosen as the most suitable base for all further reactions.
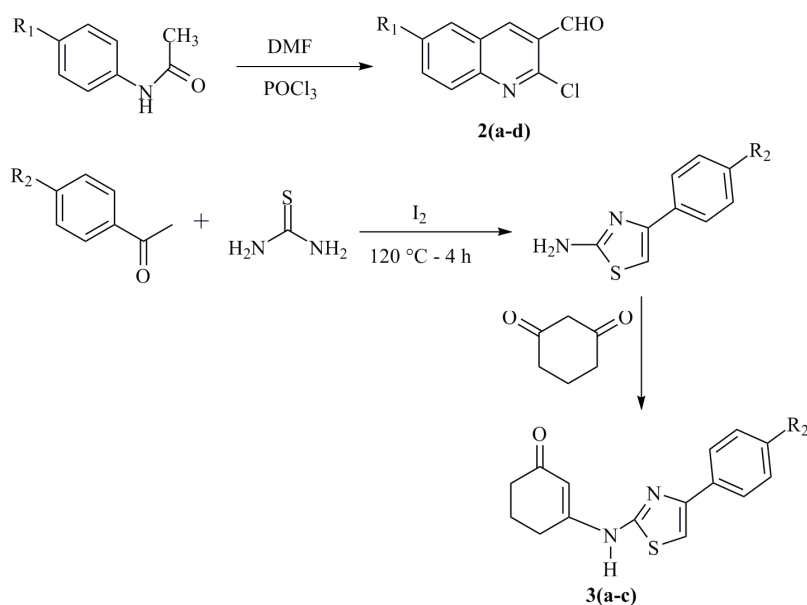
Scheme 2. Synthetic pathway for the intermediates **2(a–d)** and **3(a–c)**.

The reaction occurs *via* the initial *in situ* formation of the heteroarylidene-nitriles, containing an electron-poor C=C double bond, by the Knoevenagel condensation of a 2-chloro-3-formylquinoline and ethyl cyanoacetate with the loss of water molecules. Finally, Michael addition of or to the initially formed unsaturated nitrile, *i.e.*, nucleophilic attack of the cyano olefins by an enaminone afforded the cyclized quinoline derivatives **4(a–l)**.

The structures of the compounds were confirmed based on elemental analysis and spectral data (given as supplementary material). As an example, the IR spectrum of compound **4d** (R_1=Cl, R_2=H) showed a band at 3445 cm^{-1} of the asym. N–H stretching, 3345 cm^{-1} of the sym. N–H stretching and at 1660 and 1640 cm^{-1} for the C=O stretching of the carbonyl group. The ^{1}H-NMR spectra of **4d** showed a triplet signal at δ 1.01 ppm for the methyl group, a multiplet signal at δ 1.71–2.25 pmm for the three methylene groups, a quartet signal at δ 3.92 ppm for the OCH$_2$ group, a singlet at δ 5.30 ppm and at δ 8.45 ppm for the methine group and amino group, respectively, and a multiplet due to the aromatic protons at around δ 7.37–8.24. The ^{13}C-NMR spectrum of **4d** was in good agree-

ment with the assigned structure. The peak at δ 14.74 is attributed to one methyl group, the peaks at δ 21.19, 27.46 and 36.58 ppm are attributed to the three methylene carbons, the peak at δ 35.82 pm is attributed to the methine carbon. The peak at δ 77.93 ppm is assigned to the carbon attached to the carboxylate and the peaks at δ 114.17–156.98 ppm are attributed to aromatic carbons. The peak at δ 168.99 and 195.77 ppm are assigned to the carbonyl carbons. The mass spectra of compounds **4d** and **4j** showed an M^++1 peak in agreement with their exact molar mass.

Biological evaluation

The antibacterial activities of the biquinolines given in Table I indicate that among all the compounds **4a**, **4c**, **4d**, **4e**, **4h**, **4k** and **4l** exhibited good antibacterial activity against the bacterial strain *Escherichia coli*. Similarly, compounds **4a**, **4c**, **4d**, **4g**, **4h**, **4k** and **4l** showed good activity against the Gram-positive bacterial species *Bacillus subtilis* and compounds **4a**, **4c**, **4d**, **4f**, **4h**, **4k** and **4l** against the Gram-positive bacterial species *Staphylococcus aureus*. The remaining compounds showed moderate activity against the tested bacterial strains.

TABLE I. Antimicrobial activity of the compounds **4(a–l)** (Zone of inhibition, in mm). NT = = not tested. Control (DMF) (–) – no activity

Compound	Antibacterial activity			Antifungal activity		
	E. coli	*B. subtilis*	*S. aureus*	*F. oxysporum*	*A. niger*	*R. oryzae*
4a	23	25	22	16	15	18
4b	17	19	18	15	19	16
4c	25	24	23	20	22	25
4d	24	23	25	14	16	21
4e	20	17	18	17	16	18
4f	18	19	20	16	18	17
4g	19	20	18	21	24	22
4h	25	22	24	19	20	21
4i	19	18	15	17	17	14
4j	18	17	16	15	14	18
4k	24	22	23	21	25	24
4l	21	23	25	19	20	17
Ampicillin	28	30	30	NT	NT	NT
Ciprofloxacin	35	34	33	NT	NT	NT
Griseofulvin	NT	NT	NT	26	28	30

The antifungal evaluation of the synthesized compounds revealed that compounds **4c**, **4g** and **4k** displayed excellent antifungal activity towards *Fusarium oxysporum*. Against *Aspergillus niger*, compounds **4c**, **4g**, **4h**, **4k** and **4l** and compounds **4c**, **4d**, **4g**, **4h** and **4k** towards *Rhizopus oryzae* showed good activity. The remaining compounds showed mild to moderate antifungal activity.

A close examination of the structures of the active compounds in Table I revealed that their antimicrobial activity was strongly bound to the nature of the substituent at the quinoline-C_6, together with the substituent linked to the aryl-thiazole part of the structure. In general, it could be clearly recognized that compound **4c** without a substituent in the arylthiazole moiety (R_2 = H) and with the quinoline containing a methoxy substituent (R_1 = OCH_3) showed the greatest activity compared to the other studied compounds. Moreover, compound **4k** with the quinoline containing a methoxy substituent (R_1 = OCH_3) and with a hydroxyl substituent in the arylthiazole moiety (R_2 = OH) had a good antimicrobial profile while compound **4g** with the quinoline also containing a methoxy substituent (R_1 = OCH_3) and with a chloro substituent in the arylthiazole moiety (R_2 = Cl) exhibited moderate to good antimicrobial activity. On the other hand, the introduction of a methyl group at position 6 of the quinoline (compounds **4b**, **4j** and **4f**) resulted in a noticeable decrease in the antimicrobial potential of these compounds. Compounds **4a** (R_1 = H, R_2 = H), **4h** (R_1 = Cl, R_2 = Cl) and **4l** (R_1 = Cl, R_2 = OH) showed good antibacterial activity together with a moderate antifungal profile. It is worth mentioning that the biological activity of the target compounds depended not only on the bicyclic heteroaromatic pharmacophore but also on the nature of the substituents and maybe on their spatial relationships. Here, the thiazole moiety was introduced along with a biquinoline ring for activity reinforcement. However, based on the presented observations, it is immature to arrive at any conclusion on the structure–activity aspect of these molecules and further evaluation is required.

EXPERIMENTAL

Chemistry

Solvents used were of analytical grade. All melting points were taken in open capillaries and are uncorrected. Thin-layer chromatography (TLC, on aluminum plates precoated with silica gel, $60F_{254}$, 0.25 mm thickness) (Merck, Darmstadt, Germany) was used for monitoring the progress of all reactions and the purity and homogeneity of the synthesized compounds. The eluent was hexane:ethyl acetate 6:4 and UV radiation and/or iodine were used as the visualizing agents. Elemental analysis (% C, H and N) was performed on a Perkin-Elmer 2400 series-II elemental analyzer (Perkin-Elmer, USA) and all compounds were within ±0.4 % of their calculated composition. The IR spectra were recorded in KBr pellets on a Perkin-Elmer Spectrum GX FT-IR spectrophotometer (Perkin-Elmer, USA), and only the characteristic peaks are reported in cm^{-1}. The ^{1}H-NMR and ^{13}C-NMR spectra were recorded in DMSO-d_6 on a Bruker Avance 400F spectrometer (Bruker, Switzerland) using the solvent peak as an internal standard at 400 and 100 MHz, respectively. The chemical shifts were reported in ppm. The mass spectra were scanned on a Shimadzu LCMS 2010 spectrometer (Shimadzu, Tokyo, Japan). Analytical and spectral data of the synthesized compounds are given in the Supplementary material.

General procedure for the synthesis of 2-amino-4-arylthiazole

The 2-amino-4-arylthiazoles were synthesized, according to a literature procedure[12] by the solid phase reaction of thiourea, a 4-substituted acetophenone and iodine (Scheme 2).

General procedure for the synthesis of 3-[(4-arylthiazole-2-yl)amino]cyclohex-2-en-1-ones 3(a–c)

A 1,3-dicarbonyl compound 1,3-cyclohexanedione (30 mmol), 2-amino-4-arylthiazole (30 mmol), methanol (15 mL) and 2 drops of acetic acid were charged into a 100 mL round--bottom flask equipped with reflux condenser. The reaction mixture was slowly heated and refluxed for 1 h. On completion of reaction, monitored by TLC using 30 % EtOAc in toluene as the eluent, the reaction mixture was cooled to room temperature and the solid that separated was filtered and washed with methanol to obtain the pure compounds.

General procedure for the synthesis of ethyl 2-amino-1-(4-arylthiazol-2-yl)-4-(2-chloro-6- -(un)substituted-3-quinolyl)-5-oxo-1,4,5,6,7,8-hexahydroquinoline-3-carboxylates 4(a–l)

A mixture of 2-chloro-3-formylquinolines (1.0 mmol), ethyl cyanoacetate (1.0 mmol), and an appropriate *β*-enaminone (1.0 mmol) in ethanol (10 ml) containing a catalytic amount of piperidine was slowly heated and refluxed for 3–4 h. On completion of the reaction, monitored by TLC (ethyl acetate:toluene 3:7), the reaction mixture was cooled to room temperature and the solid that separated was filtered and washed with mixture of chloroform and methanol (1:1) to obtain the pure compounds.

Antimicrobial activity

The *in vitro* antimicrobial activity was realized against 24 h old cultures of three bacteria and three fungi by the disc diffusion method.[13,14] Compounds **4(a–l)** were tested for their anti-bacterial activity against *E. coli* as Gram-negative bacteria and *B. subtilis* and *Staphylococcus aureus* as Gram-positive bacteria and antifungal activity against *A. niger*, *F. oxysporum* and *R. oryzae*. Nutrient agar and potato dextrose agar were used to culture the bacteria and fungi, respectively. The compounds were tested at 1000 ppm in DMF solution. Ciprofloxacin, ampicillin and griseofulvin were used as standards for comparison of antibacterial and antifungal activities, respectively. Inhibition was recorded by measuring the diameter of the inhibition zone at the end of 24 h for bacteria at 35 °C and 48 h for the fungi at 28 °C. Details of the evaluation of the antimicrobial activity of compounds **4(a–l)** are given in the Supplementary material.

CONCLUSIONS

In conclusion, a simple and efficient method for the synthesis of biquinoline derivatives is developed. The straightforward approach, simplicity and one-step method make it an interesting approach for the synthesis of said compounds. Most of the compounds showed better antibacterial activity. Further optimization and development is needed in designing more potent antibacterial and antifungal agents for therapeutic use.

SUPPLEMENTARY MATERIAL

Analytical and spectral data of synthesized compounds, as well as the details of the evaluation of their antimicrobial activity are available electronically from http:// //www.shd.org.rs/JSCS/, or from the corresponding author on request.

И З В О Д

ДИЗАЈН, СИНТЕЗА И АНТИМИКРОБНА АКТИВНОСТ НОВИХ БИХИНОЛИНСКИХ ДЕРИВАТА

NIRAV K. SHAH, NIMESH M. SHAH, MANISH P. PATEL и RANJAN G. PATEL

Department of Chemistry, Sardar Patel University, Vallabh Vidyanagar-388120, Gujarat, India

Развијен је једноставан и ефикасан поступак за синтезу нових бихинолинских деривата који садрже тиазолински структурни фрагмент. Поступак се састоји из трокомпонентне кондензације 2-хлор-3-формилхинолина, етил-цијаноацетата и β-енаминона у једном реакционом кораку, катализоване пиперидином у кључалом етанолу. Испитана је *in vitro* антибактеријска и антифунгална инхибиторна активност добијених једињења. Већина испитаних једињења показује умерену активност према испитиваним сојевима.

(Примљено 30. јуна, ревидирано 19. октобра 2011)

REFERENCES

1. a) C. Vittorio, B. Guyen, Y. Opoku-Boahen, J. Mann, S. M. Gowan, M. Lloyd, A. R. Martin, N. Stephen, *Bioorg. Med. Chem. Lett.* **10** (2000) 2063; b) P. Senthilkumar, M. Dinakaran, Y. Chandraseakaran, P. Yogeeswari, D. Sriram, *Arch. Pharm.* **342** (2009) 100; c) M. A. Khalil, O. A. El-Sayed, H. A. El-Shamy, *Arch. Pharm.* **326** (1993) 489; d) M. Flipo, I. Florent, P. Grellier, C. Sergheraert, R. Deprez-Poulain, *Bioorg. Med. Chem. Lett*. **13** (2003) 2659; e) L.-P. Guan, Q.-H. Jin, S.-F. Wang, F.-N. Li, Z.-S. Quan, *Arch. Pharm.* **341** (2008) 774; f) X.-Y. Sun, C.-X. Wei, K.-Y. Chai, H.-R. Piao, Z.-S. Quan, *Arch. Pharm*. **341** (2008) 288; g) S. Bawa, S. Kumar, *Indian J. Chem., Sect B* **48** (2009) 142; h) J. M. McCall, R. E. Brink, B. V. Kamdar, L. L. Skaletzky, S. C. Perricone, R. C. Piper, P. J. Delehanty, *J. Med. Chem.* **29** (1986) 133; i) K. K. Luciana, C. H. Pavam, D. Veronese, F. Coelho, J. E. De Carvalho, W. P. Almeida, *Eur. J. Med. Chem*. **41** (2006) 738; j) C. M. Meléndez Gómez, V. V. Kouznetsov, M. A. Sortino, S. L. Álvarez, S. A. Zacchino, *Bioorg. Med. Chem*. **16** (2008) 7908; k) A. A. Bekhita, O. A. El-Sayeda, H. Y. Aboul-Eneinb, Y. M. Siddiquic, M. N. Al-Ahdalc, *J. Enzyme Inhib. Med. Chem.* **19** (2004) 33; l) G. Sathi, V. R. Gujrati, M. Sharma, C. Nath, K. P. Bhargava, K. Shanker, *Arch. Pharm.* **316** (1983) 767
2. H. Liebig, H. Pfetzing, A. Grafe, *Arzneim.-Forsch.* **24** (1974) 887
3. R. B. Pathak, B. Jahan, S. C. Bahel, *Bokin Bobai* **9** (1981) 477
4. F. C. Spector, L. Liang, H. Giordano, M. Sivaraja, M. G. Peterson, *J. Virol.* **72** (1998) 6979
5. Z. Fan, Z. Shi, X. Liu, Z. Fan, Y. Ai, Faming Zhuanli Shenqing Gongkai Shuomingshu, 2006, Chinese patent: CNXXEV CN 1810808 A 20060802
6. K. M. Sytnik, I. Ye. Bylov, S. N. Kovalenko, *Zh. Org. Farm. Khim.* **1** (2003) 71
7. B. Holla, K. Malini, B. Rao, B. Sarojini, N. Kumari, *Eur. J. Med. Chem.* **38** (2003) 313

8. J. Das, J. Furch, C. Liu, R. Moquin, J. Lin, S. Spergel, K. McIntyre, D. Shuster, K. O'Day, B. Penhallow, *Bioorg. Med. Chem. Lett*. **16** (2006) 3706

9. H. I. El-Subbagh, A. H. Abadi, J. Lehmann, *Arch. Pharm*. **332** (1999) 137

10. a) N. M. Shah. M. P. Patel, R. G. Patel, *J. Heterocycl. Chem.* (2011) DOI 10.1002/jhet.918; b) D. C. Mungra, M. P. Patel, D. P. Rajani, R. G. Patel, *Eur. J. Med. Chem*. **46** (2011) 4192; c) N. K. Shah, M. P. Patel, R. G. Patel, *Phosphorus Sulfur Silicon Relat. Elem*. **184** (2009) 2704; d) N. K. Shah, M. P. Patel, R. G. Patel, *Indian J. Chem. Sect. B* **48** (2009) 1170; e) J. A. Makawana, M. P. Patel, R. G. Patel, *Med. Chem. Res*. (2011) DOI 10.1007/s00044-010-9568-6; f) C. B. Sangani, M. P. Patel, R. G. Patel, *Cent. Eur. J. Chem*. **9** (2011) 635; g) N. K. Ladani, M .P. Patel, R .G. Patel, *Arkivoc* **vii** (2009) 292

11. O. Meth-Cohn, N. A. Bramha, *Tetrahedron Lett*. **23** (1978) 2045

12. R. M. Dodson, L. C. King, *J. Am. Chem. Soc*. **67** (1945) 2242

13. C. H. Collins, P. M. Lyne, *Microbial Methods,* University Park Press, Baltimore, USA, 1970

14. T. D. Thangadurai, K. Natarajan, *Indian J. Chem. Sect. A* **40** (2001) 573.

SUPPLEMENTARY MATERIAL TO

The design, synthesis and antimicrobial activity of new biquinoline derivatives

NIRAV K. SHAH, NIMESH M. SHAH, MANISH P. PATEL and RANJAN G. PATEL*

Department of Chemistry, Sardar Patel University, Vallabh Vidyanagar-388120, Gujarat, India

TABLE S-I. Physical data for compounds **2(a–d)**

Compound	R_1	M.p., °C	M.W., g mol⁻¹	Molecular formula	Yield, %
2a	H	145	191.61	$C_{10}H_6ClNO$	71
2b	Me	125–26	205.64	$C_{11}H_8ClNO$	73
2c	OMe	148–49	221.64	$C_{11}H_8ClNO_2$	68
2d	Cl	165–66	226.06	$C_{10}H_5Cl_2NO$	42

Analytical and spectroscopic characterization data of 3-[(4-arylthiazole-2-yl)amino]cyclohex-2-en-1-ones 3(a–c)

3-[(4-Phenylthiazol-2-yl)amino]cyclohex-2-en-1-one (3a). Yield: 74 %; m.p. 188–189 °C; Anal. Calcd. for $C_{15}H_{14}N_2OS$: C, 66.64; H, 5.22; N, 10.36 %. Found: C, 66.87; H, 4.98; N, 10.51 %; IR (KBr, cm⁻¹): 3395 (N–H str.), 1665 (C=O str.); ¹H-NMR (400 MHz, DMSO-d_6, δ / ppm): 1.89–2.27 (6H, *m*, 3×CH₂), 5.23 (1H, *s*, CH), 6.72–7.85 (6H, *m*, Ar–H), 10.48 (1H, *s*, N–H); ¹³C-NMR (100 MHz, DMSO-d_6, δ / ppm): 20.19, 26.98 (CH₂), 37.02 (**CH₂**–CO), 106.41, 106.89, 112.47, 128.06, 132.79, 147.78, 153.56, 159.05, 161.67 (Ar-C), 197.28 (C=O).

3-{[4-(4-Chlorophenyl)thiazol-2-yl]amino}cyclohex-2-en-1-one (3b). Yield: 70 %; m.p. 199–201 °C; Anal. Calcd. for $C_{15}H_{13}ClN_2OS$: C, 59.11; H, 4.30; N, 9.19 %. Found: C, 58.95; H, 4.44; N, 9.27 %; IR (KBr, cm⁻¹): 3430 (N–H str.), 1655 (C=O str.); ¹H-NMR (400 MHz, DMSO-d_6, δ / ppm): 1.87–2.26 (6H, *m*, 3×CH₂), 5.27 (1H, *s*, CH), 6.87–7.94 (5H, *m*, Ar–H), 10.55 (1H, *s*, N–H); ¹³C-NMR (100 MHz, DMSO-d_6, δ / ppm): 20.37, 27.60 (CH₂), 36.79 (**CH₂**–CO), 105.35, 106.78, 127.93, 129.25, 131.82, 148.63, 154.41, 159.30, 162.11 (Ar-C), 197.49 (C=O).

* Corresponding author. E-mail: patelranjanben@yahoo.com

3-{[4-(4-Hydroxyphenyl)thiazol-2-yl]amino}cyclohex-2-en-1-one (*3c*). Yield: 75 %; m.p. 210–212 °C; Anal. Calcd. for $C_{15}H_{14}N_2O_2S$: C, 62.92; H, 4.93; N, 9.78 %. Found: C, 63.07; H, 4.75; N, 9.66 %; IR (KBr, cm^{-1}): 3415 (N–H str.), 1680 (C=O str.); ^{1}H-NMR (400 MHz, DMSO-d_6, δ / ppm): 1.83–2.29 (6H, *m*, 3×CH$_2$), 5.25 (1H, *s*, CH), 6.81–7.71 (5H, *m*, Ar–H), 9.62 (1H, *s*, O–H), 10.34 (1H, *s*, N–H); ^{13}C-NMR (100 MHz, DMSO-d_6, δ / ppm): 20.27, 27.33 (CH$_2$), 37.00 (**C**H$_2$–CO), 105.21, 106.62, 118.21, 127.10, 129.53, 148.87, 157.65, 159.48, 162.02 (Ar-C), 197.66 (C=O).

Analytical and spectroscopic data for compounds *4(a–l)*

Ethyl 2-amino-4-(2-chloro-3-quinolyl)-5-oxo-1-(4-phenylthiazol-2-yl)--1,4,5,6,7,8-hexahydroquinoline-3-carboxylate (*4a*). Yield: 87 %; m.p. 245–247 °C; Anal. Calcd. for $C_{30}H_{25}ClN_4O_3S$: C, 64.68; H, 4.52; N, 10.06 %. Found: C, 64.82; H, 4.48; N, 9.90 %; IR (KBr, cm^{-1}): 3425 & 3280 (asym. & sym. str. of –NH$_2$), 1678 (C=O str.), 1640 (C=O str.); ^{1}H-NMR (400 MHz, DMSO-d_6, δ / / ppm): 1.11 (3H, *t*, *J* = 7.16 Hz, CH$_3$), 1.71–2.20 (6H, *m*, 3×CH$_2$), 3.90 (2H, *q*, *J* = 7.16 Hz, OCH$_2$), 5.36 (1H, *s*, CH), 7.31–8.28 (11H, *m*, Ar–H), 8.42 (2H, *s*, NH$_2$); ^{13}C-NMR (100 MHz, DMSO-d_6, δ / ppm): 14.45 (CH$_3$), 21.30, 26.82 (2C, CH$_2$), 35.40 (C4), 36.12 (**C**H$_2$–CO), 57.32 (OCH$_2$), 78.25 (**C**–COOEt), 113.31, 117.78, 119.89, 126.65, 126.96, 128.54, 129.12, 129.41, 131.23, 131.30, 133.30, 140.28, 144.93, 150.41, 150.60, 152.53, 152.73, 152.82, 156.91 (19C, Ar-C), 168.75 (**C**OOEt), 195.88 (C=O).

Ethyl 2-amino-4-(2-chloro-6-methyl-3-quinolyl)-5-oxo-1-(4-phenylthiazol-2--yl)-1,4,5,6,7,8-hexahydroquinoline-3-carboxylate (*4b*). Yield: 89 %; m.p. 169–171 °C; Anal. Calcd. for $C_{31}H_{27}ClN_4O_3S$: C, 65.20; H, 4.77; N, 9.81 %. Found: C, 65.28; H, 4.72; N, 9.93 %; IR (KBr, cm^{-1}): 3437 and 3333 (asym. and sym. str. of –NH$_2$), 1672 (C=O str.), 1620 (C=O str.); ^{1}H-NMR (400 MHz, DMSO-d_6, δ / ppm): 1.09 (3H, *t*, *J* = 7.4 Hz, CH$_3$), 2.23 (3H, *s*, CH$_3$), 1.71–2.20 (6H, *m*, 3×CH$_2$), 3.93 (2H, *q*, *J* = 7.2 Hz, OCH$_2$), 5.31 (1H, *s*, CH), 7.29–8.25 (10H, *m*, Ar–H), 8.38 (2H, *s*, NH$_2$); ^{13}C-NMR (100 MHz, DMSO-d_6, δ / ppm): 14.23 (CH$_3$), 20.14 (CH$_3$), 21.41, 26.02 (2C, CH$_2$), 35.10 (C4), 36.32 (**C**H$_2$–CO), 57.10 (OCH$_2$), 78.74 (**C**–COOEt), 113.14, 117.14, 119.41, 126.41, 126.47, 128.25, 129.45, 129.74, 131.13, 131.15, 133.25, 140.47, 144.78, 150.41, 150.45, 152.13, 152.71, 152.92, 156.45 (19C, Ar-C), 168.79 (**C**OOEt), 195.45 (C=O).

Ethyl 2-amino-4-(2-chloro-6-methoxy-3-quinolyl)-5-oxo-1-(4-phenylthiazol-2-yl)-1,4,5,6,7,8-hexahydroquinoline-3-carboxylate (*4c*). Yield: 83 %; m.p. 221––223 °C; Anal. Calcd. for $C_{31}H_{27}ClN_4O_3S$: C, 63.42; H, 4.64; N, 9.54 %. Found: C, 63.58; H, 4.72; N, 9.73 %; IR (KBr, cm^{-1}): 3446 and 3240 (asym. and sym. str. of –NH$_2$), 1668 (C=O str.), 1635 (C=O str.); ^{1}H-NMR (400 MHz, DMSO-d_6, δ / ppm): 1.01 (3H, *t*, *J* = 7.4 Hz, CH$_3$), 1.71–2.25 (6H, *m*, 3×CH$_2$), 3.89 (3H, *s*, OCH$_3$), 3.90 (2H, *q*, *J* = 7.1 Hz, OCH$_2$), 5.35 (1H, *s*, CH), 7.29–8.22 (10H, *m*,

Ar-H), 8.32 (2H, *s*, NH$_2$); ^{13}C-NMR (100 MHz, DMSO-*d$_6$*, *δ* / ppm): 14.64 (CH$_3$), 21.23, 27.12 (2C, CH$_2$), 35.14 (C4), 36.00 (**C**H$_2$–CO), 57.23 (OCH$_3$), 59.10 (OCH$_2$), 77.74 (**C**–COOEt), 105.27, 114.41, 119.32, 126.40, 126.84, 128.23, 129.18, 129.78, 131.41, 131.97, 133.41, 140.40, 144.68, 150.74, 150.92, 152.44, 152.64, 152.90, 156.01 (19C, Ar-C), 168.14 (**C**OOEt), 195.38 (C=O).

Ethyl 2-amino-4-(2,6-dichloro-3-quinolyl)-5-oxo-1-(4-phenylthiazol-2-yl)--1,4,5,6,7,8-hexahydroquinoline-3-carboxylate (4d). Yield: 76 %; m.p. 232–234 °C; Anal. Calcd. for C$_{30}$H$_{24}$Cl$_2$N$_4$O$_3$S: C, 60.92; H, 4.09; N, 9.47 %. Found: C, 60.86; H, 4.05; N, 9.60 %; IR (KBr, cm^{-1}): 3445 and 3345 (asym. and sym. str. of –NH$_2$), 1660 (C=O str.), 1640 (C=O str.); ^{1}H-NMR (400 MHz, DMSO-*d$_6$*, *δ* / / ppm): 1.01 (3H, *t*, *J* = 7.12 Hz, CH$_3$), 1.71–2.25 (6H, *m*, 3×CH$_2$), 3.92 (2H, *q*, *J* = 7.12 Hz, OCH$_2$), 5.30 (1H, *s*, CH), 7.37–8.24 (10H, *m*, Ar–H), 8.45 (2H, *s*, NH$_2$); ^{13}C-NMR (100 MHz, DMSO-*d$_6$*, *δ* / ppm): 14.74 (CH$_3$), 21.19, 27.46 (2C, CH$_2$), 35.82 (C4), 36.58 (**C**H$_2$–CO), 59.24 (OCH$_2$), 77.93 (**C**–COOEt), 114.17, 117.70, 119.34, 126.61, 126.85, 128.22, 129.37, 129.87, 131.05, 131.81, 133.95, 140.70, 144.35, 150.66, 150.93, 152.55, 152.76, 152.87, 156.98 (19C, Ar-C), 168.99 (**C**OOEt), 195.87 (C=O); MS: 591.1 (M$^+$+1).

Ethyl 2-amino-1-[(4-chlorophenyl)thiazol-2-yl]-4-(2-chloro-3-quinolyl)-5--oxo-1,4,5,6,7,8-hexahydroquinoline-3-carboxylate (4e). Yield: 87 %; m.p. 195––197 °C; Anal. Calcd. for C$_{30}$H$_{24}$Cl$_2$N$_4$O$_3$S: C, 60.92; H, 4.09; N, 9.47 %. Found: C, 60.96; H, 4.00; N, 9.65 %; IR (KBr, cm^{-1}): 3441 and 3260 (asym. and sym. str. of –NH$_2$), 1668 (C=O str.), 1645 (C=O str.); ^{1}H-NMR (400 MHz, DMSO-*d$_6$*, *δ* / ppm): 1.10 (3H, *t*, *J* = 7.16 Hz, CH$_3$), 1.70–2.21 (6H, *m*, 3×CH$_2$), 3.94 (2H, *q*, *J* = 7.12 Hz, OCH$_2$), 5.40 (1H, *s*, CH), 7.30–8.22 (10H, *m*, Ar–H), 8.40 (2H, *s*, NH$_2$); ^{13}C-NMR (100 MHz, DMSO-*d$_6$*, *δ* / ppm): 14.98 (CH$_3$), 21.78, 26.54 (2C, CH$_2$), 35.45 (C4), 36.12 (**C**H$_2$–CO), 57.98 (OCH$_2$), 78.32 (**C**––COOEt), 113.87, 117.36, 119.74, 126.45, 126.65, 128.54, 129.56, 129.74, 131.36, 131.70, 133.12, 140.56, 144.56, 150.23, 150.45, 152.03, 152.65, 152.85, 156.19 (19C, Ar-C), 168.23 (**C**OOEt), 195.98 (C=O).

Ethyl 2-amino-4-(2-chloro-6-methyl-3-quinolyl)-1-[(4-chlorophenyl)thiazol--2-yl]-5-oxo-1,4,5,6,7,8-hexahydroquinoline-3-carboxylate (4f). Yield: 81 %; m.p. 208–210 °C; Anal. Calcd. for C$_{31}$H$_{26}$Cl$_2$N$_4$O$_3$S: C, 61.49; H, 4.33; N, 9.25 %. Found: C, 61.41; H, 4.23; N, 9.35 %; IR (KBr, cm^{-1}): 3442 and 3280 (asym. and sym. str. of –NH$_2$), 1678 (C=O str.), 1660 (C=O str.); ^{1}H-NMR (400 MHz, DMSO-*d$_6$*, *δ* / ppm): 1.07 (3H, *t*, *J* = 7.2 Hz, CH$_3$), 1.72–2.45 (6H, *m*, 3×CH$_2$), 2.47 (3H, *s*, CH$_3$), 3.87 (2H, *q*, *J* = 7.2 Hz, OCH$_2$), 5.25 (1H, *s*, CH), 7.25–8.31 (9H, *m*, Ar–H), 8.48 (2H, *s*, NH$_2$); ^{13}C-NMR (100 MHz, DMSO-*d$_6$*, *δ* / ppm): 14.12 (CH$_3$), 20.23 (CH$_3$), 21.39, 27.28 (2C, CH$_2$), 35.17 (C4), 36.36 (**C**H$_2$––CO), 59.65 (OCH$_2$), 78.54 (**C**–COOEt), 113.07, 114.78, 116.89, 122.54, 125.41, 126.65, 128.10, 128.32, 129.21, 140.14, 141.74, 141.90, 147.12, 149.23, 152.00, 152.36, 156.03, 158.36, 158.96 (19C, Ar-C), 169.19 (**C**OOEt), 195.37 (C=O).

*Ethyl 2-amino-4-(2-chloro-6-methoxy-3-quinolyl)-1-[(4-chlorophenyl)thia-zol-2-yl]-5-oxo-1,4,5,6,7,8-hexahydroquinoline-3-carboxylate (**4g**).* Yield: 79 %; m.p. 225–227 °C; Anal. Calcd. for $C_{31}H_{26}Cl_2N_4O_4S$: C, 59.91; H, 4.22; N, 9.01. Found: C, 59.82; H, 4.42; N, 9.23 %; IR (KBr, cm^{-1}): 3445 and 3285 (asym. and sym. str. of –NH$_2$), 1670 (C=O str.), 1650 (C=O str.); ^{1}H-NMR (400 MHz, DMSO-d_6, δ / ppm): 1.01 (3H, t, J = 7.2 Hz, CH$_3$), 1.75–2.41 (6H, m, 3×CH$_2$), 3.85 (2H, q, J = 7.1 Hz, OCH$_2$), 3.95 (3H, s, OCH$_3$), 5.32 (1H, s, CH), 7.29–8.24 (9H, m, Ar–H), 8.46 (2H, s, NH$_2$); ^{13}C-NMR (100 MHz, DMSO-d_6, δ / ppm): 14.78 (CH$_3$), 21.89, 27.96 (2C, CH$_2$), 35.65 (C4), 36.54 (**C**H$_2$–CO), 56.41 (OCH$_3$), 59.12 (OCH$_2$), 78.23 (**C**–COOEt), 105.32, 114.21, 116.14, 116.45, 122.55, 125.65, 128.85, 128.96, 129.74, 140.17, 141.20, 141.39, 147.23, 149.11, 152.75, 152.85, 156.63, 158.74, 158.32 (19C, Ar-C), 169.32 (**C**OOEt), 195.97 (C=O).

*Ethyl 2-amino-1-[(4-chlorophenyl)thiazol-2-yl]-4-(2,6-dichloro-3-quinolyl)--5-oxo-1,4,5,6,7,8-hexahydroquinoline-3-carboxylate (**4h**).* Yield: 75 %; m.p. 198–200 °C; Anal. Calcd. for $C_{30}H_{23}Cl_3N_4O_4S$: C, 57.56; H, 3.70; N, 8.95. Found: C, 57.72; H, 3.85; N, 8.77 %; IR (KBr, cm^{-1}): 3439 and 3281 (asym. and sym. str. of –NH$_2$), 1670 (C=O str.), 1635 (C=O str.); ^{1}H-NMR (400 MHz, DMSO-d_6, δ / ppm): 1.03 (3H, t, J = 7.4 Hz, CH$_3$), 1.72–2.41 (6H, m, 3×CH$_2$), 3.87 (2H, q, J = 7.16 Hz, OCH$_2$), 5.20 (1H, s, CH), 7.25–8.28 (9H, m, Ar–H), 8.40 (2H, s, NH$_2$); ^{13}C-NMR (100 MHz, DMSO-d_6, δ / ppm): 14.98 (CH$_3$), 21.23, 27.45 (2C, CH$_2$), 35.32 (C4), 36.89 (**C**H$_2$–CO), 59.97 (OCH$_2$), 78.56 (**C**–COOEt), 112.71, 114.82, 116.10, 116.98, 122.38, 125.30, 128.56, 128.91, 129.13, 140.17, 141.88, 141.99, 147.06, 149.12, 152.58, 152.30, 156.85, 158.06, 158.12 (19C, Ar-C), 169.87 (**C**OOEt), 195.74 (C=O).

*Ethyl 2-amino-4-(2-chloro-3-quinolyl)-1-[(4-hydroxyphenyl)thiazol-2-yl]-5--oxo-1,4,5,6,7,8-hexahydroquinoline-3-carboxylate (**4i**).* Yield: 73 %; m.p. 198––200 °C; Anal. Calcd. for $C_{30}H_{25}ClN_4O_4S$: C, 62.88; H, 4.40; N, 9.78. Found: C, 63.07; H, 4.56; N, 9.67 %; IR (KBr, cm^{-1}): 3439 and 3295 (asym. and sym. str. of –NH$_2$), 1675 (C=O str.), 1640 (C=O str.); ^{1}H-NMR (400 MHz, DMSO-d_6, δ / ppm): 1.05 (3H, t, J = 7.12 Hz, CH$_3$), 1.68–2.44 (6H, m, 3×CH$_2$), 3.90 (2H, q, J = 7.12 Hz, OCH$_2$), 5.21 (1H, s, CH), 7.20–8.26 (10H, m, Ar–H), 8.29 (2H, s, NH$_2$), 9.65 (1H, s, OH); ^{13}C-NMR (100 MHz, DMSO-d_6, δ / ppm): 14.11 (CH$_3$), 20.92, 27.14 (2C, CH$_2$), 35.47 (C4), 36.85 (**C**H$_2$–CO), 59.52 (OCH$_2$), 78.36 (**C**––COOEt), 113.36, 114.69, 116.78, 116.92, 122.12, 125.98, 128.32, 128.87, 129.40, 140.71, 141.43, 141.61, 147.91, 149.73, 152.82, 152.49, 156.93, 158.71, 158.25 (19C, Ar-C), 169.61 (**C**OOEt), 195.40 (C=O).

*Ethyl 2-amino-4-(2-chloro-6-methyl-3-quinolyl)-1-[(4-hydroxyphenyl)thia-zol-2-yl]-5-oxo-1,4,5,6,7,8-hexahydroquinoline-3-carboxylate (**4j**).* Yield: 64 %; m.p. 236–238 °C; Anal. Calcd. for $C_{31}H_{27}ClN_4O_4S$: C, 63.42; H, 4.64; N, 9.54 %. Found: C, 63.22; H, 4.48; N, 9.74 %; IR (KBr, cm^{-1}): 3442 and 3280 (asym. and sym. str. of –NH$_2$), 1678 (C=O str.), 1630 (C=O str.); ^{1}H-NMR (400 MHz,

DMSO-d_6, δ / ppm): 1.03 (3H, t, J = 7.2 Hz, CH$_3$), 1.70–2.41 (6H, m, 3×CH$_2$), 2.45 (3H, s, CH$_3$), 3.89 (2H, q, J = 7.16 Hz, OCH$_2$), 5.24 (1H, s, CH), 7.25–8.23 (9H, m, Ar–H), 8.30 (2H, s, NH$_2$), 9.62 (1H, s, OH); ^{13}C-NMR (100 MHz, DMSO-d_6 / δ , ppm): 14.23 (CH$_3$), 20.98 (Ar–CH$_3$), 21.12, 27.78 (2C, CH$_2$), 35.45 (C4), 36.98 (CH$_2$–CO), 59.56 (OCH$_2$), 78.89 (C–COOEt), 112.54, 114.32, 116.36, 116.52, 122.00, 125.35, 128.34, 128.47, 129.10, 140.87, 141.71, 141.99, 147.40, 149.59, 152.81, 152.99, 156.63, 158.25, 158.86 (19C, Ar-C), 169.10 (COOEt), 195.32 (C=O); MS: 586.6 (M$^+$+1).

Ethyl 2-amino-4-(2-chloro-6-methoxy-3-quinolyl)-1-[(4-hydroxyphenyl)thia-zol-2-yl]-5-oxo-1,4,5,6,7,8-hexahydroquinoline-3-carboxylate (4k). Yield: 81 %; m.p. 244–246 °C; Anal. Calcd. for C$_{31}$H$_{27}$ClN$_4$O$_5$S: C, 61.74; H, 4.51; N, 9.29 %. Found: C, 61.88; H, 4.70; N, 9.07 %; IR (KBr, cm^{-1}): 3445 and 3260 (asym. and sym. str. of –NH$_2$), 1680 (C=O str.), 1660 (C=O str.); ^{1}H-NMR (400 MHz, DMSO-d_6, δ / ppm): 1.05 (3H, t, J = 7.4 Hz, CH$_3$), 1.70–2.41 (6H, m, 3×CH$_2$), 3.91 (2H, q, J = 7.2 Hz, OCH$_2$), 3.91 (3H, s, OCH$_3$), 5.28 (1H, s, CH), 6.87–8.17 (9H, m, Ar–H), 8.27 (2H, s, NH$_2$), 9.72 (1H, s, OH); ^{13}C-NMR (100 MHz, DMSO-d_6, δ / ppm): 14.72 (CH$_3$), 21.26, 27.47 (2C, CH$_2$), 35.63 (C4), 36.60 (CH$_2$–CO), 56.08 (Ar–OCH$_3$), 59.13 (OCH$_2$), 78.35 (C–COOEt), 105.79, 114.48, 116.04, 116.25, 122.99, 125.28, 128.09, 128.59, 129.14, 140.27, 141.20, 141.90, 147.47, 149.01, 152.69, 152.91, 156.73, 158.10, 158.38 (19C, Ar-C), 169.06 (COOEt), 195.81 (C=O).

Ethyl 2-amino-4-(2,6-dichloro-3-quinolyl)-1-[(4-hydroxyphenyl)thiazol-2--yl]-5-oxo-1,4,5,6,7,8-hexahydroquinoline-3-carboxylate (4l). Yield: 79 %; m.p. 256–258 °C; Anal. Calcd. for C$_{30}$H$_{24}$Cl$_2$N$_4$O$_4$S: C, 59.31; H, 3.98; N, 9.22 %. Found: C, 59.50; H, 4.05; N, 9.47 %; IR (KBr, cm^{-1}): 3440 and 3275 (asym. and sym. str. of –NH$_2$), 1675 (C=O str.), 1640 (C=O str.); ^{1}H-NMR (400 MHz, DMSO-d_6, δ / ppm): 1.02 (3H, t, J = 7.12 Hz, CH$_3$), 1.70–2.41 (6H, m, 3×CH$_2$), 3.91 (2H, q, J = 7.12 Hz, OCH$_2$), 5.25 (1H, s, CH), 7.25–8.20 (9H, m, Ar–H), 8.26 (2H, s, NH$_2$), 9.70 (1H, s, OH); ^{13}C-NMR (100 MHz, DMSO-d_6, δ / ppm): 14.12 (CH$_3$), 21.23, 27.36 (2C, CH$_2$), 35.32 (C4), 36.21 (CH$_2$–CO), 59.45 (OCH$_2$), 78.56 (C–COOEt), 105.65, 114.23, 116.10, 116.98, 122.34, 125.30, 128.23, 128.87, 129.13, 140.17, 141.78, 141.99, 147.56, 149.32, 152.23, 152.30, 156.30, 158.96, 158.32 (19C, Ar-C), 169.87 (COOEt), 195.96 (C=O).

DETERMINATION OF THE ANTIMICROBIAL ACTIVITY

Sample preparation

A 1000 ppm solution of newly synthesized compounds was prepared in DMF.

Culture media for the study of antibacterial activity

The media: Nutrient broth (Hi-Media, Mumbai, India) having following composition was used for the preparation of inoculums.

Ingredient	g L^{-1}
Peptic digest of animal tissue	5.00

Yeast extract	1.50
Beef extract	1.50
Sodium chloride	5.00

Weighed quantities of all the components were dissolved in freshly prepared hot distilled water.

Sterilization for the study of antibacterial activity

The sterilization of culture media, culture tubes, and other materials was realized by autoclaving them at 15 lbs/sq. inch pressure for 15 min. The Petri-dishes were sterilized by keeping them overnight in an electrically heated air oven at 140 °C.

Preparation of nutrient plates for the study of antibacterial activity

Sterilized media (20 mL) was poured into each sterilized Petri dish and allowed to solidify.

Preparation of inoculums for the study of antibacterial activity

The inoculums of the organisms were prepared by transferring a loop full of the corresponding organism from the stock culture into the sterile broth and incubated at 37 °C for 24 h under shaking conditions. The organisms were sub-cultured on the nutrient agar slants. The inoculums were prepared by dispensing colonies in sterile distilled water to prepare a suspension.

Antibacterial susceptibility testing

A test tube containing sterile melted soft agar (approximately 15 ml) was cooled to 45 °C and inoculated with 0.2 ml of a suspension of the test culture, mixed thoroughly and poured into a Petri dish containing sterile nutrient agar medium and allowed to solidify for five minutes. A cup-borer (8 mm) was sterilized by dipping into absolute alcohol and flaming and then left to cool. Cups were bored in the agar with the sterile cup-borer and marked. The cups were filled with 0.1 ml of the required test sample solution and the test sample was allowed to diffuse for 10 to 15 min in a refrigerator. The plate was incubated at 37 °C for 24 h and on the next day, the zone of inhibition of surrounding each cup was observed and measured in mm.

Sample preparation for the study of antifungal activity

A 1000 ppm solutions of freshly synthesized compounds were prepared in DMF.

Culture media for the study of the antifungal activity

The media: potato-dextrose agar (Hi-Media, Mumbai, India) having the following composition was used for the preparation of inoculums for the antifungal study:

Ingredient	g L^{-1}
Potatoes infusion	200.00
Dextrose	20.0
Agar	15.0

Weighed quantities of all the components were dissolved in freshly prepared hot distilled water.

All experimental conditions for the antifungal activity were the same as those for the antibacterial activity except for the culture media and the plate was incubated at 28 °C for 48 h before the zone of inhibition surrounding each cup was observed and measured in mm.

SHORT COMMUNICATION

Catalytic tetrahydropyranylation of phenols and alcohols using vanadium(V)-substituted polyoxomolybdates

ALI GHARIB[1,2*] and MANOUCHEHR JAHANGIR[1]

[1]Department of Chemistry, Islamic Azad University, Mashhad, Iran and
[2]Agricultural Research and Services Centre, Mashhad, Iran

Abstract: Alcohols and phenols were tetrahydropyranylated in the presence of $H_7[PMo_8V_4O_{40}]$ in good to excellent yields in acetonitrile and under solvent-free reaction conditions. A mild and convenient method for the formation and deprotection of ethers (THP ethers) is described. The formation of THP ethers from the corresponding alcohols was accomplished in the presence of acid-sensitive functional groups.

Keywords: tetrahydropyranyl ethers; heteropolyacid; protecting group; tetrahydropyranylation.

INTRODUCTION

Due to the easy preparation and good stability of tetrahydropyranyl groups in the presence of hydrides, alkylating agents, Grignard reagents, organometallic reagents, *etc*.,[1] they are frequently used for the protection of alcohols and phenols. In addition, they serve as stable protecting groups in peptide, nucleoside, nucleotide, carbohydrate and steroid chemistry. Tetrahydropyranylation of alcohols can be accomplished using *p*-toluenesulfonic acid (*p*-TSA),[2] $BF_3·OEt_2$[3] and pyridinium ptoluenesulfonate (PPTS).[4] Recently, some developed reagents have been used for this purpose, such as $ZrCl_4$,[5] I_2,[6] LiBr,[7] acetonyltriphenylphosphonium bromide,[8] tetrabutylammonium tribromide (TBATB),[9] aluminium chloride hexahydrate,[10] indium(III) trifluoromethanesulfonate ($In(OTf)_3$),[11] alkylimidazolium tetrachloroaluminates,[12] $InCl_3$ immobilized in ionic liquids,[13] polystyrene-bound tin(IV) porphyrin,[14] Dowex 50WX4-100,[15] pyridinium chloride,[16] $SiO_2·p$-TSA,[17] *N*,*N'*-bis[3,5-bis(trifluoromethyl)phenyl]thiourea and a polystyrene-bound analogue,[18] $Al(OTf)_3$,[19] and bromodimethylsulphonium bromide.[20] The employment of protective groups is an important procedure in organic synthesis.[21]

---

* Corresponding author. E-mail: aligharib5@yahoo.com

Among numerous protecting groups of alcohols, the tetrahydropyranyl (THP) group is one of the most frequently employed protecting groups due to its stability towards most non-acidic reaction conditions, ease of preparation, and facile removal under mild acidic conditions. Recent examples include stannous chloride dihydrate,[22] and heterogeneous catalysts such as sulphuric acid adsorbed on silica gel,[23] ionic liquids[24] and polyoxometalate.[25] For the deprotection of tetrahydropyranyl ethers (THP ethers), reagents including tetrafluoroborate anion,[26] sodium bromate,[27] CBr_4,[28] and montmorillonite clays[29,30] have been employed. Also, reductive reaction of tetrahydropyranyl ethers were reported in the literature.[31] Mild and chemoselective protection and deprotection of hydroxyl functionality are essential parts in the synthetic operation of polyfunctional organic compounds,[21] especially in the context of natural product and carbohydrate chemistry. Furthermore, its precursor, 3,4-dihydro-2*H*-pyran (DHP) is relatively inexpensive, rendering the process amenable to large-scale processes.[32] A heteropolyacid is an oxide cluster that has a type of phosphorus/silicon oxo acid and oxo acids with molybdenum, tungsten and other elements. The application of heteropolyacid as catalytic materials is growing continuously in the field of catalysis.[33] These compounds possess unique properties, such as: well-defined structure, Brønsted acidity, possibility to modify their acid–base and redox properties by changing their chemical composition (substituted HPAs), ability to accept and release electrons, high proton mobility, *etc*.[34] Acidity, basicity, and pseudo liquid behaviour are the principal factors governing the acid catalysis by solid heteropolyacids. The acidic properties are mainly controlled by *i*) the structure and composition of the heteropoly anion itself, *ii*) the counter cations and *iii*) the dispersion on supports. The acid strength can be controlled mainly by *i*), and the number of acid sites is greatly influenced by *ii*) and *iii*). Besides, soft basicity of the heteropoly anion itself sometimes plays an important role for high catalytic activity in acid-catalyzed reactions. The acid strength of hydrogen forms in the solid state reflects on the general the acidity in solution and it decreases when W is replaced by Mo and when the central P atom is replaced by Si in Keggin heteropolyacids, whereby Keggin heteropolyacids are stronger acids than Dawson heteropolyacids.[35]

EXPERIMENTAL

Materials and methods

All chemical materials were purchased from Merck and used without further purifycation.

Instruments

The ^{1}H-NMR spectra were recorded on a FT NMR Bruker 300 MHz spectrometer at 298 K. Chemical shifts were reported in ppm (*δ*-scale) relative to the internal standard TMS (0.00 ppm); the solvent was used as a reference. Melting points (m.p.) were recorded on an Electro-

thermal type 9100 melting point apparatus and are uncorrected. The products were identified by comparison of their m.p., IR and NMR spectra with those of authentic samples.

Catalyst preparation

The catalysts $H_4[PMo_{11}VO_{40}]$, $H_5[PMo_{10}V_2O_{40}]$, $H_6[PMo_9V_3O_{40}]$, $H_7[PMo_8V_4O_{40}]$ and Wells–Dawson, $H_6[P_2W_{18}O_{62}]$ were prepared in accordance to literature methods.[36–41]

General procedure for the protection of alcohols using the heteropolyacid catalysts in the presence of solvents

To a mixture of benzyl alcohol (1.0 mmol) and DHP (1.0 mmol) in dry CH_3CN (5 mL) was added a heteropolyacid catalyst (1.2 mol), and the resulting mixture was stirred at room temperature for the appropriate time until the complete disappearance of the starting alcohol was confirmed by thin layer chromatography (TLC). After completion of the reaction, the solid catalyst was removed by simple filtration. Evaporation of the solvent under reduced pressure gave the almost pure THP ether. Column chromatography of the filtrate on silica gel using *n*-hexane:EtOAc (6:1) as eluent gave benzyl tetrahydropyranyl ether in high yield.

General procedure for the solvent-free protection of alcohols using heteropolyacid catalysts

To a mixture of benzyl alcohol (1.0 mmol) and DHP (1.0 mmol) was added a heteropoly-acid catalyst (1.2 mol), and the resulting mixture was stirred at room temperature for the appropriate time until the complete disappearance of the starting alcohol (as monitored by TLC). After completion of the reaction, reaction, $CHCl_3$ (5 ml) was added and the organic phase was obtained by simple filtration. Evaporation of the solvent under reduced pressure gave the almost pure THP ether. Column chromatography of the filtrate on silica gel using *n*-hexane:EtOAc (6:1) as eluent gave benzyl tetrahydropyranyl ether in high yield.

RESULTS AND DISCUSSION

Alcohols, phenols, 3,4-dihydro-2*H*-pyran (DHP), and $H_7[PMo_8V_4O_{40}]$ and other heteropolyacid catalysts were stirred in CH_3CN at room temperature to yield the corresponding THP ethers. The tetrahydropyranylation of alcohols and phenols in the presence of $H_7[PMo_8V_4O_{40}]$ was investigated and herein, a mild and efficient method for the conversion of alcohols to THP compounds is reported. First, the protection of benzyl alcohol in the presence of $H_7[PMo_8V_4O_{40}]$ and other heteropolyacid catalysts was studied. Benzyl tetrahydropyranyl ether was formed after appropriate times. Then, these conditions were applied for the protection of structurally different alcohols and phenols (Scheme 1).
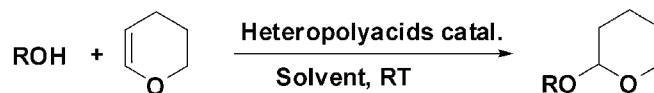
Scheme 1. Tetrahydropyranylation of phenols and alcohols using heteropolyacid catalysts.

Various aromatic and aliphatic alcohols were tetrahydropyranylated to THP compounds using $H_7[PMo_8V_4O_{40}]$ heteropolyacid catalyst in good to high yields under ambient conditions without any by-products. Employing the ratios shown in Table I, the best results were obtained and THP ethers were produced in good to excellent yields. The results of tetrahydropyranylation of alcohols to THP

GHARIB and JAHANGIR

ethers are presented in Table I. As can be seen in Table I, primary, secondary and tertiary alcohols and phenols were all protected under the employed conditions. Thus, this method is very suitable for the protection of various types of alcohols and phenols, providing a novel application of $H_7[PMo_8V_4O_{40}]$ heteropolyacid catalyst in organic synthesis.

TABLE I. Preparation of THP ethers in the presence of $H_7[PMo_8V_4O_{40}]$ catalyst in MeCN and under solvent-free conditions (The products were characterized by their physical properties, comparison with authentic samples, and by spectroscopic methods. The reaction was performed at room temperature. Molar ratios for ROH/DHP/$H_7[PMo_8V_4O_{40}]$, (HPAs) catalysts were 1:1:1.2)
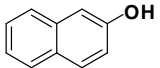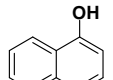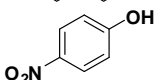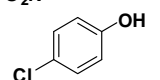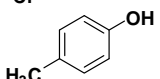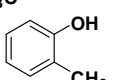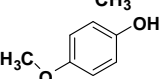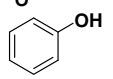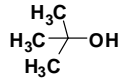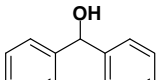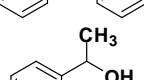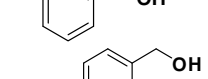
Entry	ROH	CH$_3$CN		Solvent-free	
		meTi, min	Isolated yield, %	Time, min	Isolated yield, %
1		32	65.5	20	69
2		33	80	23	82
3		23	91	21	80.5
4		25	95	24	93.4
5		8	96	10	94.4
6		9	90	9	90
7		10	98	8	95.5
8		9	96	10	97
9		7	89	6	88
10		15	91	16	93
11		18	98	20	99
12		8	96.3	11	98

TABLE I. Continued
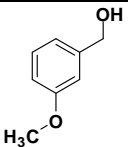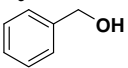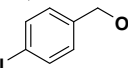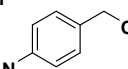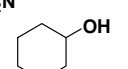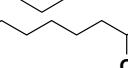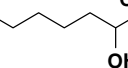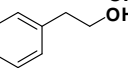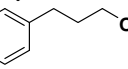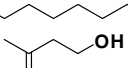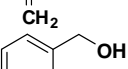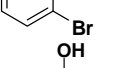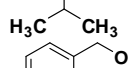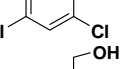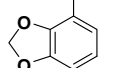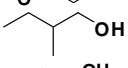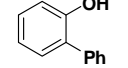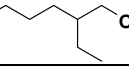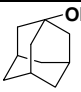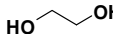
Entry	ROH	CH₃CN		Solvent-free	
		Time, min	Isolated yield, %	Time, min	Isolated yield, %
13		5	97.5	7	95
14		11	98	10	97
15		16	90.6	19	93
16		17	86	15	88
17		23	97.5	25	98
18		30	98.5	30	96
19		31	97.5	29	96
20		7	98	11	98
21		6	97	9	97
22		9	91.5	10	94
23		9.5	93.5	9	91
24		14	94.5	17	95
25		8	92	12	94
26		7	94	9	90.5
27		16	93	15	93
28		11	93.2	12	95.5
29		19.5	87	18	89.5
30		8.5	91.2	11.5	93

TABLE I. Continued

Entry	ROH	CH$_3$CN		Solvent-free	
		Time, min	Isolated yield, %	eTim, min	Isolated yield, %
31	OH	27.5	94.5	29	91.6
32	HO⌒⌒OH	21	92.4	20	90.5

This method was found to be highly selective for primary alcohols. In a binary mixture of 3-phenyl-1-propanol and 2-octanol, the primary alcohol was completely converted to corresponding THP ether, while only 8 % of 2-octanol reacted. Similarly, excellent selectivity was observed for tetrahydropyranylation of benzyl alcohol in the presence of 1-phenylethanol (Table II, entry 2). Primary and secondary alcohols were selectively converted to THP ethers in the presence of a tertiary alcohol (Table II, entries 5 and 6). Furthermore, this method showed excellent selectivity in the tetrahydropyranylation of alcohols in the presence of phenols (Table II, entry 7).

TABLE II. Selectivity of the reactions of different binary mixtures with DHP/H$_7$[PMo$_8$V$_4$O$_{40}$]
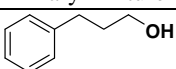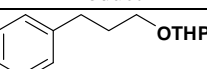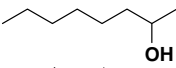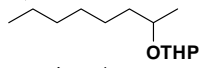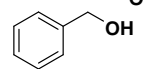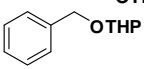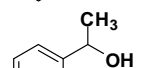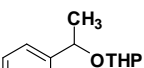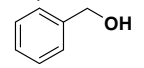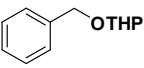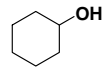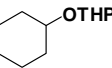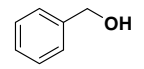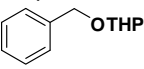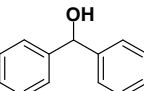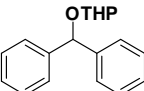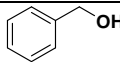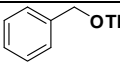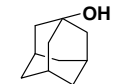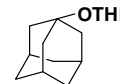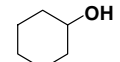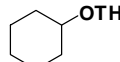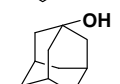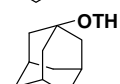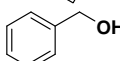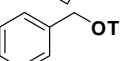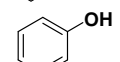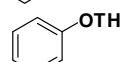
Entry	Binary mixture	Product	Time, min	Yield[a], %
1			11	91.5
				8
2			18	93.2
				6
3			22	83
				16
4			14	100
				0

TABLE II. Continued

Entry	Binary mixture	Product	Time, min	Yield[a], %
5	⟨benzyl alcohol⟩ OH	⟨benzyl⟩ OTHP	23	91
	⟨2-adamantanol⟩ OH	⟨2-adamantyl⟩ OTHP		9
6	⟨cyclohexanol⟩ OH	⟨cyclohexyl⟩ OTHP	21	82
	⟨2-adamantanol⟩ OH	⟨2-adamantyl⟩ OTHP		18
7	⟨benzyl alcohol⟩ OH	⟨benzyl⟩ OTHP	18	92
	⟨phenol⟩ OH	⟨phenyl⟩ OTHP		8

[a]GC yield using internal standard; ROH:DHP:$H_7[PMo_8V_4O_{40}]$ = 1:1:1.2; the reaction was performed at room temperature

Effect of the catalyst type
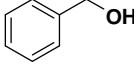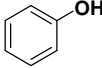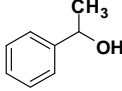
In order to compare the kinds of vanadium(V)-substituted polyoxomolybdates, *i.e.*, $H_4[PMo_{11}VO_{40}]$, $H_5[PMo_{10}V_2O_{40}]$, $H_6[PMo_9V_3O_{40}]$, and Wells–Dawson catalysts, with the $H_7[PMo_8V_4O_{40}]$ catalyst in the tetrahydropyranylation of alcohols and phenols, these catalysts were used for the tetrahydropyranylation of alcohols and phenols. The results are shown in Table III. The yield of product decreased in the following order: $H_7[PMo_8V_4O_{40}]$ > $H_6[P_2W_{18}O_{62}]$ > $H_6[PMo_9V_3O_{40}]$ > $H_5[PMo_{10}V_2O_{40}]$ > $H_4[PMo_{11}VO_{40}]$. The results showed that $H_7[PMo_8V_4O_{40}]$ was the most efficient catalyst for THP with a higher activity than the Keggin and Dawson heteropolyacids. The larger number of protons in its structure may lower the activation barrier for the alkylation reaction. In addition, the large anion also provides many "sites" on the molecule that are likely to contribute to the effectiveness of the catalyst. Comparison of the results obtained using vanadium (V)-substituted polyoxomolybdates types of heteropolyacids and Wells–Dawson catalysts with those reported for $H_7[PMo_8V_4O_{40}]$ and Dawson type catalysts shows some advantages of the former catalysts in these reactions (Table III).

Spectroscopic data for the new compound 16

Compound 16 (Table I). Yellowish oil (eluted with *n*-hexane: EtOAc, 6:1). ^{1}H-NMR (300 MHz, CDCl$_3$, δ / ppm): 1.48–1.90 (6H, *m*), 3.52 (1H, *m*), 3.89 (1H, *m*), 4.42 (1H, *d, J* = 11.6 Hz), 4.70 (1H, *m*), 4.80 (1H, *d, J* = 12.0 Hz), 7.25 (4H, *m*); ^{13}C-NMR (75 MHz, CDCl$_3$, δ / ppm): 147.6, 146.6, 128.1, 123.9, 98.7,

68.0, 62.6, 30.8, 25.7, 19.6; HRMS (EI): Calcd. for $C_{12}H_{15}O_4N$ [M]$^+$, 237.1001. Found: 237.1003.

TABLE III. The role of the heteropolyacid on the tetrahydropyranylation under solvent-free reaction conditions

Entry	Substrate	Catalyst	Time, min	Yield[a], %
1	OH	$H_7[PMo_8V_4O_{40}]$	10	97.3
2	A	$H_6[P_2W_{18}O_{62}]$	10	94.5
3	A	$H_6[PMo_9V_3O_{40}]$	10	92.2
4	A	$H_5[PMo_{10}V_2O_{40}]$	10	91.5
5	A	$H_4[PMo_{11}VO_{40}]$	10	88.6
6	OH	$H_7[PMo_8V_4O_{40}]$	10	97
7	B	$H_6[P_2W_{18}O_{62}]$	10	94
8	B	$H_6[PMo_9V_3O_{40}]$	10	91.5
9	B	$H_5[PMo_{10}V_2O_{40}]$	10	90
10	B	$H_4[PMo_{11}VO_{40}]$	10	88.5
11	CH$_3$ OH	$H_7[PMo_8V_4O_{40}]$	22	99
12	C	$H_6[P_2W_{18}O_{62}]$	22	96.5
13	C	$H_6[PMo_9V_3O_{40}]$	22	94.3
14	C	$H_5[PMo_{10}V_2O_{40}]$	22	91.5
15	C	$H_4[PMo_{11}VO_{40}]$	22	90.4

[a]Isolated yield determined by GC. The reaction was performed at room temperature. Substrate of entry **1**: compound A, substrate of entry **6**: compound B and substrate of entry **11**: compound C

CONCLUSIONS

In summary, a novel method using different vanadium(V)-substituted poly-oxomolybdates and Wells–Dawson heteropolyacids as inexpensive, non-corrosive and environmentally benign catalysts for protection of phenols and alcohols as THP ethers was developed. The advantages of the presented procedure are simplicity of operation and work-up and good yields of products, mild conditions, short reaction times and high yields (> 90 %).

И З В О Д

КАТАЛИТИЧКА ТЕТРАХИДРОПИРАНИЛАЦИЈА ФЕНОЛА И АЛКОХОЛА ВАНАДИЈУМ(V)-СУПСТИТУИСАНИМ ПОЛИОКСОМОЛИБДАТИМА

ALI GHARIB[1,2] и MANOUCHEHR JAHANGIR[1]

[1]*Department of Chemistry, Islamic Azad University, Mashhad и* [2]*Agricultural Research and Services Center, Mashhad, Iran*

Успешно је извршена реакција алкохола и фенола са тетрахидропираном у присуству $H_7[PMo_8V_4O_{40}]$ у добром до одличном приносу, без присутног растварача. Описани су бла-

ги реакциони услови за формирање и депротекцију тетрахидропиранил етара (THP етри). Грађење THP етара са одговарајућим алкохолима извршено је у присуству функционалних група које су осетљиве на киселе реакционе услове.

REFERENCES

1. T. W. Greene, P. G. M. Wuts, *Protective Groups in Organic Synthesis*, 3rd ed., Wiley, New York, 1999
2. E. J. Corey, H. Niwa, J. Knolle, *J. Am. Chem. Soc.* **100** (1978) 1942
3. H. Alper, L. Dinkes, *Synthesis* (1972) 81
4. M. Miyashita, A. Yoshikoshi, P. A. Grieco, *J. Org. Chem.* **42** (1977) 3772
5. N. Rezai, F. A. Meybodi, P. Salehi, *Synth. Commun.* **30** (2000) 1799
6. N. Deka, J. C. Sarma, *Synth. Commun.* **30** (2000) 4435
7. M. A. Reddy, L. R. Reddy, N. Bhanumathi, K. R. Rao, *Synth. Commun.* **30** (2000) 4323
8. Y. S. Hon, C. F. Lee, *Tetrahedron Lett.* **40** (1999) 2389
9. S. Naik, R. Gopinath, B. K. Patel, *Tetrahedron Lett.* **42** (2001) 7679
10. V. V. Namboodiri, R. S. Varma, *Tetrahedron Lett.* **43** (2002) 1143
11. T. Mineno, *Tetrahedron Lett.* **43** (2002) 7975
12. V. V. Namboodiri, R. S. Varma, *Chem. Commun.* (2002) 342
13. J. S. Yadav, B. V. S. Reddy, D. Gnaneshwar, *New J. Chem.* **27** (2003) 202
14. M. Moghadam, S. Tangestaninejad, V. Mirkhani, I. Mohammadpoor-Baltork, S. Gharaati, *J. Mol. Catal., A* **337** (2011) 95
15. P. S. Poon, A. K. Banerjee, L. Bedoya, M. S. Laya, E. V. Cabrera, K. M. Albornoz, *Synth. Commun.* **39** (2009) 3369
16. A. R. Hajipour; M. Kargosha, A. E. Ruoho, *Synth. Commun.* **39** (2009) 1084
17. A. A. Dos Santos, G. A. Brito Jr., M. V. L. Archilha, T. G. A. Bele, G. P. Dos Santos, M. B. M. De Mello, *J. Braz. Chem. Soc.* **20** (2009) 42
18. M. Kotke, P. R. Schreiner, *Synthesis* (2007) 779
19. D. B. G. Williams, S. B. Simelane, M. Lawton, H. H. Kinfe, *Tetrahedron*. **66** (2010) 4573
20. A. T. Khan, E. Mondal, B. M. Borah, S. Ghosh, *Eur. J. Org. Chem.* (2003) 4113
21. P. J. Kocienski, *Protecting Groups*, Thieme, Stuttgart, 1994
22. K. J. Davis, U. T. Bhalerao, B. V. Rao, *Synth. Commun.* **29** (1999) 1679
23. M. M. Heravi, D. Ajami, M. Ghassemzadeh, *Synth. Commun.* **29** (1999) 1013
24. L. C. Branco, C. A. M. Afonso, *Tetrahedron* **57** (2001) 4405
25. M. H. Habibi, S. Tangestaninejad, I. Mohammadpoor-Baltork, V. Mirkhani, B. Yadollahi, *Tetrahedron Lett.* **42** (2001) 2851
26. K. S. Ramasamy, D. Averett, *Synlett* (1999) 709
27. I. Mohammadpoor-Baltork, A. R. Nourozi, *Synthesis* (1999) 487
28. A. S.-Y. Lee, F.-Y. Su, Y.-C. Liao, *Tetrahedron Lett.* **40** (1999) 1323
29. T. Taniguchi, K. Kadota, A. S. ElAzab, K. Ogasawara, *Synlett* (1999) 1247
30. T.-S. Li, Z.-H. Zhang, T.-S. Jin, *Synth. Commun.* **29** (1999) 181
31. A. Srikrishna, J. A. Sattigeri, R. Viswajanani, C. V. Yelamaggad, *J. Org. Chem.* **60** (1995) 2260
32. B. M. Kim, S. J. Bae, S. M. So, H. T. Yoo, S. K. Chang, J. H. Lee, J. Kang, *Org. Lett.* **3** (2001) 2349
33. H. Firouzabadi, A. A. Jafari, *J. Iran. Chem. Soc.* **2** (2005) 85

34. L. E. Briand, G. T. Baronetti, H. J. Thomas, *Appl. Catal., A* **256** (2003) 37
35. G. I. Kapustin, T. R. Brueva, A. L. Klyachko, M. N. Timofeeva, S. M. Kulikov, I. V. Kozhevnikov, *Kinet. Katal.* **31** (1990) 1071.
36. I. V. Kozhevnikov, *Chem. Rev.* **98** (1998) 171
37. F. F. Bamoharram, M. M. Heravi, M. Roshani, M. Jahangir, A. Gharib,. *J. Mol. Catal., A* **271** (2007) 126
38. F. F. Bamoharram, M. M. Heravi, M. Roshani, A. Gharib, M. Jahangir, *J. Mol. Catal., A* **252** (2006) 90
39. G. A. Tsigdinos, C. Hallada, *J. Inorg. Chem.* **7** (1968) 437
40. Y. Mahha, A. Atlamsani, J. C. Blais, M. Tessier, J. M. Brégeault, L. Salles, *J. Mol. Catal. A* **234** (2005) 63
41. Y. Ding, Q. Gao, G. Li, H. P. Zhang, J. M. Wang, L. Yan, J. S. Suo, *J. Mol. Catal. A* **218** (2004) 161.

Irreversible UV-induced quercetin and rutin degradation in solution studied by UV spectrophotometry and HPLC chromatography

JELENA B. ZVEZDANOVIĆ, JELENA S. STANOJEVIĆ, DEJAN Z. MARKOVIĆ*
and DRAGAN J. CVETKOVIĆ

University of Niš, Faculty of Technology, Bulevar oslobodjenja 124, 16000 Leskovac, Serbia

Abstract: The irreversible degradation of quercetin and rutin, dissolved in methanol and water, induced by continuous UV-irradiation from two different sub-ranges (UV-B and UV-C) were studied in this work. The degradation of both flavonoids is related to the formation of UV-induced degradation products: both processes follow first-order kinetics. The degradation and rate constants of the formation of the products are both dependent on the involved UV-photons energy input in both solvents.

Keywords: quercetin; rutin; UV-irradiation; degradation; products; kinetics.

INTRODUCTION

Ultraviolet (UV) radiation is part of the natural sunlight spectrum that reaches the Earth's surface. Depending on the source, the reported UV-portion of the total sunlight does not exceed 5–6 %, of which, under normal circumstances, >95 % is UV-A (320–400 nm) radiation, the rest being UV-B (290–320 nm) light;[1] UV-C radiation (200–280 nm) is completely absorbed by the atmosphere. Besides being the obligatory driving force of photosynthesis, light may also be damaging factor in the biosphere.[2] The recent depletion of the stratospheric ozone layer has led to an increase on the biologically most damaging UV-B portion of light at ambient levels. Plants generally respond to an increase in UV-B radiation through very different mechanisms, including the synthesis of UV-absorbing, protective pigments, such as flavonoids.[3,4]

Flavonoids are a large class of natural polyphenol compounds of low molecular mass, widely distributed in plant world, where they perform several very important functions, including anti-oxidation.[5–7] They are benzo-γ-pyrane derivatives consisting of pyrane and phenolic rings. The most important structural

---

297

elements related to their functions are: an *o*-dihydroxy group in the B ring (catechol structure) as a potential radical target, a double bond between positions 2 and 3 of the C-ring conjugated with keto group in position 4 (because of its capacity to delocalize the uncoupled electron of the flavonoid radical) and C-3, C-5 and C-7 hydroxyl groups (of the C and A rings) as potential free radical scavengers (Fig. 1).[8–10] Quercetin (flavonol) and rutin (flavon) are members of the flavonoid family, with the structures shown in Figs. 1A and 1B, respectively. The main difference in their structures lies in position C-3, where instead of an OH group (quercetin), a glycoside residue has been inserted (rutin). Updated studies connect the antioxidant activity of flavonoids with presence (or absence) of an OH group at position 3 of the C-ring, in combination with a catechol B-ring structure.[5–11] The importance of this position may be estimated – among other ways – by comparing the stabilities of quercetin and rutin toward an externally induced stress, such as UV-irradiation.
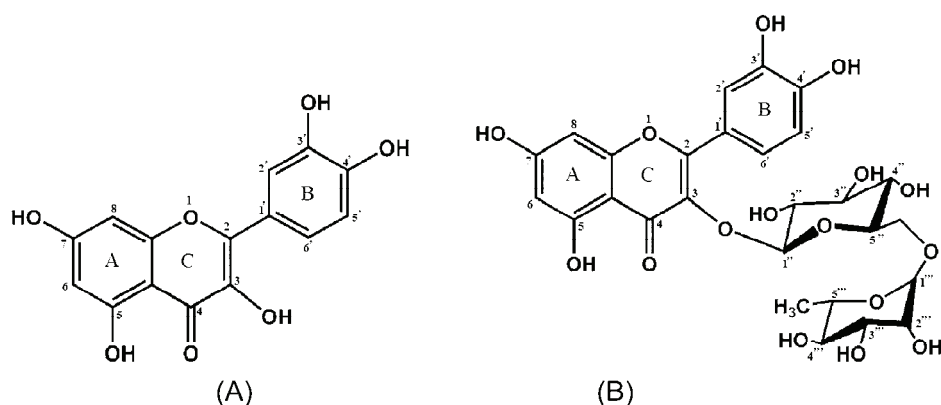
Fig. 1. Structure of A – quercetin and B – rutin.

Quercetin and its glycosides (such as rutin) are believed to be responsible for prevention of extended UV radiation-induced damage to a variety of plants. Quercetin absorbs UV radiation with absorbance maxima in the UV-A ($\lambda_{max} = 365$ nm, $\varepsilon = 28400$ M^{-1} cm^{-1}) and UV-C range ($\lambda_{max} = 256$ nm, $\varepsilon = 28300$ M^{-1} cm^{-1}), suggesting that one plausible photoprotective mechanism could be direct absorption of UV radiation, thereby preventing the formation of reactive oxygen species (ROS) and consequent direct DNA damage.[12] The UV energy absorbed by quercetin may be dissipated as heat[13] or converted into decomposition products.[11] UV-irradiation of flavonoids in solution and in liposome systems (*in vitro*), as well as *in vivo*, results in their irreversible breakdown, accompanied by the appearance of a number of decomposition products.[14,15]

In the recently accepted report,[16] the stability of quercetin and rutin in solution toward UV-irradiation from the three ranges (UV-A, UV-B and UV-C)

were compared, as were their antioxidant activities in the presence of a lipoidal mixture as a protection target. It was concluded that: 1) rutin expressed higher stability than quercetin toward UV-irradiation, while the stability of both flavonoids was found to be affected by the energy of incident photons; 2) however, the higher stability of rutin had only a partial effect on its antioxidant ability to protect a lipid mixture from peroxidation, *i.e.*, its dominance in stability over quercetin (towards UV-irradiation) was not supported by its antioxidant ability compared to that of quercetin under the same experimental conditions.

This study is a continuation of the previous investigation.[16] Thus, quercetin and rutin were again irradiated in solution but this time reversed phase HPLC techniques in combination with absorption spectrophotometry were employed to analyze the formation of the degradation products quercetin and rutin induced by continuous UV-irradiation to provide the data for a kinetic analysis to follow.

EXPERIMENTAL

Samples preparations

Quercetin and rutin standards were purchased from Merck. Quercetin was dissolved in methanol and rutin in both methanol and water to give a concentration of 0.1 mM.

UV-Irradiation treatment

The irradiation of the pigments in solution was performed in a cylindrical photochemical reactor "Rayonnet", with 7 symmetrically placed lamps, with emission maxima in two different UV sub-ranges, 300 (UV-B) and 254 nm (UV-C). The total emitted energy flux (measured using a UV-meter, Solarmeter, model 8.0 UV meter, Solartech) was about 10.5 W m^{-2} for 300 nm and 12.5 W m^{-2} for 254 nm at a 10 cm distance from the lamps. The samples (2 ml) were irradiated in quartz cuvettes placed on a rotating circular holder.

UV Spectroscopy

The UV spectra of rutin and quercetin in different solvents were recorded on a Varian Cary-100 spectrophotometer. All spectra, before and after irradiation with UV-light, were recorded in the range from 200 to 500 nm.

High performance liquid chromatography – photodiode array detector (HPLC–DAD)

The HPLC analyses were performed at 15 °C on an Agilent 1100 Series system, Waldbron, Germany, using a diode array detector set at 257, 295 and 372 nm. Aliquots of 20 µl were injected into a 4.6×250 mm RPC-18 column (Zorbax Eclipse XDB-C18) with 5 µm particle size. Elution was realized in the gradient mode proposed by Veit *et al.* using two mobile phase components: A = 0.15 % phosphoric acid in water–methanol (77:23 v/v) mixture, B = methanol.[17] The gradient mode was set as follows: 0 to 3.6 min, isocratic 100 % A; 3.6–24.0 min, linear gradient from 100 to 80.5 % A; 24–30 min, isocratic 80.5 % A; 30–60 min, linear gradient from 80.5 to 51.8 % A; 60–67.2 min, linear gradient to 100 % B; 67.2––90.0 min, isocratic 100 % B. The flow rate was 1.0 cm^3 min^{-1}. The HPLC peaks (areas) recorded at 372 nm were used for the determination of quercetin and rutin degradation (bleaching) induced by UV-irradiation, *i.e.*, kinetic analysis. New peaks were detected at 295 and 257 nm because of quercetin and rutin UV-irradiation in solution; their areas were plotted against irradiation time, providing possibilities for kinetic analysis.

RESULTS

The changes in chromatograms of UV-irradiated quercetin (in methanol) and rutin (in methanol and in water) are shown in Figs. 2 and 3, respectively. The changes of absorption spectra of quercetin and rutin exposed to UV-irradiation are shown in the related inserted spectra in Figs. 2 and 3 (right), respectively.
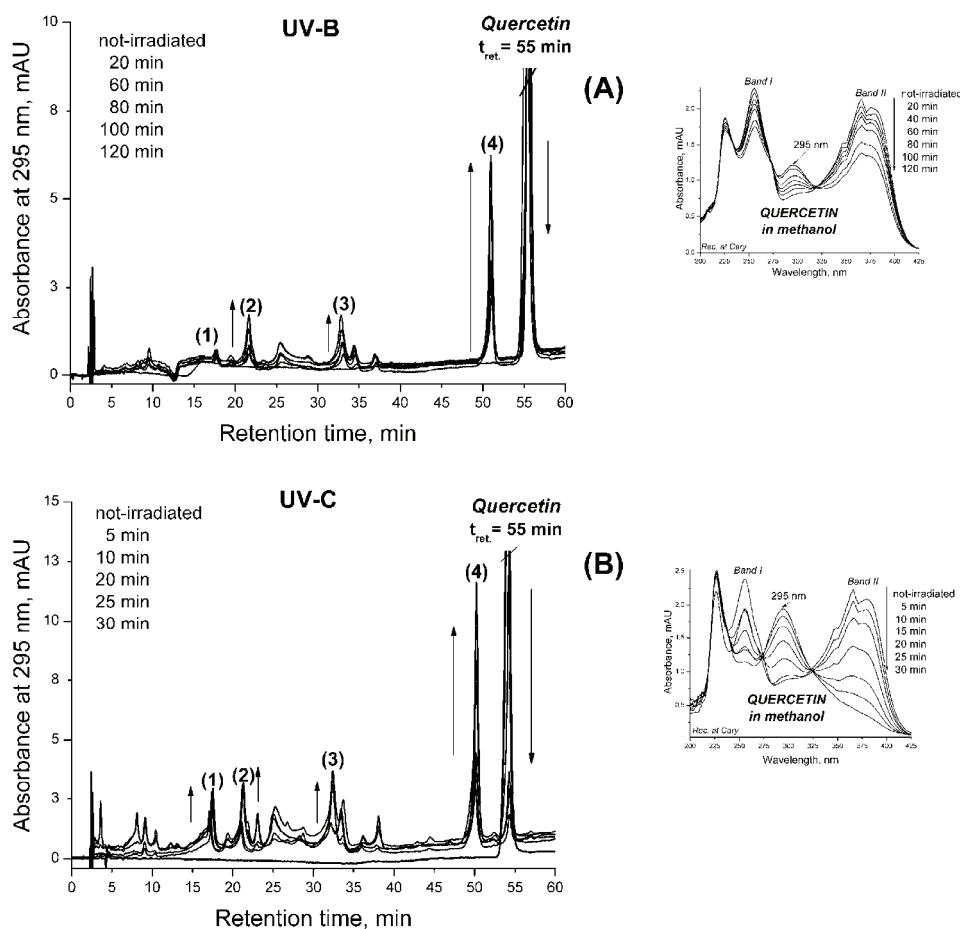
Fig. 2. Quercetin in methanol, irradiated with continuous UV-B (A) and UV-C (B) radiation. The changes in HPLC-chromatograms recorded at 295 nm (A, B: left); the corresponding changes in the samples absorption spectra, recorded in the spectral range 200–425 nm (A, B: right). The exposure times are displayed on the graphs and the arrows show the change in direction: down (↓) in the case of quercetin, and up (↑) in the case of the degradation products. Main observed products of UV-induced degradation of quercetin (at different retention times, $t_{ret.}$: 17, 21, 32 and 50 min) were numerated with the numbers 1–4, respectively, in the chromatograms. mAU – mili (10^{-3}) relative absorbance units.
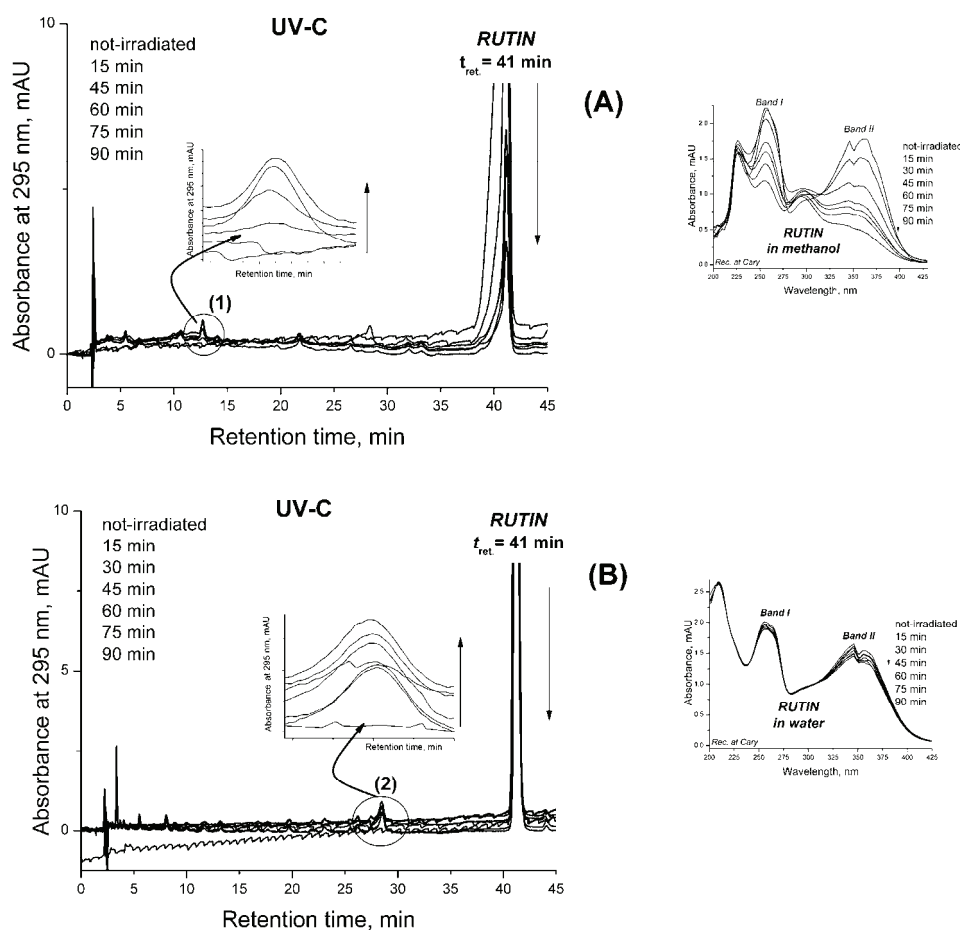
Fig. 3. Rutin in methanol (A) and water (B), irradiated with continuous UV-C irradiation. The chromatograms explanation is the same as for Fig. 2. The only observed products (at different retention times, $t_{ret.}$, 13 and 28 min, respectively) were numerated with numbers 1 and 2, respectively, in the chromatograms.

Irradiation of quercetin in methanol with either UV-B or UV-C radiation resulted in a decrease in quercetin ($t_{ret.}$ = 55 min) and the appearance of new peaks, *i.e.*, four major peaks (corresponding to UV-induced products) at the following retention times: 1) 17, 2) 21, 3) 32 and 4) 50 min (Fig. 2). Irradiation of rutin in methanol and in water with UV-C radiation resulted in rutin degradation ($t_{ret.}$ = 41 min) and the appearance of two new peaks, at 1) 13 and 2) 28 min, respectively (Fig. 3). The absorption spectra of the four observed UV-induced degradation products of quercetin and the two of rutin are shown in Figs. 4A and 4B, respectively. The proposed, possible structures of the degradation products of quercetin are shown in Fig. 4A. These compounds, together with their names,

positions of the absorption maxima (λ_{max}) and related references are given in Table I.[18–23]

(A) - Quercetin in methanol, the degrad. products
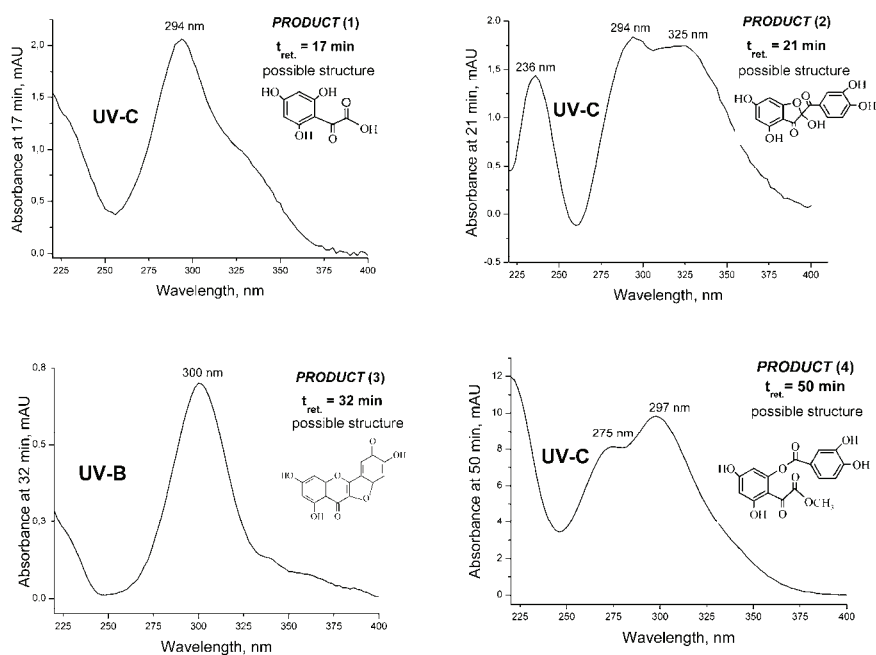
(B) - Rutin, the degrad. products
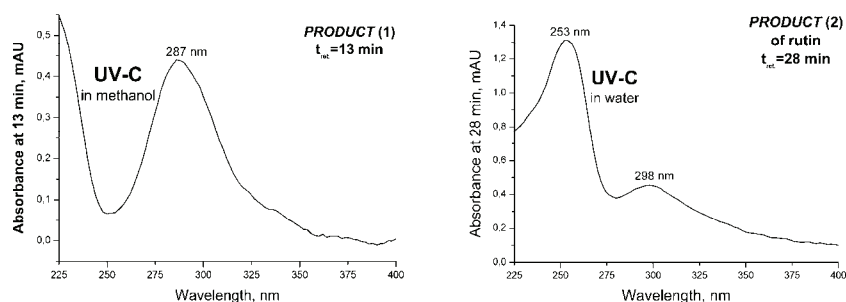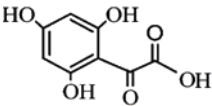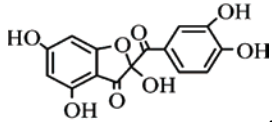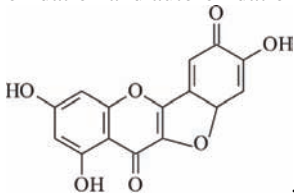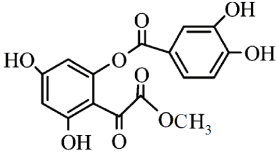
Fig. 4. Absorption spectra of UV-B and UV-C induced quercetin degradation products (A), as well as UV-C induced rutin degradation products (B), corresponding to the main observed peaks in the related HPLC chromatograms (the retention times are marked).

TABLE I. Possible structures of the products formed as the result of UV-B and UV-C irradiation of quercetin in methanol, detected by HPLC. The proposals are based on comparisons of the absorption spectra of the products with literature spectral data

Product	$t_{ret.}$ min	Name of product	Structure, obtained by	λ_{max} nm	References cited
1	17	2,4,6-Trihydroxy-phenylglyoxylic acid	electrochemical oxidation	292	Spectrum taken from Zhou *et al.*[18] The compound is also cited in refs.[19–21]
2	21	2-(3,4-Dihydroxybenzoyl)-2,4,6-trihydroxy-3(2*H*)-benzofuranone	electrochemical, enzymatic, 2,2'-azoisobutyronitrile oxidation and auto-oxidation	294, 325	Taken from Zhou and Sadik.[19] The compound is also cited in ref.[19]
3	32	1,3,8-Trihydroxy-9*aH*,11*H*-benzofuro[3,2-*b*]-[1]benzopyran-7,11-dione cyclic ether connecting AC-system with B-ring	electrochemical oxidation	300	Taken from Timbola *et al.*[22]
4	50	Methyl 2-{2-[(3,4-dihydroxybenzoyl)oxy]-4,6-dihydroxyphenyl}-2-oxoacetate	*γ*-irradiation-induced degradation	275, 297	Taken from Marfak *et al.*[23]

Decreasing kinetic plots of quercetin and rutin degradation obtained using the quercetin ($t_{ret.}$ = 55 min) and rutin ($t_{ret.}$ = 41 min) peaks from the chromatograms recorded at 372 nm (not shown), $\ln S_{372nm} = f(t_{irr})$, are shown in Fig. 5. The plots show a good linear fit, with R^2 values 0.95–0.99. The degradation kinetics seems to obey a first-order law. The calculated rate constants, k_{degrad} (min^{-1}), for the UV-B and UV-C sub-ranges in the two solvents, are given in Table II.

The analogue kinetic ln plots obtained using the peaks areas recorded at 295 nm, $\ln S_{295nm} = f(t_{irr.})$ for the four observed major products of UV-irradiated quercetin, **1**, **2**, **3** and **4**, are shown in Fig. 6A–D, respectively. The plots show good linear fits, with R^2 values 0.92–0.99. The calculated rate constants for the

formation of the UV- induced degradation products of quercetin, for UV-B and UV-C sub-ranges in methanol are given in Table III.
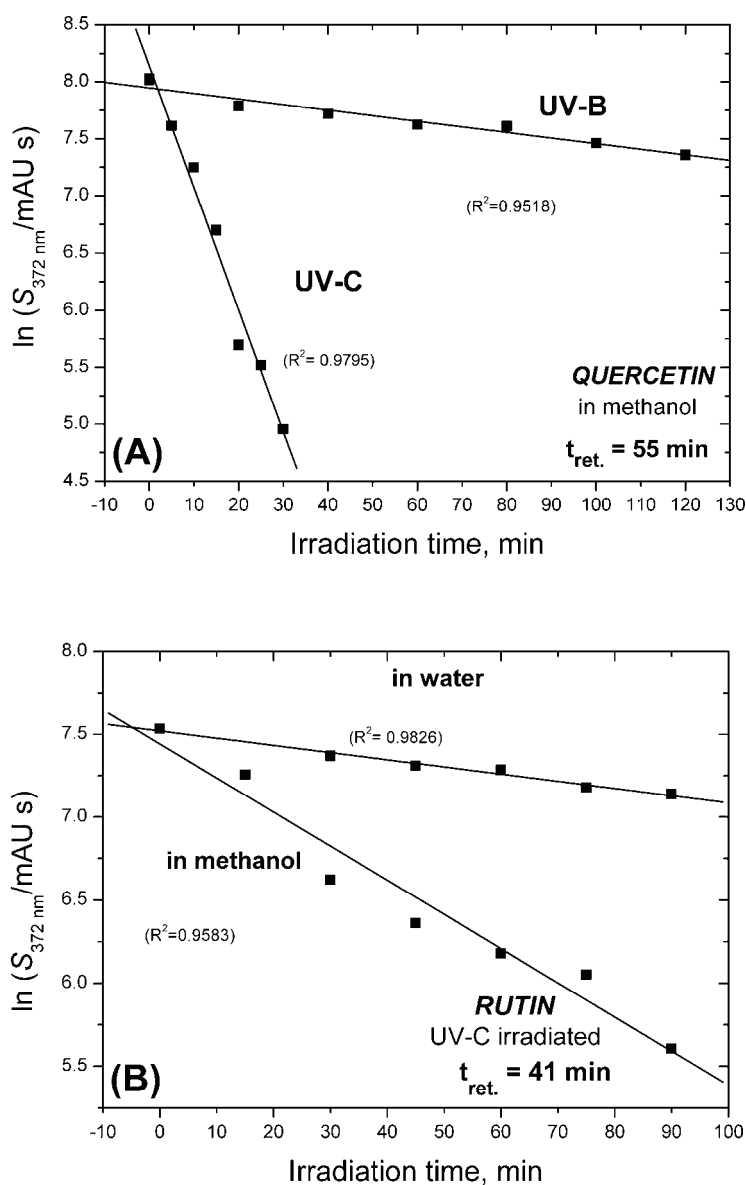
Fig. 5. Kinetic ln plots of UV-B and UV-C induced quercetin (A) and UV-C induced rutin (B) changes, obtained from the HPLC-chromatograms recorded at 372 nm, as a function of UV-B and C irradiation time, ln $S_{372nm} = f(t_{irr.})$. The plots show good linear fits, with R^2 values 0.95–0.99. The corresponding rate constants calculated from the slopes of the linear plots are given in Table II.

TABLE II. Kinetics of quercetin and rutin degradation in methanol and water (shown in Fig. 5), during increasing UV-irradiation time in two different UV sub-ranges: 300 (UV-B) and 254 nm (UV-C). Peak areas were taken from the corresponding HPLC-chromatograms at 372 nm (analogues to Figs. 2 and 3, not shown). $\ln S_{372nm} = k_{degrad.} \, t_{irr.} + n$, where S_{372nm} – peak area of quercetin and rutin from the corresponding chromatograms recorded at 372 nm, $t_{irr.}$ – UV-irradiation time, $k_{degrad.}$ – rate constants for UV-induced degradation of quercetin and rutin in methanol and water, given as the slopes of the linear plots in Fig. 5, in min^{-1}; $c = 1.0 \times 10^{-4}$ M

UV-irradiation wavelength, nm	Quercetin, $t_{ret.}$=55 min		Rutin, $t_{ret.}$=41 min
	In methanol		In water
300 (UV-B)	–0.0049	–	–
254 (UV-C)	–0.1069	–0.0206	–0.0043
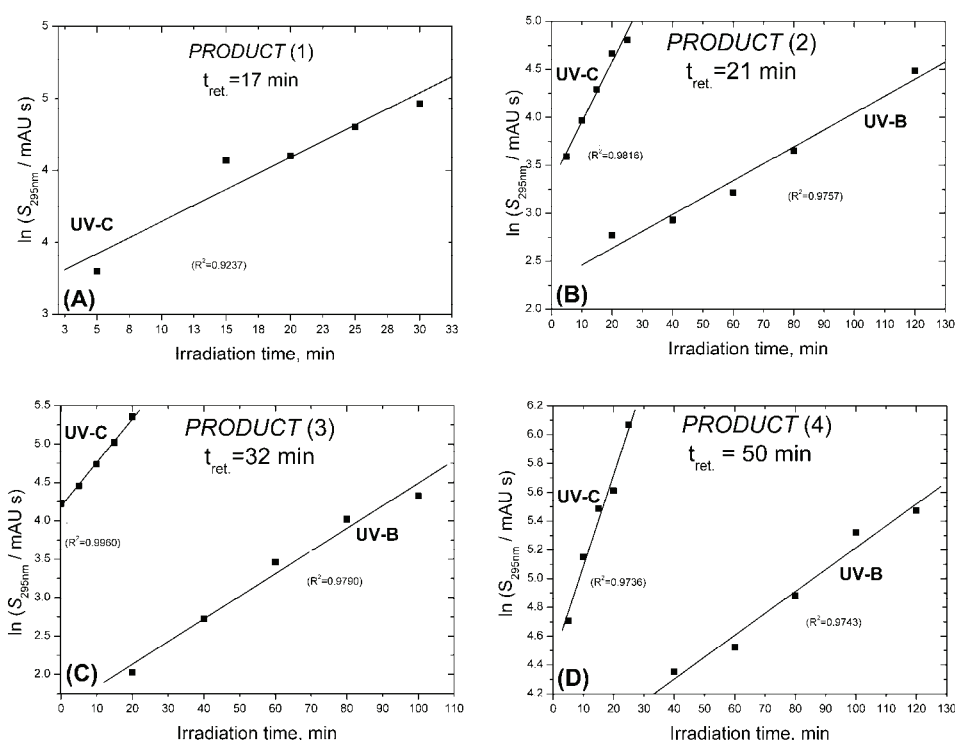
Fig. 6. Kinetic ln plots of UV-B and C induced quercetin degradation products, obtained from the HPLC-chromatograms recorded at 295 nm, as a function of UV-B and C irradiation time, $\ln S_{295nm} = f(t_{irr.})$. The plots show good linear fits, with R^2 values 0.95–0.99. The corresponding rate constants calculated from the slopes of the linear plots are are given in Table III.

DISCUSSION

Absorption spectra

The absorption spectra of flavonoids generally consist of two distinctive bands, in a broad range of 240–400 nm.[24] Band I, covering the range 300–380

nm, is attributed to the B-ring (with the A_{max} position around 350–370 nm), while band II, covering the range of 240–280 nm (with the A_{max} position around 260–270 nm) is attributed to the A–C benzoyl system; a weak band with an absorption maximum around 300 nm is also detected, which is attributed to the C-ring only – shown in Fig. 1 and in the related inserted spectra in Figs. 2 and 3. Both the investigated flavonoids expressed clear sensitivity to UV-irradiation, from both UV-ranges. Continuous UV-irradiation of quercetin and rutin in methanol induced a gradual decrease of the absorbance intensity, *i.e.*, a hypochromic effect, as shown in the related inserted spectra in Figs. 2A, 2B and 3A; similar spectral behavior of the absorption spectra was also observed for rutin in water under UV-C-irradiation (Fig. 3B). Thus, continuous irradiation of quercetin and rutin in solution resulted in their degradation, which increased with increasing irradiation time. However, rutin underwent a slower degradation in methanol, compared to quercetin (Figs. 3A and 2B, respectively). These results again confirmed that presence or absence of 3-OH group (quercetin, rutin, respectively) plays a major role in the stability of the flavonoids toward UV-irradiation.[11,16]

TABLE III. Kinetics of the formation of UV-B and UV-C-induced quercetin degradation products in methanol (the analogues plots to the ones for Table II). The peak areas were taken from the corresponding HPLC-chromatograms recorded at 295 nm (Fig. 2), *i.e.* the products A_{max} value. $k_{degrad.prod.}$ – rate constant for the formation of the degradation products in methanol was calculated from Fig. 6, in min^{-1}

UV-irradiation wavelength, nm	Product			
	1, $t_{ret.}$ = 17 min	**2**, $t_{ret.}$ = 21 min	**3**, $t_{ret.}$ = 32 min	**4**, $t_{ret.}$ = 50 min
300 (UV-B)	–	0.0176	0.0295	0.0152
254 (UV-C)	0.0405	0.0628	0.0568[a]	0.0637

[a]Until 20 min of UV-C irradiation

A clear increase in the absorbance was observed between 270 and 325 nm for quercetin in methanol, with a maximum at 295 nm (the related spectra are inserted in Fig. 2) for the two UV-ranges (UV-B and UV-C). For UV-C-irradiated rutin in methanol and especially rutin in water, the analogue increase in the absorbance was not so clear (the related spectra are inserted in Fig. 3). The existence of $A_{max,295nm}$ indicates the formation of product(s) as a result of UV-induced quercetin degradation that absorb in the spectral region 270–325 nm (for this reason, a monitoring wavelength of 295 nm was chosen in the HPLC–DAD experiments to estimate the UV-induced changes of quercetin and rutin in solution). The same spectral behaviors of UV-irradiated quercetin and rutin in solution were previously observed, but under slightly different conditions of UV-irradiation compared to the present experiments, *i.e.*, with about two times larger UV-B and UV-C incident energy.[16]

HPLC–DAD Analysis

The results of the HPLC analysis proved quercetin and rutin underwent irreversible UV-induced bleaching: a clear decrease of the corresponding main peaks areas at t_{ret} = 55 min and 41 min, assigned to quercetin and rutin, respectively, at all three monitoring wavelengths was observed (at 257 nm, 372 nm – not shown, and at 295 nm, as can be seen in Figs. 2 and 3). Irradiation of quercetin in methanol with either UV-C radiation for 30 min or with UV-B light for 120 min resulted in about 95 and 50 % decreases in the quercetin content, respectively, and its conversion into four major products (Figs. 2 and 4A). For both UV-B and UV-C radiation, the peak observed at t_{ret} = 50 min was dominant on the chromatograms (Fig. 2). However, the product corresponding to the peak observed at $t_{ret.}$ = 17 min was formed in a better yield as a result of UV-C compared to UV-B irradiation (Fig. 2). The UV-spectra corresponding to the four observed products induced by UV-irradiation (either by UV-B or by UV-C) of quercetin in methanol are shown in Fig. 4A. The proposed, possible structures of the products, based on a comparison of their absorption spectra with the ones found in the respective literature related to different methods of quercetin oxidation (Table I), are inserted in Fig. 4A.

The absorption spectra of the products **1** and **3** (in the mobile phase, acidic methanol–water solution, see experimental section), obtained from the peaks at t_{ret} = 17 min and 32 min in chromatograms of UV-irradiated quercetin in methanol, are shown in Fig. 4A. These products have absorbance maximums positioned at 294 nm (product **1**) and 300 nm (product **3**) Similar absorption spectra to that of product **1** were found for di- and tri-hydroxy-phenylglyoxylic acid, products obtained by electrochemical oxidation of quercetin, with maximums at about 288 and 292 nm, respectively (Table I).[18] This proposed, possible structure requires a C-ring opening (product **1**). In the case of product **3**, an additional molecular rearrangement might occur finishing in a closed structure again *via* a furan type of chromophore as a "bridge".[18,19]

Absorption spectra of the products **2** and **4** (in the mobile phase) obtained from the peaks registered at 21 and 50 min are shown in Fig. 4A and the proposed structures are given in Table I.[18–23] Product **2** has two unresolved bands in spectral range between 250 and 400 nm (with broad, "shoulder-like" A_{max} at 294 and 325 nm) and another clear A_{max} at 236 nm, as shown in Fig. 4A. Product **4** has two unresolved bands with A_{max} at 275 and 297 nm, as shown in Fig. 4A. A comparison with literature data suggests again C-ring opening for product **4**, while possible structure for product **3** appears to be of a similar type as product **2**, Table I.[18–23] Hence, it may be concluded that although obtained by different manners of quercetin oxidation (Table I), the formation of the degradation products were very probably initiated by C-ring opening, followed by stabilization

of such structures (products **1** and **4**) or further molecular rearrangements (products **2** and **3**).

However, to date, none of the four proposed (quercetin-related) structures (Table I) have been induced by UV-irradiation. In a similar study by Fahlman and Krol (2009),[12] it was shown that UV-A and UV-B irradiated quercetin in methanol (under energy flux conditions very similar to those used in the present study, *i.e.*, 7.4 W m^{-2} at 365 nm, and 13.3 W m^{-2} at 310 nm, respectively) underwent decomposition as the result of C-ring opening[12] followed by the formation of the three products (independent of the presence of oxygen in the system), which were identified as 2,4,6-trihydroxybenzaldehyde, 2-[(3,4-dihydroxybenzoyl)-oxy]-4,6-dihydroxybenzoic acid and 2(3,4-dihydroxyphenyl)ethanol. Unlike in the present study, they also used the well-known UV-photosensitizer benzophenone to observe its effect on quercetin decomposition*, and found that the photoconversion yield was increased in the presence of benzophenone, *i.e.*, in the absence of benzophenone, only 20 % of the quercetin underwent decomposition over 11 h, whereas 90 % of the quercetin was decomposed under both UV-A or UV-B irradiation in less than 1 h when benzophenone was present, by the same C-ring opening mechanism as in the absence of benzophenone.[12] Unfortunately, the authors did not present the absorption spectra of their proposed degradation products, for their comparison with those presented in the present work.[12]

Irradiation of rutin (0.1 mM) in methanol and water with UV-C radiation for 90 min resulted in about 85 % and 30 % decrease of the initial rutin content and its conversion to two barely visible products, with retention times of **1** 13 min and **2** 28 min, respectively, as determined by the chromatograms recorded at 295 nm (Fig. 3). Absorbance spectrum of product **1** in the mobile phase, which is related to the peak with $t_{ret.}$ = 13 min in the chromatogram of UV-C-irradiated rutin in methanol (Fig. 3A), is shown in Fig. 4B. The spectrum shows one clear band with absorbance maximum at 287 nm (Fig. 4B). The absorbance spectrum of product **2** (in the mobile phase), which is related to the peak with $t_{ret.}$ = 28 min in the chromatogram of UV-C-irradiated rutin in water (Fig. 3B), is shown in Fig. 4B. The spectrum shows two bands: the first one is intensive with an absorbance maximum at 253 nm and the second one has a significantly lower A_{max} value at 298 nm (Fig. 4B).

While UV-induced decomposition of quercetin and rutin seem to be unquestionable,[11] the possible mechanisms are still much disputed and very rarely published. For the three detected products as a result of quercetin irradiation in methanol, Fahlman and Krol (2009) proposed two distinct mechanisms, both requiring C-ring opening:[12] one occurred by direct reaction with singlet oxygen (the creation of which was assured in the used aerated system by energy transfer from

---

* Benzophenone was recently employed with similar idea to study its effect on bleaching of carotenoids in a similar *in vitro* system.[25]

the sensitizer, *i.e.*, the benzophenone triplet state, to a normal, triplet oxygen),[26] while in the case of the other two products, a precedent molecular rearrangement occurred; in both cases, the quercetin AC–B system (Fig. 1) was decomposed, and very simple, one-ring benzoyl-type molecules were finally formed. The spectra of the four separated quercetin degradation products in methanol obtained in this work (Fig. 4A), as well as of the two rutin degradation products in methanol and water (Fig. 4B), with a clear absence of the flavonoids band I, attributed to the B-ring of the flavonoids AC–B system (Fig. 1), suggest that the flavonoid structure was irreversibly decomposed and probably smaller-sized molecules were formed. The results obtained in the pre-work might support these suggestions, since the formation of all four quercetin-degradation products were possibly initiated by C-ring opening.

Flavonoids degradation: kinetic analysis

Both flavonoids undergo substantial degradation expressed through the proportional decrease of peak areas obtained from the related HPLC-chromatograms recorded at 295 nm (Figs. 2 and 3), and at 257 and 372 nm (data not shown), as a function of the UV-irradiation time ($t_{irr.}$), *i.e.*, ln $S_{372nm} = f(t_{irr.})$. This dependence is expressed as a linear plot (Fig. 5), indicating first order kinetics of the degradation of the flavonoids, as already reported.[16,27]

The values of the calculated quercetin and rutin degradation rate constants, $k_{degrad.}$ (min^{-1}), are comparable but also different in comparison to already published k values,[16] which is in agreement with the somewhat different conditions of continuous UV-irradiation (such as energy flux and distance from the lamps), as well as with the different employed techniques (UV-spectrophotometry *vs.* HPLC). The ratio of degradation rate constant values for quercetin irradiated with UV-C and UV-B, $k_{Querc.,degrad.UVC}$ / $k_{Querc.,degrad.UVB}$, is about 21 (Table II). This trend was already observed in a previous study:[16] thus, the degradation of flavonoids is highly dependent on the UV-energy input. This behavior was observed in another study related to the continuous UV-irradiation of a very similar compound, 3-hydroxyflavone.[28]

However, rutin was generally more stable against UV-irradiation than quercetin (by a factor of 5), as shown in Table II. Obviously, the substituted position 3 in the C-ring (Fig. 1) makes a major difference in the structures of quercetin and rutin; rutin reportedly has two intra-molecular hydrogen bonds related to the B-ring and the glycoside residue, *i.e.*, interactions of O-3' with H-4', and O-2''' with H-3' (Fig. 1B),[29] while in the case of quercetin, three hydrogen-bonds were reported, *i.e.*, the interaction of O-3' with H-4', and =O-4 with H-5 and H-3 (Fig. 1A).[30] Hence, it is evident that the 3-OH position makes the main difference in the response of quercetin and rutin to continuous UV-irradiation, making the gly-

coside residue in quercetin more susceptible to the action of UV radiation than the glycoside residue in rutin.[11]

In the case of rutin exposed to continuous UV-C radiation, the degradation rate constant in methanol was higher than in water: 0.0206 *vs*. 0.0043 min^{−1}, as given in Table II. The solubility of rutin in methanol is slight higher than in water (the corresponding free energies of solvation are –56.35 and –49.42 kcal mol^{−1}, respectively).[31] However, the influence of oxygen can not be neglected because of the formation of singlet oxygen[26] that could potentially play a certain role in the UV-induced degradation of rutin and quercetin. In such circumstances, flavonoids would need to act as sensitizers (for singlet oxygen creation if other sensitizers are not present) while, on the other hand, they could become objects of degradation themselves. The relevant data to be born in mind when referring to the susceptibility of rutin *vs*. quercetin to UV-irradiation are: the solubility of oxygen in methanol and water at 20 °C are 2.12 and 0.265 g dm^{−3}, respectively; the viscosity under the same conditions are 0.597 mPa s for methanol and 1.002 mPa s for water; the lifetimes of singlet oxygen in methanol and water are 10 and 4 µs, respectively.[31] Thus, during UV-C irradiation, the higher solubility of oxygen, the longer lifetime of singlet oxygen and the smaller viscosity of methanol than water[31] makes rutin more susceptible to UV-induced degradation in methanol than in water, which is documented by the corresponding $k_{\text{degrad.}}$ values given in Table II.

Kinetic analysis of the formation of the UV-induced products

The kinetics of the formation of the main quercetin degradation products seem to be first order (Fig. 6). The formation of the products was faster when quercetin was irradiated with UV-C than with UV-B radiation (Table III). For example, UV-C-induced formation of quercetin product **2**, detected at $t_{\text{ret.}} = 21$ min in HPLC chromatogram recorded at 295 nm, was about 3.6 times faster than when UV-B radiation was used (Table III). Similarly, UV-C-induced formation of the quercetin products **3** and **4**, detected at $t_{\text{ret.}}$ 32 and 50 min, respectively, were about 1.9 and 4 times faster than for their formation induced by UV-B radiation (Table III). The obvious reason again lies in the increased energy input. A comparison of the rate constants revealed at least: 1) three of the four products, *i.e.*, products 2–4 (Table III) were formed during continuous irradiation of quercetin with both UV-B and UV-C radiation, in other words changing the energy input (from UV-B to UV-C) did not lead to a significant qualitative change in the outcome; 2) however, change in the energy input was reflected in significantly higher formation rates, by factors of 3.5 (product **2**), 1.9 (product **3**) and 4.2 (product **4**) – Table III; 3) this undoubtedly indicates that the formation of the products was directly related to quercetin degradation, which was also energy dependent (Table II).

When rutin was exposed to UV-C radiation in methanol and water, formation of degradation products was also observed over irradiation time (chromatograms in Fig. 3), but their formation kinetics was not so clear (not shown). The reasons for this behavior could be either in already cited higher stability of rutin to UV-irradiation compared to quercetin,[16] or in the insufficiently long irradiation time used in the related experiments. However, extension of the irradiation times could possibly make comparison of quercetin and rutin responses toward UV-irradiation more difficult and less relevant.

ИЗВОД

ИРЕВЕРЗИБИЛНА UV-ИНДУКОВАНА ДЕГРАДАЦИЈА КВЕРЦЕТИНА И РУТИНА У РАСТВОРУ, ИСПИТИВАНА UV-СПЕКТРОФОТОМЕТРИЈОМ И HPLC ХРОМАТОГРАФИЈОМ

ЈЕЛЕНА Б. ЗВЕЗДАНОВИЋ, ЈЕЛЕНА С. СТАНОЈЕВИЋ, ДЕЈАН З. МАРКОВИЋ и ДРАГАН Ј. ЦВЕТКОВИЋ

Универзитет у Нишу, Технолошки факултет, Булевар ослобођења 124, 16000 Лесковац

У овом раду је проучавана иреверзибилна деградација кверцетина и рутина, растворених у метанолу и води, индукована континуалним UV-озрачивањем из две подобласти, UV-A и UV-B. Деградација оба флавоноида је повезана са UV-индукованим формирањем деградационих продуката: оба процеса прате кинетику првог реда. Константе брзина и деградације флавоноида и формирања продуката у оба растварача су зависне од енергије упадних UV--фотона.

(Примљено 18. јуна, ревидирано 8. августа 2011)

REFERENCES

1. G. T. Wondrak, M. K. Jacobson, E. L. Jacobson, *Photochem. Photobiol. Sci*. **5** (2006) 215
2. F. Hollósy, *Micron* **33** (2002) 179
3. A. Strid, R. J. Porra, *Plant Cell Physiol.* **33** (1992) 1015
4. A. Strid, W. S. Chow, J. M. Anderson, *Photosynth. Res*. **39** (1994) 475
5. E. M. Middleton, A. H. Teramura, *Plant Physiol*. **103** (1993) 741
6. K. E. Heim, A. R. Tagliaferro, D. J. Bobilya, *J. Nutrit. Biochem*. **13** (2002) 572
7. W. Bors, W. Heller, C. Michel, M. Saran, *Meth. Enzymol*. **186** (1990) 343
8. D. Amić, D. Davidović-Amić, D. Bešlo, N. Trinajstić, *Croat. Chem. Acta* **76** (2003) 55
9. D. P. Makris, J. T. Rossiter, *Food Chem*. **77** (2002) 177
10. S. Erkoc, F. Erkoc, N. Keskin, *J. Mol. Struct. Theochem* **631** (2003) 141
11. G. J. Smith, S. J. Thomsen, K. R. Markham, C. Andary, D. Cardon, *J. Photochem. Photobiol., A* **136** (2000) 87
12. B. M. Fahlman, E. S. Krol, *J. Photochem. Photobiol., B* **97** (2009) 123
13. E. Falkovskaia, P. K. Sengupta, M. Kasha, *Chem. Phys. Lett*. **297** (1998) 109
14. E. S. B. Ferreira, A. Quye, H. McNab, A. N. Hulme, *Dyes Hist. Archaeol*. **18** (2002) 63
15. B. M. Fahlman, E. S. Krol, *J. Agric. Food Chem*. **57** (2009) 5301

16. D. Cvetkovic, D. Markovic, D. Cvetkovic, B. Radovanovic, *J. Serb. Chem. Soc.* **76** (2011) 973
17. M. Veit, C. Beckert, C. Höhne, K. Bauer, H. Geiger, *Phytochem.* **38** (1995) 881
18. A. Zhou, S. Kikandi, O. A. Sadik, *Electrochem. Commun.* **9** (2007) 2246
19. A. Zhou, O. A. Sadik, *J. Agric. Food Chem.* **56** (2008) 12081
20. U. Takahama, S. Hirota, T. Nishioka, K. Yoshitama, *Food Sci. Technol. Res.* **8** (2002) 148
21. U. Takahama, S. Hirota, *Plant Cell Physiol.* **41** (2000) 1021
22. A. K. Timbola, C. D. de Souza, C. Giacomelli, A. Spinelli, *J. Braz. Chem. Soc.* **17** (2006) 139
23. A. Marfak, P. Trouillas, D.-P. Allais, Y. Champavier, C.-A. Calliste, J.-L. Duroux, *J. Agric. Food Chem.* **50** (2002) 4827
24. K. R. Markham, *Techniques of Flavonoid Identification*, Academic Press, London, UK, 1982
25. D. Cvetković, D. Marković, *Rad. Phys. Chem.* **80** (2011) 76
26. A. B. Girotti, *J. Photochem. Photobiol., B* **63** (2001) 103
27. J. S. Almeida, F. Lima, S. Da Ros, L. O. S. Bulhões, L. M. de Carvalho, R. C. R. Beck, *Nanoscale Res. Lett.* **5** (2010) 1603
28. S. Tommasini, M. L. Calabro, P. Donato, D. Raneri, G. Guglielmo, P. Ficarra, R. Ficarra, *J. Pharmaceut. Biomed. Anal.* **35** (2004) 389
29. S. A. Payán-Gómez, N. Flores-Holguín, A. Pérez-Hernández, M. Piñón-Miramontes, D. Glossman-Mitnik, *Chem. Cent. J.* **4** (2010) 12
30. A. M. Mendoza-Wilson, D. Glossman-Mitnik, *J. Mol. Struct. Theochem* **681** (2004) 71
31. J. Fiedor, L. Fiedor, N. Kammhuber, A. Scherz, H. Scheer, *Photochem. Photobiol.* **76** (2002) 145.

In vitro antibacterial activities of the essential oils of aromatic plants against *Erwinia herbicola* (Lohnis) and *Pseudomonas putida* (Kris Hamilton)

ABHAY K. PANDEY[1], POOJA SINGH[1]*, UMA T. PALNI[2] and N. N. TRIPATHI[1]

[1]*Bacteriology and Natural Pesticide Lab, Department of Botany, DDU Gorakhpur University, Gorakhpur 273009, India and* [2]*Department of Botany, DSB Campus, Kumaun University, Nainital 263002, India*

Abstract: This study was designed to examine the *in vitro* antibacterial activities of the essential oils extracted from 53 aromatic plants of the Gorakhpur Division (UP, INDIA) for the control of two phytopathogenic bacteria, namely *Erwinia herbicola* and *Pseudomonas putida*, which cause several post-harvest diseases in fruits and vegetables. Out of the 53 oils screened, 8 oils, *i.e.*, *Chenopodium ambrosioides*, *Citrus aurantium*, *Clausena pentaphylla*, *Hyptis suaveolens*, *Lippia alba*, *Mentha arvensis*, *Ocimum sanctum* and *Vitex negundo*, completely inhibited the growth of the test bacteria. Furthermore, the minimum inhibitory concentration (*MIC*) and the minimum bactericidal concentration (*MBC*) values of *C. ambrosioides* oil were lower for *E. herbicola* (0.25 and 2.0 µl ml^{-1}) and *P. putida* (0.12 and 1.0 µl ml^{-1}), respectively, than those of the other 7 oils, as well as than those of agromycin and streptomycin, the drugs used in the current study. Gas chromatography (GC) and GC–mass spectroscopy (GC–MS) analysis of the *Chenopodium* oil revealed the presence of 125 major and minor compounds, of which 14 compounds were recognized. The findings led to the conclusion that *Chenopodium* oil may be regarded as a safe antibacterial agent for the management of post-harvest diseases of fruits and vegetables.

Keywords: phytopathogenic bacteria; *Chenopodium ambrosioides* oil; GC/GC––MS.

INTRODUCTION

Bacterial pathogens and their control are serious problems in agricultural practices. They cause great damage to many fruits and vegetables during transit and storage, amounting to 30–40 % losses and even much higher in some developing countries.[1] In traditional societies, appreciation of medicinal and aromatic

---

plants was based largely on benefits to human beings, including those of pest control. For a long time, plants have been a valuable source of natural products for maintaining food commodities, and have proved themselves the best substitutes for synthetic drugs.[2] Green plants represent a reservoir of effective chemotherapeutants and can provide valuable sources of natural pesticides. The use of plant essential oils and phytochemicals, both with known antibacterial properties, is of great consequence. In the past few years, investigations have been conducted worldwide to prove antimicrobial, antioxidant, anti-inflammatory, cytotoxic, antinociceptive and anti-malarial behaviour of plant essential oils.[3–5] In recent years, several reports have been published on the use of numerous plant by-products that possess antimicrobial properties towards a number of plant and human pathogenic bacteria.[6,7] Essential oils have been investigated for their antibacterial properties and were proved to be better substitutes for synthetic antibiotics due to their non-phytotoxic,[3] more systemic, renewable and easily biodegradable nature.[1] As a part of systematic research on the antibacterial properties of Indian plants, the present study deals with the evaluation of 53 essential oils for their antibacterial activities towards two test bacteria, *i.e.*, *Erwinia herbicola* and *Pseudomonas putida*. In addition, the *MIC* and *MBC* values of the more toxic oils were determined. To ascertain the chemical constituents of the most potent oil, gas chromatography (GC) and GC–mass spectroscopy (GC–MS) analysis were performed.

<div align="center">EXPERIMENTAL</div>

Reference strains

　　The bacterial cultures used in the present work, *E. herbicola* (MTCC 3609) and *P. putida* (MTCC 1190), were procured from the Institute of Microbial Technology, Chandigarh, India. The purity of the bacterial strains was clarified using MM2Cu medium[8] for *E. herbicola* and King's B medium[9] for *P. putida*. The stock cultures were maintained on nutrient agar (NA) and Luria Bertani agar (LBA) slants at 4 °C and sub-cultured monthly. Working cultures were prepared by inoculating a loopful of each test microorganism in 3 ml of nutrient broth (NB) from NA/LBA slants. Broths were incubated at 37±2 °C for 12 h. The inocula were adjusted photometrically at 600 nm to a cell density equivalent to approximately 0.5 McFarland standards (10^8 cfu ml^{-1}).

Plant collection and essential oil extraction

　　The plant samples were collected from different forests and forest ranges of Gorakhpur Division during 2009–2010, brought to the laboratory and identified with the help of literature[10] and Departmental herbarium of Gorakhpur University, India. The plant collecting sites were located in the eastern part of Uttar Pradesh, India between latitude 27°05' and 27°25' North and longitude 83°20' and 84°10' East at an elevation of about 91 m above sea level. Voucher specimens of individual species were deposited in the Botanical Survey of India (NRC) Dehradun, India. Each fresh plant material (300 g) was separately submitted for hydrodistillation in a Clevenger's apparatus for 4 h to derive the volatile constituents in the form of essential oils. Each volatile oil was dried over anhydrous sodium sulphate and then kept separately in sealed clean glass vials at 4 °C until needed.

Disc diffusion bioassay

The disc diffusion method of Andrews[11] was adopted for the antibacterial bioassay. The target bacterial suspensions (0.1 ml) containing 1×10^8 cfu ml^{-1} inocula were spread using a sterile spreader on Nutrient Agar (*P. putida*) and Wilbrink Agar (WA) (sucrose, 10 g l^{-1}, bacto-peptone, 5 g l^{-1}, K$_2$HPO$_4$, 0.5 g l^{-1}, MgSO$_4$·7H$_2$O, 0.25 g l^{-1} and agar, 18 g l^{-1}) medium (*E. herbicola*). Sterile Whatman filter paper discs (6 mm diameter) soaked with 5 µl (v/v) of each essential oil were aseptically positioned separately in the centre on the bacterial suspension-seeded plates in order to define the toxicity of the volatiles in terms of the inhibition zone. The treatments also included agromycin and streptomycin. The inoculated plates were incubated at 37 ± 2 °C for 24–72 h and the zone of inhibition, if any, around the discs were measured in mm. The experiments were replicated three times. The data were statistically analyzed.

Agar dilution bioassay

The performed agar dilution susceptibility test was based on modified methods of NCCLS and CLSI[12,13] to determine the minimum inhibitory concentration (*MIC*) of the potent oils. A series of dilutions of each potent oil and antibiotic in a final concentration ranging from 0.06–16 µl ml^{-1} for the oils and 0.06–16 µg ml^{-1} for the antibiotics were prepared in a NA or WA plate, depending on the bacterial species. Tween 80 was used as an emulsifier to ensure proper mixing of the oils with the medium. After solidification, the plates were aseptically spotted with 5 µl of overnight-grown bacterial cultures containing approximately 1×10^8 cfu ml^{-1} inocula. Plane media plates inoculated with the bacteria served as the positive control and a non-inoculated plate served as the negative control. The plates were incubated at 37 ± 2 °C for 24–72 h. The inhibition of the bacterial growth was compared with the growth in the control plates. The *MIC* was defined as the lowest concentration of the oil inhibiting the visible growth of each bacterium on the agar plate. Furthermore, the poisoned plates showing no growth were sub-cultured onto fresh medium (without oil and antibiotic) for determination of the minimum bactericidal concentration (*MBC*).[14] The least concentration from which the bacteria did not recover growth on the fresh medium was considered as the *MBC*. Each test was replicated three times.

Gas chromatographic analysis of the Chenopodium *oil*

About 0.1 µl of pure oil sample was subjected to GC and GC–MS analysis. The GC was composed of an Agilent Technology 6890 N gas chromatograph data handling system equipped with a split–splitless injector and fitted with a flame ionization detector (FID) using N$_2$ as the carrier gas. The column was a HP-5 capillary column (30 m×0.32 mm, 0.25 µm film thickness) and the employed temperature program was as follows: initial temperature of 60 °C (hold: 2 min) programmed at a rate of 3 °C min^{-1} to a final temperature of 220 °C (hold: 5 min). The temperatures of the injector and FID were maintained at 210 and 250 °C, respectively.

Gas chromatography–mass spectrometry analysis of the Chenopodium *oil*

The GC–MS analysis was performed using a Perkin Elmer Clarus 500 GC/MS, coupled with an RTX-5 capillary column (60 m×0.32 mm, film thickness: 0.25 µm). The carrier gas was helium (1 ml min^{-1}), the injector temperature was 210 °C, and the oven temperature was programmed from 60 to 210 °C at a rate of 3 °C min^{-1} and finally held isothermally for 15 min. The ionization of the sample components was performed in the EI mode of 70 eV.

Qualitative and quantitative analysis

Identification of the individual components was realized by matching their recorded mass spectra with those in a library (NIST/Pfleger/Wiley) provided by the instrument software, and by comparing their calculated retention indices with a GC alkane standard solution (C_8–C_{20}) as well as literature values.[15] The relative percentage area of the individual components was obtained from the GC–FID analysis.

<div align="center">RESULTS</div>

Disc diffusion bioassay

The presence of a fluorescent pigment on the King's B medium and a yellowish pink colour on the MM2Cu medium showed that the procured bacteria were *P. putida* and *E. herbicola*, respectively. The present study was an attempt to investigate and evaluate 53 essential oils against plant pathogenic bacteria. The antibacterial spectra of each essential oil showing the zone of inhibition for each test bacteria are presented in Table I. All the essential oils showed more or less antagonist activity against the test pathogens while no inhibition zone was incurred by *Cleome gynandra* and *Cyperus brevifolius* oils against *E. herbicola* and *Hygrophila*, *Leonotis*, *Leonurus* and *Melia* oils against *P. putida*. The most successful results were obtained with *Chenopodium*, *Citrus aurantium*, *Clausena*, *Hyptis*, *Lippia*, *Mentha*, *Ocimum sanctum* and *Vitex* oils that completely inhibited the growth of both test bacteria at the recommended concentration. Surprisingly, *Citrus aurantifolia* completely inhibited the growth of *E. herbicola* only. Among the other oils, *Acorus calamus*, *Anisomeles indica*, *Clerodendrum inermae*, *C. viscosum* and *Curcuma zedoaria* were superior to the antibiotics against both test bacteria, having a zone of inhibition ranging from 14.0–25.8 mm.

TABLE I. Antibacterial potency of the essential oils of aromatic plants of the Gorakhpur Division (L: leaf, T: twig, W: whole plant, R: rhizome)

Plant species (essential oil)	Family	Parts used	Zone of inhibition, mm[a]	
			E. herbicola	*P. putida*
Acorus calamus Linn.	Araceae	R	14.0±2.1	15.3±1.2
Adhatoda vasica Ness	Acanthaceae	L	10.3±1.0	1.9±0.4
Aegle marmelos (L) Corr.	Rutaceae		14.3±3.8	10.9±1.9
Anethum graveolens Linn.	Apiaceae	T	8.4±1.5	10.4±0.5
Anisomeles indica (L.) Kuntz	Lamiaceae	L	24.2±2.2	23.2±0.1
Ashphodelus tenuifolius Cav.	Liliaceae	W	3.0±0.7	5.7±1.0
Callicarpa macrophylla (L.) Vahl.	Verbenaceae	L	10.4±4.3	16.1±5.7
Callistemon lanceolatus (R.Br.) DC	Myrtaceae		7.2±0.6	18.9±2.7
Cannabis sativa Linn.	Cannabinaceae	T	12.0±1.2	10.5±3.8
Chenopodium ambrosioides Linn.	Chenopodiaceae		#[b]	#
Citrus aurantifolia (Christm) Swingle	Rutaceae	L	#	12.1±0.9
C. aurantium Linn.			#	#
C. limon (L.) Burm			7.3±2.1	10.9±3.6
Clausena pentaphylla (Roxb.)DC			#	#

TABLE I. Continued

Plant species (essential oil)	Family	Parts used	Zone of inhibition, mm[a]	
			E. herbicola	*P. putida*
Cleome gynandra (L.) Briq.	Capparidaceae	T	No inhibition	7.1±1.2
Clerodendrum inermae (L.) Gaertn.	Verbenaceae	L	16.0±2.5	17.1±1.9
Clerodendrum viscosum (L.) Vent.		L	17.6±0.7	14.9±1.4
Colebrookea oppositaefolia Sm.	Lamiaceae	L	13.0±0.5	9.8±1.6
Curcuma aromatica Salisb.	Zingiberaceae	L	7.2±0.9	9.8±1.2
C. zedoaria Rosc.		R	25.8±0.3	25.2±1.9
Cyperus brevifolius (Rottb.) Hassk	Cyperaceae	W	No inhibition	12.5±2.9
C. monocephalus Endl.			6.3±2.7	6.6±1.9
C. rotundus Linn.			3.1±0.9	6.1±1.3
C. triceps (Rottb.) Endl.			3.4±0.9	8.6±0.5
Eugenia heyneana (L.) Wall	Myrtaceae	L	15.9±1.1	11.8±0.4
Glycosmis pentaphylla (Retzz.) Corr; Hook.	Rutaceae		7.2±2.0	3.4±1.2
Hygrophila difformis Linn.	Acanthaceae	T	14.2±1.3	10.8±3.7
H. pinnatifida Linn.			3.2±2.7	No inhibition
Hyptis suaveolens (L.) Poit.	Lamiaceae		#	#
Lantana camara Linn.	Verbenaceae	L	9.1±1.3	7.9±3.1
L. indica Roxb.			11.8±0.3	9.0±2.3
Leonotis nepetaefolia R.Br.	Lamiaceae		7.8±0.6	No inhibition
Leonurus sibiricus Linn.		T	2.3±1.8	No inhibition
Leucas aspera Spreng.			5.8±0.1	3.8±0.6
L. cephalotes Spreng.			11.3±3.1	13.2±2.2
Lippia alba Rich.	Verbenaceae	L	#	#
Melia azedarach Linn.	Meliaceae		4.9±2.2	No inhibition
Mentha arvensis Linn.	Lamiaceae		#	#
Murraya koenigii Spreng.	Rutaceae		7.5±0.8	1.70±0.53
M. paniculata (L.) Jack	–		2.9±0.1	4.8±0.9
Ocimum basilicum Linn.	Lamiaceae		9.9±2.8	24.6±3.4
O. canum Sims.		T	6.7±0.8	7.2±3.2
O. gratissimum Linn.		L	2.9±0.3	6.6±0.4
O. sanctum Linn.			#	#
Piper longum Linn.	Piperaceae		10.2±1.6	13.1±1.2
P. sylvaticum Roxb.	–		7.1±0.6	11.8±1.5
Pogostemon heyneanus Benth.	Lamiaceae		3.4±1.6	3.2±1.0
P. plectranthoides Desf.			3.8±0.6	7.3±1.4
Polygonum glabrum Willd.	Polygonaceae	T	4.2±1.0	1.9±0.4
Putranjiva roxburghii Wall.	Euphorbiaceae	L	6.0±1.8	8.3±0.9
Salvia plebeia R.Br.	Lamiaceae	T	2.6±0.3	5.2±2.0
Vitex negundo Linn.	Verbenaceae	L	#	#
Zingiber officinale Rosc.	Zingiberaceae	R	5.1±3.0	14.2±3.0
Agromycin 20 µg			12.5±2.4	11.88±1.2
Streptomycin 10 µg			13.0±2.0	16.7±3.7

[a]Values given are the mean of three replicates ± standard deviation; [b]oils caused complete inhibition of the bacteria

Agar dilution bioassay

The determination of the *MIC* and *MBC* values of the oils that completely inhibited the growth of the test bacteria showed that *Chenopodium* oil was highly effective with the lowest *MIC* and *MBC* values against *E. herbicola* (0.25 and 2.0 µl ml^{-1}) and *P. putida* (0.12 and 1.0 µl ml^{-1}) followed by *Clausena* and *Mentha* oils which had *MIC* and *MBC* values of 0.50 and 4.0 µl ml^{-1} for *E. herbicola*, and 0.25 and 2.0 µl ml^{-1} for *P. putida*, respectively (Table II). *E. herbicola* was susceptible to *C. aurantium* and *P. putida* to *Hyptis*, *Lippia* and *Vitex* oil (in terms of their *MIC* values) but *MBC* values could not be obtained within the recommended assay range. Of the antibiotics, streptomycin was more effective than agromycin against both test bacteria.

TABLE II. *MIC* and *MBC* of potent oils and the antibiotics against phytopathogenic bacteria

Oil/antibiotic	*E. herbicola*		*P. putida*	
	MIC[a]	*MBC*[a]	*MIC*	*MBC*
C. ambrosioides	0.25	2.0	0.12	1.0
C. aurantium	8.0	Static	4.0	Static
C. pentaphylla	0.50	4.0	0.25	2.0
H. suaveolens	2.0	16.0	8.0	Static
L. alba	4.0	Static	4.0	Static
M. arvensis	0.50	4.0	0.25	2.0
O. sanctum	2.0	8.0	1.0	4.0
V. negundo	4.0	16.0	8.0	Static
Agromycin	4.0	16.0	2.0	8.0
Streptomycin	8.0	Static	4.0	8.0

[a]Values in µl ml^{-1} for the oils and µg ml^{-1} for the antibiotics

Chemical constituents of Chenopodium *oil*

GC and GC–MS analysis of the *Chenopodium* oil led to the recognition of fourteen compounds comprising 97.70 % of the oil sample, with *α*-terpinene (37.74 %), *p*-cymene (16.71 %), limonene (1.90 %), ascaridole (38.03 %) and isoascaridole (2.55 %) being the major components (Table III).

TABLE III. Chemical constituents of *C. ambrosioides* oil

No.	Component	Kovats index	Composition, %
1	*α*-Thujone	924	0.01
2	*α*-Pinene	932	0.01
3	Sabinene	969	0.02
4	*β*-Myrcene	974	0.04
5	*α*-Terpinene	1014	37.74
6	*p*-Cymene	1020	16.71
7	Limonene	1024	1.90
8	*γ*-Terpinene	1054	0.34
9	Myrcenol	1103	0.02

TABLE III. Continued

No.	Component	Kovats index	Composition, %
10	*trans*-Pinene hydrate	1139	0.14
11	Camphor	1143	0.04
12	Ascaridole	1237	38.03
13	*trans*-Chrysanthenyl acetate	1262	0.15
14	Isoascaridole	1390	2.55
Total			97.70

DISCUSSION

The test bacteria *E. herbicola* and *P. putida* used in the current study are widespread in nature as bio-control agent.[16,17] However, some strains of these bacteria have evolved into plant pathogens that cause several post-harvest evils in fruits and vegetables, resembling lesions to rot of alfalfa (*Medicago sativa* L.), internal rot of peach (*Prunus persica* L.), apricot (*Prunus armeniaca* L.), plum (*Prunus cerasifera* Ehrh.) and apple (*Malus domestica* Borkh) fruits[18] and internal discoloration to tomato (*Lycopersicon esculentum* Mill),[19] rot of potato (*Solanum tuberosum* L.).[20]

Plant based antimicrobial compounds have enormous therapeutic potential as they can serve their purpose without any of the side effects that are often associated with synthetic antimicrobials. The plants screened in the present study are used to treat various gastrointestinal disorders, diarrhoea, dysentery, cough cold and asthma.[21] A large number of volatile and non-volatile plant products have been evaluated for their toxicity against human and plant pathogenic bacteria.[22,23] However, the literature seems to be lacking in reports on the potentiality of such volatiles with respect to *E. herbicola* and *P. putida*. In the present study, some essential oils, such as *Ashphodelus tenuifolius*, *Callicarpa macrophylla*, *Clausena pentaphylla*, *Colebrookea oppositaefolia*, *Cyperus* spp., *Curcuma aromatica*, *Glycosmis pentaphylla*, *Hygrophila* spp., *Pogostemon* spp. and *Polygonum glabrum*, were subjected to preliminary screening for their antibacterial potency. It is clear from the presented results that 8 oils, namely *Chenopodium ambrosioides*, *Citrus aurantium*, *C. pentaphylla*, *Hyptis suaveolens*, *Lippia alba*, *Mentha arvensis*, *Ocimum sanctum* and *Vitex negundo*, exhibited pronounced activities against both tested bacteria through complete inhibition of their colony growth. This shows the variations in the active ingredients of the essential oils. The absence of antibacterial activities of *Cleome*, *Cyperus brevifolius*, *Leonotis*, *Leonurus*, *Hygrophila pinnatifida* and *Melia* oils indicates the poorly toxic active substances in these oils, which were less toxic than the standard antibiotics used in this study.

The determination of bactericidal and bacteriostatic concentrations are more sensitive techniques than the disc diffusion technique, which was used purely as a screening tool, to eliminate those oils with no or very slight inhibitory activities

against the test pathogens.[24] The obtained results illustrate that of the 53 screened oils, 8 oils have a greater inhibitory effect, hence, they were considered for *MIC* and *MBC* determination. Additionally, during the *MIC* determination, the addition of the emulsifying agent Tween 80 introduced an extra component with respect to the activity and possible interaction, its use was unavoidable.[25] Earlier the oils of *Chenopodium*, *Citrus*, *Clausena*, *Hyptis*, *Lippia*, *Mentha*, *Ocimum* and *Vitex* were reported to be strong fungicidal agents[26–30] and are now being reported as strong antibacterial agents against both the studied phytopathogenic bacteria. The present findings are also in accordance with Vasinauskiene *et al.*[31] who found streptomycin to be a poorer antibacterial agent than essential oils against several phytopathogenic bacteria. These might be due to the presence of monoterpenes, sesquiterpenes, phenolic compounds, ketones and coumarins.[32] *Chenopodium* oil was the most toxic and was found to be bacteriostatic and bactericidal in nature at lower concentration than the other potent oils.

Essential oil from the fresh plant part of *C. ambrosioides* was previously found to contain ascaridole (40–70 %) as the major component, followed by *α*-terpinene, *p*-cymene, glycol and isoascaridole.[33] Similarly in the present research, *α*-terpinene and ascaridole were found in higher percents, followed by *p*-cymene and isoascaridole. In another investigation, *cis*-ascaridole was found as a major peroxy-monoterpenoid (up to 46.9 %) in the oil. Three minor isomers *cis*-isoascaridole (1.1–6.4 %), *trans*–ascaridole (1–2 %) and *trans*-isoascaridole (1–2 %) were also detected.[34] However, no such components were detected in the current study. This may be due to the period of isolation and the places of origin.

The herb *C. ambrosioides* (Chenopodiaceae) is a plant widely known in popular medicine as anthelminthic, vermifuge, emmenagogue and abortifacient.[21] It is used for the treatment of digestive, respiratory, uro–genital, vascular and nervous disorders, for metabolic disturbances such as diabetes and hypercholesterolemia and as a sedative, antipyretic and antirheumatic.[34] The oil of the plant contains ascaridole as a major component. Ascaridole (also known as ascarisin; 1,4-epidioxy-*p*-menth-2-ene) is a bicyclic monoterpene that has an unusual bridging peroxide functional group. Ascaridole has been documented with sedative and pain-relieving properties as well as antifungal effects, and was found to be a potent inhibitor of the *in vitro* development of *Plasmodium falciparum*, *Trypanosoma cruzi* and *Leishmania amazonensis*.[35,36] The findings are thus a hint that ascaridole may be an interesting novel candidate drug against several pathogens.

It has been shown that essential oils from different plants possessed a wide range of antibacterial properties because they inhibited the growth and the diameter of inhibition varied depending upon the susceptibility of the test organisms. The increased awareness of the environmental problems associated with conventional non-biodegradable agrochemicals has led to the search for non-con-

ventional chemicals of biological origin for the management of post-harvest disease in fruits and vegetables. The observed antibacterial properties of *C. ambrosioides* essential oil show its potential for the practical use of the essential oil towards plant pathogenic bacteria as a natural bactericide. The obtained results suggest that the use of *Chenopodium* oil as antibacterial agent may be judiciously applied to prevent the decay of fruits and vegetables due to bacteria.

CONCLUSIONS

To best of our knowledge, this is the first study to provide data on the evaluation of essential oils against *E. herbicola* and *P. putida*. According to the obtained results, it is possible to conclude that *C. ambrosioides* has a strong antibacterial activity. The antibacterial activities of *Chenopodium* oil reported herein could be associated with the presence of α-terpinene (37.74%), *p*-cymene (16.71 %) and ascaridole (38.03 %). Based on the observed results, *C. ambrosioides* oil could be used as a preservative in food products, to protect them from microbial spoilage.

И З В О Д

АНТИБАКТЕРИЈСКА АКТИВНОСТ ЕТАРСКИХ УЉА АРОМАТИЧНИХ БИЉАКА СПРАМ БАКТЕРИЈА *Erwinia herbicola* (LOHNIS) И *Pseudomonas putida* (KRIS HAMILTON)

АБХАҮ К. ПАНДЕҮ[1], ПООЈА СИНГХ[1], УМА Т. ПАЛНИ[2] и Н. Н. ТРИПАТХИ[1]

[1]*Bacteriology & Natural Pesticide Lab, Department of Botany, DDU Gorakhpur University, Gorakhpur, 273009 и* [2]*Department of Botany, DSB Campus, Kumaun University, Nainital, 263002, India*

У овој студији испитана је *in vitro* антибактеријска активност етарских уља из 53 ароматичне биљке из колекције Универзитета у Горакпуру (Индија) према фитопатогеним бактеријама *Erwinia herbicola* и *Pseudomonas putida*, изазивачима болести воћа и поврћа. Осам уља је инхибирало раст бактерија; из биљака *Chenopodium ambrosioides*, *Citrus aurantium*, *Clausena pentaphylla*, *Hyptis suaveolens*, *Lippia alba*, *Mentha arvensis*, *Ocimum sanctum* и *Vitex negundo*. MIC и MBC вредности за уље из *C. ambrosioides* су биле најниже; за *E. herbicola* 0,25 и 2,0 µl ml^{-1} и за *P. putida* 0.12 и 1.0 µl ml^{-1}. GC и GC–MS анализом уља биљке *Chenopodium* нађено је 125 састојака, од којих је 14 идентификовано. Резултати су показали да се уље биљке *Chenopodium* може сматрати погодним антибактеријским агенсом за третирање болести воћа и поврћа.

(Примљено 24. маја, ревидирано 4. октобра 2011)

REFERENCES

1. L. Claflin, *Control of Pseudomonas syringae pathovars*, in *Pseudomonas syringae and related pathogens*, N. S. Iacobellis, A. Collmer, S. W. Hutcheson, J. W. Mansfield, C. E.

Morris, J. Murillo, N. W. Schaad, D. E. Stead, G. Surico, M. S. Ullrich, Eds., Kluwer, Dordrecht, The Netherlands, 2001, p. 423

2. P. Steiner, in *Fire Blight: The disease and its causative agent, Erwinia amylovora,* J. L. Vanneste, Ed., CABI Publishing, New York, 2000, p. 339
3. N. N. Tripathi, N. Kumar, *J. Stored Prod. Res.* **43** (2007) 435
4. S. Dordevic, S. Petrovic, S. Dobric, M. Milenkovic, D. Vucicevic, S. Zizic, J. Kukic, *J. Ethnopharmacol.* **109** (2007) 458
5. T. Patharakorn, T. Arpornsuwan, N. Nuanchawee Wetprasit, A. Promboon, S. Ratanapo, *J. Med. Plants Res.* **4** (2010) 837
6. P. L. Cantore, N. S. Iacobellis, A. D. Marco, F. Capasso, F. Senatore, *J. Agric. Food Chem.* **52** (2004) 7862
7. R. Karami-Osboo, M. Khodaverdi, F. Ali-Akbari, *J. Agric. Sci. Tech.* **12** (2010) 35
8. S. Bereswill, S. Jock, P. Bellemann, K. Geider, *Plant Dis.* **82** (1998) 158
9. E. O. King, M. K. Ward, D. E. Raney, *J. Lab. Clin. Med.* **44** (1954) 301
10. T. N. Srivastava, *Flora Gorakhpurensis*, Today & Tomorrow Printers and Publishers, New Delhi, 1976
11. J. M. Andrews, *J. Antimicrob. Chemother.* **48** (Suppl. S1) (2001) 43
12. National Committee for Clinical Laboratory Standards (NCCLS), *Methods for dilution antimicrobial susceptibility tests for bacteria that grow aerobically*, Approved Standard - NCCLS document 6th ed., M7-A6, Wayne, PA, USA, 2003
13. Clinical and Laboratory Standards Institute (CLSI), *Method for dilution antimicrobial susceptibility tests for bacteria that grow aerobically*, Approved standard - 8th ed., CLSI document M07-A8, Wayne, PA, USA, 2009
14. A. K. Mishra, A. Mishra, S. Tripathi, N. N. Tripathi, *J. Microbial World* **10** (2008)108
15. R. P. Adams, *Identification of essential oils components by gas chromatography/mass spectroscopy*, Allured Pub Corp., Carol Stream, IL, 2007
16. J. Handelsman, W. J. Brill, *Appl. Environ. Microbiol.* **49** (1985) 818
17. P. D. Colyer, M. S. Mount, *Plant Dis.* **68** (1984) 703
18. G. T. I. Abdel, S. A. M. El-Sadek, A. A. Galal, J. D. Janse, *Egypt. J. Microbiol.* **36** (2001) 477
19. A. A. Galal, in *Proceedings of 10th Congress of Phytopathology*, Giza, Egypt, 2003, p. 325
20. D. K. Pandey, A. Asthana, N. N. Tripathi, S. N. Dixit, *Indian Perfumer* **25** (1982) 10
21. S. P. Ambasta, *The Useful Plants of India*, National Institute of Science Communication Dr K. S. Krishnan Marg, New Delhi, India, 2006
22. T. Mangena, N. Y. O. Muyima, *Lett. Appl. Microbiol.* **28** (1999) 291
23. S. Kizil, F. Uyar, *Asian J. Chem.* **18** (2006) 1455
24. A. Smith-Palmer, J. Stewart. L. Fyfe, *Lett. Appl. Microbiol.* **26** (1998) 118
25. A. M. Janssen, J. J. C. Scheffer, A. B. Svendsen, *Planta Med.* **53** (1987) 395
26. D. K. Pandey, N. N. Tripathi, R. D. Tripathi, S. N. Dixit, *J. Plant Dis. Prot.* **89** (1981) 344
27. N. K. Dubey, K. S. Bhargava, S. N. Dixit, *Int. J. Trop. Plant Dis.* **1** (1983) 177
28. R. Kumar, A. K. Mishra, N. K. Dubey, Y. B. Tripathi, *Int. J. Food Microbiol.* **115** (2007) 159
29. R. Kumar, N. K. Dubey, O. P. Tiwari, Y. B. Tripathi, K. K. Sinha, *J. Sci. Food Agric.* **87** (2007) 1737

30. A. K. Pandey, P. Singh, U. T. Palni, N. N. Tripathi, in *Proceedings of 33rd Conference of Indian Botanical Society and International Symposium on the New Horizons of Botany*, (2010), Shivaji University, Kolhapur (MS), India, 2010, p. 19
31. M. Vasinauskiene, J. Radusiene, I. Zitikaite, E. Surviliene, *Agronomy Res.* **4** (2006) 437
32. M. M. Cowan, *Clin. Microbiol. Rev.* **12** (1999) 564
33. J. F. Cavalli, F. Tomi, A. F. Bernardini, J. Casanova, *Phytochem. Anal.* **15** (2004) 275
34. V. Dembitsky, I. Shkrob, O. L. Hanus, *Biomed. Pap. Med. Fac. Univ. Palacky Olomouc Czech Repub.* **152** (2008) 209
35. Y. Pollack, R. Segal, J. Golenser, *Parasitol. Res.* **76** (1990) 570
36. L. Monzote, A. M. Montalvo, S. Almanonni, R. Scull, M. Miranda, J. Abreu, *Chemotherapy* **52** (2006) 130.

Studies on nickel(II) and palladium(II) complexes with some tetraazamacrocycles containing tellurium

NITU RATHEE and KRISHAN KUMAR VERMA*

Department of Chemistry, Maharshi Dayanand University, Rohtak – 124001, Haryana, India

Abstract: The synthesis of 10-membered and 12-membered tellurium-containing tetraazamacrocyclic complexes of divalent nickel and palladium by template condensation of diaryltellurium dichlorides, (aryl = *p*-hydroxyphenyl, 4-hydroxy-3-methyl-phenyl, *p*-methoxyphenyl) with 1,2-diaminoethane and 1,3--diaminopropane in the presence of metal dichloride is reported. The resulting complexes were subjected to elemental analyses, magnetic measurements, and electronic absorption, infrared, and proton magnetic resonance spectral studies. The formation of the proposed macrocyclic skeletons and their donor sites were identified based on the spectral studies. A distorted octahedral structure for the nickel complexes and a square-planar structure for the palladium complexes in the solid state are suggested.

Keywords: tetraazamacrocycles; diaryltellurium dichlorides; template condensation; ethylenediamine; 1,3-diaminopropane.

INTRODUCTION

The coordination chemistry of organotellurium ligands containing hard donor atoms, such as nitrogen and oxygen, along with soft tellurium is interesting as such ligand framework can provide insight into the competitive coordination behavior between hard and soft donors towards a metal center.[1,2] Such molecular systems may be important in transition metal catalyzed asymmetric synthesis,[3,4] and as single source precursors in metal–organic chemical vapor deposition processes.[5–7] In addition, macrocycle complexes are significant as they have been found to act as possible models for biochemically important proteins and enzymes.[8–12]

Some recent publications[13–15] show the development of tellurium-containing macrocycles. Srivastava *et al.*[16] reported the route to the synthesis of metal complexes with tellurium-containing macrocycles. In continuation of earlier work,[17,18]

325

herein the synthesis and characterization of divalent nickel and palladium complexes with six novel tellurium tetraazamacrocycles (Te_2N_4 system) are reported.

RESULTS AND DISCUSSION

The formation of diaryltellurium(IV) dichlorides by the reactions of $TeCl_4$ with phenol,[19] o-cresol[20] and anisole[21] involves two-step reactions. The first step is an electrophilic substitution of the phenyl ring by a trichlorotellurium moiety at the *para* position to the hydroxyl or the methoxy groups. This can be represented by the following equation:

$$R–H + TeCl_4 \rightarrow RTeCl_3 + HCl \qquad (1)$$

(R = *p*-hydroxyphenyl, *p*-methoxyphenyl or 4-hydroxy-3-methyl-phenyl).

In the second step, these aryltellurium trichlorides further react with phenol//o-cresol or anisole to give the diaryltellurium(IV) dichlorides as per the following equation:

$$RTeCl_3 + R–H \rightarrow R_2TeCl_2 + HCl \qquad (2)$$
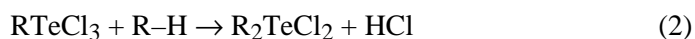
These diaryltellurium dichlorides when refluxed with 1,2-diaminoethane or 1,3-diaminopropane in presence of $NiCl_2$/$PdCl_2$ in 2:2:1 molar ratios yielded 10--membered and 12-membered tetraazamacrocyclic complexes, respectively, as shown in Scheme 1.
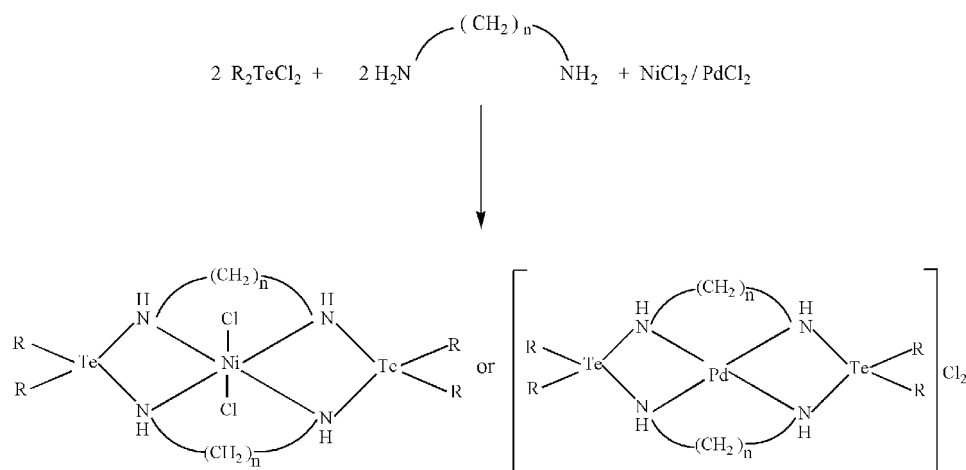
where: L^1; R = *p*-hydroxyphenyl, $n = 2$, L^2; R = 4-hydroxy-3-methyl-phenyl, $n = 2$, L^3; R = = *p*-methoxyphenyl, $n = 2$, L^4; R = *p*-hydroxyphenyl, $n = 3$, L^5; R = 4-hydroxy-3-methyl--phenyl, $n = 3$ and L^6; R = *p*-methoxyphenyl, $n = 3$.

Scheme 1. Formation of the Ni(II) and Pd(II) complexes.

These complexes are colored, crystalline solids, fairly stable in dry air and soluble only in polar donor organic solvents. The analytical data and physical properties of the complexes are presented in Table I.

TABLE I. Physical characteristics and analytical results of the metal complexes

Complex	Empirical formula (*FW*)	Color	M.p. °C	Yield %	Found (Calcd.), %					
					C	H	N	Cl	Te	M
[NiL^{1}Cl$_2$]	C$_{28}$H$_{32}$Cl$_2$N$_4$NiO$_4$Te$_2$ (873.4)	Pink	85–88	70	38.15 (38.51)	3.37 (3.69)	6.11 (6.41)	8.15 (8.12)	28.81 (29.22)	6.45 (6.51)
[NiL^{2}Cl$_2$]	C$_{32}$H$_{40}$Cl$_2$N$_4$NiO$_4$Te$_2$ (929.5)	Red brown	145–147	81	40.95 (41.35)	3.87 (4.34)	6.11 (6.03)	7.61 (7.63)	26.71 (27.46)	6.18 (6.31)
[NiL^{3}Cl$_2$]	C$_{32}$H$_{40}$Cl$_2$N$_4$NiO$_4$Te$_2$ (929.5)	Light brown	157–160	68	41.30 (41.35)	4.44 (4.34)	6.26 (6.03)	7.59 (7.63)	26.97 (27.46)	6.06 (6.31)
[NiL^{4}Cl$_2$]	C$_{30}$H$_{36}$Cl$_2$N$_4$NiO$_4$Te$_2$ (901.4)	Light orange	150–152	70	39.52 (39.97)	3.89 (4.03)	5.99 (6.22)	7.85 (7.87)	28.22 (28.31)	6.45 (6.51)
[NiL^{5}Cl$_2$]	C$_{34}$H$_{44}$Cl$_2$N$_4$NiO$_4$Te$_2$ (957.5)	Red brown	135–138	78	42.26 (42.65)	4.33 (4.63)	5.37 (5.85)	7.43 (7.41)	26.10 (26.65)	6.04 (6.13)
[NiL^{6}Cl$_2$]	C$_{34}$H$_{44}$Cl$_2$N$_4$NiO$_4$Te$_2$ (957.5)	Light green	177–180	69	42.37 (42.65)	4.41 (4.63)	5.68 (5.85)	7.27 (7.41)	27.19 (26.65)	5.88 (6.13)
[PdL^1]Cl$_2$	C$_{28}$H$_{32}$Cl$_2$N$_4$O$_4$PdTe$_2$ (921.1)	Dark brown	155–158	55	36.12 (36.51)	3.21 (3.50)	5.78 (6.08)	7.65 (7.70)	27.70 (27.71)	11.18 (11.55)
[PdL^2]Cl$_2$	C$_{32}$H$_{40}$Cl$_2$N$_4$O$_4$PdTe$_2$ (977.2)	Orange	210–212	68	39.03 (39.33)	3.93 (4.13)	5.24 (5.73)	7.38 (7.26)	26.40 (26.12)	10.62 (10.89)
[PdL^3]Cl$_2$	C$_{32}$H$_{40}$Cl$_2$N$_4$O$_4$PdTe$_2$ (977.2)	Orange	118–120	50	39.16 (39.33)	3.98 (4.13)	5.44 (5.73)	7.14 (7.26)	25.94 (26.12)	10.66 (10.89)
[PdL^4]Cl$_2$	C$_{30}$H$_{36}$Cl$_2$N$_4$O$_4$PdTe$_2$ (949.2)	Brown	168–170	75	37.67 (37.96)	3.53 (3.82)	5.46 (5.90)	7.47 (7.41)	26.09 (26.27)	10.83 (11.21)
[PdL^5]Cl$_2$	C$_{34}$H$_{44}$Cl$_2$N$_4$O$_4$PdTe$_2$ (1005.3)	Dark orange	222–225	66	40.22 (40.62)	4.11 (4.41)	5.17 (5.57)	7.09 (7.05)	24.90 (25.39)	10.21 (10.59)
[PdL^6]Cl$_2$	C$_{34}$H$_{44}$Cl$_2$N$_4$O$_4$PdTe$_2$ (1005.3)	Orange	87–90	53	40.46 (40.62)	4.23 (4.41)	5.29 (5.57)	6.97 (7.05)	25.11 (25.39)	10.25 (10.59)

Infrared spectra

The important IR bands and their assignments are reported in Table II. The spectra are quite complex and an attempt has thus been made to draw the conclusions by comparing the spectra of metal complexes with those of corresponding constituent diarytellurium dichlorides and diaminoalkanes.

The metal complexes under study did not show bands characteristic of free NH$_2$ group, instead the entire complexes exhibit a single sharp absorption band at around 3180–3250 cm^{-1} (sometimes overlapped with O–H) attributed to ν_{N-H} vibrations. The assignment of this sharp band is based on the fact that macrocyclic ligands that have a coordinated secondary amino group have bands[18,22–24] in the vicinity of 3200 cm^{-1}. This contention finds support[22] from appearance of bands of medium to strong intensity at 1627–1655 cm^{-1} and 809–827 cm^{-1}, assigned as N–H deformation coupled with N–H out-of-plane bending vibrations.

The bands at 1156–1185 cm^{-1} may reasonably be assigned to C–N stretching vibrations.[18,25,26] The above observation strongly suggests[18,22,25,26] that the proposed macrocyclic framework was formed. The formation of a tellurium-containing macrocyclic ring is supported by appearance of new weak intensity bands around 420–410 cm^{-1} due to Te–N.[18,27] Evidence for the formation of proposed macrocycles and coordination through N atoms is further supported by new medium to weak intensity bands at around 480–450 cm^{-1}, assignable to Ni–N stretching.[28] The M–Cl and Pd–N vibrations could not be ascertained due to the non-availability of far-infrared data.

TABLE II. Important IR data (cm^{-1}) for the metal complexes (mixed with moisture band; s – strong, m – medium, vs – very strong)

Complex	ν_{N-H}	N–H Def.	N–H Out-of-plane bending	ν_{C-N}
[NiL^{1}Cl$_2$]	3180 m	1630 m	825 s	1185 m
[NiL^{2}Cl$_2$]	3191 m	1640 m	812 s	1176 m
[NiL^{3}Cl$_2$]	3210 m	1649 m	819 vs	1176 vs
[NiL^{4}Cl$_2$]	3250 m	1635 m	827 s	1173 s
[NiL^{5}Cl$_2$]	3250 m	1630 m	813 s	1178 m
[NiL^{6}Cl$_2$]	3215 m	1645 m	822 s	1176 vs
[PdL^1]Cl$_2$	3210 m	1640 m	824 vs	1172 s
[PdL^2]Cl$_2$	3180 m	1635 m	809 vs	1173 m
[PdL^3]Cl$_2$	3230 m	1650 m	816 s	1176 s
[PdL^4]Cl$_2$	3190 s	1630 m	825 m	1156 vs
[PdL^5]Cl$_2$	3210 m	1627 m	809 s	1172 m
[PdL^6]Cl$_2$	3210 m	1655 m	822 s	1177 vs

Proton magnetic resonance spectra

The proton chemical shifts for metal complexes with 10-membered and 12--membered tetraazamacrocycles that are soluble in DMSO-d_6 are presented in Tables III and IV, respectively.

TABLE III. ^{1}H-NMR data (δ / ppm) for the 10-membered macrocyclic metal complexes in DMSO-d_6 (s – singlet, d – doublet, m – multiplet, b – broad)

Complex	–NH–	–CH$_2$–	–OCH$_3$	Phenyl	–OH
[NiL^{1}Cl$_2$]	1.45 (4H, s)	2.17 (8H, m)	–	6.93 (8H, d, J = 8.7 Hz) 7.83 (8H, d, J = 8.7 Hz)	9.85 (4H, b)
[PdL^1]Cl$_2$	1.40 (4H, s)	2.50 (8H, m)	–	6.91 (8H, d, J = 8.7 Hz) 7.74 (8H, d, J = 8.7 Hz)	8.35 (4H, b)
[PdL^3]Cl$_2$	1.75 (4H, s)	2.50 (8H, m)	3.78 (12H, s)	7.11 (8H, d, J = 8.4 Hz) 7.87 (8H, d, J = 8.4 Hz)	–

The phenyl protons in metal complexes resonated slightly upfield (6.89–7.88 ppm) from those of the parent diaryltellurium dichlorides,[19,20,29] due to an increase in electron density at the tellurium atom as a result of the replacement of 2

Cl by 2 N atoms. Ethylenediamine, $H_2N–(CH_2)_2–NH_2$ shows[30] two sets of four equivalent protons each at 1.19 (a) and 2.74 ppm (b). The metal complexes did not show any signal attributable to free $–NH_2$ groups, instead a broad singlet at around 1.74–2.04 ppm, which may be assigned to coordinated secondary amino group,[31] was observed. This confirms the formation of the proposed 10-membered macrocycle skeleton. The deshielding of the –NH– protons further suggests the donation of electron density to the metal ions. The methylene protons in these metal complexes resonated at 2.17–2.50 ppm, as a multiplet as reported for other tetraazamacrocyles derived from ethylenediamine.[18,24,26]

TABLE IV. ^{1}H-NMR data (δ / ppm) for 12-membered macrocyclic metal complexes in DMSO-d_6 (s – singlet, d – doublet, m – multiplet, b – broad)

Complex	–NH–	–CH$_2$– (middle)	–CH$_2$– (adjacent to N)	–CH$_3$[a]	–OCH$_3$	Phenyl	–OH
[NiL^{4}Cl$_2$]	1.89 (4H, s)	2.27 (4H, m)	2.86 (8H, m)	–	–	6.89 (8H, d, J = 8.7 Hz) 7.77 (8H, d, J = 8.7 Hz)	8.63 (4H, b)
[PdL^4]Cl$_2$	1.91 (4H, s)	2.50 (4H, m)[a]	2.88 (8H, m)	–	–	6.92 (8H, d, J = 8.7 Hz) 7.74 (8H, d, J = 8.7 Hz)	8.14 (4H, b)
[NiL^{5}Cl$_2$]	1.91 (4H, s)	2.06 (4H, m)	2.90 (8H, m)	2.49 (12H, s)	–	6.92 (4H, d, J = 8.4 Hz) 7.34 (4H, s) 7.64 (4H, d, J = 8.4 Hz)	8.10 (4H, b)
[NiL^{6}Cl$_2$]	1.78 (4H, s)	2.01 (4H, m)	3.33 (8H, m)	–	3.72 (12H, s)	6.89 (8H, d, J = 8.7 Hz) 7.88 (8H, d, J = 8.7 Hz)	–

[a]May be overlapped with the solvent peak

1,3-Diaminopropane, $NH_2–CH_2–CH_2–CH_2–NH_2$, exhibited[32] protons resonances at 1.15 (4H), 2.76 (4H) and 1.59 (2H) ppm due to amino, methylene (adjacent to N) and middle methylene groups, respectively. The metal complexes did not show any signal due to free amino groups. Instead, a broad singlet at 1.78–1.91 ppm, assignable to a coordinated secondary amino group,[31] confirms the formation of a 12-membered tellurium-containing tetraazamacrocycle skeleton. The middle methylene protons and those adjacent to the N-atoms resonate at 2.01–2.50 ppm and 2.86–3.33 ppm, respectively. This behavior of the complexes under study is quite similar to those of other tetraazamacrocycles derived from 1,3-diaminopropane.[18,24,33]

Furthermore, the independence of aryl proton chemical shifts on the nature of metal ions precludes the possibility of a Te–M bond. The proton magnetic resonance studies on these Ni(II) and Pd(II) complexes support the tetradentate nature of these ligands through four N-atoms, as predicted by infrared studies.

Electronic absorption spectra and magnetic studies

The electronic absorption and magnetic moment data for the complexes are presented in Table V.

TABLE V. Electronic absorption spectra and magnetic moment data for the metal complexes

Nickel(II) complex	Absorption, cm^{-1}			Observed magnetic moment, μ_B
	$^3A_{2g} \rightarrow {}^3T_{2g}$	$^3A_{2g} \rightarrow {}^3T_{1g}(F)$	$^3A_{2g} \rightarrow {}^3T_{1g}(P)$	
[NiL^{1}Cl$_2$]	9994	14500	29740	3.44
[NiL^{2}Cl$_2$]	9850	14040	24096	2.99
[NiL^{3}Cl$_2$]	10100	13600	25700	3.19
[NiL^{4}Cl$_2$]	10700	14525	28668	3.10
[NiL^{5}Cl$_2$]	10428	15052	27689	3.00
[NiL^{6}Cl$_2$]	9941	13855	26550	2.90
Palladium(II) complex	$^1A_{1g} \rightarrow {}^1A_{2g}$		$^1A_{1g} \rightarrow {}^1B_{1g}$	
[PdL^1]Cl$_2$	24500[a]		27737	Diamagnetic
[PdL^2]Cl$_2$	21700		28490	Diamagnetic
[PdL^3]Cl$_2$	24752[a]		26815	Diamagnetic
[PdL^4]Cl$_2$	22026		27600	Diamagnetic
[PdL^5]Cl$_2$	20829		28800	Diamagnetic
[PdL^6]Cl$_2$	21100		26900	Diamagnetic

[a] $^1A_{1g} \rightarrow {}^1E_g$

The electronic spectral data of all the six Ni(II) complexes exhibited three spin allowed transitions from $^3A_{2g} \rightarrow {}^3T_{2g}$, $^3T_{1g}(F)$, and $^3T_{1g}(P)$, which appeared 9850–10700 cm^{-1}, 13600–15052 cm^{-1} and 24096–28668 cm^{-1}, respectively. This spectral pattern corresponds to an octahedral/distorted octahedral geometry[16,34,35] Also, the ratio of $\nu_2/\nu_1 \approx 1.4$ is indicative[36,37] of an octahedral stereochemistry for all these Ni(II) complexes. The third spin allowed d–d transitions appeared as a broad shoulder on the CT bands and extended up to 22×10^3 cm^{-1}, as reported[38] for other tetraazamacrocyclic complexes of Ni(II). The magnetic moment values of the studied Ni(II) complexes (2.90–3.44 μ_B) also suggest an octahedral stereochemistry for these complexes and rules out the possibility of a square-planar geometry.[39,40] The Pd(II) complexes under study displayed two bands at 20829–24752 cm^{-1} and 26900–28800 cm^{-1}, which may be assigned to $^1A_{1g} \rightarrow {}^1A_{2g}$, and $^1A_{1g} \rightarrow {}^1B_{1g}$. These transitions in the Pd(II) complexes establish a square-planar coordination around palladium.[34,41] This was further supported by their diamagnetic nature.

Based on the above studies, nickel appears to be hexa-coordinated, especially in the solid state, presumably in a distorted octahedral fashion involving four N atoms of the tetraazamacrocycles and two chlorine atoms, whereas palladium is tetra-coordinated in a square-planar arrangement involving four N atoms of the macrocyclic ring. However, the proton magnetic resonance spectral pattern of the nickel complexes also indicated[42] the presence of diamagnetic square-planar configuration. Probably, dissociation of the chloride anions occurs in solution and the nickel (II) complexes form an equilibrium of octahedral (paramagnetic) and square-planar (diamagnetic) species.

EXPERIMENTAL

All the preparations were performed under a dry N_2 atmosphere and the solvents were dried and purified by standard methods before use.

Preparation of diaryltellurium dichlorides

The bis(p-hydroxyphenyl), bis(4-hydroxy-3-methyl-phenyl), and bis(p-methoxyphenyl) tellurium dichlorides were prepared by the reactions of tellurium tetrachloride with phenol, o-cresol, and anisole, respectively.[19–21]

Synthesis of metal complexes with tellurium containing 10-membered and 12-membered tetraazamacrocycles

The complexes were prepared by template condensation of the diaryltellurium dichlorides with diaminoalkanes in the presence of metal dichlorides in 2:2:1 molar ratio. A general procedure is given below.

A saturated methanolic solution of 4.0 mmol of diaryltellurium dichloride (1.538 g, 1.650 g, 1.650 g for bis(p-hydroxyphenyl), bis(4-hydroxy-3-methyl-phenyl) and bis(p-methoxyphenyl) tellurium dichlorides, respectively) was added to ethylenediamine (0.240 g, 4.0 mmol) or 1,3-diaminopropane (0.296 g, 4.0 mmol) in about 10 mL dry methanol under constant stirring. An immediate change in color was observed along with a little turbidity. The contents were stirred and refluxed for about 3 h. This was followed by addition of a solution of 2.0 mmol of metal dichloride (0.575 g and 0.355 g for $NiCl_2.6H_2O$ and $PdCl_2$, respectively) in about 10 mL methanol. This resulted in a distinct color change along with slight precipitation of a solid product. The solution was then refluxed for about 6 h and cooled. The small amount of colored solid that separated was filtered off and the filtrate was concentrated to about one third of its original volume and kept in a freezer (0 °C) overnight to obtain a second crop of the crystalline product. This was filtered and washed with benzene and dried in a vacuum desiccator over P_4O_{10}. The purity of these compounds was controlled by TLC using silica gel-G.

Analytical methods and physical measurements

Carbon, hydrogen, and nitrogen analyses were obtained micro-analytically from the Sophisticated Analytical Instrumentation Facility (SAIF), Panjab University, Chandigarh. The tellurium and chlorine contents were determined volumetrically[43] and palladium gravimetrically.[43] Nickel was estimated by atomic absorption spectrophotometry. The IR spectra were recorded in the region 4000–400 cm^{-1} at the SAIF on a Perkin Elmer Model 2000 FTIR spectrometer using the KBr pellet technique. The ^{1}H-NMR spectra were recorded at the Kurukshetra University, Kurukshetra on a Bruker XWIN-NMR Avance 300 operating at 300.13 MHz in DMSO-d_6 using tetramethylsilane as an internal reference. The magnetic suscepti-

bility data were obtained from National Physical Laboratory, New Delhi on a Gouy balance (model Johnson Matthey Alfa products) using glycerin as a calibrant. The electronic spectra were recorded in dimethyl sulphoxide on a Thermo Spectronic UV-1 UV–Vis spectrophotometer (Electron Corporation, India).

CONCLUSIONS

Nickel (II) and palladium (II) complexes have been prepared by condensation of diaryltellurium dichlorides with diaminoalkanes in the presence of metal chlorides. These metal complexes have been characterized using elemental analyses, magnetic measurements, and electronic absorption, infrared and proton magnetic resonance spectral techniques. A distorted octahedral structure for the Ni (II) complexes in the solid state and a square-planar structure for the Pd (II) complexes were assigned based on these studies. The Ni(II) complexes probably form an equilibrium of octahedral and square-planar species in solution.

ИЗВОД

ИСПИТИВАЊЕ КОМПЛЕКСА НИКЛА(II) И ПАЛАДИЈУМА(II) СА НЕКИМ ТЕРААЗАМАКРОЦИКЛИЧНИМ ЛИГАНДИМА КОЈИ САДРЖЕ ТЕЛУР

NITU RATHEE и KRISHAN KUMAR VERMA

Department of Chemistry, Maharshi Dayanand University, Rohtak – 124001, Haryana, India

Темплатном кондензационом реакцијом полазећи од диарилтелур-дихлорида (арил = = *p*-хидроксифенил, 4-хидрокси-3-метил-фенил, *p*-метоксифенил) и 1,2-диаминоетана и 1,3--диаминопропана у присуству одговарајућег хлорида метала (Ni(II) и Pd(II)) синтетизовани су комплекси никла(II) и паладијума(II) са десеточланим и дванаесточланим тетраазамакроцикличним лигандима који садрже телур. Синтетисани комплекси су окарактерисани на основу резултата елементалне микроанализе, магнетних мерења, UV–Vis, IR и ^{1}H-NMR спектара. Грађење макроцикличног скелета са одговарајућим донорским атомима је праћено на основу спектроскопских мерења. На основу ових резултата је нађено да комплекси никла(II) имају дисторговану окатедарску, док комплекси паладијума(II) имају квадратно-планарну геометрију.

(Примљено 11. децембра 2010, ревидирано 13. јула 2011)

REFERENCES

1. P. G. Jones, M. Carman, R. D. Arellano, *J. Chem. Soc. Dalton Trans.* (1996) 2713
2. C. O. Kienitz, C. Thone, P. G. Jones, *Inorg. Chem.* **35** (1996) 3990
3. Y. Nishibayashi, K. Segawa, J. D. Singh, S. I. Fukuzawa, K. Ohe, S. Uemura, *Organometallics* **15** (1996) 370
4. Y. Nishibayashi, J. D. Singh, Y. Arikawa, S. Uemura, M. Hidai, *J. Organomet. Chem.* **531** (1997) 13
5. Y. Chang, T. Emge, J. G. Brennan, *Inorg. Chem.* **35** (1996) 7339
6. M. L. Steigerwald, C. R. Sprinkle, *J. Am. Chem. Soc*. **109** (1987) 7200

7. W. Hirpo, S. Dhingra, A. C. Sutorik, M. G. Kanatzidis, *J. Am. Chem. Soc.* **115** (1993) 1597
8. R. R. Gagne, J. L. Allison, R. S. Gall, C. A. Koval, *J. Am. Chem. Soc.* **99** (1977) 7170
9. J. W. L. Martin, J. H. Johnson, N. F. Curtis*, J. Chem. Soc. Dalton Trans.* (1978) 68
10. M. N. Hughes, *Inorganic Chemistry of Biological Processes*, 2nd ed., Wiley, New York, 1981
11. L. Casella, M. Gullotii, L. D. Gioia, M. Monzani, F. Chillemi*, J. Chem. Soc. Dalton Trans.* (1991) 2945
12. S. R. James, D. W. Margerum, *Inorg. Chem.* **19** (1980) 2784
13. W. Levason, S. D. Orchard, G. Reid, *Coord. Chem. Rev*. **225** (2002) 159
14. A. K. Singh, S. Sharma, *Coord. Chem. Rev.* **209** (2000) 49
15. A. Panda, *Coord. Chem. Rev*. **253** (2009) 1947
16. S. Srivastava, A. Kalam, *J. Indian Chem. Soc.* **83** (2006) 563
17. Nitu, K. K. Verma, *J. Chem. Pharm. Res.* **2(4)** (2010) 793
18. Nitu, K. K. Verma, *Int. J. Chem. Sci*., **9(1)** (2011) 229
19. B. L. Khandelwal, K. Kumar, F. J. Berry, *Inorg. Chim. Acta* **47** (1981) 135
20. B. L. Khandelwal, K. Kumar, K. Raina, *Synth. React. Inorg. Met.-Org. Chem*. **11** (1981) 65
21. J. Bergman, *Tetrahedron* **28** (1972) 3323
22. V. B. Rana, P. Singh, D. P. Singh, M. P. Teotia, *Polyhedron* **1** (1982) 377
23. D. A. House, N. F. Curtis, *J. Am. Chem. Soc.* **86** (1964) 1331
24. M. Shakir, S. P. Varkey, P. S. Hameed, *Polyhedron* **13** (1994) 1355
25. A. K. Panda, A. Panda, S. Sutar, P. Mishra, S. Pradhan, S. Ghos, S. Pany, *J. Indian Chem. Soc.* **86** (2009) 908
26. S. Srivastava, A. Kalam, *Synth. React. Inorg. Met.-Org. Chem*. **34** (2004) 1529
27. Y. D. Kulkarni, S. Srivastava, *Indian J. Chem., A* **24** (1985) 429
28. K. Nakamoto, *Infrared and Raman Spectra of Inorganic and Coordination Compounds*, Part-B, 5th ed., Wiley, New York, 1997, p. 15
29. K. Raina, B. L. Khandelwal, *Indian J. Chem., Sect A* **14** (1976) 63
30. *Handbook of Proton NMR Spectra and Data*, Vol. 1, Ed. Asahi Research Centre, Academic Press, New York, p. 47
31. S. C. Menon, H. B. Singh, R. P. Patel, S. K. Kulshreshtha, *J. Chem. Soc. Dalton Trans*. (1996) 1203
32. K. Kawakami, M. Miya-Uchi, T. Tanaka, *J. Inorg. Nucl. Chem.* **33** (1971) 3773
33. M. G. B. Drew, F. S. Esho, S. M. Nelson, *J. Chem. Soc. Dalton Trans*. (1983) 1653
34. A. B. P. Lever, *Inorganic Electronic Spectroscopy*, Elsevier, Amsterdam, 1968
35. T. M. Dunn, in *Modern Coordination Chemistry*, J. Lewis, R. G. Wilkins, Eds., Interscience, New York, 1960, p. 230
36. K. Abe, K. Matsufuji, M. Ohba, H. Okawa, *Inorg. Chem*. **41** (2002) 4461
37. M. J. M Campbell, R. Grzeskowiak, *J. Chem. Soc. A* (1967) 396
38. S. Chandra, K. Gupta, S. Sharma, *Synth. React. Inorg. Met.-Org. Chem.* **31** (2000) 1205
39. M. L. Dianu, A. Kriza, N. Stanica, A. M. Musuc, *J. Serb. Chem. Soc.* **75** (2010) 1515
40. Y. Baran, L. Yilmaz, *Transition Met. Chem*. **26** (2001) 36
41. S. Chandra, S. Verma, P. Meera, *J. Indian Chem. Soc*. **85** (2008) 896
42. A. Dei, *Inorg. Chem.* **18** (1979) 891
43. A. I. Vogel, *A Text Book of Quantitative Inorganic Analysis Including Elementary Instrumental Analysis*, 3rd ed., Longman, London, 1975, pp. 266, 324, 511.

Synthesis and properties of 5,10,15,20-tetrakis[4-(3,5-dioctyloxybenzamido)phenyl]porphyrin and its metal complexes

WENHUI LIAN, YUANYUAN SUN, BINBIN WANG, NING SHAN and TONGSHUN SHI*

College of Chemistry, Jilin University, Changchun 130023, P. R. China

Abstract: A novel 5,10,15,20-tetrakis[4-(3,5-dioctyloxybenzamido)phenyl]-porphyrin and its transition metal complexes are reported in this paper. Their molecular structures were characterized by elemental analysis as well as IR, ^{1}H-NMR and UV–Vis spectroscopy. Their spectroscopic properties were studied by Raman and fluorescence spectroscopy, and X-ray photoelectron spectroscopy (XPS). The fluorescence quantum yields were measured at room temperature. The fluorescence intensity of the porphyrin ligand was stronger than the intensity of the complexes. There were large differences in the Raman spectrum of the porphyrin ligand and those of the metal complexes due to changes in the symmetry of porphyrin plane. In the XPS spectra, the replacement of the free-base protons by a metal ion to form the metalloporphyrin not only increases the symmetry of the molecule, but also introduces an electron withdrawing group into the center of the porphyrin ligand, which increases the N_{1s} binding energy.

Keywords: porphyrin; transition metal complex; XPS spectra; Raman spectra; fluorescence spectra.

INTRODUCTION

Recently, investigation of porphyrins has become of increasing interest.[1,2] Porphyrins and metalloporphyrins are functional molecules that are used for a variety of applications and devices, such as optoelectronic, luminescent and, molecular logic devices, supramolecular self-assembly, solar energy harvesting systems, photonic materials, and therapeutics.[3–7]. These applications are affected by the diverse electrochemical and photophysical properties of the porphyrins and the ability to fine-tune these properties by the exocyclic substituents on the macrocycle and *via* the choice of chelated metal ion.

Porphyrins have many desirable features, such as high stability, intense absorption of sunlight, a highly conjugated plane and a small gap between the high-

335

est occupied molecular orbital (HOMO) and lowest unoccupied molecular orbital (LUMO) energy level. The highly conjugated π-electron skeleton of a porphyrin provides an adequate number of π electrons and π–π* transitions normally give a strong absorption in the UV and visible regions of the spectrum.[8] Metalloporphyrins generally have high thermal stability and show strong electronic transitions in the visible and ultraviolet regions. In order to evaluate the applications of metalloporphyrins, it is necessary to understand the electronic structure and photophysical properties. Raman spectroscopy, fluorescence spectra, X-ray photoelectron spectroscopy, *etc*, have been widely used to study the porphyrin ligand and metalloporphyrins, and the results could provide important information to determine their electronic structure. X-Ray photoelectron spectroscopy (XPS) is a powerful tool for the characterization of both the chemical composition and the electronic environments of each atom in a molecular system.[9–11]

To date, the synthesis and application of the substituent tetraphenylporphyrin (TPP) bearing special functional groups have caused great interest, but those bearing an amide group as side chains have been little reported. In this research, a novel TPP derivative bearing an amide group and its transition metal complexes were synthesized. The benzene core was replaced by a rigid porphyrin core, which is linked *via* amide bonds to four triphenylenes. Since the porphyrin dimension is much larger than that of a benzene ring and the symmetry changes from three-fold to four-fold, an entirely different self-assembly *via* hydrogen bonding was to be expected. Their structures were characterized by their UV––Vis, IR and ^{1}H-NMR spectra and the changes in the fluorescence, Raman spectra and XPS behavior of these compounds were investigated.

RESULTS AND DISCUSSION

*Physical, analytic and spectral data for **7a**–**7d***

*5,10,15,20-Tetrakis[4-(3,5-dioctyloxybenzamido)phenyl]porphyrin (**7a**)*. Purple solid. Yield: 62.4 %; Anal. Calcd. for $C_{136}H_{178}N_8O_{12}$: C, 77.12; H, 8.42; N, 5.26 %. Found: C, 77.16; H, 8.48; N, 5.20 %. IR (KBr, cm^{-1}): 3314 (N–H, pyrrole), 2925, 2855 (C–H), 1674 (C=O), 1523 (N–H, amide), 1245 (Ar–O–C), 966 (N–H, pyrrole), 721 (–(CH$_2$)$_n$–, $n > 4$). ^{1}H-NMR (500MHz, CDCl$_3$, δ / ppm): 8.92 (8H, *s*, pyrrole ring), 8.30 (4H, *s*, –NH–CO–), 8.20–8.26 (8H, *d*, $J = 30$ Hz, *o*–C$_6$H$_4$), 8.08–8.03 (8H, *d*, $J = 25$ Hz, *m*-C$_6$H$_4$), 6.98–7.04 (8H, *d*, $J = 30$ Hz, *o*–C$_6$H$_3$), 6.64–6.69 (4H, *d*, $J = 25$ Hz, *m*–C$_6$H$_3$), 4.10–4.22 (16H, *m*, –O–CH$_2$–), 1.78–1.98 (16H, *m*, –O–C–CH$_2$–), 1.49–1.64(16H, *m*, –CH$_2$–CH$_3$), 1.21–1.40 (64H, *m*, –O–C–C–(CH$_2$)$_4$–C–CH$_3$), 0.85–0.95 (24H, *t*, $J = 25$ Hz, –O–C–C–(C)$_4$–C–CH$_3$), –2.74 (2H, *s*, N–H, pyrrole). UV–Vis (CHCl$_3$, λ_{max} / nm): 425 (Soret band), 520, 555, 595, 650 (four Q bands).

*Zinc 5,10,15,20-tetrakis[4-(3,5-dioctyloxybenzamido)phenyl]porphyrin (**7b**)*. Purple red solid. Yield: 90.5 %; Anal. Calcd. for $C_{136}H_{176}N_8O_{12}Zn$: C, 74.93; H,

8.35; N, 5.02 %. Found: C, 74.99; H, 8.30; N, 5.07 %. IR (KBr, cm^{-1}): 3285 (N–H, imide), 2924, 2851 (C–H), 1664 (C=O), 1527 (N–H, amide), 1245 (Ar–O–C), 996 (N–Zn), 721 (–(CH$_2$)$_{n-}$, $n > 4$). ^{1}H-NMR (500 MHz ,CDCl$_3$, δ / ppm), 8.99 (8H, s, pyrrole ring), 8.12–8.30 (8H, d, $J = 40$ Hz, o–C$_6$H$_4$), 8.06 (4H, s,–CON–H), 7.95–7.96 (8H, d, $J = 5$ Hz, m–C$_6$H$_4$), 7.26–7.27 (8H, d, $J = 5$ Hz, o–C$_6$H$_3$), 6.96–6.87 (4H, t, $J = 22.5$ Hz, m-C$_6$H$_3$), 3.92–4.03 (16H, t, $J = 7.5$ Hz, –O–CH$_2$–), 1.68–1.98 (16H, m, –O–C–CH$_2$–), 1.22–1.52 (80H, m, –C–C–(CH$_2$)$_5$–CH$_3$), 0.861–0.905 (24H, t, $J = 11$ Hz, –C–C–(C)$_5$–CH$_3$). UV–Vis (CHCl$_3$, λ_{max} / nm): 425 (Soret band), 551, 592 (two Q bands).

Manganese   5,10,15,20-tetrakis[4-(3,5-dioctyloxybenzamido)phenyl]porphyrin (7c). Dark green solid. Yield: 82.4 %; Anal. Calcd. for C$_{136}$H$_{176}$MnN$_8$O$_{12}$Cl: C, 74.12; H, 7.99; N, 5.04 %. Found: C, 74.07; H, 8.04; N, 5.08 %. IR (KBr, cm^{-1}): 3282 (N–H, imide), 2925, 2854 (C–H), 1677 (C=O), 1519 (N–H, amide), 1244 (Ar–O–C), 1008 (N–Mn), 721 (–(CH$_2$)$_{n-}$, $n > 4$). UV–Vis (CHCl$_3$, λ_{max} / nm): 480 (Soret band), 585, 625 (two Q bands).

Cobalt 5,10,15,20-tetrakis[4-(3,5-dioctyloxybenzamide)phenyl]porphyrin (7d). Purple red solid. Yield: 85.7 %; Anal. Calcd. for C$_{136}$H$_{176}$CoN$_8$O$_{12}$: C, 75.21; H, 8.11; N, 5.09 %. Found: C, 75.14; H, 8.16 N, 5.15 %. IR (KBr, cm^{-1}) 3280 (N–H (imide)), 2925, 2854 (C–H), 1658 (C=O), 1517 (N–H, amide), 1252 (Ar–O–C), 1000 (N–Co), 717 (–(CH$_2$)$_{n-}$, $n > 4$). UV–vis (CHCl$_3$, λ_{max} / nm): 415 (Soret band), 530, 675 (two Q bands).

UV–Vis spectra

The electronic absorption spectra of porphyrins result from electronic transitions from the ground state (S$_0$) to the two lowest singlet excited states S$_1$ and S$_2$. The S$_0 \rightarrow$S$_1$ transition gives rise to weak Q bands in the visible region while the S$_0 \rightarrow$S$_2$ transition produces a strong Soret band in the near UV region.[12,13] The absorption bands of **7a** appear at 425, 520, 555, 595 and 650 nm. Compared with the absorption bands of TPP, the absorption bands of **7a** are red-shifted.[14] Possibly, this is because the substituent group on the phenyl group at the meso-position of the porphyrin ring is an electron-donating group, thereby enabling the electronic density on the phenyl ring to strengthen. Thus, the phenyl ring conjugates to a certain degree with the porphyrin macrocycle. This kind of conjugation action causes a reduction of the electron transition energy of the porphyrin macrocycle, resulting in red shifts of the absorption bands.

When a metal atom is bonded to the central nitrogen atoms of a porphyrin, the metal ion accepts the lone-pair-electrons of the N atoms of the pyrrole rings, while the metal ion donates the electrons to the porphyrin molecule, forming de-localized π bonds, which permit the easy flow of electrons within the delocalized π system. In this work, the UV–Vis spectra of the metalloporphyrins exhibited one Soret band and either one or two Q bands; the number of Q band decreases

and the absorption frequencies shift. When the metal ion coordinates with porphyrin ligand, the symmetry of the molecule is changed from D_{2h} to D_{4h}, the cleavage degree of the molecular orbital decreases and the degeneracy increases; hence, the number of Q bands therefore decreases.

Infrared spectra

The IR bands at 3314 and 966 cm^{-1} of **7a** are attributed to N–H stretching and bending vibrations of the porphyrin ligand core, respectively, but they were absent in the spectra of the complexes, because the hydrogen atom in the N–H bond was replaced by a transition metal ion.[15] In addition, a new band in the spectrum of **7b**, **7c** and **7d** appeared at 996, 1008 and 1000 cm^{-1}, respectively, which is characteristic of metalloporphyrins. The bands at about 3280–3285 cm^{-1} of the complexes are assigned to N–H stretching vibrations of the amide group on the side chains, but in the spectrum of the porphyrin ligand, it overlapped the N–H stretching vibration of the porphyrin core and could not be distinguished. The bands in the range of 1652–1670 cm^{-1} are assigned to C=O stretching vibration (amide I). The bands at about 1517–1521 cm^{-1} are assigned to N–H in-plane bending and C–N stretching (imide II). The bands at about 1245–1252cm^{-1} are assigned to Ar–O–C stretching vibrations. The bands at 717–721 cm^{-1} are assigned to the methylene in-plane rocking vibration of a straight alkyl chain containing more than four carbon atoms.

Fluorescence spectra

Excited-state processes in porphyrins are extremely important for their application in molecular devices. The room temperature fluorescence spectra of the porphyrin ligand and metalloporphyrins in chloroform (2×10^{-6} mol L^{-1}) were recorded. No fluorescence signal was detected for the metalloporphyrins **7c** and **7d**
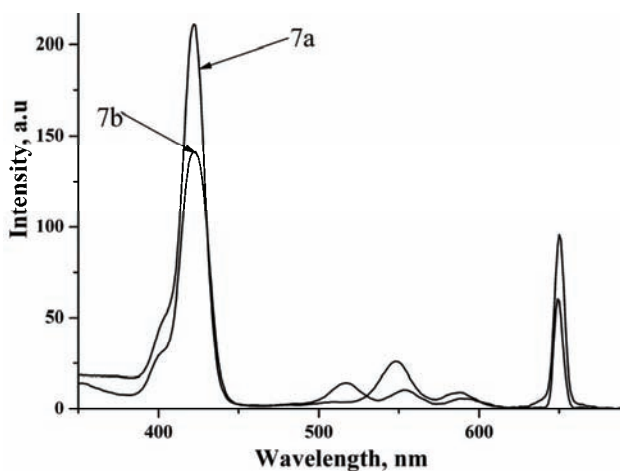
Fig. 1. Excitation spectra of **7a** and **7b** in chloroform.

under the employed experimental conditions. The excitation spectra of **7a** and **7b** are shown in Fig. 1. In the region of 350–700 nm, the excitation spectra are approximately mirror images of the absorption spectra, indicating that they correspond to a similar electron transition process.

The emission spectra of **7a** and **7b** are shown in Fig. 2 for an excitation wavelength of 420 nm. The emission spectra data of **7a** and **7b** are given in Table I. Excitation to the S_2 (B band) and the S_1 (Q band) in porphyrin compounds results in fluorescence. The fluorescence of the S_2 (B band) is attributed to the transition from the second excited singlet state S_2 to the ground state S_0, $S_2 \rightarrow S_0$, and it corresponds with the Soret band in the electronic absorption spectra. In addition, fluorescence of the Q band is attributed to the transition from the lowest excited singlet state S_1 to the ground state S_0. The fluorescence of $S_2 \rightarrow S_0$ was too weak to be observed in this study, owing to light scattering and resorption of strong Soret absorption band. It is well known that metal-free porphyrins usually show two strong emission bands around 650 and 720 nm.[16] The fluorescence bands of **7a** were at 653 and 716 nm. Compared with the fluorescent bands at 650 and 713 nm of TPP, the emission peaks of porphyrin ligand were red-shifted by 3 nm. The fluorescence bands of the Zn complex were at 597 and 644 nm, which were red-shifted compared to ZnTPP (592 and 641 nm). These red shifts may be due to the interaction of the arylamido group with the conjugated π-electron system of the porphyrin macrocycle. The conjugation of the porphyrin macrocycle is affected by the electronic donating groups. The conjugation is enhanced when the alkylamide groups are linked on the phenyl group.
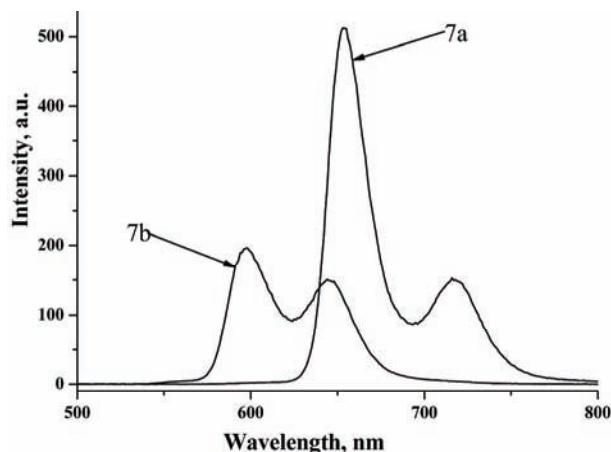
Fig. 2. Fluorescence spectra of **7a** and **7b** in chloroform.

The quantum yield of porphyrin ligand and Zn complex were calculated according to the following equation:

$$\phi_{\text{sample}} = \frac{F_{\text{sample}}}{F_{\text{ZnTPP}}} \frac{A_{\text{ZnTPP}}}{A_{\text{sample}}} \phi_{\text{ZnTPP}}$$

where F_{sample} and F_{ZnTPP} are the measured fluorescence integral areas of the sample and the reference ZnTPP, respectively. A_{sample} and A_{ZnTPP} are the absorbance of the sample and the reference, respectively. ϕ_{sample} and ϕ_{ZnTPP} ($\phi_{\text{ZnTPP}} = 0.033$)[17] are the quantum yields of the sample and the reference ZnTPP at same excitation wavelength. The quantum yields of the porphyrin ligand are much lower than that of TPP ($\phi_{\text{TPP}} = 0.11$[18]). As is known, porphyrins can be considered as specific donor–acceptor systems, and the decrease in the fluorescence quantum yields of the porphyrin ligand in comparison to that of TPP could be the result of intramolecular energy migration or electron transfer from the donor part of the molecule to the acceptor part. The fluorescence quantum yields of **7a** and **7b** were very small. Thus, the excited state S_1 was primarily deactivated by radiationless decay in porphyrins. This indicates fairly certainly that the spin forbidden process $S_1 \rightarrow T_n$ is dominant for the radiationless deactivation of S_1 in porphyrin compounds. The fluorescence yield of **7b** was much smaller than that of **7a** because zinc weakened the fluorescence radiation.

TABLE I. Emission spectra data and quantum yields (ϕ_f) of **7a** and **7b**

Compound	$Q(0–0)$ / nm	$Q(0–1)$ / nm	ϕ_f
7a	653	716	0.064
7b	597	644	0.032

Resonance Raman spectra

The resonance Raman spectra of the porphyrin ligand and complexes were obtained by excitation at 514.5 nm. The important Raman frequencies and their assignments are listed in Table II. The Raman spectra of the porphyrin ligand and the Mn complex are shown in Fig. 3. The resonance Raman spectra of tetraphenylporphyrin derivatives have been studied extensively.[19–21] Thus, the assignments of Raman bands of porphyrin ligand and complexes are only discussed briefly here.

TABLE II. Raman spectra and assignment of the porphyrin ligand and its complexes (*vs*: very strong, *s*: strong, *m*: medium, *w*: weak)

Compound				Assigned
7a	**7b**	**7c**	**7d**	
1553*vs*	1550*s*	1573*vs*	1561*vs*	ν_2, $\nu(C_\beta C_\beta)$
1496*m*	1494*m*	1497*s*	1502*m*	ϕ_5, phenyl
1455*s*	1454*w*	1456*m*	1455*w*	ν_3, $\nu(C_\alpha C_m)$
1360*m*	1353*s*	1372*m*	1367*s*	ν_4, $\nu(C_\alpha–N)$ / $\nu(C_\alpha C_\beta)$
1330*m*	–	1341*w*	–	ν_{20}, ν(pyr. quarter-ring)

1240m	1242w	1241m	1242w	ν_1, $\nu(C_m–Ph)$
1081w	1067w	1086m	1076m	ν_{17}, $\delta(C_\beta–H)$
1002m	1008m	1002m	997w	ν_{15}, ν(pyr. breath.) + phenyl

TABLE II. Continued

Compound				Assigned
7a	**7b**	**7c**	**7d**	
963w	–	–	–	ν_6, ν(pyrrole breath.)
719w	717w	713w	710w	π_3, phenyl
	404w	397w	395	$\nu(M–N)$
335	–	313w	312w	ν_8, ν(pyr. translation)
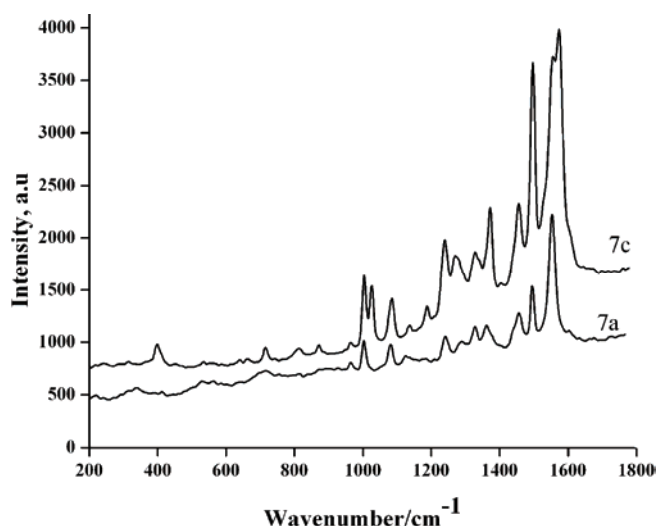
Fig. 3. Raman spectra of the porphyrin ligand and the Mn complex.

In the 900–1650 cm^{-1} high-frequency region of the Raman spectra of porphyrin ligand and complexes, Raman bands generally arise from the totally symmetric vibrational modes, such as $C_\beta C_\beta$, $C_\alpha C_\beta$, $C_\alpha C_m$, pyrrole quarter-ring, and pyrrole half-ring stretching. The wavenumber positions of Raman bands in the high-frequency region are sensitive to the core size, axial ligation and electron density of the central metal ion. In this region, the band at 1553 cm^{-1} of porphyrin ligand was assigned to the $C_\beta C_\beta$ stretch ν_2 mode, which was up-shifted to 1573 cm^{-1} in the Mn complex and to 1561 cm^{-1} in Co complex, but it was down-shifted to 1548 cm^{-1} in the Zn complex. The ν_2 mode was observed with enhanced intensity in the complexes. In fact, it is one of the most intense bands in the high-frequency region. The band at 1496 cm^{-1} of porphyrin ligand was assigned to the vibration of phenyl ring, and it was little shifted in the complexes, which confirmed that the metal ion had little effect on the phenyl at the meso

positions. Raman bands in 1300–1450 cm^{-1} were due to the out-of-phase coupled $C_\alpha C_\beta/C_\alpha N$ stretching modes. The 1360 and 1330 cm^{-1} bands of the porphyrin ligand were assigned to the ν_4 and ν_{20} mode, respectively. The ν_4 mode of **7b**, **7c** and **7d** appeared at 1353, 1372 and 1367 cm^{-1}, respectively. The ν_{20} mode of **7c** shifted to 1341 cm^{-1}, while the ν_{20} mode of **7b** and **7d** were too weak to be observed in the present experiments. The 1240 cm^{-1} band of the porphyrin ligand and the 1240–1242 cm^{-1} band of the complexes were attributed to the Cm−ph stretching ν_1 mode. The band at 1081 cm^{-1} of the porphyrin ligand was assigned to the vibrations of the pyrrole C_β–H stretching ν_9 mode, which shifted to 1067, 1086 and 1076 cm^{-1} in **7b**, **7c** and **7d**, respectively. The band at 1002 cm^{-1} of the porphyrin ligand was assigned to the vibration of pyrrole breathing and phenyl stretching ν_{15} mode, which did not shift in the Mn complex, but was up-shifted to 1008 cm^{-1} in the Zn complex and downshifted to 997 cm^{-1} in the Co complex. The band at 963 cm^{-1} of the porphyrin ligand was assigned to pyrrole breathing ν_6 mode, but it was absent in the spectra of the metalloporphyrins because the hydrogen atom in the N−H bonding had been replaced by a metal ion. In the low--frequency region, the Raman bands of the metalloporphyrin complexes were very different to those of the porphyrin ligand because the structures or vibrational dynamics, especially around the $C_\alpha C_m C_\beta$ bond-angles, were altered by the metal ions. For the porphyrin ligand, the only weak Raman band was observed at 335 cm^{-1}, which was assigned to the ν_8 mode. The ν_8 mode consists of the in--plane translational motion of the pyrrole, which can be described as a uniform breathing of the whole porphine ring accompanied by an in-plane deformation of $C_\alpha C_m C_\beta$ in the pyrrole ring.[22]

X-Ray photoelectron spectra

The XPS spectra of the porphyrin films were obtained. All elements of the porphyrins, including C, N, O and different metals for the metalloporphyrins, were found in the XPS spectra of their films grafted on Si (100). The X-ray photoelectron spectra data of the porphyrin ligand and its complexes are given in Table III. The XPS spectra of the N_{1s} region are shown in Fig. 4.

TABLE III. Binding energies (eV) of the porphyrin ligand and complexes obtained in the XPS experiments

Signal	Compound			
	7a	7b	7c	7d
=N–	397.65	–	–	–
–NH–	399.75	399.60	399.85	399.49
–N–M–	–	397.84	398.65	398.70
C1s	285.03	284.75	284.69	284.60
M2p3/2	–	1021.10	642.40	780.08
O1s	532.9	532.95	532.95	532

Free base porphyrins exhibit two distinct N_{1s} signals corresponding to the imine (–C=N–) nitrogen and the pyrrole (–NH–) nitrogen. The pyrrole nitrogen usually has a higher N_{1s} binding energy than the imine nitrogen.[23–26] The N_{1s} binding energies of these species were ≈400 and ≈397 eV, respectively, so that they should have been readily resolved in the performed experiment. In the porphyrin ligand **7a**, two N signals could be observed, one related to the N atoms of unprotonated porphyrin rings (397.65 eV), and the other to the N atoms of protonated porphyrin-rings and the N atoms of the amide around the porphyrin-ring (399.75 eV). The N_{1s} spectra of the metalloporphyrins also exhibited two signals, the signal with the lower binding energy can be assigned to the metal-binding nitrogen atoms. The binding energy of the protonated porphyrin-ring nitrogen coincides with the amide nitrogen, and their band energies were higher than for the unprotonated porphyrin-ring. This is because of the protonation of the imine nitrogen atoms, which decreases the intensity of the N_{1s} peak at the lower binding energy.
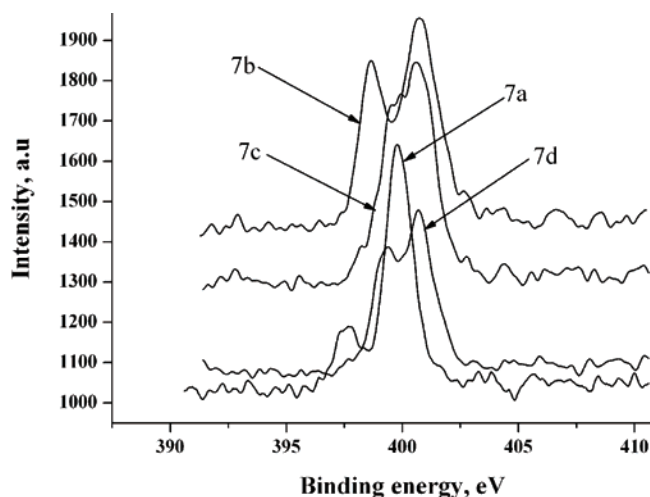
Fig. 4. N_{1s} region of the porphyrin ligand and its complexes.

The metal ion region of the XPS spectra of the films of metalloporphyrins **7b**, **7c**, and **7d** on the Si (100) surface are shown in Fig. 4. The metalloporphryins exhibit a $2p_{3/2}$ signal. The $M2p_{3/2}$ (M = Zn, Mn or Co) region of **7b**, **7c** and **7d** shows sharp peaks with bonding energy at 1021.10, 642.40 and 780.08 eV, respectively, and it is lower than the $M2p_{3/2}$ binding energy of corresponding metal salt. This indicates that the metal atoms accept electrons from the porphyrin ring when they generate complexes. The electrons of the porphyrin-ring nitrogens transfer to an unoccupied metal orbital, *i.e.*, they formed electron donor–acceptor complexes.

EXPERIMENTAL

General synthesis procedures

Chemicals and solvents were obtained from various commercial sources and used without further purification unless otherwise stated. Pyrrole was freshly distilled before use. DMF was pre-dried over activated 4Å molecular sieve and vacuum distilled from calcium hydride (CaH$_2$) prior to use. Dry CHCl$_3$ and Et$_3$N were obtained by redistillation from CaH$_2$. Acetone was dried with anhydrous magnesium sulfate. Anhydrous potassium carbonate was dried under vacuum at 80 °C for 30 min.

The synthesis procedures are illustrated in Schemes 1 and 2. 5,10,15,20-Tetra-(4-nitrophenyl)porphyrin was synthesized through the reaction between pyrrole and *p*-nitrobenzaldehyde in the presence of lactic acid according to a published procedure.[27] 5,10,15,20-Tetra(4-aminophenyl)porphyrin (TAPPH$_2$) was prepared using SnCl$_2$/HCl according to the method of Kruper.[28]
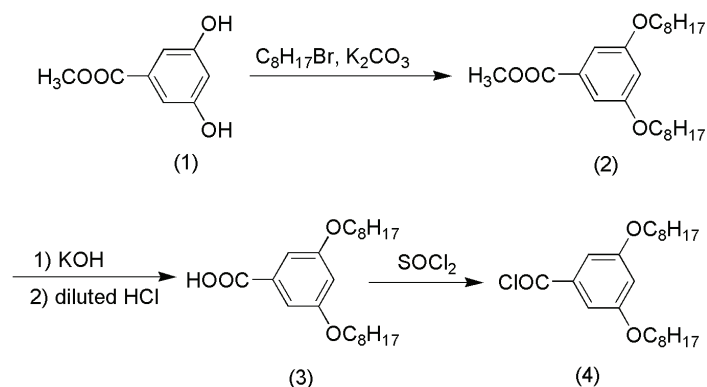
Scheme 1. Synthetic route to 3,5-dioctyloxybenzoyl chloride.

Methyl 3,5-dioctyloxybenzoate (2). Compound **1** (3.36 g, 20.0 mmol), anhydrous potassium carbonate (8.28 g, 60.0 mmol) and a catalytic amount of KI in acetone (150 ml) were refluxed for 0.5 h and then 1-bromooctane (9.6 g, 50 mmol) was added in the solution. The reaction mixture was gently refluxed for 36 h under an N$_2$ atmosphere. The resulting mixture was filtered to remove the impurities. The solution was evaporated to dryness. The solid remaining was recrystallized from methanol to obtain **2** (m.p. 32 °C; yield: 89 %).

3,5-Dioctyloxybenzoic acid (3). It was synthesized according to a method similar to that described in previous papers.[29,30] The product was recrystallized from ethanol (m.p. 53 °C; yield: 92 %).

3,5-Dioctyloxybenzoyl chloride (4). Compound **3** (3.78 g, 10.0 mmol) was dissolved in 20 ml thionyl chloride. The solution was refluxed for 12 h and then the solvent was evaporated using a water vacuum pump.

Synthesis of the ligand 5,10,15,20-tetrakis[4-(3,5-dioctyloxybenzamido)phenyl]porphyrin (7a)

A mixture of TAPPH$_2$ (1.2 g, 1.8 mmol) and 3,5-dioctoxybenzoyl chloride (3.96 g, 10.0 mmol) was dissolved in 150 ml freshly distilled CHCl$_3$ and then 3 ml triethylamine was added into the system. The mixture was stirred at room temperature for 2 h, then refluxed for 10 h and cooled to room temperature. The resulting mixture was poured into 150 ml distilled water,

extracted four times with freshly distilled chloroform and then dried over anhydrous magnesium sulfate. The solvent was removed on a rotary evaporator. The residue was further purified by column chromatography (silica gel); the eluent was chloroform followed by chloroform/ethanol=50:1 (v:v). The first band was collected and evaporated to dryness to give a purple solid, which was further recrystallized from chloroform/methanol.
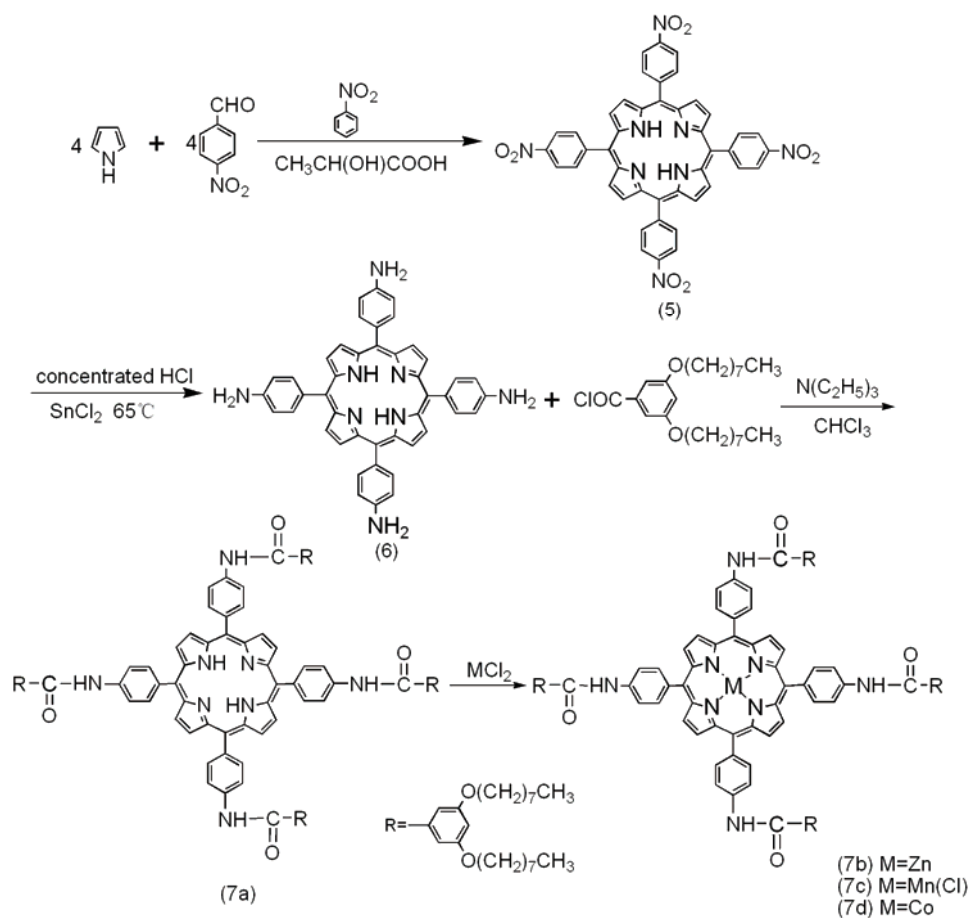
Scheme 2. Synthetic route to the porphyrin ligand and its metal complexes.

*Synthesis of zinc 5,10,15,20-tetrakis[4-(3,5-dioctyloxybenzamido)phenyl]porphyrin (**7b**)*

Compound **7a** (80 mg) and $ZnCl_2$ (100 mg) were dispersed in a mixture of $CHCl_3$ and methanol (2:1). The reaction mixture was refluxed for about 1.5 h. The progress of the reaction was monitored by measuring the UV–Vis spectrum of the reaction solution. The resulting mixture was washed with saturated aqueous NaCl solution and then concentrated. The product was purified by column chromatography on silica gel; eluent: $CHCl_3/C_2H_5OH$, 10:1 (v:v). The second band was collected, dried under vacuum to give a purple red solid.

*Synthesis of manganese 5,10,15,20-tetrakis[4-(3,5-dioctyloxybenzamido)phenyl]porphyrin (**7c**)*

Complex **7c** was prepared by reaction of **7a** (100 mg) with MnCl$_2$·4H$_2$O (120 mg) in a mixture of freshly distilled CHCl$_3$ (10 ml) and dried DMF (15 ml) at 70 °C under an N$_2$ atmosphere for about 4 h. The progress of the reaction was also monitored by measuring the UV–Visible spectrum of the reaction mixture. After completion of the reaction, the resulting mixture was cooled, extracted several times with CHCl$_3$ and distilled water. Then the solvent was removed to dryness, and the product was chromatographed on a silica gel column using the eluent CHCl$_3$/C$_2$H$_5$OH 10:1 (v:v).

*Synthesis of cobalt 5,10,15,20-tetrakis[4-(3,5-dioctyloxybenzamido)phenyl]porphyrin (**7d**)*

Compound **7d** was synthesized in a similar manner to that described for **7c**.

Characterization

The ^{1}H-NMR spectra were acquired on a Varian Unity-500 (MHz) NMR spectrometer using standard pulse sequences. The spectra were recorded at 298 K in CDCl$_3$, unless otherwise stated. Chemical shifts are reported on the δ scale relative to TMS. Elemental analyses were performed on a Perkin-Elmer 240 C auto elementary analyzer. The infrared spectra were obtained using a Nicolet 5PC-FT-IR spectrometer in the region of 4000–400 cm^{-1}. The electronic absorption spectra were measured with a Shimadzu UV-3000 spectrometer. Steady-state emission measurements were obtained on a Shimadzu RF-5301PC fluorescence spectrometer with both the excitation and emission slit set at 5 nm. The resonance Raman (RR) spectra were obtained using a Renishaw inVia microscopic instrument. Radiation of 514.5 nm was obtained from an Ar$^+$ laser. The chemical composition of the surface was investigated by X-ray photoelectron spectroscopy using an ESCALAB Mark II spectrometer.

CONCLUSIONS

In this study, a novel *meso*-tetrakis[4-(3,5-dioctyloxybenzamido)phenyl]porphyrin and its transition metal complexes were synthesized and characterized. Their properties were clearly influenced by the nature of the central transition metal ions. Compared with the porphyrin ligand, the number of the electronic absorption bands of the complexes decreased and exhibited some shifts. The fluorescence results showed that the transition metal in the central porphyrin ring quenched the fluorescence of porphyrin. From the XPS spectra, the information concerning the character of the chemical bonding in the porphyrin ligand and its complexes was obtained. In addition, the investigation could provide very useful information for further study of these derivatives.

ИЗВОД

СИНТЕЗА И СВОЈСТВА 5,10,15,20-ТЕТРАКИС[4-(3,5-ДИОКТИЛОКСИБЕНЗАМИДО)-ФЕНИЛ]ПОРФИРИНА И ЊЕГОВИХ МЕТАЛНИХ КОМПЛЕКСА

WENHUI LIAN, YUANYUAN SUN, BINBIN WANG, NING SHAN и TONGSHUN SHI

College of Chemistry, Jilin University, Changchun 130023, P. R. China

Приказан је нови 5,10,15,20-тетракис[4-(3,5-диоктилоксибензамидо)фенил]порфирин и његови комплекси са прелазним металима. Молекулске структуре окарактерисане су елемен-

талном анализом као и IR, ^{1}H-NMR и UV–Vis спектрима. Спектроскопска својства проучавана су раманском, флуоресцентном и фотоелектронском спектроскопијом X-зрачења (XPS). Квантни флуоресцентни приноси одређивани су на собној температури. Нађено је да је интензитет флуоресценције за порфирински лиганд већи него за комплекс. Уочена је и већа разлика између раманских спектара порфиринског лиганда и његових комплекса, што потиче од симетрије порфиринске равни. Из XPS спектара произилази да замена протона металним јоном у формирању метал-порфирина повећава молекулску симетрију и уводи у центар порфирина електрон-привлачну групу, што повећава N_{1s} енергију везивања.

REFERENCES

1. G. A. Bogdanovic, V. Medakovic, M. K. Milcic, S. D. Zaric, *Int. J. Mol. Sci.* **5** (2004) 174
2. P. I. Premović, I. R. Tonsa, D. M. Đorđević, M. S. Pavlović, *J. Serb. Chem. Soc.* **65** (2000) 113
3. R. K. Lammi, A. Ambroise, T. Balasubramanian, R. W. Wagner, D. F. Bocian, D. Holten, J. S. Lindsey, *J. Am. Chem. Soc.* **122** (2000) 7579
4. C. M. Drain, X. Chen, *Encyclopedia of Nanoscience & Nanotechnology*, American Scientific Press, New York, 2004, pp. 593–616
5. F. Remacle, S. Speiser, R. D. Levine, *J. Phys. Chem., B* **105** (2001) 5589
6. P. Bhyrappa, G. Vaijayanthimala, B. Verghese, *Tetrahedron Lett.* **43** (2002) 6427
7. C. M. Drain, I. Goldberg, I. Sylvain, A. Falber, *Top. Curr. Chem.* **245** (2005) 55
8. R. H. Jin, *Chem. Commun.* (2002) 198
9. D. M. Chen, T. J. He, D.-F. Cong, Y.-H. Zhang, F.-C. Liu, *J. Phys. Chem., A* **105** (2001) 3981
10. C. Y. Lin, T. G. Spiro, *Inorg. Chem.* **35** (1996) 5237
11. A. Rienzo, L. C. Mayor, G. Magnano, C. J. Satterley, E. Ataman, *J. Chem. Phys.* **132** (2010) 084703
12. M. H. Qi, G. F. Liu, *Solid State Sci.* **6** (2004) 287
13. D. M. Chen, Y. H. Zhang, T. J. He, F. C. Liu, *Spectrochim. Acta, A* **58** (2002) 2291
14. M. B. Lan, H. L. Zhao, H. H. Yuan, C. R. Jiang, S. H. Zou, Y. Jiang, *Dyes Pigm.* **74** (2007) 357
15. W. Liu, Y. H. Shi, T. S. Shi, *Chem. J. Chin. Univ.* **24** (2003) 200
16. X. Zhang, Y. Li, D. Qi, J. Jiang, X. Yan, Y. Bian, *J. Phys. Chem., B* **114** (2010) 13143
17. S. S. Song, D. M. Li, J. F. Wu, C. F. Zhuang, H, Ding, *Eur. J. Inorg. Chem.* (2007) 1844
18. B. D. Stasio, C. Frochot, D. Dumas, P. Even, J. Zwier, F. Guillemin, M. L. Viriot, M. Barberi-Heyob, *Eur. J. Med. Chem.* **40** (2005) 1111
19. G. S. S. Saini, *Spectrochim. Acta, A* **64** (2006) 981
20. F. Paulat, V. K. K. Praneeth, C. Nather, N. Lehnert, *Inorg. Chem.* **45** (2006) 2835
21. I. Halvorsen., E. Steene., A. Ghosh, *J. Porphyrins Phthalocyanines* **5** (2001) 721
22. P. M. Kozlowski, A. A. Jarzecki, P. Pulay, X. Y. Li, M. Z. Zgierski, *J. Phys. Chem.* **100** (1996) 13885
23. J. M. Gottfried, K. Flechtner, A. Kretschmann, T. Lukasczyk, H. P. Steinruck, *J. Am. Chem. Soc.* **128** (2006) 5644
24. N. Nishimura, M. Ooi, K. Shimazu, H. Fujii, K. Uosaki, *J. Electroanal. Chem.* **473** (1999) 75
25. D. K. Sarkar, X. J. Zhou, A. Tannous, M. Louis, K. T. Leung, *Solid State Commun.* **125** (2003) 365
26. M. Lu, B. Chen, T, He, J. M. Tour, *Chem. Mater.* **19** (2007) 4447

27. B. K. Zhu, Z. K. Xu, *Chin. J. Appl. Chem.* **16** (1999) 68
28. W. J. Kruper, T. A. Chamberlin, M. Kochanny, *J. Org. Chem.* **5**4 (1989)
29. T. Ohtake, M. Ogasawara, K. Ito-Akita, N. Nishina, S. Ujiie, H. Ohno, T. Koto, *Chem Mater.* **12** (2000) 782
30. M. Lehmann, R. I. Gearba, M. H. J. Koch, D. A. Ivanov. *Chem. Mater.* **16** (2004) 374.

Variation of ratio kinetic profiles as a simple and novel spectrophotometric method for the simultaneous kinetic analysis of binary mixtures

ABDOLHOSSEIN NASERI[1]* and SHOKOOFEH MALAKZADEH-ROUSTA[2]

[1]*Department of Analytical Chemistry, Faculty of Chemistry, University of Tabriz, 51666-16471, Tabriz and* [2] *Department of Chemistry, Faculty of Science, Islamic Azad University, Tabriz Branch, Tabriz, Iran*

Abstract: In this paper, a new and very simple kinetic – spectrophotometric method is developed for the simultaneous determination of binary mixtures without prior separation steps. The method is based on the calculation of the variation of ratio kinetic profiles. The mathematical explanation of the procedure is also illustrated. The proposed method can be used for the simultaneous determination of two analytes A and B that react with the same reagent to give the same absorbing species. In order to evaluate the applicability of the method, theoretical and experimental data were tested. The results from experimental data relating to the simultaneous spectrophotometric determination of Co(II) and V(IV) based on their oxidation reactions with Fe (III) in the presence 1,10-phenanthroline (Phen) in micellar media are presented as a real model for the resolution of the binary systems. The applicability of the method to tap water and synthesized alloy samples was also assessed by spiking experiments with different amounts of Co(II) and V(IV).

Keywords: kinetic analysis; binary mixture; variation of ratio kinetic profiles; spectrophotometry.

INTRODUCTION

The spectrophotometric analysis of multicomponent mixtures shows that the quantification of compounds continues to be a difficult problem when there is no spectral difference between the components. Kinetic – spectrophotometric methods are good alternatives in such cases.[1] A number of differential kinetic methods have been developed for resolving mixtures of analytes with similar or identical spectra that cannot be resolved by equilibrium-based methods.[2–5] The simultaneous kinetic determination of such analytes is usually based on the diffe-

---

349

rence in their reaction rate constants. The difference between the rate constants must be large enough for differential kinetic methods to discriminate the rate constants and for a successful handling of the univariate data.[6] However, in cases where the sample matrix is complex or the analytes are present at low concentration levels, their reaction rates might be very similar and their similar chemical properties result in mutual interference. Under such conditions, the selectivity of the univariate approach is very low and the prediction is poor.[7]

Recently, different two-way and three-way chemometric methods were used for multicomponent determination using kinetic – spectrophotometric data.[8–10] Chemometric methods have been used for the determination of different analytes and several reviews have been published on the subject.[11–13] However, the development of a simple method is very important. Afkhami and Bahram developed a new method for the simultaneous determination of binary mixtures of analytes with different kinetic profiles. The method is based on the mean centering (MC) of ratio kinetic profiles.[7]

Bosch-Reig *et al.* established the fundamentals for the application of the H-point standard addition method (HPSAM) to kinetic data,[14] for the simultaneous determination of binary mixtures or for the calculation of analyte concentrations completely free from bias errors. For these purposes, there are two variants of the HPSAM. One is applied when the reaction of one component is faster than that of the other or when the latter does not occur at all; this variant of the method is based on the assumption that only analyte X evolves with time and the other species Y or interferents do not evolve with time or have the same absorbance over the study interval. The other variant of the method is used when the rate constants of the two components are time-dependent. In this case, the two species in a mixture of X and Y evolve with time, c_X (concentration of analyte) and A_Y (the absorbance of the interferent) can be calculated by plotting the analytical signal ΔA_{t1-t2} against the added concentration of X at two wavelengths λ_1 and λ_2. The absorbances of the Y component provided at these two wavelengths are the same (A_Y), and, thus, so are the ΔA_{t1-t2} values.[14–16] However, when X and Y react with the same reagent to give the same absorbing species, this variant of HPSAM cannot be applied.

So far, a considerable amount of research effort has been devoted towards introducing and exploiting the concept of variation for analyzing kinetic systems.[17,18] The variation of signals is obtained by subtracting the zero-point signal (first signal) from each signal at each time. The contribution of inert compounds, compounds with constant signal over a period of time, can be easily removed in the calculation of variation. This approach can be useful for eliminating the interference from signal-stable components.

In the present work, variation of the ratio profiles was used for binary kinetic profiles resolution as well as the simultaneous determination of binary mixtures.

The mathematical explanation of the procedure is also demonstrated. After a modeling procedure, the method was successfully applied to the simultaneous analysis of binary mixtures of cobalt and vanadium based on their oxidation reactions with Fe(III) and 1,10-phenantroline in micellar media without any preliminary separation. The resolution procedure was based on the reaction rate differences.

EXPERIMENTAL

Apparatus and software

The absorption measurements were realized on a Shimadzu UV-1650 PC spectrophotometer, using 1.0 cm quartz cells. All spectra were saved in ASCII format and transferred to a PC computer for subsequent manipulation. The data were handled using Microsoft Excel and Matlab software (version 7.1).

Reagents and solutions

All experiments were performed with analytical grade chemicals and doubly distilled water. A stock Fe(III) solution (7.14×10^{-3} mol dm^{-3}) was prepared by dissolving 0.144 g of Fe(NO$_3$)$_3 \cdot$9H$_2$O (Merck) in water and diluting to 50 ml. Stock solutions of Co(II) (1.69×10^{-3} mol dm^{-3}) and V(IV) (1.96×10^{-3} mol dm^{-3}) were prepared by dissolving appropriate amounts of Co(NO$_3$)$_6 \cdot$4H$_2$O and VOSO$_4 \cdot$5H$_2$O (Merck), respectively, in water. A stock solution of 1,10-phenantroline (0.04 mol dm^{-3}) was prepared by dissolving 0.369 g of the hydrochloride form of the compound in 2–3 ml ethanol in a 50 ml volumetric flask and dilution to the mark with double-distilled water. Acetate buffer solution (0.1 mol dm^{-3}) of pH 3.5 was prepared from sodium acetate and acetic acid. A cetyl trimethyl ammonium bromide (CTAB) stock solution (0.05 mol dm^{-3}) was prepared by dissolving 0.456 g of the compound in double-distilled water.

Procedure

The proposed method was used for the simultaneous determination of cobalt and vanadium based on the different rates of their oxidation reaction with Fe(III) in the presence of 1,10-phenanthroline (phen) in micellar media without any preliminary separation.

Two ml buffer solution (pH 3.5), 0.50 ml of Phen stock solution, 0.2 ml of CTAB stock solution, 1.0 ml of Fe(III) and appropriate volumes of V(IV) and Co(II) were added to a 5.0 ml volumetric flask and made up to the mark with water. For each measurement, about 2.0 ml of the above solution was transferred to a spectrophotometric cell and the kinetic profile *vs.* time was recorded at 510 nm in the time range 10–300 s.

RESULTS AND DISCUSSION

Theoretical background

Consider two analytes, X and Y, that react with the same reagent to give the same absorbing species, P, according to the following scheme:

$$X + R \xrightarrow{\ k_X\ } P \tag{1}$$

$$Y + R \xrightarrow{\ k_Y\ } P \tag{2}$$

$$\frac{d[P]}{dt} = k_X c_X + k_Y c_Y \tag{3}$$

where, k_X, k_Y and c_X, c_Y are the rate constants and concentrations for X and Y, respectively.

The formation of the product, P, can be monitored by recording its absorption spectrum as a function of time or by measuring the absorbance at a fixed wavelength. It is assumed that the reactions involved in both processes follow first or pseudo-first order kinetics with respect to the concentrations of the analytes. If the absorbance is assumed proportional to the amount of formed product, then, in the absence of interactions, between the kinetics of both analytes, it will be given by:

$$A_t = \varepsilon \sum_i E_{(i,t)} c_i^0 \tag{4}$$

where, c^0 is the initial concentration of the specie i to be quantified for first-order reactions and E is the kinetic profile, which can be given as:

$$E_{(i,t)} = \varepsilon(1 - \exp(-k_i t)) \tag{5}$$

By analogy between $E_{(i,t)}$ and the molar absorptivity in the Beer–Lambert Law in spectrophotometric determinations, the variation of the absorbance as a function of time at a given wavelength can be used to construct a "kinetic profile", A_{t1}, A_{t2},..., A_{tn} at times t_1, t_2,..., t_n.

For a binary mixture of X and Y, if Eq. (4) is divided by $E_{Y(t)}$, corresponding to the kinetic profile of a standard solution of Y in a binary mixture, the ratio profile (R) is obtained in the form of Eq. (6) (to enable the dividing operation, zero values of $E_{Y(t)}$ should not be used in the divisor):

$$R = \frac{A_{(t)}}{E_{Y(t)}} = \frac{E_{X(t)} C_X}{E_{Y(t)}} + C_Y \tag{6}$$

where $E_{X(t)}$ and $E_{Y(t)}$ are the kinetic profiles of X and Y, respectively. If the variation of R is calculated (by subtracting the zero-point signal (first signal) from each signal at each time), since the variation of a constant C_Y is zero, Eq. (7) is obtained:

$$\mathrm{Var}(R) = \mathrm{Var}\left(\frac{E_{X(t)} C_X}{E_{Y(t)}} \right) \tag{7}$$

Equation (7) is the mathematical foundation of the multi-component analysis that enables the determination of the concentration of each of the active compounds in the solution (X in this equation) without interference from the other compound of the binary system (Y in these equations). As Eq. (7) shows, a linear relation exists between the magnitude of Var(R) and the concentration of X in the solution.

A calibration curve can be constructed by plotting Var(R) against the con-centration of X in standard solutions of X or in standard binary mixtures. For more sensitivity, the magnitude of Var(R) corresponding to maximum time can be measured.

Calibration graphs for Y are constructed as described for X.

Simulations

With the view of evaluating the performance of the proposed method for the analysis of a binary mixture, several sets of synthetic data were created to model the spectrophotometric data of two kinetic reactions (X and Y) with overlapping kinetic profiles (Fig. 1A). The use of simulated data enabled the effect of each variable on the performance of the considered method to be determined. The data were generated under a known model, *i.e.*, a first order kinetic reaction, and arti-ficial noise was added. The kinetic profiles were created for six different samples with different concentrations of X, shown in Fig. 1B. The ratio profiles were ob-tained were obtained by dividing the kinetic profiles of the samples by the kinetic profile of B (Fig. 1C). Then, the variation of the ratio profiles was obtained by subtraction of the magnitude of the first point from the magnitude at each time (Fig. 1D). Finally, the concentration of compound X was determined by measur-ing the magnitude of the resulting profiles at 300 s, corresponding to the maxi-mum on the time profile shown in Fig. 1D.

The obtained model can be validated with a series of 8 synthetic mixtures, containing the considered concentrations of components X and Y in different proportions those are randomly selected. The kinetic profiles of these samples are created (Fig. 2A). To predict the concentration of compound X in these synthetic binary mixtures, the kinetic profiles of the binary mixtures are divided by kinetic profile of Y, whereby the ratio profiles are obtained (Fig. 2B). Finally, variations of ratio profiles for these mixtures are obtained (Fig. 2C). In this step, the effect of the compound Y is removed from the profiles of the mixtures. The concentra-tion of X in these synthetic mixtures was determined by measuring the magnitude at 300 s, corresponding to the maximum in the time profile. Plotting the actual *vs.* the predicted concentration of analyte in eight mixture samples was used to show the average error analysis and the quality of all data to a straight line (Fig. 2D). As can be seen, good agreement between both the actual and predicted concen-trations is evident. The results unveil the applicability of the method for sample mixtures.

Preliminary study of the system

1,10-Phenanthroline (Phen) is frequently used for the spectrophotometric de-termination of bivalent iron.[19] In the presence of 1,10-phenanthroline, Fe(III) be-comes a stronger oxidant and can easily oxidize some metal cations. The reduced
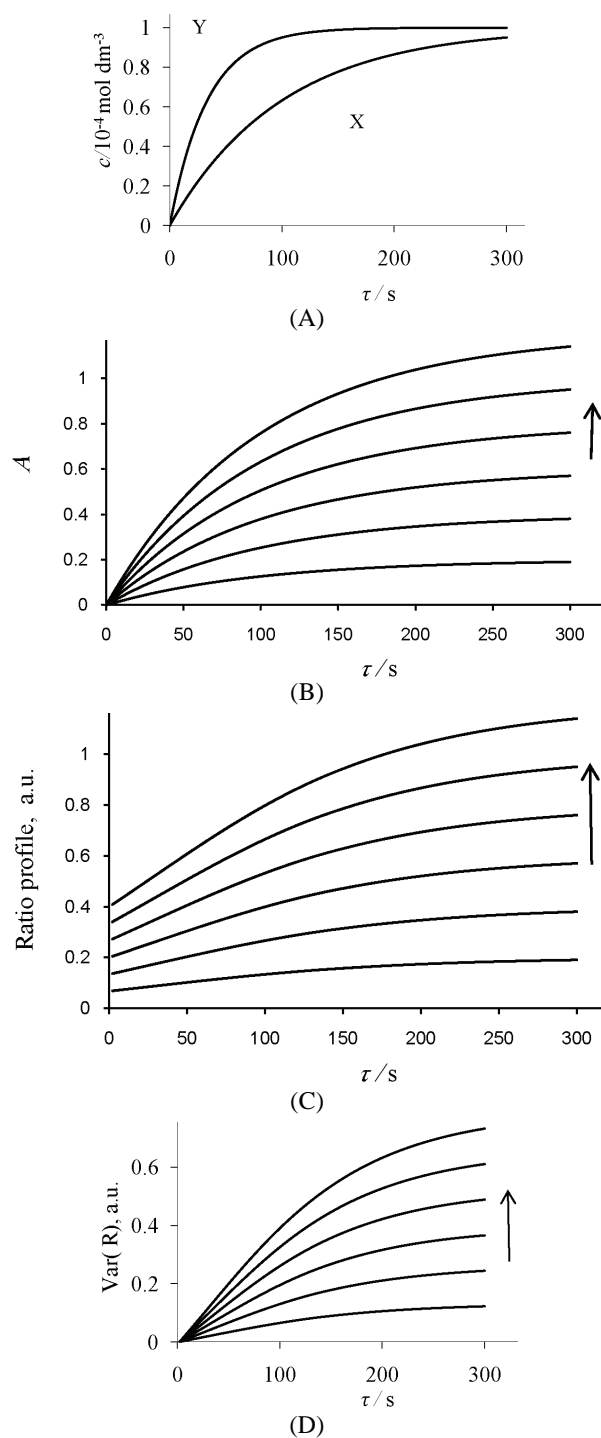
Fig. 1. The simulated pseudo-first order kinetic profiles of compounds X and Y (A), the simulated kinetic profiles of 2×10^{-5}–2×10^{-4} mol dm^{-3} of X (B), the ratio profiles that were obtained by dividing the kinetic profiles of X by the kinetic profile of Y (C), and variation of the ratio profiles (D).

(A)

(B)

(C)

(D)
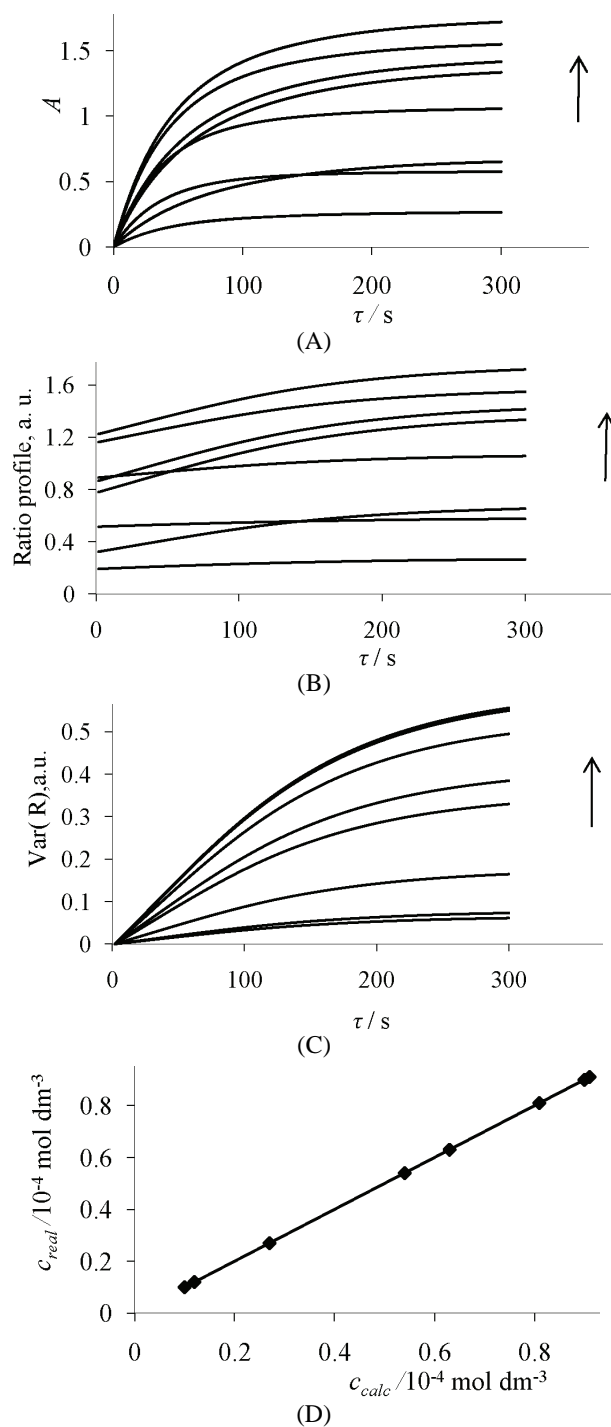
Fig. 2. The simulated kinetic profiles of randomly selected mixtures of X and Y (A), the ratio profiles that were obtained by dividing the kinetic profiles of the mixtures by the kinetic profile of Y (B), variation of the ratio profiles (C) and plots of the real values of concentration of X *vs.* the values found by proposed method (D).

product of the reaction, Fe (II), can form a colored complex with Phen. Its spectrum is shown in Fig. 3A. Thus, a visible spectrophotometric signal for the indirect monitoring the concentration of oxidizable analytes is formed.[20,21] Preliminary investigations showed that at pH 3.5 and 0.01 M cationic micellar solution of CTAB, V(IV) and Co(II) can be oxidized by Fe(III) in the presence of Phen at different rates. The common product in these reactions is the Fe(II)–Phen complex. The oxidation of V(IV) and Co(II) can be indirectly monitored by recording the absorbance at 510 nm, the λ_{max} of the Fe(II)–Phen complex. As Fig. 3B shows, the kinetic profiles of the oxidation reactions of Co(II) and V(IV) are different and hence can be used to their simultaneous determination.
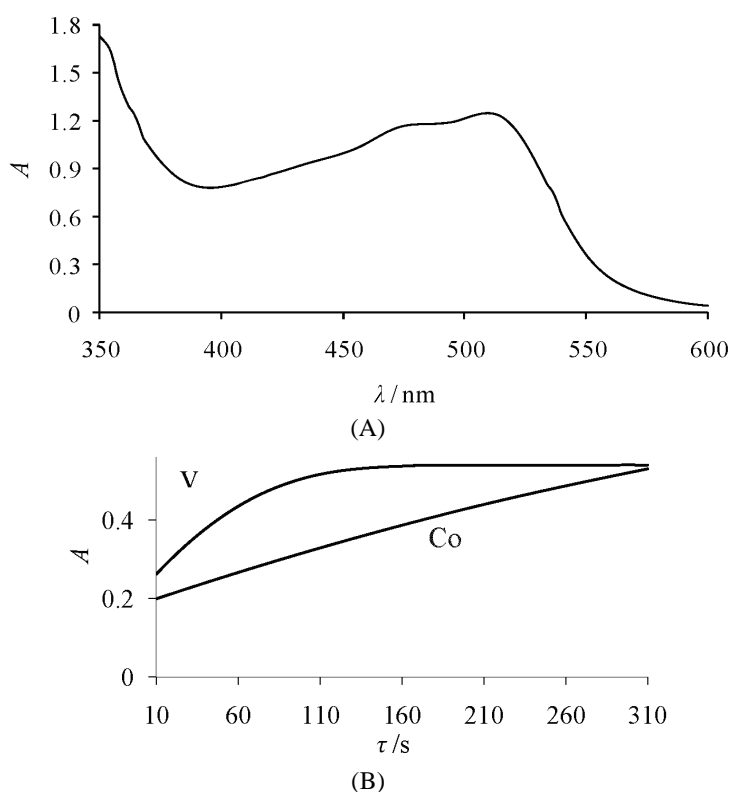
Fig. 3. Kinetic profiles of oxidation reaction of Co(II) (5×10^{-5} mol dm^{-3}) and V(IV) (5×10^{-5} mol dm^{-3}) with Fe(III) and Phen in micellar media, observed at 510 nm.

A 2×10^{-3} mol dm^{-3} Phen and 1.25×10^{-3} mol dm^{-3} Fe(III) solution (at least a 15-fold excess over the maximum concentration of the metal ions) was applied to obtain a pseudo-first order reaction with respect to the each of analyte concentrations.

Proposed method

The absorption kinetic profiles of standard Co(II) solutions of different concentrations were recorded at 510 nm in the time range 10–300 s (Fig. 4A) at 2 s
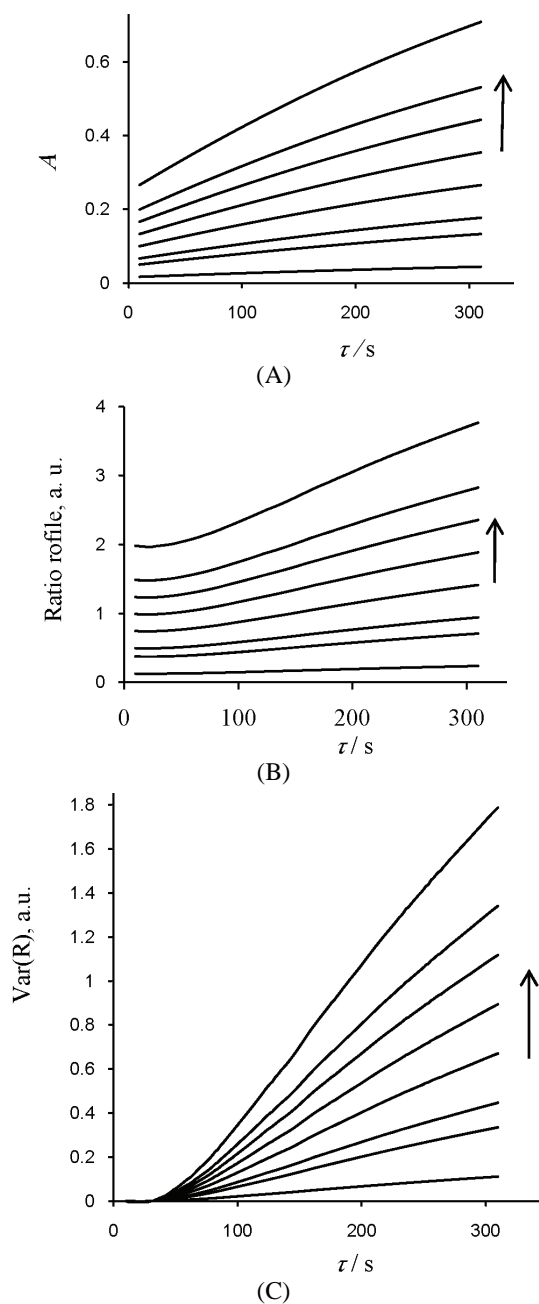
Fig. 4. The absorption kinetic profiles of standard solutions of Co(II) of different concentrations (A), the ratio profiles that were obtained by dividing the kinetic profiles of Co(II) by the kinetic profile of V(IV) (B) and the variation of the ratio profiles (C).

intervals and divided by the normalized kinetic profile of V(IV), whereby the ratio profiles were obtained (Fig. 4B). The variations of the ratio profiles were obtained by subtraction of the magnitude of the first point from all the other points of the ratio kinetic profile (Fig. 4C). The concentration of Co(II) was determined by measuring the magnitude at 300 s, corresponding to the maximum time shown in Fig. 4C. For the prediction of the concentration of Co(II) in synthetic binary mixtures and real samples, the same procedure was applied except that the kinetic profiles of the mixture were used instead of the kinetic profiles of a standard solution of Co(II).

For determination of V(IV) in the presence of Co(II), the same procedure was used except that the kinetic profiles were divided by the normalized kinetic profile of Co(II).

Analytical characteristics

Calibration curves of both components were obtained by plotting the magnitude of variation at 300 s against the concentration of the analytes and evaluation by linear regression. The characteristics of the calibration graph and the statistical parameters for determination of Co(II) and V(IV) are summarized in Table I.

TABLE I. Analytical characteristics of the analysis of Co(II) and V(IV) in binary mixtures by the proposed method

Analyte	Linear range mol dm^{-3}	Equation	Squared correlation coefficient (R^2)	Limit of detection (LOD) mol dm^{-3}
Co(II)	8.50×10^{-6}–1.35×10^{-4}	$Y = 1.30\times10^4 c + 0.0025$	0.9983	2.30×10^{-6}
V(IV)	9.80×10^{-6}–1.56×10^{-4}	$Y = 9.25\times10^3 c + 0.0063$	0.9958	4.11×10^{-6}

The model obtained in the calibration step was validated by the analysis by the proposed method of ten randomly selected synthetic mixtures containing different proportions of Co(II) and V(IV). The obtained results are given in Table II. The values of the root mean square difference (*RMSD*), the square of the correlation coefficient obtained when plotting the actual *vs.* the predicted concentrations (R^2), and the relative error of prediction (*REP*) for each component in the ten synthetic samples are included in Table II to show the average error in the analysis and the fitting quality of all data to a straight line.

Interference studies

For studying interferences, the influence of several ions was tested, including those that most frequently accompany Co(II) and V(IV) in real samples. The effect of interfering ions at different concentrations on the kinetic curve of the absorbance of a solution containing 5×10^{-5} mol dm^{-3} of each analyte was studied. An ion was considered as an interferent when its presence produced a variation in the absorbance of the sample greater than 5 %.

TABLE II. Statistical parameters of the analysis of Co(II) and V(IV) in the validation set by the proposed method ($RMSD = [(\text{sum}(c_{\text{real}}-c_{\text{found}})^2)/\text{sum}(c_{\text{found}})^2]^{1/2}$; $REP = 100\times$ $\times[(\text{sum}(c_{\text{real}}-c_{\text{found}})^2)/n]^{1/2}$; R^2: correlation coefficient for the plot of c_{real} *vs.* c_{found})

Parameter	Co(II)	V(IV)
Recovery, %	101.04	98.01
RMSD	0.08	0.15
REP	3.52	5.18
R^2	0.9941	0.9915

Among the interfering ions tested, Mn(II), Ni(II), V(V), As(V), Cu(II), Cd(II), Zn(II), Al(III), Bi(III), Ce(III), Te(IV), Se(IV), Se(VI), Pb(II), Na(I), K(I), Ca(II) and the anions HSO_3^-, SO_4^{2-}, SO_3^{2-}, F^-, Cl^-, CO_3^{2-}, MoO_4^{2-}, CH_3COO^-, NO_3^- and I^- did not interfere at concentrations 1000 times higher than those of the analytes. However, Sn(II) and Sb(III) interfered at levels similar to those of Co(II) and V (IV) as they can also be oxidized by the Fe(III) and Phen system. The kinetic profiles of the oxidation reaction of Sn(II) and Sb(III) with Fe(III) and Phen in micellar media are shown in Fig. 5.
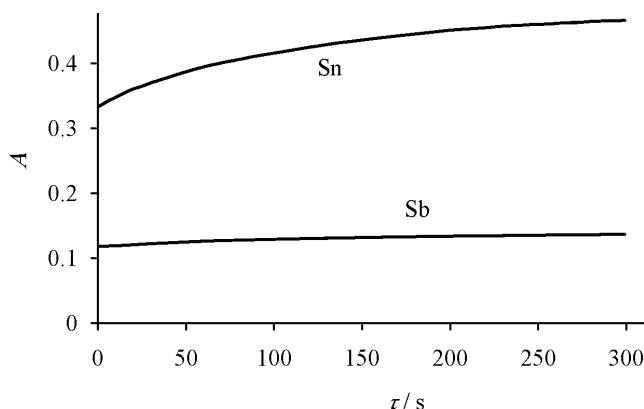
Fig. 5. Kinetic profiles of the oxidation reaction of Sn(II) and Sb(III) with Fe(III) and Phen in micellar media, observed at 510 nm.

Application

In order to assess the applicability of the proposed method, it was applied to the simultaneous determination of Co(II) and V(IV) in two samples: 1) a synthetic alloy sample and 2) tap water. The synthetic alloy sample contained Mn(II), Ni(II), V(V), Mo(VI), Al(III), Co(II) and V(IV). Moreover, the proposed method was applied for the simultaneous determination of Co(II) and Ni(II) in this synthetic sample. The results are given in Table III. The good agreement between the obtained results and known values indicate the successful application of the proposed method for simultaneous determination of Co(II) and Ni(II) in complex samples.

TABLE III. Statistical parameters of the analysis of Co(II) and V(IV) in real samples by the proposed method

Parameter	Co(II)		V(IV)	
	Synthetic alloy sample	Tap water	Synthetic alloy sample	Tap water
Recovery, %	104.21	102.14	106.31	97.62
RMSD	0.17	0.12	0.21	0.16
REP	3.67	2.09	6.75	5.58
R^2	0.9912	0.9938	0.9913	0.9926

Tap water samples were spiked with Co(II) and V(IV) and the proposed method was applied to determine the analytes. The accuracy of the proposed method was validated by a recovery method. As can be judged from Table III, the results can be considered acceptable.

CONCLUSIONS

A very simple and easy to understand method was proposed for resolving binary mixtures. Inert interferon (species having constant signal during the time range) do not interfere in the analysis. The proposed method is suitable for the analysis of binary mixtures with completely overlapping absorption spectra (same product formed in different reactions) that show a difference in their rate constants in a given reaction.

The proposed method is superior to other methods for the analysis of binary mixtures, namely: multivariate calibration methods (partial least square (PLS), net analyte signal (NAS) and artificial neural networks (ANN)) and the HPSAM. In comparison with multivariate calibration methods (PLS, NAS and ANN), the proposed method is simple, rapid and easy to understand and apply. In comparison with the HPSAM, the proposed method is simpler and more rapid and the presence of species with a constant absorbance at the measuring wavelength during the time of the experiment cannot interfere, while they interfere in the HPSAM. In addition, the proposed method eliminates the necessity of searching to find suitable wavelength. Furthermore, when both analytes react with the same reagent to give the same absorbing species but at different rates, the proposed method can be used for determining the analytes, whereas the HPSAM cannot be applied.

И З В О Д

ВАРИЈАЦИЈА ОДНОСА КИНЕТИЧКИХ ПРОФИЛА КАО ЈЕДНОСТАВАН
НОВИ СПЕКТРОФОТОМЕТРИЈСКИ МЕТОД ЗА СИМУЛТАНУ
КИНЕТИЧКУ АНАЛИЗУ БИНАРНИХ СМЕША

ABDOLHOSSEIN NASERI[1] и SHOKOOFEH MALAKZADEH-ROUSTA[2]

[1]*Department of Analytical Chemistry, Faculty of Chemistry, University of Tabriz, 51666-16471, Tabriz и* [2]*Department of Chemistry, Faculty of Science, Islamic Azad University, Tabriz Branch, Tabriz, Iran*

У раду је развијен нови једноставан кинетички спектрофотометријски модел за одређивање бинарних смеша, без њихове предходне сепарације. Метод је заснован на израчунавању промене односа кинетичког профила. Приказано је математичко објашњење процедуре. Предложени метод може бити коришћен за симултано одређивање два аналита, А и Б, који реагују са истим реагенсом а који даје исту абсорбујућу врсту. Да би се испитала применљивост методе, модел је тестиран експериментално. Експериментални резултати се односе на симултано одређивање Co(II) и V(IV) базирано на њиховој оксидацији са Fe(III) у присуству 1,10-фенантролина у мицеларном медијуму који представља реални модел за раздвајање бинарних система. Применљивост методе је оцењивана у узорцима воде за пиће и синтетисаним легурама који су имали различит садржај Co(II) и V(IV).

REFERENCES

1. M. Bahram, A. Afkhami, *J. Iran. Chem. Soc.* **5** (2008) 325
2. J. Zolgharnein, H. Abdollahi, D. Jafarifar, G. H. Azimi, *Talanta* **57** (2002) 1067
3. Y. Ni, C. Liu, S. Kokot, *Anal. Chim. Acta* **419** (2000) 185
4. M. J. C. Taylor, J. F. Van Staden, *Analyst* **119** (1994) 1263
5. Y. Ni, C. Liu, Chin. *J. Anal. Chem.* **27**(1999) 596
6. I. A. Pettas, M. I. Karayannis, *Anal. Chim. Acta* **491** (2003) 219
7. A. Afkhami, M. Bahram, *Anal. Chim. Acta* **526** (2004) 211
8. Y. L. Xie, J. J. Baeza-Baeza, G. Ramis-Ramos, *Chem. Intell. Lab. Syst.* **27** (1995) 211
9. Y. Ni, C. Huang, S. Kokot, *Anal. Chim. Acta* **599** (2007) 209
10. S. R. Crouch, J. Coello, S. Maspoch, M. Porcel, *Anal. Chim. Acta* **424** (2000) 115
11. Y. Ni, C. Huang, S. Kokot, *Anal. Chim. Acta* **480** (2003) 53
12. Y. Ni, Y. Wang, S. Kokot, *Talanta* **78** (2009) 432
13. A. Niazi, B. Jafarian, J. Ghasemi, *Spectrochim. Acta, A* **71** (2008) 841
14. F. Bosch-Reig, P. Campins-Falco, A. Sevillano-Cabeza, R. Herraez-Hernandez, C. Molins-Legua, *Anal. Chem.* **63** (1991) 2424
15. J. Zolgharnein, H. Abdollahi, D. Jafarifar, G. H. Azimi, *Talanta* **57** (2002) 1067
16. A. Safavi, H. Abdollahi, F. Sedaghatpour, S. Zeinali, *Anal. Chim. Acta* **409**(2000) 275
17. H. Abdollahi, S. M. Sajjadi, *J. Chemomet.* **23** (2009) 139
18. J. Jiang, S. Sasic, R. Yu, Y. Ozaki, *J. Chemomet.* **17** (2003) 186
19. W. A. E. McBryde, *A Critical Review of Equilibrium Data for Proton- and Metal Complexes of 1,10-Phenanthroline, 2,2'-Bypyridyl and Related Compounds*, Pergamon Press, Oxford, 1975
20. A. Safavi, H. Abdollahi, M. R. Hormozi Nezhad, *Spectrosc. Lett.* **35** (2002) 681
21. A. Safavi, H. Abdollahi, M. R. Hormozi Nezhad, *Talanta* **59** (2003) 515.

Excess molar volumes of 1,3-propanediol + (C₁–C₅) alkan-1-ols: application of a cubic equation of state

MOHAMMAD ALMASI* and LADAN KHOSRAVI

Department of Chemistry, Science and Research Branch, Islamic Azad University, Khouzestan, Iran

Abstract: The densities of binary mixtures consisting of methanol, ethanol, 1-propanol, 1-butanol and 1-pentanol with 1,3-propanediol were measured at the temperatures 293.15, 298.15, 303.15 and 313.15 K and at atmospheric pressure. Measurements were made over the full range of compositions and for the pure compounds using a vibrating tube densimeter. Excess molar volumes were obtained from these experimental results and were fitted to a Redlich–Kister type expansion. The results were interpreted in terms of molecular interactions and structural factors of the alcohols. It was observed that an increase in the carbon chain length of the alcohol led to lower interactions on mixing. The Peng–Robinson–Stryjek–Vera (PRSV) Equation of state was used to correlate the binary excess molar volumes.

Keywords: excess molar volumes; 1-alkanols; 1,3 propanediol; cubic EOS.

INTRODUCTION

Volumetric properties of mixtures are of interest from both theoretical and engineering points of view. These properties depend not only on solute–solute and solvent–solvent interactions, but also on the interstitial accommodations of unlike molecules arising from differences in molar volume and free volume of the solution components.[1]

Some useful information can be derived from density data, such as excess molar volumes and partial molar volumes. In addition, densities for mixtures at different temperatures are required for engineering design and for the succeeding operations.

The Peng–Robinson–Stryjek–Vera (PRSV) cubic equations of state (CEOS) were applied to predict the binary excess molar volumes[2,3] in combination with simple mixing rules. Although EOS are quite valuable tools for correlation and/or predictive purposes, in practice they are not the most useful for determining fluid

---

363

properties at a microscopic level.[4] The necessary data for calculations with the PRSV EOS are the critical properties, fitting parameters and the Pitzer acentric factor of the pure substances,[5] which can be estimated in the lack of experimental information.

In continuation of prior investigations,[6–8] the present paper reports the excess molar volumes of methanol, ethanol, 1-propanol, 1-butanol and 1-pentanol with 1,3-propanediol over the entire composition interval at temperatures ranging from 293.15 to 313.15 K, with the aim of analyzing the influence of temperature and chain length of the alkanols on the excess molar volumes.

EXPERIMENTAL

1,3-Propanediol, methanol, ethanol, 1-propanol, 1-butanol and 1-pentanol, were purchased from Merck with mass fraction higher than 99 %, and used without further purifications.

The densities of the pure compounds and mixtures were measured by an Anton Parr DMA 4500 instrument, provided with automatic viscosity correction. The uncertainty of the density measurements was estimated to be better than $\pm 1 \times 10^{-5}$ g cm^{-3}. The apparatus was calibrated daily with dry air and bidistilled water. The temperature in the cell was regulated to ± 0.01 K with a solid-state thermostat. The mixtures were prepared by weighing known masses of pure liquids in airtight, narrow-mouth ground stoppered bottles taking due precautions to minimize evaporation losses. All of the mass measurements were performed on an electronic balance (model Mettler AE 163, Switzerland) accurate to 0.01 mg. The uncertainty in the mole fraction was estimated to be $\pm 1 \times 10^{-4}$.

RESULTS AND DISCUSSION

The experimental densities of the pure materials are presented at various temperatures in Table I-S of the Supplementary material, along with corresponding literature values.[9–12]

The excess molar volumes of the solutions of molar composition x, measured at the temperatures 293.15, 298.15, 303.15 and 313.15 K were calculated from the densities of the pure liquids and their mixtures according to following equation:

$$V_m^E = \sum_{i=1}^{N} x_i M_i (\rho^{-1} - \rho_i^{-1}) \tag{1}$$

where ρ is the density of the mixture, ρ_i is the density of pure component i, x_i is the mole fraction, M_i is the molar mass of component i, and N stands for the number of components in the mixture.

The corresponding V_m^E values of binary mixtures of 1,3-propanediol (1) + alkanols (2) plotted against the mole fraction of 1,3-propanediol at 298.15 K are presented in Fig. 1. The excess molar volumes of 1,3-propanediol with methanol at 298.15 K are compared literature values[13] in Fig. 2. The discrepancy between experimental data and the literature values may be due to the viscosity correction

on the density measurements in the vibrating tube density meter. The employed instrument has an automatic viscosity correction. The values of densities and excess molar volumes for binary mixtures, at different temperatures are reported in Table II-S in the Supplementary material. Each set of results was fitted using a Redlich–Kister polynomial,[14] which for binary mixtures is:

$$Y^E = x_1(1-x_1) \sum_{k=0}^{N} A_k (1-2x_1)^k \qquad (2)$$

where $Y^E \equiv V_m^E$ and x_1 is the mole fraction of 1,3-propanediol. A_k is an adjustable parameter obtained by the least-squares method and k is the degree of the polynomials. In each case, the optimum number of coefficients was ascertained from an examination of the variation of standard deviation σ. The values of the parameter A_k together with the standard deviation σ are presented in Table I.
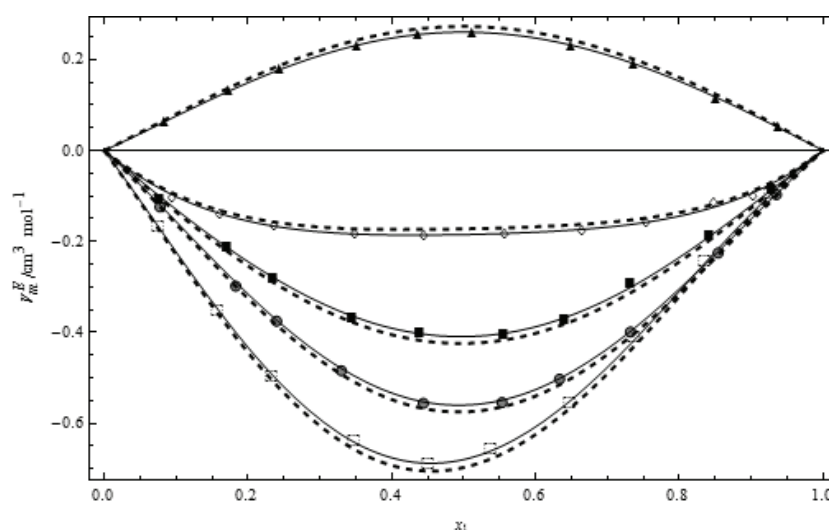
Fig. 1. Excess molar volumes, V_m^E, vs. mole fraction of 1,3-propanediol for binary mixtures of 1,3-propanediol with ( ) methanol, (●) ethanol, (■) 1-propanol, (◊) 1-butanol, (◄) 1-pentanol at 298.15 K. (——) Redlich–Kister Equation, (---) PRSV CEOS. The numerical data for this Figure as well as for all systems at all the studied temperatures are given in Table II-S of the Supplementary Material to this paper.

Over the whole composition range, the values of V_m^E for the binary mixtures of methanol, ethanol, 1-propanol and 1-butanol with 1,3-propanediol are negative but the values of V_m^E for the 1-pentanol 1 + 1,3-propanediol mixtures are positive. It is obvious from Fig. 1 that the V_m^E values generally increase with increasing size of the alcohol molecules.

The magnitude and sign of V_m^E are the consequence of interactions occurring in the mixture at different temperatures. It is known that pure alkanols can form

ALMASI and KHOSRAVI

either ring- or chain-like complexes,[15] and while the fraction of ring complexes increases with the number of –CH$_2$ groups in the alkanols, the degree of association decreases. The associated rings break down to chains with increasing temperature, which is then followed by a total break down of the associated species.[16]
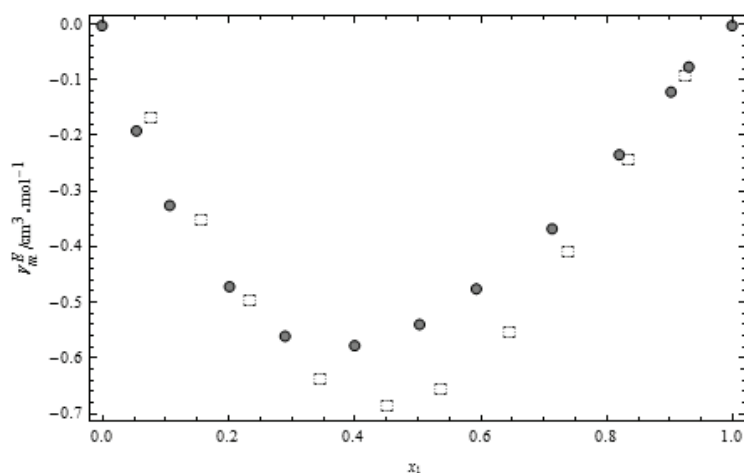
Fig, 2. Excess molar volumes, V_m^E, vs. mole fraction of 1,3-propanediol with methanol at 298.15 K; this work – □, Ref. 13 – ●.

TABLE I. Coefficients A_j and standard deviations, σ, for 1,3-propanediol (1) + alkanols (2) at various temperatures

T / K	A_0	A_1	A_2	σ
1,3-propanediol + methanol				
293.15	−2.896	−0.610	1.043	0.008
298.15	−2.721	−0.639	1.111	0.005
303.15	−2.508	−0.517	0.751	0.006
313.15	−2.344	−0.467	0.703	0.005
1,3-propanediol + ethanol				
293.15	−2.307	−0.061	0.635	0.005
298.15	−2.236	−0.065	0.829	0.002
303.15	−2.072	0.033	0.860	0.004
313.15	−1.874	0.0292	0.778	0.005
1,3-propanediol + 1-propanol				
293.15	−1.706	−0.047	0.223	0.004
298.15	−1.632	−0.041	0.380	0.004
303.15	−1.521	−0.040	0.581	0.002
313.15	−1.379	0.019	0.529	0.003
1,3-propanediol + 1-butanol				
293.15	−0.767	−0.041	−0.728	0.003
298.15	−0.742	−0.059	−0.549	0.005
303.15	−0.712	−0.052	−0.387	0.003
313.15	−0.693	−0.036	−0.200	0.002

TABLE I. Continued

T / K	A_0	A_1	A_2	σ
1,3-propanediol + 1-pentanol				
293.15	0.979	–0.085	–0.479	0.003
298.15	1.047	–0.019	–0.277	0.002
303.15	1.143	0.040	0.042	0.002
313.15	1.234	0.071	0.476	0.001

The observed negative V_m^E values for the methanol, ethanol, 1-propanol and 1-butanol with 1,3-propanediol mixtures are due to the formation of hydrogen bonding between unlike molecules, resulting in a decrease in the volume of the mixture. Another negative contribution to V_m^E comes from structural contributions that arise from the geometrical fitting of one component into the other components.[17] The positive V_m^E values for 1-pentanol + 1,3-propanediol system indicate a loose packing of the molecules in the mixtures, *i.e.*, dilatation occurs. Most likely, in this case, the different molecular sizes and shapes of 1,3-propanediol and 1-pentanol and steric hindrance between them, play important roles. Simultaneously, it seems that the disruption of hydrogen-bonded structures upon mixing should also be taken into account. The excess molar volumes increased with increasing temperature for all of the studied systems over the whole composition range. This can be expected since hydrogen bonds are more easily broken at higher temperatures. V_m^E at equimolar concentrations of 1,3-propanediol increases from methanol up to 1-pentanol, as the length of the alkanol chain increases.

PRSV CEOS

The general two-parameter CEOS has the form:

$$P = \frac{RT}{V-b} - \frac{a(T)}{(V+ub)(v+wb)} \tag{3}$$

where the EOS-dependent constants u and w for the Peng–Robinson–Stryjek––Vera Equation applied herein are: $u = 1 - \sqrt{2}$ and $w = 1 + \sqrt{2}$. For the pure substance, the energy a_i and co-volume b_i parameters of van der Waals are determined by the following set of equations:

$$a_i(T) = 0.457235 \frac{(RT_{ci})^2}{P_{ci}} [1 + m_i(1 - T_{ri}^{0.5})]^2 \tag{4}$$

$$b_i = 0.07779 \frac{RT_{ci}}{P_{ci}} \tag{5}$$

$$m_i = k_{0i} + k_{1i}(1 + T_{ri}^{0.5})(0.7 - T_{ri}) \tag{6}$$

$$k_{0i} = 0.378893 + 1.4897153\omega_i - 0.1713848\omega_i^2 + 0.0196554\omega_i^3 \tag{7}$$

where R is the gas constant, T_{ci} and P_{ci} are the critical temperature and pressure of component i, respectively, T_{ri} stands for the reduced temperature (T/T_{ci}), ω is the acentric factor, and k_{1i} represents the adjustable parameter of the pure substance.

For the mixtures, the van der Waals mixing rules in the PRSV CEOS can be presented as:[18,19]

$$a = \sum_i \sum_j x_i x_j (a_i a_j)^{0.5} [1 - k_{ij} + l_{ij}(x_i - x_j)] \qquad k_{ij} = k_{ii} = 0 \text{ and } l_{ij} \neq l_{ji} \qquad (8)$$

$$b = \sum_i \sum_j x_i x_j (1 - m_{ij}) \left(\frac{b_i + b_j}{2} \right) \qquad m_{ii} = 0 \qquad (9)$$

where k_{ij}, l_{ij} and m_{ij} are fitting parameters of the binary interaction and can be determined by simultaneously adjusting the theoretical expression of the PRSV EOS to the experimental V_m^E. The necessary data, such as critical properties and the Pitzer acentric factor, of the pure substances for the calculations with the PRSV CEOS were taken from the literature.[20] The PRSV CEOS parameters of the pure compound (k_{1i}) are given in Table II. The binary coefficients for Eqs. (8) and (9) are listed in Table III together with the standard deviations, σ. From the results of Fig. 2 and Table II, it must be emphasized that the equations of state offer good agreement with the experimental data of the binary excess molar vo–lumes.

TABLE II. Adjustable parameter of PRSV CEOS for the pure substances

Component	k_{1i}
1,3-Propanediol	0.242
Methanol	0.325
Ethanol	0.410
1-Propanol	0.321
1-Butanol	0.256
1-Pentanol	0.434

TABLE III. Adjustable PRSV CEOS parameters and the standard deviations for the V_m^E of the binary mixtures at 298.15 K

System	m_{12}	k_{12}	l_{12}	l_{21}	σ
1,3-Propanediol + methanol	–0.1875	–0.1034	0.0154	0.3135	0.0124
1,3-Propanediol + ethanol	–0.0231	–0.1740	0.0027	0.1865	0.0080
1,3-Propanediol + 1-propanol	–0.2132	–0.0225	0.1325	0.0328	0.0091
1,3-Propanediol + 1-butanol	–0.0170	–0.1454	0.1643	0.1231	0.0087
1,3-Propanediol + 1-pentanol	0.0230	0.2734	0.0413	0.1408	0.0082

CONCLUSIONS

The experimental data of the excess molar volumes of methanol, ethanol, 1-propanol, 1-butanol and 1-pentanol with 1,3-propanediol were measured over

the entire composition ranges and at several temperatures. These data were used to compute the excess molar volumes of the systems, and a Redlich–Kister type equation was used for fitting each set of data. Moreover, the obtained results showed that the excess molar volume for the system 1-pentanol + 1,3-propanediol were positive, while for the other studied systems, they were found to be negative. Furthermore, it was observed that the values of the excess molar volumes were temperature dependent. The behavior of the excess molar volumes of these systems can be explained as a balance between the positive contributions due to hydrogen bond rupture and dispersive interactions between unlike molecules, and negative contributions due to packing effects. The PRSV CEOS is a quite valuable tool for the correlation of the excess molar volumes of the investigated systems.

SUPPLEMENTARY MATERIAL

Densities of the pure components and excess molar volumes for 1,3 propanediol (1) + alkanols (2) mixtures at various temperatures are available electronically from http:////www.shd.org.rs/JSCS/, or from the corresponding author on request.

ИЗВОД

ДОПУНСКА МОЛАРНА ЗАПРЕМИНА СМЕША 1,3-ПРОПАНДИОЛ + (C$_1$–C$_5$) 1-АЛКОХОЛИ: ПРИМЕНА КУБНИХ ЈЕДНАЧИНА СТАЊА

MOHAMMAD ALMASI и LADAN KHOSRAVI

Department of Chemistry, Science and Research Branch, Islamic Azad University, Khouzestan, Iran

Густине бинарних смеша метанола, етанола, 1-пропанола, 1-бутанола и 1-пентанола са 1,3-пропандиолом измерене су на температурама 293,15, 298,15, 303,15 и 313,15 K и на атмосферском притиску. Мерења су извршена коришћењем вибрационог густиномета у читавом концентрационом опсегу и за све чисте компоненте. На основу експерименталних мерења одређене су допунске моларне запремине које су корелисане једначином Redlich–Kister-a. Добијени резултати су објашњени на основу молекулских интеракција и структурних карактеристика алкохола. Запажа се да повећање броја угљеникових атома алкохола води ка смањењу интеракција у смеши. За корелисање допунских моларних запремина бинарних смеша коришћена је Peng–Robinson–Stryjek–Vera (PRSV) једначина стања.

(Примљено 16. јуна, ревидирано 15. августа 2011)

REFERENCES

1. M. L. Huber, R. A. Perkins, *Fluid Phase Equilib.* **227** (2005) 44
2. D. Y. Peng, D. B. Robinson, *Ind. Eng. Chem. Fund.* **15** (1976) 59
3. R. Stryjek, J. H. Vera, *Can. J. Chem. Eng.* **64** (1986) 820
4. J.V. Sengers, R. F. Kayser, C. J. Peters, H. J. White, *Equations of State for Fluids and Fluid Mixtures*, Elsevier, Amsterdam, 2000, Ch. 4
5. D. H. Chen, M. V. Dinivahi, C. Y. Jeng, *Ind. Eng. Chem. Res.* **32** (1993) 241
6. H. Iloukhani, M. Almasi, *Thermochim. Acta* **495** (2009) 139
7. M. Almasi, H. Iloukhani, *J. Chem. Eng. Data* **55** (2010) 3918
8. H. Iloukhani, M. Almasi, *J. Solution Chem.* **40** (2011) 284

9. J. W. Lee, S. B. Park, H. Lee, *J. Chem. Eng. Data* **45** (2000) 166
10. K. Kurnia, B. Ariwahjoedi, M. I. A. Mutalib, T. Murugesan, *J. Solution Chem.* **40** (2011) 470
11. J. A. Riddick, W. B. Bunger, T. K. Sakano, *Organic Solvents: Physical Properties and Methods of Purification*, 4th ed.; Wiley, New York, 1986
12. J. Troncoso, C. A. Tovar, C. A. Cerdeirinã, E. Carballo, L. Roman, *J. Chem. Eng. Data* **46** (2001) 312
13. B. Orge, B. E. De Cominges, G. Marino, M. Iglesias, J. Tojo, *Phys. Chem. Liq.* **39** (2001) 99
14. O. Redlich, T. A. Kister, *Ind. Eng. Chem.* **40** (1948) 345
15. B. A. Bauer, S. Patel, *J. Mol. Liq.* **142** (2008) 32
16. M. Costas, D. Patterson, *J. Chem. Soc., Faraday Trans. I.* **81** (1985) 635
17. A. K. Nain, *J. Chem. Thermodyn.* **39** (2007) 462
18. J. M. Resa, M. J. Iglesias, A. González, J. Lanz, *J. Chem. Thermodyn.* **33** (2001) 723
19. I. R. Grguric, S. P. Serbanovic, M. L. Kijevcanin, A. Z. Tasic, B. D. Djordjevic, *Thermochim. Acta* **412** (2004) 25
20. C. L. Yaws, *Yaws' Handbook of Thermodynamic and Physical Properties of Chemical Compounds*, Norwich, New York, 2004.

Excess molar volumes of 1,3-propanediol + (C₁–C₅) alkan-1-ols: application of a cubic equation of state

MOHAMMAD ALMASI* and LADAN KHOSRAVI

Department of Chemistry, Science and Research Branch, Islamic Azad University, Khouzestan, Iran

TABLE I-S. Densities, ρ, of the pure components at various temperatures and the corresponding literature values

Compound	T / K	ρ / g cm⁻³	
		This work	Lit.
1,3-Propanediol	293.15	1.05265	–
	298.15	1.04955	1.049717 [9]
	303.15	1.04665	1.046718 [9]
	313.15	1.03970	1.040207 [9]
Methanol	293.15	0.79155	0.79115 [10]
	298.15	0.78630	0.78637 [11]
	303.15	0.78165	0.78170 [11]
	313.15	0.77215	0.77226 [10]
Ethanol	293.15	0.78945	0.78933 [10]
	298.15	0.78498	0.78493 [11]
	303.15	0.78071	0.78064 [11]
	313.15	0.77212	0.77254 [10]
1-Propanol	293.15	0.80352	0.80323 [10]
	298.15	0.79960	0.79960 [11]
	303.15	0.79554	0.79560 [11]
	313.15	0.78747	0.78759 [10]
1-Butanol	293.15	0.80950	0.80943 [12]
	298.15	0.80570	0.80584 [11]
	303.15	0.80212	0.80220 [11]
	313.15	0.79415	–
1-Pentanol	293.15	0.81480	0.81492 [11]
	298.15	0.81082	0.81080 [11]
	303.15	0.80707	0.8072 [11]
	313.15	0.79940	–

*Corresponding author. E-mail: m.almasi@khouzestan.srbiau.ac.ir

S55

TABLE II-S. Densities, ρ, and excess molar volumes, V_m^E, for 1,3 propanediol (1) + alkanols (2) mixtures at various temperatures

x_1	ρ / g cm^{-3}	V_m^E / cm^3 mol^{-1}
1,3-propanediol (1) + methanol (2), T = 293.15 K		
0.0000	0.79155	–
0.0776	0.82915	–0.181
0.1581	0.86417	–0.371
0.2356	0.89422	–0.535
0.3482	0.93132	–0.680
0.4529	0.96009	–0.731
0.5399	0.98021	–0.700
0.6482	1.00150	–0.592
0.7394	1.01690	–0.459
0.8369	1.03104	–0.265
0.9280	1.04358	–0.121
1.0000	1.05265	–
1,3-propanediol (1) + methanol (2), T = 298.15 K		
0.0000	0.78630	–
0.0776	0.82379	–0.169
0.1581	0.85886	–0.353
0.2356	0.88872	–0.498
0.3482	0.92601	–0.639
0.4529	0.95503	–0.689
0.5399	0.97538	–0.658
0.6482	0.99704	–0.555
0.7394	1.01250	–0.411
0.8369	1.02730	–0.245
0.9280	1.03997	–0.096
1.0000	1.04955	–
1,3-propanediol (1) + methanol (2), T = 303.15 K		
0.0000	0.78165	–
0.0776	0.81918	–0.166
0.1581	0.85411	–0.337
0.2356	0.88386	–0.469
0.3482	0.92088	–0.582
0.4529	0.94999	–0.624
0.5399	0.97084	–0.610
0.6482	0.99305	–0.526
0.7394	1.00909	–0.407
0.8369	1.02412	–0.244
0.9280	1.03693	–0.094
1.0000	1.04665	–

TABLE II-S. Continued

x_1	ρ / g cm^{-3}	V_m^E / cm^3 mol^{-1}
1,3-propanediol (1) + methanol (2), T = 313.15 K		
0.0000	0.77215	–
0.0776	0.80968	–0.161
0.1581	0.84437	–0.311
0.2356	0.87411	–0.433
0.3482	0.91144	–0.547
0.4529	0.94083	–0.587
0.5399	0.96188	–0.569
0.6482	0.98455	–0.492
0.7394	1.00100	–0.380
0.8369	1.01658	–0.234
0.9280	1.02965	–0.084
1.0000	1.03970	–
1,3-propanediol (1) + ethanol (2), T = 293.15 K		
0.0000	0.78945	
0.0786	0.81642	–0.132
0.1840	0.85128	–0.312
0.2408	0.86931	–0.399
0.3310	0.89660	–0.501
0.4449	0.92878	–0.570
0.5545	0.95729	–0.565
0.6345	0.97657	–0.513
0.7331	0.99893	–0.416
0.8551	1.02443	–0.237
0.9361	1.04059	–0.116
1.0000	1.05265	
1,3-propanediol (1) + ethanol (2), T = 298.15 K		
0.0000	0.78498	–
0.0786	0.81184	–0.120
0.1840	0.84670	–0.295
0.2408	0.86465	–0.372
0.3310	0.89213	–0.481
0.4449	0.92449	–0.552
0.5545	0.95321	–0.551
0.6345	0.97262	–0.499
0.7331	0.99505	–0.396
0.8551	1.02085	–0.222
0.9361	1.03705	–0.093
1.0000	1.04955	–

ALMASI and KHOSRAVI

TABLE II-S. Continued

x_1	ρ / g cm^{-3}	V_m^E / cm^3 mol^{-1}
1,3-propanediol (1) + ethanol (2), T = 303.15 K		
0.0000	0.78071	–
0.0786	0.80744	–0.107
0.1840	0.84198	–0.252
0.2408	0.86012	–0.339
0.3310	0.88745	–0.431
0.4449	0.92005	–0.510
0.5545	0.94901	–0.514
0.6345	0.96861	–0.467
0.7331	0.99137	–0.374
0.8551	1.01740	–0.202
0.9361	1.03400	–0.091
1.0000	1.04665	–
1,3-propanediol (1) + ethanol (2),T = 313.15 K		
0.0000	0.77212	–
0.0786	0.79872	–0.095
0.1840	0.83311	–0.225
0.2408	0.85122	–0.307
0.3310	0.87865	–0.399
0.4449	0.91121	–0.464
0.5545	0.94024	–0.460
0.6345	0.96019	–0.426
0.7331	0.98317	–0.333
0.8551	1.00990	–0.189
0.9361	1.02680	–0.085
1.0000	1.03970	–
1,3-propanediol (1) + 1-propanol (2), T = 293.15 K		
0.0000	0.80352	–
0.0794	0.82401	–0.119
0.1737	0.84823	–0.231
0.2385	0.86498	–0.306
0.3480	0.89298	–0.387
0.4425	0.91691	–0.421
0.5594	0.94622	–0.421
0.6433	0.96697	–0.389
0.7345	0.98915	–0.318
0.8453	1.01579	–0.200
0.9309	1.03637	–0.104
1.0000	1.05265	–

TABLE II-S. Continued

x_1	ρ / g cm^{-3}	V_m^E / cm^3 mol^{-1}
1,3-propanediol (1) + 1-propanol (2), T =298.15 K		
0.0000	0.79960	
0.0794	0.81998	−0.108
0.1737	0.84415	−0.213
0.2385	0.86085	−0.282
0.3480	0.88895	−0.367
0.4425	0.91295	−0.402
0.5594	0.94235	−0.403
0.6433	0.96319	−0.371
0.7345	0.98533	−0.291
0.8453	1.01230	−0.188
0.9309	1.03290	−0.085
1.0000	1.04955	
1,3-propanediol (1) + 1-propanol (2), T =303.15 K		
0.0000	0.79554	
0.0794	0.81571	−0.085
0.1737	0.83982	−0.181
0.2385	0.85651	−0.246
0.3480	0.88470	−0.332
0.4425	0.90881	−0.370
0.5594	0.93830	−0.368
0.6433	0.95916	−0.331
0.7345	0.98160	−0.263
0.8453	1.00870	−0.157
0.9309	1.02960	−0.066
1.0000	1.04665	
1,3-propanediol (1) + 1-propanol (2), T = 313.15 K		
0.0000	0.78747	
0.0794	0.80756	−0.077
0.1737	0.83153	−0.159
0.2385	0.84820	−0.220
0.3480	0.87638	−0.301
0.4425	0.90055	−0.338
0.5594	0.93018	−0.338
0.6433	0.95124	−0.308
0.7345	0.97388	−0.245
0.8453	1.00130	−0.149
0.9309	1.02250	−0.066
1.0000	1.03970	

TABLE II-S. Continued

x_1	ρ / g cm^{-3}	V_m^E / cm^3 mol^{-1}
1,3-propanediol (1) + 1-butanol (2), T = 293.15 K		
0.0000	0.80950	–
0.0964	0.82945	–0.115
0.1636	0.84349	–0.154
0.2400	0.85980	–0.180
0.3523	0.88456	–0.193
0.4471	0.90637	–0.195
0.5605	0.93369	–0.191
0.6669	0.96070	–0.186
0.7576	0.98474	–0.173
0.8510	1.01032	–0.134
0.9062	1.02595	–0.107
1.0000	1.05265	–
1,3-propanediol (1) + 1-butanol (2), T = 298.15 K		
0.0000	0.80570	–
0.0964	0.82555	–0.102
0.1636	0.83957	–0.138
0.2400	0.85592	–0.166
0.3523	0.88077	–0.184
0.4471	0.90263	–0.186
0.5605	0.93003	–0.183
0.6669	0.95706	–0.174
0.7576	0.98113	–0.157
0.8510	1.00675	–0.114
0.9062	1.02260	–0.099
1.0000	1.04955	–
1,3-propanediol (1) + 1-butanol (2), T = 303.15 K		
0.0000	0.80212	–
0.0964	0.82190	–0.093
0.1636	0.83590	–0.125
0.2400	0.85227	–0.153
0.3523	0.87719	–0.174
0.4471	0.89913	–0.180
0.5605	0.92660	–0.177
0.6669	0.95370	–0.167
0.7576	0.97780	–0.146
0.8510	1.00355	–0.106
0.9062	1.01931	–0.080
1.0000	1.04665	–

TABLE II-S. Continued

x_1	ρ / g cm^{-3}	V_m^E / cm^3 mol^{-1}
1,3-propanediol (1) + 1-butanol (2), T = 313.15 K		
0.0000	0.79415	–
0.0964	0.81373	–0.070
0.1636	0.82785	–0.114
0.2400	0.84425	–0.143
0.3523	0.86925	–0.167
0.4471	0.89125	–0.172
0.5605	0.91885	–0.172
0.6669	0.94601	–0.157
0.7576	0.97022	–0.135
0.8510	0.99615	–0.097
0.9062	1.01200	–0.069
1.0000	1.03970	–
1,3-propanediol (1) + 1-pentanol (2), T = 293.15 K		
0.0000	0.81480	–
0.0847	0.82833	0.041
0.1739	0.84329	0.103
0.2451	0.85591	0.152
0.3546	0.87675	0.212
0.4381	0.89402	0.236
0.5138	0.91079	0.244
0.6511	0.94442	0.216
0.7384	0.96814	0.179
0.8521	1.00228	0.104
0.9391	1.03112	0.036
1.0000	1.05265	–
1,3-propanediol (1) + 1-pentanol (2), T = 298.15 K		
0.0000	0.81082	–
0.0847	0.82422	0.062
0.1739	0.83914	0.132
0.2451	0.85179	0.180
0.3546	0.87275	0.232
0.4381	0.89008	0.254
0.5138	0.90692	0.261
0.6511	0.94066	0.232
0.7384	0.96450	0.192
0.8521	0.99881	0.114
0.9391	1.02770	0.051
1.0000	1.04955	–

ALMASI and KHOSRAVI

TABLE II-S. Continued

x_1	ρ / g cm^{-3}	V_m^E / cm^3 mol^{-1}
1,3-propanediol (1) + 1-pentanol (2), T = 303.15 K
0.0000	0.80707	
0.0847	0.82028	0.090
0.1739	0.83513	0.172
0.2451	0.84781	0.219
0.3546	0.86887	0.264
0.4381	0.88627	0.282
0.5138	0.90320	0.284
0.6511	0.93698	0.260
0.7384	0.96089	0.220
0.8521	0.99533	0.140
0.9391	1.02445	0.069
1.0000	1.04665	
1,3-propanediol (1) + 1-pentanol (2), T = 313.15 K
0.0000	0.79940	
0.0847	0.81239	0.121
0.1739	0.82717	0.214
0.2451	0.83988	0.258
0.3546	0.86101	0.296
0.4381	0.87852	0.305
0.5138	0.89549	0.306
0.6511	0.92931	0.285
0.7384	0.95321	0.251
0.8521	0.98765	0.180
0.9391	1.01715	0.087
1.0000	1.03970	

Development of a new model for the calculation of the detonation parameters of high explosives

RADUN JEREMIĆ and JOVICA BOGDANOV*

Military Academy Belgrade, Generala Pavla Jurišića Šturma 33, 11000 Belgrade, Serbia

Abstract: A simple semi-empirical model for the calculation of the detonation pressure and velocity for CHNO explosives has been developed, which is based on experimental values of the detonation parameters. Model uses the Avakyan method for the determination of the chemical composition of the detonation products, and is applicable over a wide range of densities. Compared with the well-known Kamlet method and the numerical model of detonation based on the Becker–Kistiakowsky–Wilson Equation of state (BKW EOS), the calculated values from the proposed model have significantly better accuracy.

Keywords: detonation modeling; detonation velocity; detonation pressure; CHNO high explosives.

INTRODUCTION

The possibility of accurate prediction of their detonation characteristics significantly shortens the process of the development of new explosives, consequently lowering the development costs.

Two approaches are usually used in this issue. The first is based on numerical modeling of detonation and the second on much simpler empirical and semi-empirical models.

Laboratories in developed countries, especially in the USA, developed the first computer programs for numerical modeling of detonation more than 40 years ago. In the last years, they have work on improvements of the numerical models for non-stationary detonation.

Mader and his co-workers from the Los Alamos National Laboratory, using the Becker-Kistiakowsky-Wilson Equation of state (BKW EOS), developed the program STRETCH BKW for the calculation of detonation parameters in 1961.[1,2] For that time, the program had a high rate of calculations with acceptably accurate results. The program used only one set of parameters of the BKW Equation of state for all explosives.

* Corresponding author. E-mail: bjbogdanov@open.telekom.rs

Mader also developed computer program Fortran BKW in 1967, which has been used in research institutions in many countries. Up to now, the program was modified several times to be compatible with modern computer software.[1-4]

Other programs using the BKW EOS, such as Arpage and La Mineur, were also developed.[4] The program Tiger used the Jacobs–Cowperthwaite–Zwisler Equation of state (JCZ EOS).[5]

The numerical models are not always suitable for engineering purposes, mainly because of their complexity. Therefore, many different empirical and semi-empirical methods of calculation have been developed, which are much simpler for use. The most famous is the Kamlet method, which gives acceptably accurate results for CHNO high explosives with an initial density above 1000 kg m^{-3}.[6]

A new simple semi-empirical method for the prediction of the detonation parameters of CHNO high explosives is presented in this work. The differences between experimental values and calculation results obtained with this new method are significantly smaller when compared to the numerical model and the Kamlet method.

THEORETICAL BASICS OF THE METHOD

The relations between the detonation pressure p (in the Chapman-Jouguet or C-J point), detonation velocity D, initial density of explosive ρ_0 and heat of detonation Q are known from the hydrodynamic theory of detonation:[7]

$$D = \sqrt{2(\gamma^2 - 1)Q} \tag{1}$$

$$p = \frac{1}{\gamma + 1}\rho_0 D^2 \tag{2}$$

where γ is the polytropic exponent.
Combining Eqs. (1) and (2), it follows:

$$p = 2(\gamma - 1)\rho_0 Q \tag{3}$$

Considering the fact that the experimental values of the detonation parameters are proportional to the initial density of the explosive[1,2] and that, based on the EOS of gases, the pressure is proportional to the number of moles of gaseous detonation products, n, Eq. (3) can be written in the following general form:

$$p = A\rho_0^2 nQ \tag{4}$$

where A is an empirical constant.

Numerous experiments showed that the dependence of the detonation velocity on the initial density is linear for all explosive charges above a critical diameter, which can be represented as:[7]

$$D = D_1 + M(\rho - \rho_1) \tag{5}$$

where D_1 is the detonation velocity for an initial density ρ_1 and M is an empirical constant.

Combination of the Eqs. (4) and (2) and considering Eq. (5) the following general equation for calculation of detonation velocity can be written as:

$$D = B + C\rho_0\sqrt{nQ} \tag{6}$$

where B and C are empirical constants.

The empirical constants in Eqs. (4) and (6) can be obtained using regression analysis of the experimental data for the dependence of detonation pressure and velocity on the initial density of the explosive.

The number of moles of gaseous detonation products, n, can be easily calculated using the Avakyan method.[7] According to Avakyan's experimental data, the coefficient of realization (K) can be calculated from the oxygen coefficient (K_k) using the following equation:

$$K = 0.32\, K_k^{0.24} \tag{7}$$

in which the oxygen coefficient should be expressed in percents.

If the presence of ammoniac in the detonation products is neglected, the summary chemical reaction of detonation can be written as:

$$C_xH_yN_zO_u \rightarrow\ n_1H_2O + n_2H_2 + n_3CO_2 + n_4CO + n_5O_2 + n_6N_2 + n_7C \tag{8}$$
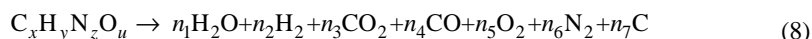
The calculation of the chemical composition of the detonation products is based on the assumption that the coefficient of realization K determines the degree of hydrogen oxidation and formation of water. In other words, it is assumed that from $y/2$ (maximal possible value) moles of hydrogen, $Ky/2$ moles of water are formed during the explosion, while $(1 - K)y/2$ moles remain as H_2. According to this:

$$n_1 = Ky/2,$$
$$n_2 = (1 - K)y/2$$

The number of moles of nitrogen can be calculated as:

$$n_6 = z/2$$

For the remaining detonation products, it is necessary to solve a system of equations, representing the mass and energy balance, considering the ratio of oxygen, carbon and hydrogen in the composition of the explosive. Depending on this ratio, three characteristic cases should be considered.

Case 1. $K_k > 100$ %: It is assumed that there is no formation of free carbon in the detonation products, *i.e.*, $n_7 = 0$. The following equations are used for the calculation of n_3–n_5:

$$n_3 = (1.4K - 0.4)x$$
$$n_4 = x - n_3 = 1.4x(1 - K)$$
$$n_5 = (x - 2n_3 - n_4 - n_1)/2$$

Case 2. $K_k < 100$ %: It is assumed that there is no formation of free oxygen in the detonation products, *i.e.* $n_5 = 0$. The remaining detonation products are determined using the following equations:

$$n_3 = 1.16u\,(K - 0.568) - 0.5n_1$$
$$n_4 = u - (2n_3 + n_1) = u\,(1 - 2.32\,(K - 0.568))$$
$$n_7 = x - (n_3 + n_4)$$

Case 3. $K_k < 100$ % and $u > (x + y/2)$: The following equations are used:

$$n_3 = 0.7\,(u - y/2)K - 0.4x$$
$$n_4 = 1.4x - 0.7\,(u - y/2)K$$
$$n_5 = 0 \text{ and } n_7 = 0$$

In the next step, the total heat of formation for the determined detonation products is calculated. The heat of explosion is then determined using the Hess Law as:

$$Q = \sum_{i=1}^{n} \Delta U_{f_{i_{prod}}}^{0} - \sum_{j=1}^{m} \Delta U_{f_{i_{EM}}}^{0} \qquad (9)$$

where $i = 1,…, n$ is the index of a particular detonation product, while $j = 1,…, m$ is the index number of the individual components of the explosion.

The heat of formation data for components of the explosion and the detonation products can be found in thermochemical tables.[2,4,7,10]

It should be noted that the Avakyan method predicts the chemical composition of the detonation products after expansion and cooling.

APPLICATION AND EVALUATION OF THE MODEL

The proposed model was applied for the calculation of the detonation parameters of 72 explosive compositions (25 different explosives with various initial densities), the detonation pressures and velocities of which had previously been experimentally determined (Table I). The amounts of the individual detonation products were first calculated using the Avakyan method.

The empirical constants in Eqs. (4) and (6) were determined using the regression analysis of the results (Figs. 1 and 2):

$$\rho = 0.00048 \rho_0^2 nQ \qquad (10)$$

$$D = 2264.1 + 7.7072 \rho_0 \sqrt{nQ} \qquad (11)$$

In the previous equations, the initial density, ρ_0, is expressed in g cm^{-3}, the total quantity of gaseous detonation products, n, is in mol kg^{-1} and the heat of explosion, Q, is in kJ kg^{-1}. The calculated detonation pressure p is in kbar, and the detonation velocity D is in m s^{-1}.

Comparisons of the calculated detonation parameters with their differences from the appropriate experimental values are presented in Tables I–III. The high value of the correlation coefficient ($R^2 > 0.98$) for the 74 considered explosive compositions shows that the proposed model could be successfully employed in the theoretical determination of the detonation parameters.

The average differences between the calculated detonation parameters and the experimental values are presented in Table IV. Compared with the BKW EOS or the Kamlet method, the proposed model gives significantly more precise calculation results. In addition, the calculation results have a similar precision to those obtained using the numerical model XWizard.[11] The proposed model is also applicable over a much wider range of initial densities, which is not possible with the other models. The precision of calculation results for explosives with high values of initial density are also acceptable, as presented in Tables I–III.

The obtained differences between the calculated results and the experimental values are within the expected experimental error. It should be mentioned that ex-

TABLE I. Comparison of differently determined detonation parameters for explosives (TNT, 2,4,6-trinitrotoluene; RDX, 1,3,5-trinitro-2,4,6-triazacyclohexane; HMX, 1,3,5,7-tetranitro-2,4,6,8-tetraazacyclooctane; PETN, pentaerythritol tetranitrate; Tetryl7. N-methyl-N-2,4,6-tetranitroaniline; NM, nitromethane; NGL, nitroglycerine; HNS, 2,2',4,4',6,6'-hexanitrodiphenylethylene (hexanitrostilbene); DATB, 1,3-diamino-2,4,6-trinitrobenzene)

Explosive	ρ_0 g cm^{-3}	Experiment p kbar	Experiment D m·s^{-1}	BKW p kbar	BKW D m·s^{-1}	Kamlet p kbar	Kamlet D m·s^{-1}	Model p kbar	Model D m·s^{-1}	BKW Δp kbar	BKW ΔD m·s^{-1}	Kamlet Δp kbar	Kamlet ΔD m·s^{-1}	Model Δp kbar	Model ΔD m·s^{-1}
RDX2.7	0.70	59.9	4989	60	5222	51.7	5026	51.2	4781	0.2	4.7	-13.7	0.7	-14.5	-4.2
	1.00	108	6030	104	6044	105.6	6052	104.5	5860	-3.7	0.2	-2.2	0.4	-3.2	-2.8
	1.29	166.2	7036	168	6922	175.7	7044	173.9	6903	1.1	-1.6	5.7	0.1	4.6	-1.9
	1.46	209.8	7626	215	7491	225.1	7626	222.7	7514	2.5	-1.8	7.3	0.0	6.2	-1.5
	1.59	259	8077	263	7962	267	8071	264.2	7982	1.5	-1.4	3.1	-0.1	2.0	-1.2
	1.72	310	8528	311	8467	312.4	8515	309.1	8449	0.3	-0.7	0.8	-0.2	-0.3	-0.9
	1.80	347	8754	339.8	8795	342.2	8789	338.6	8737	-2.3	0.5	-1.4	0.4	-2.4	-0.2
HMX2,10	1.77	323	8500	339.8	8708	327.8	8646	314.1	8499	5.2	2.4	1.5	1.7	-2.7	0.0
	1.90	393	9100	391	9288	380.5	9123	362	8957	-0.5	2.1	-3.2	0.3	-7.9	-1.6
TNT2.7	0.80	36.4	4340	55	4806	48.6	4551	45.39	4634	51.1	10.7	33.5	4.9	24.7	6.8
	1.00	62.5	5100	81	5319	75.9	5131	70.92	5227	29.6	4.3	21.4	0.6	13.5	2.5
	1.36	122.2	6200	146	6310	140.4	6175	131.2	6293	19.5	1.8	14.9	-0.4	7.3	1.5
	1.45	142	6500	166	6576	159.6	6436	149.1	6560	16.9	1.2	12.4	-1.0	5.0	0.9
	1.59	176.5	6940	198	7010	191.9	6842	179.3	6975	12.2	1.0	8.7	-1.4	1.6	0.5
	1.64	190	6950	215	7169	204.1	6987	190.8	7123	13.2	3.2	7.4	0.5	0.4	2.5
PETN2	0.25	7	2830	11	3414	6.6	3493	6.261	3144	57.1	20.6	-5.7	23.4	-10.6	11.1
	0.50	24	3800	30	4692	26.5	4349	25.04	4025	25.0	23.5	10.4	14.4	4.3	5.9
	1.00	97	6025	107	6026	106	6063	100.2	5785	10.3	0.0	9.3	0.6	3.3	-4.0
	1.67	300	7980	279	8050	295.5	8358	279.4	8144	-7.0	0.9	-1.5	4.7	-6.9	2.1
	1.77	335	8300	318	8424	332	8701	313.8	8496	-5.1	1.5	-0.9	4.8	-6.3	2.4
Tetryle7	0.90	64.6	5360	76	5316	71	5203	72.2	5253	17.6	-0.8	9.9	-2.9	11.8	-2.0
	1.36	140	6680	160	6616	162.2	6637	164.9	6781	14.3	-1.0	15.9	-0.6	17.8	1.5
	1.70	245	7560	253	7750	247.5	7634	257.6	7910	3.3	2.5	1.0	1.0	5.1	4.6
NM2	1.13	125	6523	138	6590	130.2	6383	118.8	6099	10.4	1.0	4.2	-2.1	-4.9	-6.5
NGL2	1.59	246	7580	245	7641	281.6	8289	232.3	7625	-0.4	0.8	14.5	9.4	-5.6	0.6
HNS11	1.70	210	7000	233.4	7255	219.3	7159	196.8	7199	11.1	3.6	4.4	2.3	-6.3	2.8
DATB10	1.79	259	7520	239	7637	253.3	7574	237.9	7690	-7.7	1.6	-2.2	0.7	-8.2	2.3
Average difference of the results, %										12.2	3.5	8.0	3.0	6.9	2.8

$$D = 2264.1 + 7.7072\ \rho_0\,(nQ)^{0.5}$$
$$R^2 = 0.9841$$
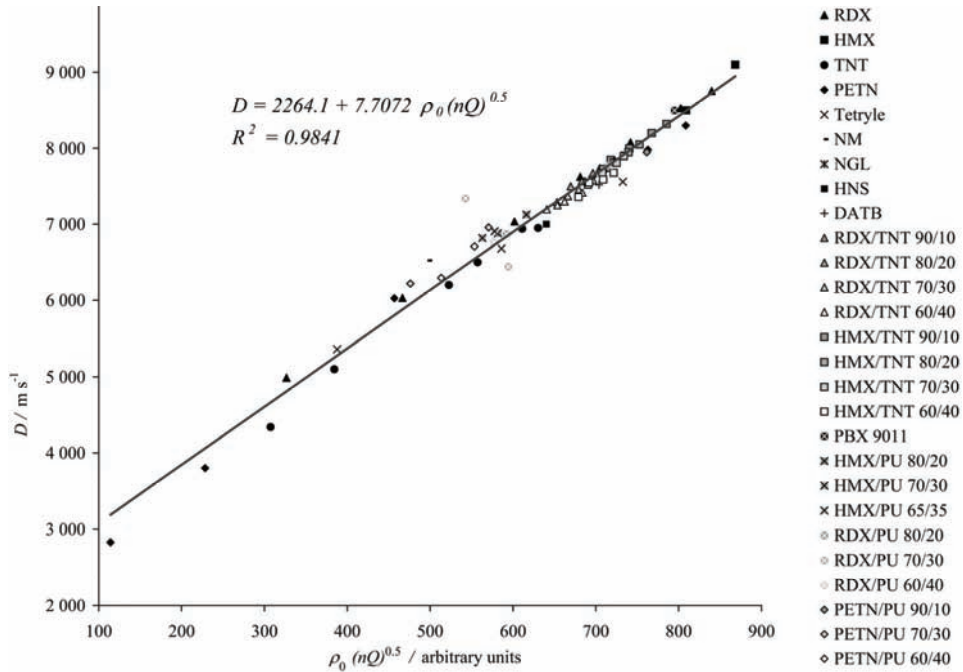
Fig. 1. Calculated and experimental values of the detonation velocity.

$$p = 0.0048\ \rho_0^{\,2}\,nQ$$
$$R^2 = 0.9875$$

Fig. 2. Calculated and experimental values of the detonation pressure.

TABLE II. Comparison of differently determined detonation parameters for explosive mixtures with TNT

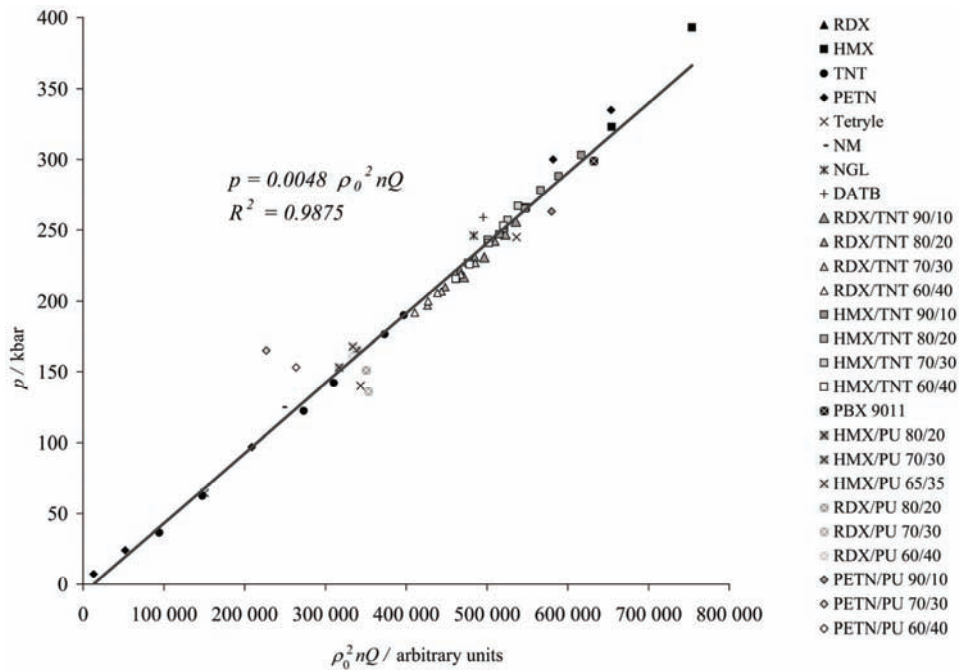| Explosive	ρ_0 g cm⁻³	Experiment		BKW		Kamlet		Model		Difference, %					
										BKW		Kamlet		Model	
		p kbar	D m·s⁻¹	p kbar	D m·s⁻¹	p kbar	D m·s⁻¹	p kbar	D m·s⁻¹	Δp kbar	ΔD m·s⁻¹	Δp kbar	ΔD m·s⁻¹	Δp kbar	ΔD m·s⁻¹
RDX/TNT 90/10[9]	1.51	217	7570	230	7599	234.1	7687	226.3	7556	6.0	0.4	7.9	1.5	4.3	-0.2
	1.55	231	7740	240	7744	245.5	7805	238.4	7696	3.9	0.1	6.3	0.8	3.2	-0.6
	1.59	247	7840	251	7892	243.6	7709	250.9	7836	1.6	0.7	-1.4	-1.7	1.6	0.0
	1.61	256	7910	264	7967	242.3	7657	257.3	7906	3.1	0.7	-5.4	-3.2	0.5	0.0
RDX/TNT 80/20[9]	1.50	210	7500	223	7494	223.7	7532	215.3	7426	6.2	-0.1	6.5	0.4	2.5	-1.0
	1.53	222	7570	231	7601	232.7	7632	224	7529	4.1	0.4	4.8	0.8	0.9	-0.5
	1.56	231	7675	238	7709	238	7709	232.9	7632	3.0	0.4	3.0	0.4	0.8	-0.6
	1.60	242	7745	256	7858	254.5	7864	244.9	7770	5.8	1.5	5.2	1.5	1.2	0.3
RDX/TNT 70/30[9]	1.49	197	7290	210	7386	213.9	7382	204.7	7298	6.6	1.3	8.6	1.3	3.9	0.1
	1.52	207	7370	224	7492	222.6	7480	213.1	7399	8.2	1.7	7.5	1.5	2.9	0.4
	1.55	216	7460	231	7600	231.5	7578	221.6	7500	6.9	1.9	7.2	1.6	2.6	0.5
	1.59	227	7580	242	7747	243.6	7709	233.1	7635	6.6	2.2	7.3	1.7	2.7	0.7
RDX/TNT 60/40[9]	1.49	192	7195	206	7312	207.5	7271	197.1	7203	7.3	1.6	8.1	1.1	2.7	0.1
	1.52	200	7250	213	7420	216	7368	205.1	7302	6.5	2.3	8.0	1.6	2.6	0.7
	1.54	206	7300	224	7490	221.7	7432	210.6	7369	8.7	2.6	7.6	1.8	2.2	0.9
	1.59	219	7415	237	7675	236.3	7593	224.5	7535	8.2	3.5	7.9	2.4	2.5	1.6
HMX/TNT 90/10[9]	1.60	247	7850	263	7967	262.4	7984	247.5	7799	6.5	1.5	6.2	1.7	0.2	-0.7
	1.65	266	8000	278	8157	279	8153	263.2	7972	4.5	2.0	4.9	1.9	-1.0	-0.4
	1.71	288	8200	305	8390	299.7	8355	282.7	8179	5.9	2.3	4.1	1.9	-1.8	-0.3
	1.75	303	8320	318	8550	313.9	8490	296.1	8317	5.0	2.8	3.6	2.0	-2.3	0.0
HMX/TNT 80/20[9]	1.61	242	7730	261	7928	257.3	7891	241.2	7727	7.9	2.6	6.3	2.1	-0.4	0.0
	1.64	251	7820	270	8042	267	7991	250.2	7829	7.6	2.8	6.4	2.2	-0.3	0.1
	1.68	265	7950	282	8197	280.2	8123	262.6	7964	6.4	3.1	5.7	2.2	-0.9	0.2
	1.71	278	8050	299	8314	290.3	8223	272	8066	7.6	3.3	4.4	2.1	-2.1	0.2
HMX/TNT 70/30[9]	1.60	227	7520	247	7815	246.5	7738	228.9	7587	8.8	3.9	8.6	2.9	0.9	0.9
	1.64	243	7680	265	7965	258.9	7869	240.5	7720	9.1	3.7	6.5	2.5	-1.0	0.5
	1.68	257	7810	277	8119	271.7	7999	252.4	7853	7.8	4.0	5.7	2.4	-1.8	0.6
	1.70	267	7900	283	8197	278.2	8065	258.5	7920	6.0	3.8	4.2	2.1	-3.2	0.2
HMX/TNT 60/40[9]	1.60	216	7360	242	7737	239	7621	221.4	7499	12.0	5.1	10.6	3.5	2.5	1.9
	1.63	226	7550	257	7850	248.1	7717	229.8	7597	13.7	4.0	9.8	2.2	1.7	0.6
	1.67	241	7590	268	8000	260.4	7846	241.2	7728	11.2	5.4	8.0	3.4	0.1	1.8
	1.70	253	7680	278	8118	269.8	7942	249.9	7826	9.9	5.7	6.6	3.4	-1.2	1.9
Average difference of the results, %										7.0	2.4	6.4	1.9	1.8	0.6

TABLE III. Comparison of differently determined detonation parameters for explosive mixtures with TNT (PBX-9011, plastic-bonded high explosive with 90 % HMX and 10 % polymer binder (polyurethane, Estane 5701 F-1); PU, polyurethane binder)

Explosive	ρ_0 g cm⁻³	Experiment		BKW		Kamlet		Model		Difference, %					
										BKW		Kamlet		Model	
		p kbar	D m·s⁻¹	p kbar	D m·s⁻¹	p kbar	D m·s⁻¹	p kbar	D m·s⁻¹	Δp kbar	ΔD m·s⁻¹	Δp kbar	ΔD m·s⁻¹	Δp kbar	ΔD m·s⁻¹
PBX-9011[10]	1.77	299	8500	331	7700	301.9	8297	303.4	8392	10.7	-9.4	1.0	-2.4	1.5	-1.3
HMX/PU 80/20[4]	1.35	165	6880	175	7026	165	6712	162.4	6748	6.1	2.1	0.0	-2.4	-1.5	-1.9
	1.43	188	7126	193	7335	185.1	6966	182.3	7013	2.7	2.9	-1.5	-2.2	-3.0	-1.6
HMX/PU 70/30[4]	1.33	153	6818	164	6920	149.4	6423	152.2	6604	7.2	1.5	-2.4	-5.8	-0.5	-3.1
HMX/PU 65/35[4]	1.39	168	6906	182	6831	156.4	6466	160.3	6718	8.3	-1.1	-6.9	-6.4	-4.6	-2.7
RDX/PU 80/20[4]	1.30	151	6870	157	6802	154.2	6579	168.3	6827	4.0	-1.0	2.1	-4.2	11.4	-0.6
	1.57	234	7778	242	7870	242	7870	245.4	7775	3.4	1.2	3.4	1.2	4.9	0.0
RDX/PU 70/30[4]	1.26	136	6441	143	6612	131.5	6146	169.6	6845	5.1	2.7	-3.3	-4.6	24.7	6.3
	1.38	167	7339	173	7090	157.7	6510	141.4	6447	3.6	-3.4	-5.6	-11.3	-15.3	-12.2
RDX/PU 60/40[4]	1.36	161	6765	172	7201	139.5	6156	159.9	6712	6.8	6.4	-13.4	-9.0	-0.7	-0.8
PETN/PU 90/10[4]	1.65	263	7950	269	8027	268.5	7997	278.4	8134	2.3	1.0	2.1	0.6	5.9	2.3
PETN/PU 70/30[4]	1.16	115	6218	119	6110	117.4	5999	108.8	5934	3.5	-1.7	2.1	-3.5	-5.4	-4.6
	1.39	165	6957	174	6870	168.6	6714	156.3	6662	5.5	-1.3	2.2	-3.5	-5.3	-4.2
PETN/PU 60/40[4]	1.28	129	6294	140	6428	128.1	6032	126.6	6221	8.5	2.1	-0.7	-4.2	-1.9	-1.2
	1.38	153	6708	164	6787	148.9	6326	147.1	6531	7.2	1.2	-2.7	-5.7	-3.9	-2.6
Average difference of the results, %										5.7	2.6	3.3	4.5	6.0	3.0

TABLE IV. Comparison of the average differences of the calculated detonation parameters

Type of explosivecomposition	Number of considered compositions	Difference, %					
		BKW		Kamlet		Model	
		Δp	ΔD	Δp	ΔD	Δp	ΔD
		kbar	m·s⁻¹	kbar	m·s⁻¹	kbar	m·s⁻¹
Explosives	27	12.2	3.5	8.0	3.0	6.9	2.8
Explosive mixtures with TNT	32	7.0	2.4	6.4	1.9	1.8	0.6
Plastic-bonded explosives	15	5.7	2.6	3.3	4.5	6.0	3.0
Average difference of results, %		8.6	2.9	6.4	2.8	4.5	1.9

perimental values of detonation pressure and velocity in literature are quite different, mainly due to the low accuracy of the experimental methods. While modern experimental methods can determine detonation velocities with an accuracy below 1 %, the experimental values of the detonation pressure are expected to have an error above 10 %.[7]

CONCLUSIONS

A new, simple semi-empirical model for the calculation detonation pressure and velocity of CHNO high explosives is presented in this paper. The model is based on the theoretical model of an ideal detonation. The Avakyan method was used for the determination of the chemical composition of the detonation products. A good correlation between the calculated and experimental detonation parameters over a wide range of initial densities was achieved, and the results are within the degree of experimental error. In addition, the proposed model can be used for the calculation of the detonation pressure and velocity for explosives with the maximum initial density. The average difference of the calculation results was approximately 50 % smaller than the results obtained from a numerical model and by the Kamlet method.

ИЗВОД

РАЗВОЈ НОВОГ МОДЕЛА ЗА ПРОРАЧУН ДЕТОНАЦИОНИХ ПАРАМЕТАРА БРИЗАНТНИХ ЕКСПЛОЗИВА

РАДУН ЈЕРЕМИЋ и ЈОВИЦА БОГДАНОВ

Војна академија Београд, Генерала Павла Јуришића Штурма 33, 11000 Београд

У складу са теоријом идеалне детонације, а на основу експерименталних вредности детонационих параметара већег броја бризантних експлозива и различитих експлозивних састава, развијен је једноставан полуемпиријски модел за прорачун притиска и брзине детонације експлозива типа "CHNO". Модел је заснован на Авакјановој методи за прорачун састава гасовитих продуката детонације и применљив је у широком опсегу густина. Добијене вредности притиска и брзине детонације много мање одступају од експерименталних вредности у односу на познату Камлетову методу и нумерички модел заснован на БКW једначини стања.

REFERENCES

1. C. L Mader, *Numerical Modeling of Detonations*, University of California Press, Los Angeles, USA, 1979, p. 57
2. C. L Mader, *Numerical Modeling of Explosives and Propellants*, CRC Press, New York, USA, 1998, p. 33
3. R. Jeremić, *Numerical Modeling of Detonation*, Vojnotehnički glasnik, Belgrade, Vol. 2, 2002, p. 74 (in Serbian)
4. M. Sućeska, *Ph.D. Thesis*, Technical Military Academy, Zagreb, Yugoslavia, 1991 (in BHS)
5. M. L. Hobbs, M. R. Baer, B. C. McGee, *Extension of the JCZ Product Species Data Base*, in *Proceedings of the 11th International Detonation Symposium,* Snowmass, Colorado, USA, 1998, p. 958
6. M. J. Kamlet, S. J. Jacobs, *J. Chem. Phys.* **48** (1968) 93
7. N. A. Imhovik, in *Fizika vzryva*, L. I. Orlenko, Ed., Fizmatlit, Moscow, Russian Federation, 2002, p. 125 (in Russian)
8. R. Dimitrijević, *M. Sc. Thesis*, VTA VJ, Belgrade, Yugoslavia, 1996 (in Serbian)
9. M. Azdejković, *Ph.D. Thesis*, Technical Military Academy, Zagreb, Yugoslavia, 1983 (in BHS)
10. B. B. Dobratz, *LLNL Explosives Handbook, Properties of Chemical Explosives and Explosive Simulants*, UCRL-52997, Lawrence Livermore National Laboratory, USA, 1981, p. 8–1
11. J. Bogdanov, R. Jeremić, Z. Bajić, in *Proceedings of the 3rd Scientific Expert Conference with International Participation on Defensive Technologies OTEH 2009*, Belgrade, Serbia, 2009.

Journal of the Serbian Chemical Society

A new approach to the analysis of the accumulation and enrichment of heavy metals in the Danube River sediment along the Iron Gate reservoir in Serbia

ŽIVORAD VUKOVIĆ[1]*, DUBRAVKA VUKOVIĆ[2], MIRJANA RADENKOVIĆ[1]
and SRBOLJUB STANKOVIĆ[1]

[1]*Institute of Nuclear Sciences Vinča, P. O. Box 502, 11001 Belgrade, Serbia and* [2]*Institute of Veterinary Medicine of Serbia, Vojvode Toze 24, 11000 Belgrade, Serbia*

Abstract: The concentrations of heavy metals (Cu, Zn, Pb and Cd) and long-
-lived radionuclides (U, Th and Cs) along the Iron Gate reservoir of the River
Danube in Serbia were determined. In the years 2005–2009, water and sedi-
ments were sampled at six sites along 200 km of the River Danube from Bel-
grade to the Djerdap (Iron Gate) hydroelectric power plant. The concentrations
of heavy metals in the sediment were found to be in the ranges of 27.9–149.3
mg kg^{-1} for Cu, 55.2–228.4 mg kg^{-1} for Zn, 13.5–71.6 mg kg^{-1} for Pb, 0.3–25.2
mg kg^{-1} for Cd and 4.0–17.5 Bq L^{-1} for ^{137}Cs. These values are in correlation
with the concentrations in the river water when expressed by the equilibrium
coefficients (K_d) between the solid and liquid phases. The behaviors of the
heavy metals were evaluated by applications models for the prediction of the
behavior of pollutants in rivers. The fluxes of heavy metals from water to se-
diment and *vice versa* were also determined.

Key words: distribution coefficients; heavy metals; MOIRA model; sediment.

INTRODUCTION

The Danube is the second largest river in Europe, spanning between its
source and mouth in the Black Sea a total length of 2,875 km and covering an
overall catchments area of 817,000 km^2. Thirteen countries are connected by the
Danube and are responsible for the protection of the water quality of the river and
its catchments. The territory of Serbia represents approximately 10 % of the Da-
nube river basin. Three large rivers, the Tisza, the Sava, and the Velika Morava,
increase the water volume of the Danube in Serbia by more than 2.5 times. On
entering Serbia at 1425.5 km from the mouth, the average flow rate of the Da-
nube is 2400 m^3 s^{-1}, while it is 5500 m^3 s^{-1} on leaving the country at 825 km

from the mouth. The largest in central Europe, the Iron Gate reservoir was constructed for a 1200 MW hydroelectric power plant on the Danube River, 933 km from its mouth in the Black Sea.

Due to the Iron Gate, the flow of the Danube in this section is retarded. A high level of suspended solids, consisting of fine sediments, causes the sedimentation rate to rise as the Danube water approaches the Iron Gate canyon. Therefore, the Iron Gate reservoir acts as a depository of fine sediments and pollutants.

In the Danube River catchment area, both large cities, such as Belgrade, and smaller settlements conjunctively rely on ground water and surface water. Other uses of the rivers and their surroundings include agriculture, forestry, power generation and recreation.

Heavy metals are known to cause deleterious effects on human health.[1] In view of the persistence of many micropollutants and their potential for bioaccumulation, sediments are regarded as important sources that seriously threaten natural ecosystems.[2,3] Unlike organic pollutants, natural processes of decomposition do not remove heavy metals. Upon entering natural waters, heavy metals and radionuclides, originating from anthropogenic sources in traceable concentrations, become part of the water sediment system and their distribution processes are controlled by a dynamic set of physical and chemical interactions and equilibria.[4]

Heavy metals of anthropogenic origin are generally introduced into river systems as inorganic complexes or hydrated ions, which are easily adsorbed on surfaces of sediment particles by relatively weak physical or chemical bonds. Thus, heavy metals of anthropogenic origin are found in sediments predominantly in the labile extractable fraction.[2,5]

The enrichment of heavy metals in the environment can result from both anthropogenic activities and natural processes. High concentrations of heavy metals with geogenic origins in sediments do not imply high potential toxicity to ecology.[6] Consequently, a clear differentiation of the anthropogenic from the geogenic heavy metals is important in evaluating the extent of pollution, preventing further environmental damages and planning remedial strategies. The trend of heavy metal accumulation in sediment surfaces over the last one hundred years showed increased concentrations of heavy metals, originating mainly from anthropogenic activities.

The results of the Joint Danube Survey for the concentrations of heavy metals in sediment along the entire course of the River Danube and several of its main tributaries performed in year 2001 showed the values: 28.3–197.7 mg kg^{-1} for Cu; 99–398 mg kg^{-1} for Zn; 18.2–85.0 mg kg^{-1} for Pb and < 1.1–7.6 mg kg^{-1} for Cd. Downstream from the Iron Gate reservoir, the concentrations of heavy metals remained stable or decreased slightly down to the Danube delta.[7] Heavy

metals are among the most common environmental pollutants. In water and biota, they indicate the presence of natural and anthropogenic sources.

In the Saricay Stream Basin of southwestern Turkey,[8] the traceable metal levels in the sediments displayed marked seasonal and regional variations, which were attributed to anthropogenic influences and natural processes.

An analysis of the sediment quality of the River Po[9] identified three major factors which explained the observed variance. The first and the second factors corresponded to anthropogenic inputs and geological factors, while the third included seasonal processes of minor importance.

The investigation of heavy metal contamination of the River Yamuna in India showed significant enrichment of the sediment with Cd and Ni.[10] Many authors use enrichment factors when assessing the pollution level of rivers. The heavy metal enrichment factor (*EF*) suggested concentrations above the background level in the study area.

The enrichment of trace elements in river-basin water indicates their impact as potentially hazardous to the environment and human health.

The present study was conducted to determine the heavy metals distribution and accumulation in the Danube Iron Gate reservoir and to estimate the traceable metal fluxes from river water to sediment and *vice versa*. This is of fundamental importance in the environmental study of river systems, especially of the Danube Iron Gate reservoir.

MATERIALS AND METHODS

From the autumn of 2005 to the spring of 2009, samples of both the sediment and water of the River Danube were collected at the six sites marked in Fig. 1: Belgrade (1), Smederevo (2), Veliko Gradište (3), Donji Milanovac (4), Tekija (5) and Kladovo (6). The specimens were taken for analysis in appropriate containers, according to the standard procedure.[11] The sediment samples were collected using grab sampler from the top 10 cm of the sediment surface.
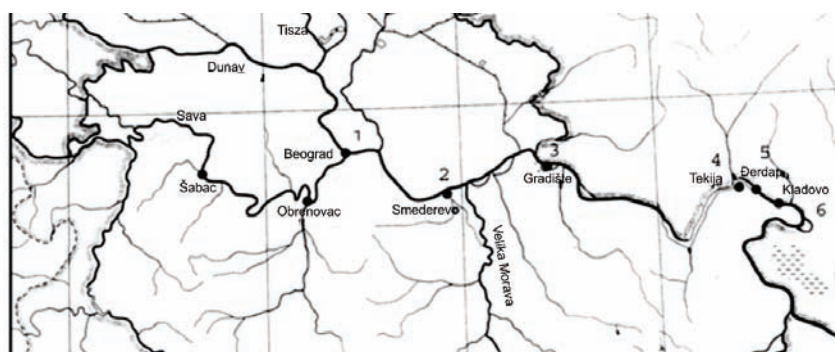

Fig. 1. Locations and distances from mouth of the sampling stations on the Danube River: 1) Belgrade, 1162 km; 2) Smederevo, 1116 km; 3) Veliko Gradište, 1059 km; 4) Donji Milanovac, 990 km; 5) Tekija, 955 km and 6) Kladovo, 944 km.

The sediment samples were dried in an oven at 105 °C to constant weight. The caked sediment material was then finely ground and 2.5 g samples were dissolved in 25 cm^3 1/1 HNO$_3$. For the investigation of the quality parameters of the river water, standard analytical methods were used, as well as atomic absorption spectrometry.[12,13] The concentrations of heavy metals were determined by flame atomic absorption spectrometry in an air/acetylene flow, using a Perkin Elmer AA 200 spectrometer. The cadmium concentration was determined by the graphite furnace technique using a Perkin Elmer AA 600 with a transversely heated graphite atomizer (THGA) with the Zeeman background correction. The THGA provides a uniform temperature distribution over the entire tube length, rapid heating and an integrated L'vov platform, resulting in an improved signal/interference ratio and high analytical sensitivity.[14] Analytical injection (20 µL) and atomization were realized in five steps, controlled by appropriate software and an auto-sampler.

For both techniques, adequate hollow cathode lamps (HCL) were used for irradiation and mixed reference standard solutions were prepared for analysis, using Merck certified atomic absorption stock standards (1000 µg mL^{-1}) and Mili-Q purified water. No modifiers were added. The standard reference material used to verify the accuracy of the methods for the determination of heavy metals in water. The precision of these methods was better than 10 %.

Activity of the gamma-ray emitters was analyzed by a multichannel analyzer using a reverse electrode HPGe detector with 23 % relative efficiency. Sediment samples were dried in a drying oven at 105 °C temperature. The radioactivity of sediment samples was measured for the fraction of particles that passed through a 1.0 mm sieve, after establishing the radioactive equilibrium between ^{220}Rn and its daughter products.

The methods of correlation analysis were applied in the treatment of the experimental data. Relative standard deviation was generally less than 15 %.

RESULTS AND DISCUSSION

Distribution of heavy metals in the Iron Gate Danube River reservoir

The quantities of heavy metals found in the sediments of the River Danube in the slowdown section from Belgrade to the Djerdap hydroelectric power station are presented in Table I. The concentrations of heavy metals in sediment were found to be in the ranges: 27.9–149.3 mg kg^{-1} for Cu, 55.2–228.4 mg kg^{-1} for Zn, 13.5–71.6 mg kg^{-1} for Pb and 0.3–25.2 mg kg^{-1} for Cd.

TABLE I. Concentrations of heavy metals in the sediments (mg kg^{-1}) at different sampling sites. Locations and distances from the mouth of the sampling stations on the Danube River: 1) Belgrade, 1162 km; 2) Smederevo, 1116 km; 3) Veliko Gradište, 1059 km; 4) Donji Milanovac, 990 km; 5) Tekija, 955 km and 6) Kladovo, 944 km

Location	Cu (min)	Cu (max)	Zn (min)	Zn (max)	Pb (min)	Pb (max)	Cd (min)	Cd (max)
1	31.70	118.20	56.60	173.20	13.50	50.10	0.40	4.20
2	35.80	107.60	55.20	199.00	15.60	59.30	0.30	4.80
3	27.90	102.30	62.50	201.30	23.20	60.70	0.50	7.80
4	35.30	125.50	69.10	205.60	21.40	67.20	0.80	12.60
5	39.70	149.30	77.20	228.40	19.60	70.30	2.30	25.20
6	33.40	111.30	70.50	223.60	19.70	71.60	1.80	20.40

The heavy metal levels in sediment displayed seasonal variation. The level of heavy metals in the sediment in autumn, when the water level was lower than in spring, was higher by up to 20 % in comparison to the spring levels. The heavy metals concentrations slightly increased down to Iron Gate reservoir (location 5, just before the dam). Compared to the values at locations 1 to 4, higher Cd concentrations were observed in the proximity of the dam. The concentrations of heavy metals in river water are presented in Table II. The heavy metals levels in the River Danube water and sediment displayed seasonal fluctuations. Many factors influence the seasonal variations in concentrations of heavy metals in river sediment. The seasonal behavior of heavy metals can be explained by the impact of wastewaters that cause high levels of metals during the dry season, and by the flushing of agricultural land, which enriches river water with compounds containing trace metals.

TABLE II. Concentrations of heavy metals in the water (μg dm^{-3}) at different sampling sites. Locations and distances from the mouth of the sampling stations on the Danube River: 1) Belgrade, 1162 km; 2) Smederevo, 1116 km; 3) Veliko Gradište, 1059 km; 4) Donji Milanovac, 990 km; 5) Tekija, 955 km and 6) Kladovo, 944 km

Location	Cu (min)	Cu (max)	Zn (min)	Zn (max)	Pb (min)	Pb (max)	Cd (min)	Cd (max)
1	25.20	106.50	63.20	147.10	4.90	15.60	0.40	1.70
2	22.30	99.80	68.50	145.70	5.10	18.30	0.80	3.10
3	18.40	103.20	67.50	154.80	3.80	16.70	0.50	2.80
4	16.70	88.50	62.10	106.80	2.80	14.60	0.50	3.10
5	18.20	132.50	79.60	104.20	2.70	11.30	0.30	2.40
6	15.30	88.20	61.60	96.60	2.20	14.40	0.20	2.50

Enrichment factors (*EF*s) have traditionally been used to evaluate possible anthropogenic inputs to the observed sediment metals. In this study, the *EF*s were calculated as follows:[15]

$$EF = (Me/Al)_{sample}/(Me/Al)_{crust} \qquad (1)$$

The *EF* is the ratio between the mass fractions of the examined metal and aluminum (Al) in the sample and their mass fractions in uncontaminated crust minerals. The baseline values for Me_{crust} were taken from published data.[16] Baseline values for Me_{crust} were as follows: 127.0 mg kg^{-1} for Zn, 32.0 mg kg^{-1} for Cu, 16.0 mg kg^{-1} for Pb, 0.2 mg kg^{-1} for Cd, and 6.9 % for Al.

Heavy metals concentrations higher than twice the background value implies anthropogenic pollution, while *EF* values higher than 2 indicate contamination.[7,17]

In the study of heavy metal contamination of the River Yamuna, enrichment factors for each of the heavy metals in the sediments was calculated based on the background value of the metal, taken as the world average of the metal in soil.[5]

This approach is not entirely satisfactory for the evaluation of a possible anthropogenic impact.

The river sediment is an integral and dynamic part of a river basin. It originates from the upstream weathering of minerals and soils, and is susceptible to transport downstream by the river water. Sediments are usually considered as sinks for trace metals.

Sediments show high capacity to accumulate and, in time, integrate low concentrations of trace elements in water. During their transport, heavy metals are distributed between the aqueous phase and the suspended sediment. Partitioning of heavy metals between the suspended matter and water is described in terms of the distribution coefficient K_d (m^3 g^{-1}), expressed as the concentration ratio under equilibrium conditions.[18,10]

The minimum and maximum values of the distribution coefficients of the four examined metals for high (spring) and low (autumn) water level at the six locations are presented in Figs. 2–5, respectively. The K_d coefficients decreased in the order Cd>Pb>Cu≈Zn. The distribution coefficients of all the investigated heavy metals demonstrate the capability of the sediment to accumulate each of the metals.

Fig. 2. The minimum K_d values at high water levels for 6 locations (spring, period 2005–2009). Locations and distances from the mouth of the sampling stations on the Danube River: 1) Belgrade, 1162 km; 2) Smederevo, 1116 km; 3) Veliko Gradište, 1059 km; 4) Donji Milanovac, 990 km; 5) Tekija, 955 km and 6) Kladovo, 944 km.
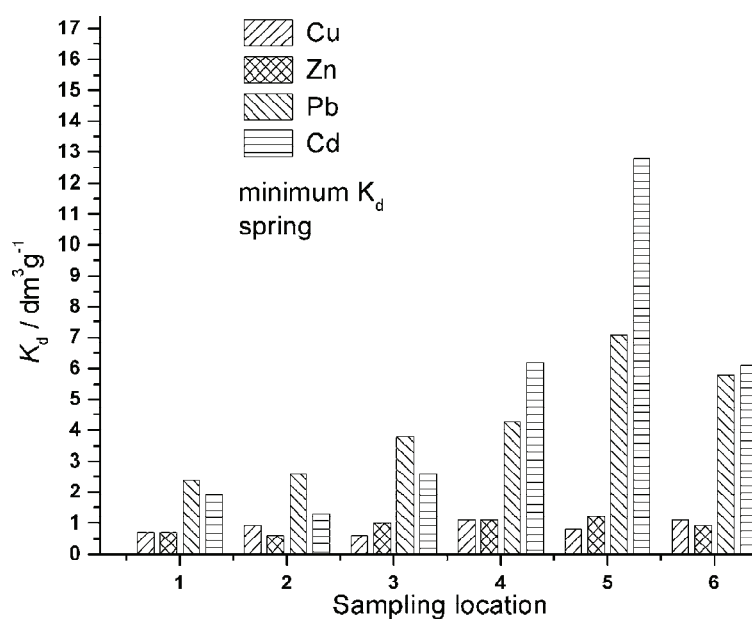
Fig. 3. The maximum K_d values at high water levels for 6 locations (spring, period 2005–2009). Locations and distances from the mouth of the sampling stations on the Danube River: 1) Belgrade, 1162 km; 2) Smederevo, 1116 km; 3) Veliko Gradište, 1059 km; 4) Donji Milanovac, 990 km; 5) Tekija, 955 km and 6) Kladovo, 944 km.
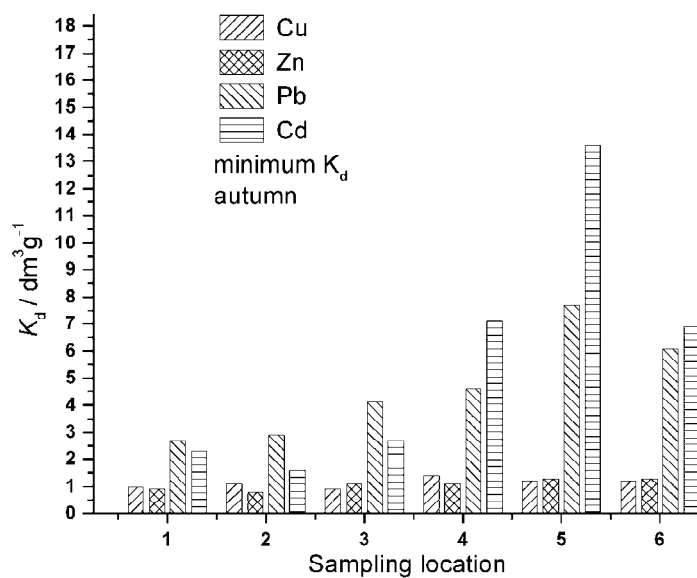
Fig. 4. The minimum Kd values at low water levels for 6 locations (autumn, period 2005–2009). Locations and distances from the mouth of the sampling stations on the Danube River:1) Belgrade, 1162 km; 2) Smederevo, 1116 km; 3) Veliko Gradište, 1059 km; 4) Donji Milanovac, 990 km; 5) Tekija, 955 km and 6) Kladovo, 944 km.
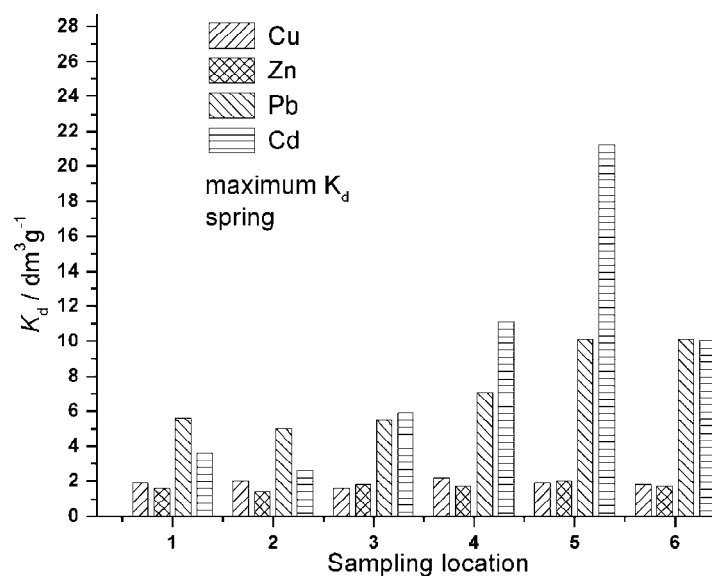
Fig. 5. The maximum K_d values at low water levels for 6 locations (autumn, period 2005–2009). Locations and distances from the mouth of the sampling stations on the Danube River: 1) Belgrade, 1162 km; 2) Smederevo, 1116 km; 3) Veliko Gradište, 1059 km; 4) Donji Milanovac, 990 km; 5) Tekija, 955 km and 6) Kladovo, 944 km.
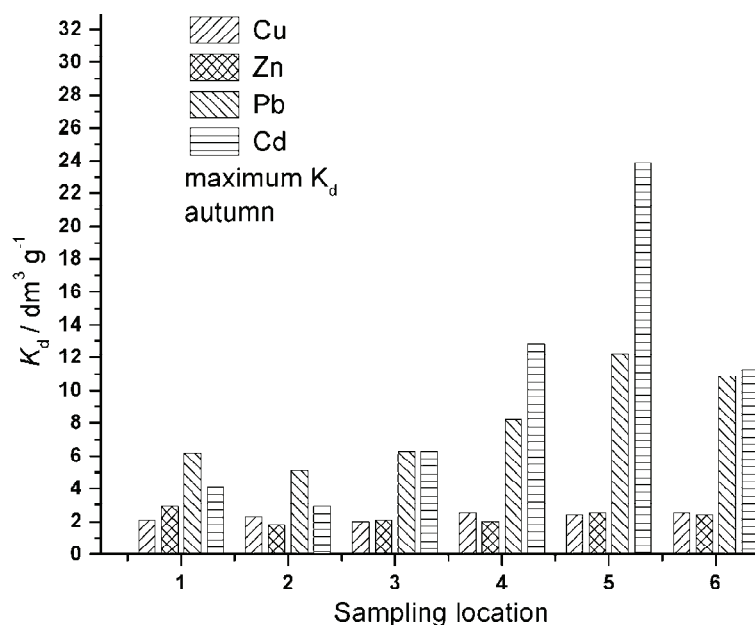
The behaviors of heavy metals depend on hydraulic and geo-chemical processes. For an evaluation of toxicity, it is important to determine the fluxes of the heavy metals from the river water to the sediment and *vice versa*, and from the sediment to the deep sediment. The fraction in the sediment is not expected to present a direct danger provided that the metal ions are immobilized due to encapsulation. Thus, distribution coefficients between the sediment and the river water indicate to the exchangeable and mobile fractions of the heavy metals responsible for the eco-toxicological potential of heavy metals.

The interaction of dissolved heavy metals in river water with suspended solids and bottom sediment is based on the hypotheses of a reversible and rapid equilibrium between dissolved (c_w, mg m^{-3}) and the adsorbed (c_s, mg kg^{-1}) phases of the heavy metals, where:

$$K_d = c_s/c_w \qquad (2)$$

The partitions of the heavy metals between the different phases presented the opportunity to apply models for predicting their behavior in the Iron Gate reservoir. In this study, models for predicting the migration of radionuclides through rivers[18] were applied in order to evaluate the contamination level of the River Danube ecosystem and its anthropogenic intake of heavy metals.

The Moira model calculated the radionuclide flux from water to sediment (F_{ws}) by multiplying the concentration of dissolved radionuclide by the migration velocity (v) and the sedimentation velocity (v_s). The Moira model was applied to calculate the heavy metal flux from water to sediment (F_{ws}):

$$F_{ws} = (v + v_s)c_w \qquad (3)$$

The flux of heavy metal migrating to the sediment due to sedimentation is given by:

$$F = S_r K_D c_w \qquad (4)$$

where S_r is the net sedimentation rate (kg m^{-2} s^{-1}).

The heavy metal flux from sediment to water (often called re-suspension) can be calculated using the formula:

$$F_{sw} = K_{sw} D_{ep} \qquad (5)$$

where K_{sw} is the rate of migration (s^{-1}) and D_{ep} is the heavy metal deposit (kg m^{-2}).

The non-reversible process of tracer interaction with bottom sediment is modeled by the equation:

$$F_{ds} = K_{ds} D_{ep} \qquad (6)$$

The fluxes from water to sediment (F_{ws}) according to Eq. 3 (in 10^8 kg m^{-2} s^{-1}) were 1.5–2.6 for Cu; 2.4–3.2 for Zn; 2.3–3.8 for Pb and 3.8–7.8 for Cd. The fluxes were calculated using a value for the velocity ($v+v_s$) of 3.5×10^{-7} m s^{-1}. This value for velocity was taken from a published modeling study,[19] while taking into account that the published data were determined for ^{90}Sr. The analogy with heavy metals comes from the similar mobility in the aquatic environment. The rate of migration, K_{sw}, according to the Moira model (Eq. (5)), was 5.6×10^{-9} s^{-1}, which implies values of heavy metal flux from sediment to water of the order of magnitude 10^{-12}–10^{-10} kg m^{-2} s^{-1}.

The migration rate to the deep sediment K_{ds} (Eq. (5)) accounts for non-reversible processes that prevent the re-suspension of heavy metals to water. These processes are significant for ^{137}Cs, while negligible for ^{90}Sr.[18] The present results lead to a similar conclusion for the investigated heavy metals. Irreversible processes of heavy metals migration to the deep sediment were not significant, and neither were processes of re-suspension. The implicit enrichment of heavy metals in the sediment can be recognized from the differences in the K_d values, which originate from the intake of heavy metals from anthropogenic sources. The high total concentrations of heavy metals in sediment may not necessarily indicate anthropogenic contamination because of the different background levels in the parent materials and sediment properties.[20] In addition, heavy metals in fluvial systems can be transported along hydraulic gradients for hundreds of kilometers in a relatively short time.[21]

The distribution coefficient K_d is often used to characterize the mobility of heavy metals in aquatic environments.[22] Low K_d values indicate that most of the metals present in the system remain in the water phase and are available for transport, chemical processes, and plant uptake; on the other hand, large K_d values reflect a large affinity of sediment for heavy metals. The relatively high K_d values in the Iron Gate reservoir of the Danube imply that the sorption capacity of its sediment is far from saturated, despite the adsorption mechanism. Heavy metals occupied an initial region on vacant sites, nearly linear for the K_d values. Enriched sediment concentrations of heavy metals originating from anthropogenic sources under such conditions do not indicate the level of contamination. In the case of contamination, the K_d values will be lower and the concentrations heavy metals in the river water higher. The enrichment of pollutants in river sediment usually reflects upstream source(s) of heavy metals resulting from anthropogenic contamination. Comparisons of the minimum and maximum K_d values (Figs. 2–5) imply a negligible anthropogenic impact of Cu and Zn, but for sites 4 to 6, it imply anthropogenic influence and enrichment of Pb and Cd in the sediment at distances of about 50 km before the dam.

This means that instead of the total metal concentration, the changes in K_d could be used as a criterion to assess potential effects of sediment concentrations of heavy metals. The use of total metal concentration as a criterion to assess the potential effect of sediment concentrations implies that all forms of a given metal have an equal impact on the environment; such an assumption is untenable.[20]

Distribution of long-lived radionuclides

The accumulation of long-lived radionuclides in the River Danube ecosystem was the subject of a previous study.[23] It was proven that the natural radioactivity of the Danube sediment reflects an equilibrium distribution. The concentrations of long-lived natural radionuclides in the sediment practically did not change in years 2005–2009. The activities measured were ^{238}U: 23–34 Bq kg^{-1} and ^{232}Th: 26–45 Bq kg^{-1}. Unlike the examined heavy metals, the input of the heavy metals uranium and thorium originated mainly from diffuse sources of geogenic origin, ascertained from the small fluctuation in concentrations and absence of point sources. Compared to results of 20 years ago, there were no oscillations in the thorium content.[23]

In addition to the natural radioactivity, there is also anthropogenic radioactivity present in the Danube river ecosystem, because of nuclear weapons tests and the Chernobyl nuclear accident. In the Danube sediment, measurable concentrations of ^{137}Cs were also detected because of the Chernobyl fallout. The concentrations of ^{137}Cs found in the sediment were between 4.0 and 11.0 Bq kg^{-1}. In earlier findings, the radioactivity from ^{137}Cs in the river water was below 0.01 Bq L^{-1} and in the sediment between 12 and 33 Bq kg^{-1}. The present results show an absence of further accumulation of radionuclides in the River Danube sedi-

ment. The equilibrium distribution of ^{137}Cs implies the rate of decline in the concentrations ^{137}Cs activity in river water, corresponding to an effective ecological half life (T_{eff}) in the 11–22-year range.[24]

The measurements of radionuclides accumulation in the sediment show that the concentration of Cs is lower near the River Danube mouth than in its estuary itself. The Cs is transported *via* sea currents, rather than by river waters. In addition, river slime sediment contains lower Cs concentration than sea slime sediment.[25]

CONCLUSIONS

This study was based on the application of the distribution law in determining the coefficients of distribution of heavy metals between solid and liquid phases, and models for predicting the migration of traceable metals (heavy metals and radionuclides) through rivers. The fluxes of heavy metals from water to sediment and *vice versa* show their accumulation in sediment, which is a mayor concern in the assessment of the effects of anthropogenic influences. This approach enables the determination of the degree of accumulation of heavy metals and their impact as potentially hazardous to the environmental and human health.

The levels of heavy metals in the Danube water and sediment along the Iron Gate reservoir displayed seasonal fluctuations, with an accumulation before the dam. Anthropogenic origin was indicated only for Cd and Pb.

Effective ecological half-life (T_{eff}) of ^{137}Cs in the river water ranged from 11 to 22 years.

И З В О Д

НОВИ ПРИСТУП У АНАЛИЗИ АКУМУЛИРАЊА И КОНЦЕНТРОВАЊА ТЕШКИХ МЕТАЛА У ЂЕРДАПСКОЈ АКУМУЛАЦИЈИ

ЖИВОРАД ВУКОВИЋ[1], ДУБРАВКА ВУКОВИЋ[2], МИРЈАНА РАДЕНКОВИЋ[1] и СРБОЉУБ СТАНКОВИЋ[1]

[1]Инсtиtуt за нуклеарне науке Винча, ū. ūр. 502, 11001 Беоīрад и [2]Научни инсtиtуt за веtеринарсtво Србије, Војводе Тозе 14, 11000 Беоīрад

Одређиване су концентрације тешких метала (Cu, Zn, Pb и Cd) и дугоживећих радионуклида (U, Th и Cs) у води и седименту Дунава и Ђердапске акумулације на шест локација дужине тока 200 km. Концентрације тешких метала у седименту биле су у опсегу од 27,9––149,31 mg kg^{-1} за бакар, 55,2–228,4 mg kg^{-1} за цинк, 13,5–71,6 mg kg^{-1} за олово, 0,3–25,2 mg kg^{-1} за кадмијум и 4,0–17,5 Bq kg^{-1} za [137]Cs. Ове вредности су у корелацији са њиховим вредностима у речној води ако се изразе помоћу коефицијента расподеле (K_d) између чврсте и течне фазе. Понашање тешких метала оцењено је на основу примене модела за прогнозирање понашања полутаната у рекама. Одређени су флуксеви тешких метала из воде у седимент и обрнуто.

(Примљено 17. фебруара, ревидирано 30. јуна 2011)

REFERENCES

1. B. Song, M. Lei, T. Chen, Y. Zheng, Y. Xie, X. Li, D. Gao, *J. Environ. Sci.* **21** (2009) 1702
2. K. P. Singh, A. Malik, N. Basant, V. K. Sing, A. Basant, *Chemom. Intell. Lab. Syst*. **87** (2007) 185
3. S. Audry, J. Schafer, G. Blanc, J. M. Jouananneau, *Environ. Pollut*. **132** (2004) 413
4. C. K. Jain, *Water Res.* **38** (2004) 569
5. W. Zhang, H. Feng, J. Chang, J. Qu, H. Xie, L. Yu, *Environ. Pollut.* **157** (2009) 4318
6. B. Xu, X. Yang, Z. Gu, Y. Zhang, Y. Chen, Y. Lv, *Chemosphere* **75** (2009) 442
7. P. Woitke, J. Wellmitz, D. Helm, M. Kube, P. Lepom, P. Litheraty, *Chemosphere* **51** (2003) 633
8. A. L Tuna, F. Yilmaz, A. Demirak, N. Ozdemir, *Environ. Monit. Assess*. **125** (2007) 47
9. M. Camusso, S. Galassi, D. Vignati, *Water Res*. **36** (2002) 2491
10. A. Kaushik, A. Kansal, S. Meena, S. Kumari, C. P. Kaushik, *J. Hazard. Mater.* **164** (2009) 265
11. Z. Vuković, M. Radenković, S. Marković, D. Vuković, *J. Serb. Chem. Soc*. **76** (2011) 795
12. R. Reeve, *Environmental Analysis*, Wiley, New York, 1994
13. S. Murko, R. Milacić, M. Veber, J. Scantar, *J. Serb. Chem. Soc*. **75** (2010) 113
14. A. E. Greenberg, Ed., *Standard methods for the Examination of Water and Wastewater*, 19th ed., American Public Health Association, Washington (DC), 1995
15. W. Salomons, U. Forsters, *Metals in Hydrosphere*, Springer, Berlin, 1984
16. S. Olivares Rieumont, D. Rosa, L. Lima, D. W. Graham, K. D. Alessandro, J. Borroto, F. Martinez, J. Sanchez, *Water Res.* **39** (2007) 3945
17. S. M. Sakan, D. S. Djordević, D. D. Manojlović, P. S. Polić, *J. Environ. Manag.* **90** (2009) 3382
18. L. Monte, P. Boyer, J. E. Brittain, L. Hakanson, S. Lepicard, J. T. Smith, *J. Environ. Radioac.* **79** (2005) 273
19. L. Monte, *Environ. Modell. Software* **669** (2001) 13
20. K. P. Singh, D. Mohan, V. K. Singh, A. Malik, *J. Hydrol.* **312** (2005) 14
21. W. X. Liu, X. D. Li, Z. G. Shen, D. C. Wang, O. W. H. Wai, Y. S. Li, *Environ. Pollut*. **121** (2003) 377
22. M. T. Morera, J. C. Echeverria, C. Mazkiaran, J. J. Garrido, *Environ. Pollut.* **113** (2001) 135
23. Ž. Vuković, V. Sipka, D. Vuković, D. Todorović, *J. Radioanal. Nucl. Chem.* **268** (2006) 247
24. J. T. Smith, R. T. Clarke, M. Saxén, *J. Environ. Radioac.* **49** (2000) 65
25. A. Strezov, M. Milanov, P. Mishev, T. Stoilova, *Appl. Radiat. Isotopes* **49** (1998) 721.

Studies of the adsorption thermodynamics and kinetics of Cr(III) and Ni(II) removal by polyacrylamide

HASSAN ZAVVAR MOUSAVI[1]*, ABDORRAHMAN HOSSEINIFAR[2]
and VAHDAT JAHED[2]

[1]*Chemistry Department, College of Sciences, Semnan University, Semnan, Iran and* [2]*Aja University of Medical Sciences, Tehran, Iran*

Abstract: Polyacrylamide (PAA) was investigated as an adsorbent for the removal of Ni(II) and Cr(III) metal ions from synthetic aqueous solutions. Different variables affecting the adsorption capacity of the adsorbent, *i.e*., contact time, pH of the sorption medium, metal ion concentration and temperature of the solution, were investigated by batch sorption experiments. The adsorption equilibrium data was best fitted by the Langmuir isotherm model. The maximum adsorption capacities were found to be 84.03 and 32.67 mg g^{-1} polyacrylamide for Cr(III) and Ni(II), respectively. Three kinetic models, *i.e*., the pseudo-first-order, pseudo-second-order and intra-particle diffusion equations, were selected to follow the adsorption process. The kinetic parameters, *i.e*., rate constants, equilibrium adsorption capacities and related correlation coefficients, for each kinetic model were calculated and are discussed. It was indicated that the adsorption of both ions onto polyacrylamide could be described by the pseudo-second-order kinetic model. Various thermodynamic parameters, such as ΔH, ΔS and ΔG, were also evaluated and it was found that the sorption was feasible, spontaneous and exothermic.

Keywords: adsorption; polyacrylamide; Cr(III); Ni(II); kinetic.

INTRODUCTION

The presence of heavy metals in the aquatic ecosystem poses human health risks and causes harmful effects to living organisms in water and to their consumers. The wastewater from mining, painting and printing processes, plumbing, automobile batteries and petrochemical industries contains undesirable amounts of heavy metals ions. Heavy metal ions, such as lead, cadmium, mercury, chromium, nickel, zinc and copper, are non-biodegradable and can be toxic and carcinogenic, even at very low concentrations. Hence, they usually pose a serious threat

---

393

to the environmental and public health.[1–3] Heavy metal containing effluents are generated in the following industrial processes: tanning, mining of chrome ore, production of steel and alloys, metal finishing, pigments manufacture, the photographic industry, glass manufacture, wood preservation, the use of chromium salts as corrosion inhibitor in industrial cooling water treatment, the textile industry and many others.[4–6]

Chromium is a highly reactive element. It exists in six oxidation states, of which Cr(III) and Cr(VI) are the two most stable states. Chromium forms stable complexes, such as $Cr_2O_7^{2-}$, $HCrO_4^-$, CrO_4^- and $HCr_2O_7^-$. The fraction of these complexes varies with pH and at low pH, Cr exists as negatively charged dichromate ions. The chronic toxicity of nickel to humans and the environment is well documented. High concentrations of nickel cause cancer of lungs, nose and bone. At very high levels of exposure, nickel salts are known to be carcinogenic. In view of the toxic effects of nickel to human and animal life, it is important to treat industrial effluents polluted with Ni(II) ions before their discharge into the receiving water bodies.[7,8]

Due to the toxic and non-degradable nature of metallic species, the scientific community has worldwide carried out significant work on their removal from aqueous solutions and industrial effluents. Several treatment processes have been developed over the years to remove heavy metals dissolved in water and wastewaters: chemical precipitation,[9] membrane processes,[10] ion-exchange,[11,12] electrochemical,[13-15] membrane filtration,[16] reverses osmosis,[17] the employment of complexing agent[18] and ion flotation.[19] However, these techniques have disadvantages including incomplete metal removal, high consumption of reagents and energy, low selectivity, high capital and operational cost and the generation of secondary wastes the disposal of which is difficult. For these reasons, cost-effective alternative technologies for treatment of metal-contaminated waste streams are required. Adsorption[20–25] has proved to be one of the respective methods, which is a simple, selective and economical process for the removal of heavy metal ions from aqueous solutions.

Many researchers have studied on the feasibility of materials such as agricultural waste,[26] sawdust,[27,28] eggshell,[29] waste brewery yeast,[30] lichen,[31] waste tire rubber ash,[32] aliphatic polyamines,[33] orange peel,[34] zeolites,[35,36] poly(ethyleneglycol methacrylate),[37] poly(ethyleneglycol dimethacrylate-1-vinyl-1,2,4-triazole),[38] polybenzoxazine,[39] and zwitterionic hybrid polymer[40] for the removal of heavy metal ions from aqueous solutions.

Polyacrylamide is one of the most widely used polymers for several purposes. Three-dimensional polyacrylamide networks can absorb large amounts of water compared with other water absorbing materials. They can also show stimuli-responsive properties to various external parameters such as temperature, pH, solvent composition, and salt composition depending on the type of func-

tional groups in the structure. Polyacrylamide is a polymer with large numbers of amide side groups. It has been successfully grafted onto the surfaces of various matrices as selective sorbents for the removal of pollutants, such as dyes and heavy metals from aqueous solutions.[41–43]

The aim of the present batch adsorption study was to study the adsorption capacity of PAA for Ni(II) and Cr(III) metal ions. The effect of variable factors, such as contact time, initial concentration of the metal ions, adsorbent dose, pH and temperature, on the removal of both ions was investigated. Langmuir and Freundlich models were used to describe the adsorption isotherms. The adsorption kinetics of both ions with PAA was studied.

EXPERIMENTAL

Materials and apparatus

All employed reagents were of analytical grade. Test solutions of heavy metal ions were prepared from their nitrate salts (Merck, Darmstadt, Germany) by serial dilution of stock nickel and chrome ion solution (1000 mg L^{-1}) using deionized distilled water (Milli-Q, Milipore). Blank solution of deionized distilled water was analyzed by atomic absorption spectroscopy (AAS) to ensure that it did not contain nickel or chromium ions. Polyacrylamide was obtained from Guangzhou Chemical Reagent Factory, Guangzhou, China. A Shimadzu AA--680/G (Japan) atomic absorption spectrophotometer equipped with single-element hollow cathode lamps and an air–acetylene burner was used for the determination of the metal ions. A Metrohm E-632 pH meter (Switzerland) with a glass combination electrode was used throughout this study.

Preparation of the adsorbent

Polyacrylamide (PAA) was immersed in distilled water for three hours. The swollen gels were taken out of the solution at regular time intervals, wiped superficially with filter paper, weighed and replaced in the same solution until a state of equilibrium swelling was obtained.

Batch adsorption studies

The batch studies were conducted by mixing PAA with Ni(II) and Cr(III) metallic solutions prepared in the laboratory. The samples were stirred at room temperature at 100 rpm and after the required time their content was filtered through 0.45 µm membrane filter using a vacuum pump. The progress of adsorption was assessed by determining the residual concentration of both ions in the sample solution by AAS.

The removal percentage of metallic cations from aqueous solution was calculated using the following equation:

$$R = 100\frac{c_i - c_e}{c_i} \tag{1}$$

where c_i and c_e are the initial and final concentration of both ions in the solution respectively. The adsorption capacity of an adsorbent, which is obtained from the mass balance on the sorbate, in a system with solution volume V is often used to acquire experimental adsorption isotherms. Under the experimental conditions, the adsorption capacities of the adsorbent at equilibrium (q_e) for each concentration of Ni(II) and Cr(III) ions were calculated using Eq. (2):

$$q_e \; (\text{mg g}^{-1}) = \frac{V(c_i - c_e)}{M} \tag{2}$$

where V is the volume of solution (L) and M is the mass of adsorbent (g) used.

The reported value of metal ions adsorbed by the adsorbent in each test was the average of at least three measurements.

RESULTS AND DISCUSSION

Effect of contact time

The rate of removal of Ni(II) and Cr(III) from solution is shown in Fig. 1, from which it can be seen that the adsorption of Ni(II) and Cr(III) reached equilibrium after a contact time of 90 min, while the removal efficiency for Ni and Cr at equilibrium was 68.0 and 94.2 %, respectively. The rate of the removal of Ni and Cr gradually decreased with increasing contact time. Initially, the uptake rate was higher because all sites on the PAA were vacant and the concentration was high, but the decrease of sorption sites reduces the uptake rate. As is shown Fig. 1, desorption occurred after saturation. Therefore, considering technical and economic aspects, a contact time of 90 min was chosen for nickel and chromium removal from aqueous solution by adsorption by PAA.
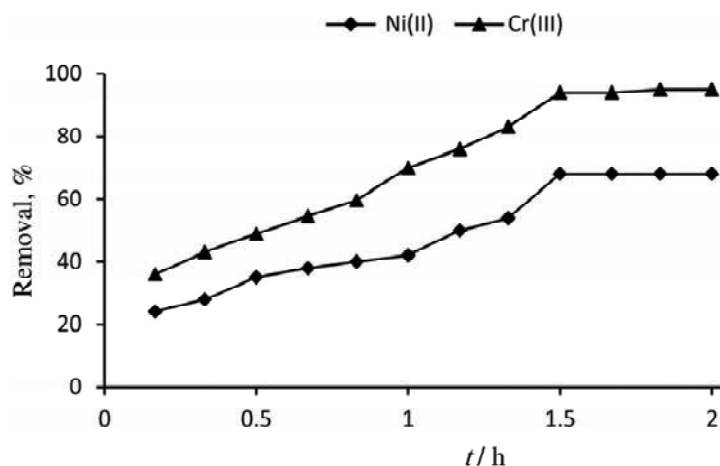

Fig. 1. Effect of contact time on the adsorption of Cr(III) and Ni(II) onto PAA. Conditions: 0.7 g L^{-1} PAA, pH 5, 100 mL 50 mg L^{-1} metal ions solution, contact time 1.5 h, temperature 298 K, agitation speed 100 rpm.

Effect of the amount of adsorbent

The effect of adsorbent dosage on the removal of Ni(II) and Cr(III) is shown in Figs. 2 and 3, respectively. It is clear from the figures that the percentage removal of the metal ions increased with increasing weight of the adsorbent. This is an expected result because as the amount of adsorbent increased, the available

surface area increased, thereby exposing more active sites for the binding of metal ions. A similar trend of the effect of the adsorbent concentration was observed and is discussed in the literature.[44]
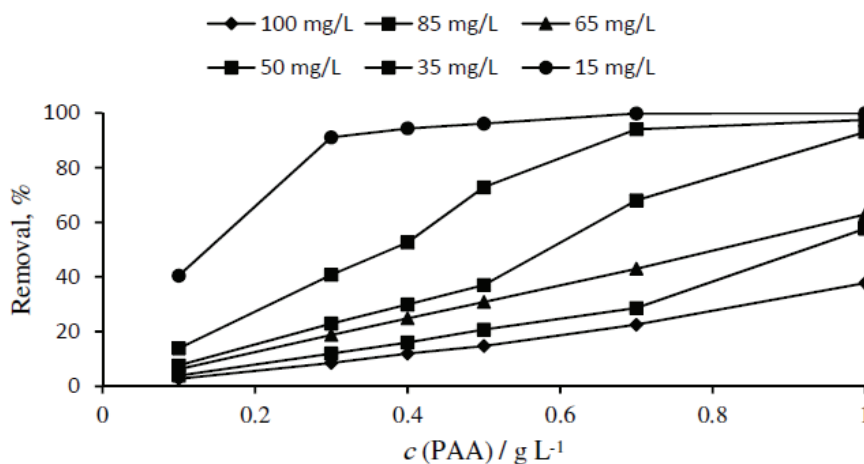

Fig. 2. Effect of adsorbent dose on the adsorption of Ni(II). Conditions: 100 ml 50 mg L^{-1} Ni(II), agitation speed: 100 rpm; contact time 1.5 h, pH 5, temperature: 298 K.
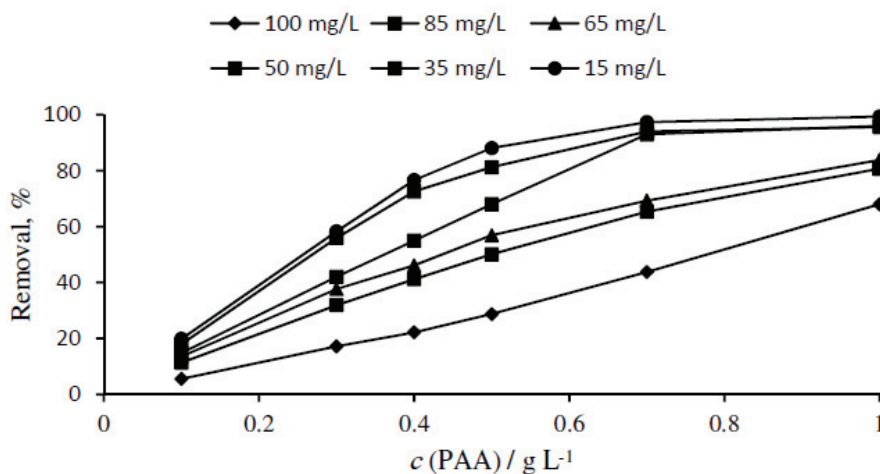

Fig. 3. Effect of adsorbent dose on the adsorption of Cr(III). Conditions: 100 ml 50 mg L^{-1} Cr(III), agitation speed: 100 rpm; contact time 1.5 h, pH 5, temperature: 298 K.

Effect of temperature

To study the thermodynamic properties of adsorption, experiments were performed at 298, 308, 318 and 328 K. The adsorption of Cr(III) and Ni(II) by PAA as a function of temperature is illustrated in Fig. 4. The results showed that the adsorption capacity for Ni(II) and Cr(III) decreased from 81.4 to 21.0 % and from

64.1 to 11.3%, respectively, with increase temperature, indicating that the process is exothermic.
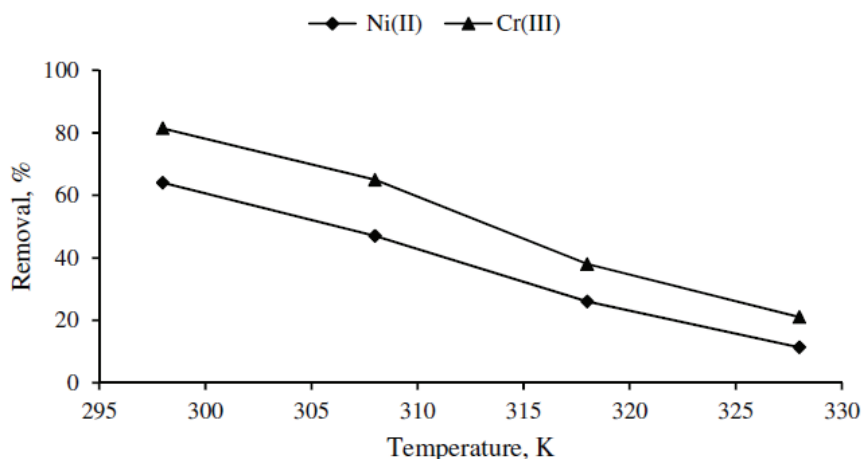

Fig. 4. Effect of temperature on the adsorption of Cr(III) and Ni(II) onto PAA. Conditions: 0.7 g L^{-1} PAA, pH 5, 100 mL 50 mg L^{-1} metal ions solution, contact time 1.5 h, temperature 298 K, agitation speed 100 rpm.

Effect of pH

The variation in the adsorption of the both ions was studied in the pH range of 2–6, at which values chemical precipitation was avoided. It is clear from the results shown in Fig. 5 that the removal was low at lower pH values; however, with increasing pH, a significant enhancement in the adsorption was recorded. The optimum pH for the removal of both ions was found to be in the range 4.0––6.0. The variation of adsorption with pH can be explained by considering the charge of the ions and the electro–kinetic behavior of PAA. At lower pH values, more protons are available to protonate the amino groups of PAA, therefore, the attractions of both cationic ions decreased. Under strongly basic conditions, the negatively charged phenolic hydroxyl groups become potential active sites (NH$_2$) and could be attracted by the ammonium groups in the absorbents. At pH value higher than 6, both ions precipitated as hydroxides, which decreased the rate of adsorption and consequently the percent removal of the metal ions).

Isotherm studies

Equilibrium data, commonly known as adsorption isotherms, are the basic requirements for the design of a sorption system. The linear form of the Langmuir and Freundlich models are given by Eqs. (3) and (4), respectively:

$$\frac{c_e}{q_e} = \frac{1}{Q_m b} + \frac{c_e}{Q_m} \tag{3}$$

$$\log q_e = \log K_F + \frac{1}{n}\log c_e \qquad (4)$$

where q_e is the amount adsorbed at equilibrium (mg g^{-1}) and c_e is the equilibrium concentration of metal ions in solution (mg L^{-1}). The other parameters are isotherm constants, which can be determined by regression of the experimental data. In the Langmuir equation, Q_m (mg g^{-1}) is a measure of adsorption capacity under the experimental conditions and b is a constant related to the energy of adsorption (L mg^{-1}). Freundlich treatment gives the parameters, n, indicative of the bond energies between the metal ion and the adsorbent and K_F (mg^{1-n} L^n g^{-1}) related to the bond strength.
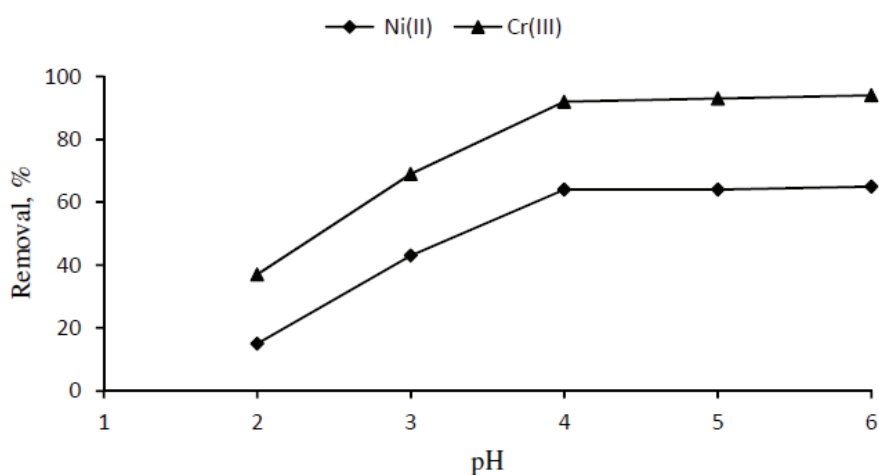

Fig. 5. Effect of pH on the adsorption of Cr(III) and Ni(II) onto PAA. Conditions: 0.7 g L^{-1} PAA, 100 mL 50 mg L^{-1} metal ions solution, contact time 1.5 h, temperature 298 K, agitation speed 100 rpm.

The plot of c_e/q_e as a function of c_e allows the calculation of the Q_m and b values. From the adsorption parameters, the maximum adsorption capacity of the both ions by the adsorbent and the Langmuir constant can be evaluated. Values of K_F and n may be calculated by plotting log q_e *vs*. log c_e. The slope is equal to *1/n* and the intercept to log K_F. As mentioned above, the isotherm constants for both models at specific pH values were determined from the respective plots and are presented in Table I. Regression values (R^2) presented in Table I indicate that the adsorption data for Ni(II) and Cr(III) removal are fitted well by the Langmuir isotherm for both metal ions.

TABLE I. Values of the Langmuir and Freundlich constants for the adsorption of Ni(II) and Cr(III)

Ion	Langmuir			Freundlich		
	Q_m / mg g^{-1}	b / L mg^{-1}	R^2	K_F / mg^{1-n} L^n g^{-1}	n	R^2
Cr(III)	84.03	0.05	0.99	13.65	2.75	0.92
Ni(II)	32.67	1.03	0.98	5.38	1.62	0.79

A comparison of adsorption capacity of PAA with some previously used adsorbents is provided in Table II. The results show that PAA is very effective for the removal of Ni(II) and Cr(III) from aqueous solutions and the removal efficiencies of Ni(II) and Cr(III) obtained by PAA were comparable with literature data.

TABLE II. Comparison of the Langmuir constants for Ni(II) and Cr(III) adsorption onto PAA

Adsorbent	Adsorbent capacity, mg g^{-1}		
	Ni(II)	Cr(III)	Reference
Ilgın lignite	13.0	–	45
Synthesized zeolite	–	75.5	46
Gum kondagogu	50.5		47
Peat	–	22.36	48
Black gram husk	19.56	–	49
PAA	32.67	84.03	This study

Adsorption kinetics

In order to investigate the controlling mechanism of the adsorption process such as mass transfer and chemical reaction, the pseudo-first-order, pseudo-second-order kinetics and the intra-particle diffusion models were used to test the experimental data of the adsorption of chromium and nickel ions by PAA.

Pseudo-first order model

The pseudo-first order model is one of the most widely used procedures for the adsorption of a solute from an aqueous solution.[50] The pseudo-first order equation can be expressed as follows:

$$\ln (q_e - q_t) = \ln q_e - k_1 t \tag{5}$$

where q_t is the amount of metal ions adsorbed at time t (mg g^{-1}), q_e (mg g^{-1}) is equilibrium solid phase concentration and k_1 is first order rate constant for adsorption (L min^{-1}). The plot of $\ln (q_e-q_t)$ *vs.* t should result in a straight line. The rate constant can be calculated from the slope of the straight line.

Pseudo-second order model

The pseudo-second order equation is based on the adsorption capacity of the solid phase. Contrary to other models, it predicts the behavior over the whole

range of adsorption.[51] Pseudo-second order model based on the equilibrium adsorption capacity may be expressed in the form:

$$\frac{t}{q_t} = \frac{1}{k_2 q_e^2} + \frac{t}{q_e} \tag{6}$$

where k_2 (g mg^{-1} min^{-1}) is the rate constant of pseudo-second order adsorption. The plot of t/q_t vs. t should yield a straight line (Fig. 6), which allows the computation of k_2.
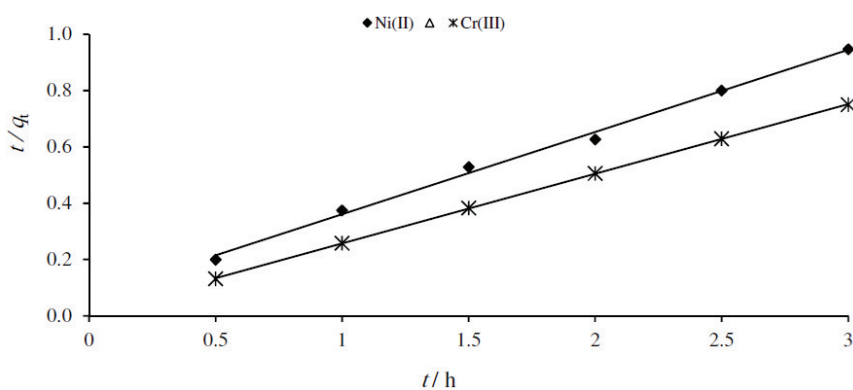

Fig. 6. Pseudo second-order sorption kinetics of Cr(III) and Ni(II) onto PAA.

Intra-particle diffusion

Intra-particle diffusion was explored using the intra-particle diffusion model given in Eq. (7)

$$q_t = k_{id} t^{1/2} \tag{7}$$

where k_{id} is the intra-particle diffusion rate constant and the meanings of the other terms have already been defined. This model predicts that the plot of q_t vs. $t^{1/2}$ should be linear if intra-particle diffusion is involved in the sorption process. Intra-particle diffusion is the rate-controlling step if the line passes through the origin.[52]

The application of the different kinetic models unveiled some interesting features regarding the mechanism and rate-controlling step of the overall sorption process. The kinetic parameters of both ions onto PAA under different conditions were calculated and are given in Table III. To quantify the applicability of each model, the correlation coefficient, R^2, was calculated for these plots. The linearity of these plots indicates the applicability of the three models. However, the correlation coefficients, R^2, showed that the pseudo-second-order model, an indication of a chemisorptions mechanism, fits better the experimental data ($R^2 \geq \geq 0.998$) than the pseudo-first-order and the intra-particle diffusion kinetic models (Table III and Fig. 5).

Thermodynamic parameters

The thermodynamic parameters, *i.e*., the Gibb's free energy (ΔG), enthalpy (ΔH) and entropy (ΔS) change of adsorption, can be evaluated from the following equations:[53]

$$K_c = \frac{c_{Ae}}{c_e} \tag{8}$$

where K_c is the equilibrium constant, c_{Ae}, and c_e (both in mg L^{-1}) are the equilibrium concentrations for the solute on the sorbent and in solution, respectively.

TABLE III. Kinetic parameters for the adsorption of Ni(II) and Cr(III) onto PAA

Parameter	Cr(III)	Ni(II)
Pseudo-first-order model		
k_1 / 10^{-2} min^{-1}	8.2	7.6
R^2	0.942	0.881
q_e (experimental), mg g^{-1}	19.25	7.54
q_e (kinetic plot), mg g^{-1}	16.35	5.37
Pseudo-second-order model		
k_2 / 10^{-4} g mg^{-1} min^{-1}	5.7	1.6
R^2	0.999	0.998
q_e (experimental), mg g^{-1}	19.25	7.54
q_e (kinetic plot), mg^{-1} g	19.21	7.38
Intra-particle diffusion model		
k_{id} / mg g^{-1} min$^{-1/2}$	5.347	1.873
R^2	0.923	0.903

To determine ΔG, the K_c values were used in Eq. (9):

$$\Delta G = -RT \ln K_c \tag{9}$$

K_c may also be expressed in terms of ΔH (kJ mol^{-1}) and ΔS (J mol^{-1} K^{-1}) as a function of temperature:

$$\ln K = \frac{\Delta S}{R} - \frac{\Delta H}{RT} \tag{10}$$

A plot of ln K_c as a function of 1/T yields a straight line. The ΔH and ΔS parameters were calculated from the slope and intercept of the plot, respectively.

The Gibbs free energy change (ΔG) was calculated to be –7.10, –5.05, –3.16, and –2.34 kJ mol^{-1} for Ni(II) adsorption and –5.83, –3.79, –2.60, and –1.34 kJ mol^{-1} for Cr(III) adsorption at 298, 308, 318 and 328 K, respectively. The negative ΔG values indicate the thermodynamically feasible and spontaneous nature of the adsorption. The decrease in ΔG values shows a decline in the feasibility of the adsorption with increasing temperature. The ΔH parameter was found to be −57.44 and −76.13 kJ mol^{-1} for Ni(II) and Cr(III) adsorption, respectively. The ne-

gative ΔH values indicate the exothermic nature of the adsorption processes. The ΔS parameter was found to be 0.21 kJ mol⁻¹ K⁻¹ for Ni(II) and 0.25 kJ mol⁻¹ K⁻¹ for Cr(III) adsorption. The positive value of $\Delta S°$ suggests increased randomness at the solid/solution interface during the adsorption of Ni(II) and Cr(III) onto PAA.

CONCLUSIONS

The experimental results indicated that polyacrylamide could be successfully used for the removal of Ni(II) and Cr(III) ions from aqueous solutions. The developed adsorption studies demonstrated that the optimum pH values for Ni(II) and Cr(III) ions were in the range 4.0–6.0. The equilibrium adsorption data were very well fitted by the Langmuir model. The maximum adsorption capacities for Ni(II) and Cr(III) ions were found to be 32.67 and 84.03 mg g⁻¹, respectively. The adsorption of both ions obeyed pseudo-second-order equations with good correlations. Different thermodynamic parameters, *i.e.*, ΔH, ΔS and ΔG were also evaluated and it was found that the sorption is feasible, spontaneous and exothermic in nature. The positive value of the entropy change suggests increased randomness. The results show that polyacrylamide may be used effectively for the removal of Cr(III) and Ni(II) ions from aqueous solutions for environmental cleaning purpose.

И З В О Д

ИСПИТИВАЊЕ АДСОРПЦИОНЕ ТЕРМОДИНАМИКЕ И КИНЕТИКЕ УКЛАЊАЊА Cr(III) И Ni(II) ПОЛИАКРИЛАМИДОМ

HASSAN ZAVVAR MOUSAVI[1], ABDORRAHMAN HOSSEINIFAR[2] и VAHDAT JAHED[2]

[1]*Chemistry Department, College of Sciences, Semnan University, Semnan u*
[2]*Aja University of Medical Sciences, Tehran, Iran*

Испитиван је полиакриламид (PAA) као адсорбент при уклањању металних јона Ni(II) и Cr(III) из водених раствора. На бази шаржне сорпције испитиване су променљиве које утичу на адсорпциони капацитет адсорбента као што је време контакта, pH сорпционог медијума, концентрација металних јона и температура раствора. Подаци о адсорпционој равнотежи најбоље су апроксимирани моделом Ленгмирове изотерме. Нађено је да су максимуми адсорпционих капацитета 84,03, односно 32,67 mg g⁻¹ полиакриламида за Cr(III), односно Ni(II). За праћење адсорпционог процеса одабрана су три модела и једначине: псеудо-први ред, псеудо-други ред и интра-честична дифузија. За сваки модел израчунати су кинетички параметри као што су константе брзина реакција, равнотежни адсорпциони капацитети и одговарајући корелациони коефицијенти. Показало се да су адсорпције оба јона на полиакриламиду могле бити описане моделом кинетике псеудо-другог реда. Одређено је неколико термодинамичких параметара као што су ΔH, ΔS и ΔG, те је закључено да је сорпција изводљива, спонтана и егзотермна.

(Примљено 10. априла, ревидирано 16. јуна 2011)

REFERENCES

1. B. M. W. P. K. Amarasinghe, R. A. Williams, *Chem. Eng. J.* **132** (2007) 299
2. A. Demirbas, E. Pehlivan, F. Gode, T. Altun, G. Arslan, *J. Colloid Interface Sci. Surf.* **282** (2005) 20
3. E. M. Mohamed, F. O. Hafez, A. Alrefaay, M. M. Osman, *Desalination* **253** (2010) 9
4. V. Sarin, T. S. Singh, K. K. Pant, *Bioresour. Technol.* **97** (2006) 1986
5. V. K. Mishra, A. R. Upadhyaya, S. K. Pandey, B. D. Tripathi, *Bioresour. Technol.* **99** (2008) 930
6. M. N. Zafar, I. Abbas, R. Nadeem, M. A. Sheikh, M. A. Ghauri, *Water Air Soil Pollut.* **197** (2009) 361
7. A. Bhatnagar, A. K. Minocha, *Colloids Surf., B* **76** (2010) 544
8. N. Boujelben, J. Bouzid, Z. Elouear, *J. Hazard. Mater.* **163** (2009) 376
9. A. Esmaeili, A. Mesdaghi Nia, R. Vazirinejad, *Am. J. Appl. Sci.* **2** (2005) 1471
10. H. A. Qdais, H. Moussa, *Desalination* **164** (2004) 105
11. S. A Cavaco., S. Fernandes, M. M. Quina, L. M. Ferreira, *J. Hazard. Mater.* **144** (2007) 634
12. B. Galan, D. Castaneda, I. Ortiz, *Water Res.* **39** (2005) 4317
13. T. Subbaiah, S. C. Mallick, K. G. Mishra, K. Sanjay, R. P. Das, *J. Power Sources* **112** (2002) 562
14. K. N. Njau, M. vd. Woude, G. J. Visser, L. J. J. Janssen, *Chem. Eng. J.* **79** (2000) 187
15. G. Mouedhen, M. Feki, M. De Petris-Wery, H. F. Ayedi, *J. Hazard. Mater.* **168** (2009) 983
16. H. Bessbousse, T. Rhlalou, J.-F. Verchère, L. Lebrun. *J. Membrane Sci.* **307** (2008) 249
17. J. Yoon, G. Amy, J. Chung, J. Sohn, Y. Yoon, *Chemosphere* **77** (2009) 228
18. D. Kołodyńska, *Chem. Eng. J.* **152** (2009) 277
19. H. Polat, D. Erdogan, *J. Hazard. Mater.* **148** (2007) 267
20. S. Gupta, B. V. Babu,. *Bioresour. Technol.* **100** (2009) 5633
21. P. M. Choksi, V. Y. Joshi, *Desalination* **208** (2007) 216
22. W. Qiu, Y. Zheng, *Chem. Eng. J.* **145** (2009) 483
23. S. Lazarevic, I. Jankovic-Castavan, Z. Radovanovic, B. Potkonjak, D. Janackovic, R. Petrovic, *J. Serb. Chem. Soc.* **76** (2011) 101
24. L. V. A. Gurgel, R. P. de Freitas, L. F. Gil, *Carbohydr. Polym.* **74** (2008) 922
25. K. G. Bhattacharyya, S. S. Gupta, *Adv. Colloid Interface Sci.* **140** (2008) 114
26. U. K. Garg, M. P. Kaur, V. K. Garg, D. Sud, *Bioresour. Technol.* **99** (2008) 1325
27. B. Yasemin, T. Zek, *J. Environ. Sci.* **19** (2007) I60
28. M. Sciban, M. Klasnja, *Eur. J. Wood Wood Prod.* **62** (2004) 69
29. H. J. Park, S. W. Jeong, J. K. Yang, B. G. Kim, S. M. Lee, *J. Environ. Sci.* **19** (2007) 1436
30. S. Tonk, R. Maicaneanu, C. Indolean, S. Burca, C. Majdik, *J. Serb. Chem. Soc.* **76** (2011) 363
31. A. Sari, M. Tuzan, O. D. Uluozlu, M. Soylak, *Biochem. Eng. J.* **37** (2007) 151
32. H. Zavvar Mousavi, A. Hosseinifar, V. Jahed, *J. Serb. Chem. Soc.* **75** (2010) 845
33. C. Liu, R. Bai, L. Hong, T. Liu, *J. Colloid Interface Sci.* **345** (2010) 454
34. S. Liang, X. Guo, N. Feng, Q. Tian, *Trans. Nonferrous Met. Soc. China* **20** (2010) 187
35. T. Motsi, N. A. Rowson, M. J. H. Simmons, *Int. J. Miner. Process.* **92** (2009) 42
36. T. S. Jamil, H. S. Ibrahim, I. H. Abd El-Maksoud, S. T. El-Wakeel, *Desalination* **258** (2010) 34

37. E. Uguzdogan, E. B. Denkbas, E. Ozturk, S. A. Tuncel, O. S. Kabasakal, *J. Hazard. Mater*. **162** (2009) 1073
38. L. Uzun, A. Kara, N. Tuzmen, A. Karabakan, N. Besirli, A. Denizli, *J. Appl. Polym. Sci*. **102** (2006) 4276
39. T. Chaisuwan, T. Komalwanich, S. Luangsukrerk, S. Wongkasemjit, *Desalination* **256** (2010) 108
40. J. Liu, Y. Ma, T. Xu, G. Shao, *J. Hazard. Mater*. **178** (2010) 1021
41. T. S. Anirudhan, P. S. Suchithra, *J. Environ. Sci*. **21** (2009) 884
42. B. Pan, B. Pan, W. Zhang, L. Lv, Q. Zhang, S. Zheng, *Chem. Eng. J*. **151** (2009) 19
43. S. S. Wong, T. T. Teng, A. L. Ahmad, A. Zuhairi, G. Najafpour, *J. Hazard. Mater*. **135** (2006) 378
44. K. Jayaram, I. Y. L. N. Murthy, H. Lalhruaitluanga, M. N. V. Prasad, *Colloid Surf., B* **71** (2009) 248
45. E. Pehlivan, G. Arslan, *Fuel Process. Technol*. **88** (2007) 99
46. D. Wu, Y. Sui, S. He, X. Wang, C. Li, H. Kong, *J. Hazard. Mater*. **155** (2008) 415
47. V. T. P. Vinod, R. B. Sashidhar, B. Sreedhar, *J. Hazard. Mater*. **178** (2010) 851
48. W. Ma, J. M. Tobin, *Biochem. Eng. J*. **18** (2004) 33
49. A. Saeed, A. M. Waheed, M. Iqbal, *Sep. Purif. Technol*. **45** (2005) 25
50. H. Yuh-Shan, *Scientometrics* **59** (2004) 171
51. Z. Aksu, *Sep. Purif. Technol*. **21** (2001) 285
52. M. Dogan, M. Aklan, A. Turkyilmaz, *J. Hazard. Mater*. **109** (2004) 141.
53. J. P. Silva, S. Sousa, J. Rodrigues, H. Antunes, J. J. Porter, I. Gonc-Alves, S. F. Dias, *Sep. Purif. Technol*. **40** (2004) 309.